

# Control and Schedule Adjustments of Battery Based Energy Storage in Low-Voltage Distribution Networks



Maximilian J. Zangs  
School of the Built Environment  
University of Reading

A thesis submitted for the degree of  
*Doctor of Philosophy in Electronic Engineering*

2018



*It is not a dream. It is a simple feat of scientific electrical engineering. Electric power can drive the world's machinery without the need of coal, oil or gas. Although perhaps humanity is not yet sufficiently advanced to be willingly lead by the inventor's keen searching sense. Perhaps it is better in this present world of ours where a revolutionary idea may be hampered in its adolescence. All this that was great in the past was ridiculed, condemned, combatted, suppressed only to emerge all the more triumphantly from the struggle. [...] Our duty is to lay the foundation for those who are to come and to point the way, yes humanity will advance with giant strides. We are whirling through endless space with an inconceivable speed, all around everything is spinning, everything is moving, everywhere there is energy.*

— Nicola Tesla



# Abstract

British national low-carbon targets have resulted in a transition within the UK energy and transport sectors. This transition entails the development and uptake of new Low-Carbon Technologies (LCTs). Some technologies (e.g. photovoltaic) can offer demand alleviating services since they can supply electricity to the grid, whilst others (e.g. Electric Vehicles - EVs) will increase demand for grid supplied electricity. Distribution System Operators (DNOs), having to keep the distribution system within statutory constraints, are thus facing significant challenges like more volatility in demand, higher voltage deviation and larger phase unbalance. Energy storage devices can be a feasible alternative to conventional reinforcement activities, since they can be managed actively. Developing novel control for Battery Energy Storage Solutions (BESS) is thus the main focus of this thesis. Extending current literature by developing control algorithms for a single energy system and distributed BESS whilst taking into account the communication requirements for effective control is its main contribution.

More specifically, this thesis explores control methods for the unique characteristics of volatile demand profiles at high temporal resolutions. The novel energy storage control algorithms are designed to incorporate both half-hourly forecasts and sub-half-hourly load volatility in order to take into account both the long term demand trends and its high volatility. Methods developed throughout this thesis address the challenges when controlling a single (i.e. DNO owned) energy store and those chal-

lenges that are encountered in distributed battery systems. Results show how energy storage can effectively improve network operation, even when the underlying demand forecast was erroneous. Real-time control algorithms are studied on a time-series and statistical basis to assess the performance of the developed control methods. All key objectives have been met for each of the presented contributions, and the comparable storage control techniques in literature are either met or exceeded in performance when subjected to the available datasets.

# **Declaration**

I confirm that this is my own work and the use of all material from other sources has been properly and fully acknowledged.

---

Maximilian J. Zangs



# **Dedication**

In gratitude to my British higher education, I dedicate this thesis to my parents.



# Acknowledgements

I would like to begin by thanking my two PhD supervisors and tutors Dr Ben Potter and Dr William Holderbaum for their continuing support, help and guidance throughout my PhD. In addition, I would like to thank the *University of Reading* and sponsors of the *NTVV Project* for providing the funding for my research. Also, I would like to thank the *ITNG* members of the former *School of Systems Engineering* for providing and maintaining the vital computational resources, and I would like to thank our industrial project partner, *Scottish and Southern Electricity Networks*, for providing thei network models and datasets; both were were vital necessities to conduct and complete my research.

I would like to thank members of the *School of the Built Environment*, the *School of Biological Sciences* and the *School of Psychology and Clinical Language Sciences* for taking their time to share, exchange and discuss ideas and for challenging my thinking and expertise throughout the journey towards the PhD. In particular I would like to express special thanks to individuals in the *Energy Research Laboratory*: Dr Timur Yunusov, Ana Rodriguez-Arguelles and Peter Adams; individuals from the *SUSPORTS Project*: Dr Ian Harrison and Stefano Pietrosanti; an individual in the *Brain Embodiment Laboratory*: Asad Malik; and individuals at the *TSBE Centre* and the *School of Construction Management and Engineering*: Alice Gunn and Vicky Papaioannou.

There are many current and past colleagues, researchers and friends who have

not only technically aided my research, but have also reminded me of life outside academia. Through their willingness to listen, motivate, support and (sometimes) distract me, they have made my time as a PhD student considerably more enjoyable; so thank you.

Last but not least, I would like to express my greatest gratitude and thanks to my family for all of their support and understanding throughout my PhD and time at university; it is much appreciated and I could not have done it without you.

# Contents

<b>Abstract</b>	iii
<b>Declaration</b>	v
<b>Dedication</b>	vii
<b>Acknowledgements</b>	ix
<b>Table of Contents</b>	xi
<b>Table of Figures</b>	xvi
<b>Nomenclature</b>	xxv
<b>1 Introduction</b>	1
1.1 Background and motivation . . . . .	2
1.1.1 Topology and challenges of the UK electricity network . . . . .	5
1.1.2 Solutions to mitigate impact of LCT . . . . .	8
1.1.3 Smart control . . . . .	9
1.2 Problem statement and research objectives . . . . .	11
1.3 Contributions to knowledge . . . . .	13
1.4 Publications . . . . .	14
1.5 Thesis structure . . . . .	15

<b>2 Literature Review</b>	<b>19</b>
2.1 Overview . . . . .	19
2.2 Role of energy storage - a survey . . . . .	20
2.3 Energy storage research for LV application . . . . .	26
2.3.1 Voltage control . . . . .	27
2.3.2 Power flow management . . . . .	30
2.4 Control of energy storage and its applications . . . . .	33
2.4.1 Off-line and on-line control . . . . .	34
2.4.2 Centralised and distributed control . . . . .	37
2.4.3 Communication-less control . . . . .	41
2.5 Summary of gaps in literature . . . . .	44
<b>3 Improving network performance by adjusting battery operation at sub-half-hourly resolution</b>	<b>47</b>
3.1 Overview . . . . .	47
3.2 Key network parameters and derived cost functions . . . . .	49
3.2.1 Voltage related cost functions . . . . .	51
3.2.2 Power related cost functions . . . . .	56
3.2.3 Current related cost functions . . . . .	60
3.3 Data, models and storage scheduling . . . . .	62
3.3.1 Load profiles . . . . .	62
3.3.2 Network model . . . . .	63
3.3.3 Battery model . . . . .	63
3.3.4 ESMU scheduling . . . . .	67
3.4 Optimisation method . . . . .	72
3.4.1 Closed-loop schedule adjustment . . . . .	72
3.4.2 Execution and result assessment procedure . . . . .	74
3.5 Results and Discussion . . . . .	77

3.5.1	Time Series Analysis . . . . .	78
3.5.2	Difference Analysis . . . . .	85
3.5.3	Probability Density Analysis . . . . .	90
3.6	Summary . . . . .	92
<b>4</b>	<b>Real-Time Adjustment of Battery Operation using MPC Guided Schedule Deviation</b>	<b>95</b>
4.1	Overview . . . . .	95
4.2	System Explanation . . . . .	97
4.2.1	ESMU model . . . . .	99
4.2.2	Load data and ESMU scheduling . . . . .	99
4.3	Control of ESMU . . . . .	104
4.3.1	Dynamic control . . . . .	105
4.3.2	Model predictive control . . . . .	108
4.4	Case studies . . . . .	111
4.5	Results and discussion . . . . .	112
4.5.1	Time-series analysis . . . . .	113
4.5.2	Daily peak reduction . . . . .	115
4.5.3	Probability of peak reduction . . . . .	117
4.5.4	Impact of varying the model's length . . . . .	119
4.6	Summary . . . . .	121
<b>5</b>	<b>Effects of Desynchronising Information Propagation when Distributing Smart-Charging</b>	<b>125</b>
5.1	Overview . . . . .	125
5.2	Coordination of EV charging . . . . .	128
5.2.1	EV Demand . . . . .	128
5.2.2	Base Load . . . . .	129

5.2.3	Scheduling Algorithm . . . . .	129
5.3	Distributed Systems . . . . .	136
5.3.1	MAS Implementation . . . . .	138
5.3.2	MAS Desynchronisation . . . . .	139
5.3.3	Cases and Performance Metrics . . . . .	141
5.4	Results and Discussion . . . . .	145
5.4.1	Algorithm performance for synchronised operation . . . . .	145
5.4.2	Algorithm performance for desynchronised operation with regular timing . . . . .	150
5.4.3	Algorithm performance for desynchronised operation with irregular timing . . . . .	153
5.5	Summary . . . . .	156

<b>6</b>	<b>Cooperative Battery Operation of without Communications Infrastructure Needs</b>	<b>159</b>
6.1	Overview . . . . .	159
6.2	Related Work . . . . .	161
6.3	System Modelling . . . . .	162
6.3.1	Assumptions . . . . .	163
6.3.2	EV charging behaviour . . . . .	164
6.3.3	Battery Modelling . . . . .	168
6.3.4	Network Models . . . . .	170
6.4	Storage Control . . . . .	171
6.4.1	Algorithm Parameters . . . . .	171
6.4.2	AIMD Algorithm Structure . . . . .	174
6.4.3	Reference Voltage Profile . . . . .	175
6.5	Scenarios and Comparison Metrics . . . . .	176
6.5.1	Test Cases and Scenarios . . . . .	176

6.5.2	Performance Metric Definition . . . . .	177
6.5.2.1	Parameter for Voltage Improvement . . . . .	177
6.5.2.2	Parameter for Line Overload Reduction . . . . .	178
6.5.2.3	Parameter for the Improvement of Battery Cycling .	180
6.6	Results and Discussion . . . . .	181
6.6.1	Voltage Violation Analysis . . . . .	181
6.6.2	Line Overload Analysis . . . . .	184
6.6.3	Battery Utilisation Analysis . . . . .	187
6.7	Summary . . . . .	190
<b>7</b>	<b>Conclusion</b>	<b>193</b>
7.1	Overview of Main Findings . . . . .	193
7.2	Knowledge Contribution . . . . .	197
7.3	Research Limits . . . . .	198
7.3.1	Energy storage model . . . . .	199
7.3.2	Electric vehicle charging . . . . .	199
7.3.3	Data . . . . .	199
7.3.4	Network models . . . . .	200
7.4	Future Work . . . . .	201
7.4.1	Energy storage model . . . . .	201
7.4.2	Network model and power flow simulation . . . . .	201
7.4.3	Different MPC . . . . .	202
7.4.4	Governance . . . . .	202
7.4.5	Data acquisition and estimation . . . . .	203
<b>References</b>		<b>204</b>
<b>A</b>	<b>Additional Results</b>	<b>233</b>

A.1	Improving operation performance of battery schedules at sub-half-hourly resolution . . . . .	233
A.1.1	Additional Time Series Analysis . . . . .	233
A.1.2	Additional Difference Analysis . . . . .	242
A.1.3	Probability Density Analysis . . . . .	251
<b>B</b>	<b>Multi-Agent Systems</b>	<b>257</b>
B.1	FIPA Implementation . . . . .	257
B.2	Communication Protocols . . . . .	258
B.2.1	FIPA Query Protocol . . . . .	258
B.2.2	FIPA Brokering protocol . . . . .	260
B.2.3	FIPA ContractNet Protocol . . . . .	261

# List of Figures

1.1	Change in residential annual electricity demand excluding electric vehicles from FES2017 [1] . . . . .	3
1.2	Rise in energy demand due to the uptake of electric vehicles as predicted by FES 2017 [1] . . . . .	4
1.3	Change in annual peak power demand as predicted by FES2017 [1] . . . . .	4
2.1	Energy storage applications and corresponding value for various discharge durations [2] . . . . .	21
2.2	Energy Storage Management Unit overview: (a) 12.5kWh Energy Storage Unit, (b) Power Electronics Unit, (c) deployed 12.5kWh system, (d) deployed 25kWh system - pictures are taken from the NTVV close down report [3] . . . . .	32
3.1	Cost function $\zeta_{\text{voltage}}(v_\phi)$ values for different substation voltages . . . . .	53
3.2	Sketch of the benefits that occur when ESMU injects power into the feeder in order to mitigate the voltage drop along the cable . . . . .	54
3.3	Voltage at the loads in the IEEE LV Test Case network for a total load of 440kVA against distance between the corresponding load and substation: for the quadratic fit $R^2 = 58.76\%$ . . . . .	55
3.4	Sample network imbalance for different phase loadings as defined in ANSI/NEMA MG 1-2011 . . . . .	58

3.5	Losses against increasing power demand . . . . .	60
3.6	Cost of line or fuse utilisation against network current . . . . .	61
3.7	A power flow plot of the IEEE-PES European Test Case Feeder, i.e. a LV distribution network in the UK. . . . .	64
3.8	Flowchart to calculate the next SOC (i.e. $SOC(t + \Delta t)$ ) based on current ESMU power (i.e. $s_{ESMU}(t)$ which is predefined) and current SOC (i.e. $SOC(t)$ which is predefined). . . . .	67
3.9	Highly variable and volatile demand profile vs half-hourly demand (i.e. a forecast under perfect foresight conditions) . . . . .	69
3.10	Impact of half-hourly ESMU schedule on sub-half-hourly power profile	71
3.11	ESMU schedule adjustment flow diagram . . . . .	73
3.12	Method execution and results assessment flowchart . . . . .	75
3.13	Voltage level modifications as noted at the ESMU's PCC by adjusting its schedule . . . . .	78
3.14	Voltage level improvements at all buses in the entire distribution network due to the ESMU schedule adjustment. . . . .	80
3.15	Reduction of the network's phase unbalance due to the adjustment of the ESMU schedule. . . . .	81
3.16	Neutral power reduction due to the ESMU schedule adjustments . . .	82
3.17	Power factor cost improvements due to the adjustment of the ESMU schedule . . . . .	83
3.18	Instantaneous losses of the distribution network when adjusting the ESMU schedule in order to reduce the former (energy lost: 75.9Wh for base; 74.7Wh for normal; 69.9Wh for minimised). . . . .	84
3.19	Improvement of the worst line utilisation across the entire network when adjusting the ESMU schedule correspondingly. . . . .	84

3.20	Cost improvement spread, when comparing against the <i>normal</i> ESMU operation case and when optimising for the underlying cost (a separate y-axis is introduced for the optimisation of “neutral power”). . . . .	86
3.21	Relative cost improvement spread, when comparing against the <i>normal</i> ESMU operation case and when optimising for the underlying cost. . . . .	87
4.1	(4.1a) Traditional forecast driven BESS control; (4.1b) Traditional on-line system; (4.1c) Proposed dynamic control system . . . . .	97
4.2	An example of applying a half-hourly ESMU schedule to its half-hourly schedule (Subfig. 4.2a) and the actual, sub-half-hourly daily load (Subfig. 4.2b). . . . .	103
4.3	Dynamic controller breakdown as previously shown in Figure 4.1c. . . . .	104
4.4	Underlying time-series based compensation strategy for compensator $\text{PID}_2$ . . . . .	106
4.5	Example of exogenous auto-regressive model that is used for model predictive control. Here, $t - \Delta t$ indicates the time delay by one sample period. . . . .	110
4.6	Time series performance over a single day when using realistic load forecasts: (4.6a) total day; (4.6b) zoomed in on critical period . . . . .	114
4.7	Daily peak reduction when using realistic forecasts as: (4.7a) peak power values; (4.7b) percentage of original case <b>B</b> . . . . .	116
4.8	Peak load probability for different prediction mechanisms. . . . .	117
4.9	Probability of peak load reduction for different prediction mechanisms. . . . .	118
4.10	Probability of peak load reduction for different prediction mechanisms and different AR/ARX model lengths. . . . .	120
4.11	Visualisation of the peak power distribution for different AR/ARX model lengths. . . . .	121

5.1	Example of agent synchronisation process before re-scheduling their EVs charging profile. . . . .	130
5.2	Charging power (green line) allocation on top of base network load (black line) for valley-filling behaviour. Here $n = 1$ for Fig. 5.2a, $n = 2$ for Fig. 5.2b, $n = 3$ for Fig. 5.2c, and $n = N$ for Fig. 5.2d. . .	132
5.3	A simplified MAS structure containing virtual seller and buyer agents (white), that negotiate power/charging profiles for physical entities (grey). . . . .	137
5.4	The implementation of FIPA on <i>HTCondor</i> . . . . .	138
5.5	Example of agent desynchronisation when running through algorithm iterations in their respective execution loop. Here, communication events may be in quick succession, but are never at the exact same time. . . . .	140
5.6	Synchronised time series evolution for $\alpha = 0.02$ and $\beta = 0.20$ , where (a) is at $n = 1$ , (b) is at $n = 2$ , (c) is at $n = 3$ , and (d) is at $n = N - 1$ . 146	
5.7	Synchronised time series evolution for $\alpha = 1.00$ and $\beta = 1.00$ , where (a) is at $n = 1$ , (b) is at $n = 2$ , (c) is at $n = 3$ , and (d) is at $n = N - 1$ . 147	
5.8	Full range analysis of $\alpha$ and $\beta$ for the synchronised MAS where, (a) shows the final $\zeta_{\text{PAR}}$ , (b) shows the convergence, $b$ , for $\zeta_{\text{PAR}}$ , (c) shows the final $\zeta_{\text{TRA}}$ , and (d) shows the convergence, $b$ , for $\zeta_{\text{TRA}}$ (red indicates missing data). . . . .	149
5.9	Desynchronised time series evolution for $\alpha = 0.02$ and $\beta = 0.20$ , where (a) is at $n = 1$ , (b) is at $n = 2$ , (c) is at $n = 3$ , and (d) is at $n = N - 1$ . 151	
5.10	Full range analysis of $\alpha$ and $\beta$ for the desynchronised MAS where, (a) shows the final $\zeta^{\text{PAR}}$ , (b) shows the convergence, $b$ , for $\zeta^{\text{PAR}}$ , (c) shows the final $\zeta^{\text{TRA}}$ , and (d) shows the convergence, $b$ , for $\zeta^{\text{TRA}}$ (red indicates missing data). . . . .	152

5.11 Desynchronised time series evolution when using irregular loop delays for $\alpha = 0.02$ and $\beta = 0.20$ , where (a) is at $n = 1$ , (b) is at $n = 2$ , (c) is at $n = 3$ , and (d) is at $n = N - 1$ . . . . .	154
5.12 Full range analysis of $\alpha$ and $\beta$ for the desynchronised MAS with irregular loop delays where, (a) shows the final $\zeta^{\text{PAR}}$ , (b) shows the convergence, $b$ , for $\zeta^{\text{PAR}}$ , (c) shows the final $\zeta^{\text{TRA}}$ , and (d) shows the convergence, $b$ , for $\zeta^{\text{TRA}}$ (red indicates missing data). . . . .	155
6.1 The probability of starting a trip at a particular time during a weekday, extrapolated into three normal distributions (RMS error: 9.482%) . . . . .	165
6.2 The probability of a trip being of a particular distance during a weekday, extrapolated into a Weibull distribution (RMS error: 3.791%). . . . .	167
6.3 Excerpt from the aggregated 50 EVs; charging powers that were each generated from the empirical models. . . . .	167
6.4 Sample OpenDSS power networks, where consumers are indicated as red crosses and 11/0.416-kV substations are marked with a green square. Here, (a) is the IEEE PES EU LV test feeder, and (b) is a SSEN Common Information Model (CIM) based feeder . . . . .	170
6.5 An example plot showing the difference between the fixed voltage threshold (AIMD) and the reference voltage profile (AIMD+) against the load's distance to its feeding substation. . . . .	175
6.6 Mean voltage profiles for all four test cases over a single day. . . . .	181
6.7 Voltage level probability distribution for the entire feeder where $\zeta_{\mathbf{C}}^* = -0.153$ and $\zeta_{\mathbf{D}}^* = -0.135$ . . . . .	182
6.8 Comparison of voltage improvement indices for (a) $\zeta_{\mathbf{C}}^*$ indices (AIMD); (b) $\zeta_{\mathbf{D}}^*$ indices (AIMD+). . . . .	183
6.9 Average $\zeta_{\mathbf{C}}^*$ and $\zeta_{\mathbf{D}}^*$ values recorded against the corresponding storage uptake. . . . .	183

6.10 Line utilisation probability distribution of all lines in the simulated feeder where $\zeta_{\mathbf{C}}^{**} = -0.360$ and $\zeta_{\mathbf{D}}^{**} = -0.518$ . . . . .	184
6.11 Comparison of line utilisation improvement indices for (a) $\zeta_{\mathbf{C}}^*$ indices (AIMD); (b) $\zeta_{\mathbf{D}}^*$ indices (AIMD+). . . . .	185
6.12 Average $\zeta_{\mathbf{C}}^{**}$ and $\zeta_{\mathbf{D}}^{**}$ values recorded against the corresponding storage uptake. . . . .	186
6.13 Battery power profiles of each load's battery storage device over four days for (a) <b>Case C</b> and (b) <b>Case D</b> . . . . .	188
6.14 Each load's battery cycling compared for (a) each BESS and (b) the two cases, where $\zeta_{\mathbf{C}}^{***} = 3.89$ and $\zeta_{\mathbf{D}}^{***} = 2.54$ . . . . .	188
6.15 Peak-to-Average Ratios (PAR) of the battery cycling profiles of each load's battery storage device over four days for (a) <b>Case C</b> and (a) <b>Case D</b> . . . . .	189
6.16 The performance index $\zeta_{\mathbf{C}}^{**}$ for AIMD storage and $\zeta_{\mathbf{D}}^{***}$ for AIMD+ storage control against storage uptake. . . . .	190
A.1 Additional substation voltage level comparison between base, normal and the case where the ESMU's schedule was adjusted. . . . .	234
A.2 Additional ESMU voltage level comparison between base, normal and the case where the ESMU's schedule was adjusted. . . . .	235
A.3 Additional voltage level comparison between base, normal and the case where the ESMU's schedule was adjusted. . . . .	236
A.4 Additional phase unbalance cost comparison between base, normal and the case where the ESMU's schedule was adjusted. . . . .	237
A.5 Additional power factor cost comparison between base, normal and the case where the ESMU's schedule was adjusted. . . . .	238
A.6 Additional comparison of the substation fuse utilisation between base, normal and the case where the ESMU's schedule was adjusted. . . . .	239

A.7 Additional line utilisation comparison between base, normal and the case where the ESMU's schedule was adjusted. . . . .	240
A.8 Additional comparison of distribution loss cost between base, normal and the case where the ESMU's schedule was adjusted. . . . .	241
A.9 Cost difference spread, based on the ESMU schedule adjustment to minimise substation voltage deviation . . . . .	242
A.10 Cost difference spread, based on the ESMU schedule adjustment to minimise ESMU's PCC voltage deviation . . . . .	243
A.11 Cost difference spread, based on the ESMU schedule adjustment to minimise the maximum voltage deviation on any bus of the network .	244
A.12 Cost difference spread, based on the ESMU schedule adjustment to minimise the network's phase unbalance . . . . .	245
A.13 Cost difference spread, based on the ESMU schedule adjustment to minimise the network's power flow in the neutral conductor . . . . .	246
A.14 Cost difference spread, based on the ESMU schedule adjustment to minimise the network's offset to unity power factor . . . . .	247
A.15 Cost difference spread, based on the ESMU schedule adjustment to minimise the substation's fuse utilisation . . . . .	248
A.16 Cost difference spread, based on the ESMU schedule adjustment to minimise the maximum line utilisation of any line in the network . . .	249
A.17 Cost difference spread, based on the ESMU schedule adjustment to minimise distribution losses . . . . .	250
A.18 Raw time-series that are supposed to be compared. . . . .	252
A.19 Rescaled time-series that are supposed to be compared. . . . .	252
A.20 Averaged log-scaled time-series. . . . .	253
A.21 Splitting of the conditioned data into two stationary sections . . . . .	253
A.22 Difference of the two pre-conditioned time-series. . . . .	254

A.23 Auto-correlation of signal for (A.23a) morning and (A.23b) afternoon sections . . . . .	254
B.1 FIPA Query Protocol flow chart . . . . .	259
B.2 FIPA Brokering Protocol flow chart . . . . .	260
B.3 FIPA ContractNet Protocol flow chart . . . . .	261

# Nomenclature

## Acronyms

ACL	Agent Communication Language
ADMD	After Diversity Maximum Demand
AIMD	Additive Increase Multiplicative Decrease
AR	Auto-Regressive
ARMAX	Auto-Regressive Moving-Average Exogenous
ARX	Auto-Regressive Exogenous
BES	Battery Energy Storage
BESS	Battery Energy Storage System
CAES	Compressed Air Energy Storage
CREST	Centre for Renewable Energy Systems Technology
DER	Distributed Energy Resource
DG	Distributed Generation
DNO	Distribution Network Operator
DOD	Depth of Discharge
DSM	Demand Side Management
DSR	Demand Side Response
ENW	Electricity North West
EPRI	Electric Power Research Institute
ERL	Energy Research Laboratory
ESMU	Energy Storage Management Unit

ESQCR	Electricity Supply Quality and Continuity Regulations
ESS	Energy Storage Solution
EV	Electric Vehicle
FCES	Fuel Cell driven Energy Storage
FES	Future Energy Scenarios
FIPA	Foundation for Intelligent Physical Agents
FIPA	Foundation for Intelligent Physical Agents
GB	Great Britain
ICT	Information and Communication Technology
IoT	Internet of Things
IoT	Internet of Things
JADE	JAVA Agent Communication Language
JADE	Java Agent Development Environment
LCT	Low Carb on Technology
MPC	Model-Predict Control
NARX	Nonlinear Auto-Regressive Exogenous
NTVV	New Thames Valley Vision
OLTC	On-Line Tap-Changer
P2N	Phase to Neutral
P2P	Phase to Phase
PCC	Point of Common Coupling
PID	Proportional Integrating Derivative (control)
PMU	Power Management Unit
PV	Photovoltaic
SCADA	Supervisory Control And Data Acquisition
SMU	Storage Management Unit
SOC	State of Charge

SPC	Set-Point Control
SQP	Sequential Quadratic Programming
SSEN	Scottish and Southern Electricity Networks
TES	Thermal Energy Storage
UK	United Kingdom
UoR	University of Reading
V2G	Vehicle to Grid
VPP	Virtual Power Plant

### Definition variables and dimensionality

$\mathbb{C}^B$	The $B$ -dimensional set of all complex numbers (e.g. $\mathbb{Z}^{N \times 3}$ is $N \times 3$ dimensional)
$\mathbb{R}_B^A$	The $A$ -dimensional set of all real numbers that lie within a range defined in $B$ (e.g. $\mathbb{R}_{\geq 0}^{N \times 3}$ is $N \times 3$ dimensional set of all real numbers greater than or equal to zero)
$\mathbb{Z}_B^A$	The $A$ -dimensional set of all integers that lie within a range defined in $B$ (e.g. $\mathbb{Z}_{\geq 0}^{N \times 3}$ is $N \times 3$ dimensional set of all integers greater than or equal to zero)
$\mathbf{x} = (x(t))$	The element $x(t)$ is part of the vector $\mathbf{x}$
$\mathbf{X}$	A matrix named $\mathbf{X}$
$\mathbf{x}$	A vector named $\mathbf{x}$
$x \in (0, 1)$	Scalar named $x$ can take any number within in the exclusive range between zero and one
$x \in [0, 1]$	Scalar named $x$ can take any number within in the inclusive range between zero and one
$x \in \{0, \dots, N\}$	Scalar named $x$ can take any number within the discrete set of numbers of the sequence $\{0, \dots, N\}$
$x$	A scalar named $x$

### Symbols used in Chapter 3

$\Delta E_{\text{bat}}(t)$	Change in stored energy at time $t$ , where $\Delta E_{\text{bat}}(t) \in \mathbb{R}$
$\delta s_{\text{ESMU},\phi}(t)$	Three-phase apparent ESMU power adjustment vector at time $t$ , where $(\delta s_{\text{ESMU},\phi}(t)) = \delta \mathbf{s}_{\text{ESMU}}(t)$ and $\delta s_{\text{ESMU},\phi}(t) \in \mathbb{C}$

$\Delta t$	Sample time, where $\Delta t \in \mathbb{Z}_{\geq 0}$
$\delta \mathbf{s}_{\text{ESMU}}(t)$	Three-phase apparent ESMU power adjustment vector at time $t$ , where $(\delta s_{\text{ESMU},\phi}(t)) = \delta \mathbf{s}_{\text{ESMU}}(t)$ and $\delta \mathbf{s}_{\text{ESMU}}(t) \in \mathbb{C}^\Phi$
$\eta$	Round-trip efficiency of power electronics, where $\eta \in (0, 1]$
$\mu$	Self-discharge losses of battery, where $\mu \in (0, 1]$
$\Phi$	Number of phases, where $\Phi \in \mathbb{Z}_{>0}$ here $\Phi = 3$
$\phi$	Phase number, where $\phi \in \{1, \dots, \Phi\}$
$\mathbf{i}_{\text{line}}(t)$	Multi-phase line currents at time $t$ , where $\mathbf{i}_{\text{line}}(t) = (i_{\text{line},l,\phi}(t))$ , and $\mathbf{i}_{\text{line}}(t) \in \mathbb{R}^{L \times \Phi}$
$\mathbf{i}_{ss}(t)$	Multi-phase substation current at time $t$ , where $\mathbf{i}_{ss}(t) \in \mathbb{R}^\Phi$
$\mathbf{s}_{\text{net}}^*$	Half-hourly network load, where $\mathbf{s}_{\text{net}}^* \in \mathbb{C}^{\frac{T_{\text{sch}}}{K}}$
$\mathbf{s}_{\text{ESMU}}(t)$	Three-phase apparent ESMU power at time $t$ , where $\mathbf{s}_{\text{ESMU}}(t) = (s_{\text{ESMU},\phi}(t))$ and $\mathbf{s}_{\text{ESMU}}(t) \in \mathbb{C}^\Phi$
$\mathbf{s}_{\text{load}}(t)$	Apparent load power vector of all loads at time $t$ , where $\mathbf{s}_{\text{load}}(t) \in \mathbb{C}^I$
$\mathbf{s}_{ss}(t)$	Apparent multi-phase power at substation level at time $t$ , where $\mathbf{s}_{ss}(t) \in \mathbb{C}^\Phi$
$\mathbf{v}_{\text{ESMU}}(t)$	Multi-phase voltage vector at ESMU at time $t$ , where $\mathbf{v}_{\text{ESMU}}(t) = (v_{\text{ESMU},\phi}(t))$ and $v_{\text{ESMU},\phi}(t) \in \mathbb{C}^\Phi$
$\mathbf{v}_{\text{load}}(t)$	Multi-phase load voltage vector at time $t$ , where $\mathbf{v}_{\text{load}}(t) = (v_{\text{load},i,\phi}(t))$ and $\mathbf{v}_{\text{load}}(t) \in \mathbb{C}^{I \times \Phi}$
$\mathbf{v}_{ss}(t)$	Phase voltage vector at time $t$ , where $\mathbf{v}_{ss}(t) \in \mathbb{R}^\Phi$
$\text{UF}(\mathbf{x})$	Function calculating the Unbalance Factor (UF) for any multidimensional vector $\mathbf{x}$ , where $\mathbf{x} = (x_n)$ , $n \in \mathbb{Z}_{>0}$ and $\text{UF}(\mathbf{x}) \in \mathbb{R}_{\geq 0}$
$\zeta_{\text{fuse utilisation}}(\mathbf{i}_{ss}(t))$	Fuse utilisation cost, derived from multi-phase substation current vector $\mathbf{i}_{ss}$ at time $t$ , where $\zeta_{\text{fuse utilisation}}(\mathbf{i}_{ss}(t)) \in \mathbb{R}_{\geq 0}$
$\zeta_{\text{load voltage}}(\mathbf{v}(t))$	Voltage deviation cost for load voltage vector $\mathbf{v}$ at time $t$ and $\zeta_{\text{load voltage}}(\mathbf{v}(t)) \in \mathbb{R}_{\geq 0}$
$\zeta_{\text{losses}}(s(t))$	Losses based cost function, where $\zeta_{\text{losses}}(s(t)) \in \mathbb{R}_{\geq 0}$
$\zeta_{\text{MMD}}(\mathbf{s})$	Cost of the underlying power profile $\mathbf{s}$ , based on the Minimum-Maximum Difference (MMD), where $\zeta_{\text{MMD}}(\mathbf{s}) \in \mathbb{R}_{\geq 0}$

$\zeta_{\text{neutral load}}(\mathbf{s}(t))$	Neutral load cost function for multi-phase apparent power vector $\mathbf{s}$ at time $t$ , where $\zeta_{\text{neutral load}}(\mathbf{s}(t)) \in \mathbb{R}_{\geq 0}$
$\zeta_{\text{PAR}}(\mathbf{s})$	Cost of the underlying power profile $\mathbf{s}$ , based on the Peak to Average Ratio (PAR), where $\zeta_{\text{PAR}}(\mathbf{s}) \in \mathbb{R}_{\geq 0}$
$\zeta_{\text{PF}}(\mathbf{s}(t))$	Power Factor (PF) cost function for multi-phase apparent power vector $\mathbf{s}$ at time $t$ , where $\zeta_{\text{PF}}(\mathbf{s}(t)) \in \mathbb{R}_{\geq 0}$
$\zeta_{\text{TRA}}(\mathbf{s})$	Cost of the underlying power profile $\mathbf{s}$ , based on the power transients (TRA), where $\zeta_{\text{MMD}}(\mathbf{s}) \in \mathbb{R}_{\geq 0}$
$\zeta_{\text{unbalance}}(\mathbf{s}(t))$	Power unbalance for multi-phase apparent power vector $\mathbf{s}$ at time $t$ , where $\zeta_{\text{unbalance}}(\mathbf{s}(t)) \in \mathbb{R}_{\geq 0}$
$\zeta_{\text{voltage}}(\mathbf{v}(t))$	Voltage deviation cost for voltage vector $\mathbf{v}$ at time $t$ , where $\zeta_{\text{voltage}}(\mathbf{v}(t)) \in \mathbb{R}_{\geq 0}$
$C_{\text{bat}}$	Battery capacity, where $C_{\text{bat}} \in \mathbb{R}_{>0}$
$C_f$	Charge factor or “C-factor” of the battery, where $C_f \in \mathbb{R}_{>0}$
$E_{\text{bat}}(t)$	Energy stored in battery at time $t$ , where $E_{\text{bat}}(t) \in \mathbb{R}_{>0}$
$I_{\text{fuse}}$	Nominal fuse rating at substation, where $I_{\text{fuse}} \in \mathbb{R}$
$i_{\text{line},l,\phi}(t)$	Single-phase line current for phase $\phi$ of line $l$ at time $t$ , where $i_{\text{line},l,\phi}(t) \in \mathbb{R}$
$I_{\text{nom},l}$	Nominal line current for line $l$ , $I_{\text{nom},l} \in \mathbb{R}$
$i_{\text{ss},\phi}(t)$	Single-phase substation current for phase $\phi$ at time $t$ , where $i_{\text{ss},\phi}(t) \in \mathbb{R}$
$K$	Number of sample periods over which the sub-half-hourly is to be downsampled, where $K \in \mathbb{Z}_{>0}$ and $\frac{T_{\text{sch}}}{K} \in \mathbb{Z}_{>0}$
$k(t)$	Synchronisation function used to downsample the sub-half-hourly profile
$L$	Number of lines, where $L \in \mathbb{Z}_{>0}$
$l$	Line number, where $l \in [1, \dots, L]$
$p_{\text{bat}}(t)$	Single-phase active battery power at time $t$ , where $p_{\text{bat}}(t) \in \mathbb{R}$
$s_{\text{net}}^*(t)$	Half-hourly network load, where $\mathbf{s}_{\text{net}}^* = (s_{\text{net}}^*(t))$ and $s_{\text{net}}^*(t) \in \mathbb{C}$
$s_{\text{losses}}(t)$	Total apparent power losses in the network $s_{\text{losses}}(t) \in \mathbb{C}$
$s_{\text{net}}(t)$	Apparent network load at time $t$ , where $s_{\text{net}}(t) \in \mathbb{C}$

$S_{\text{rating}}$	Rating of battery's power electronics, where $S_{\text{rating}} \in \mathbb{R}_{>0}$
$s_{\text{ESMU},\phi}(t)$	Single-phase apparent ESMU power for phase $\phi$ at time $t$ , where $\mathbf{s}_{\text{ESMU}}(t) = (s_{\text{ESMU},\phi}(t))$ and $s_{\text{ESMU},\phi}(t) \in \mathbb{C}$
$s_{\text{load},i}(t)$	Apparent load power for load $i$ at time $t$ , where $\mathbf{s}_{\text{load}}(t) = (s_{\text{load},i}(t))$ and $s_{\text{load},i}(t) \in \mathbb{C}$
$s_{\text{ss},\phi}(t)$	Apparent single-phase power at substation level for phase $\phi$ at time $t$ , where $\mathbf{s}_{\text{ss}}(t) = (s_{\text{ss},\phi}(t))$
$SOC(t)$	State of charge at time $t$ , where $SOC(t) \in (0, 1)$
$T$	Length of simulation, where $T \in \mathbb{Z}_{\geq 0}$
$t$	Time-steps of the simulation, where $t \in \{1, \Delta t, 2\Delta t, \dots, T\}$
$T_{\text{sch}}$	Scheduling horizon, where $T_{\text{sch}} \in \mathbb{Z}_{>0}$
$V_{\text{ss}}$	Nominal substation voltage, where $V_{\text{ss}} \in \mathbb{R}$
$V_h$	High-voltage threshold of statutory voltage band, where $V_h \in \mathbb{R}$
$V_l$	Low-voltage threshold of statutory voltage band, where $V_l \in \mathbb{R}$
$v_{\text{ESMU},\phi}(t)$	Phase voltage at ESMU for phase $\phi$ at time $t$ , where $\mathbf{v}_{\text{ESMU}}(t) = (v_{\text{ESMU},\phi}(t))$ and $v_{\text{ESMU},\phi}(t) \in \mathbb{C}$
$v_{\text{load},i,\phi}(t)$	Phase voltage of load $i$ for phase $\phi$ at time $t$ , where $\mathbf{v}_{\text{load}}(t) = (v_{\text{load},i,\phi}(t))$ and $v_{\text{load},i,\phi}(t) \in \mathbb{C}$
$v_{\text{ss},\phi}$	Phase voltage at substation for phase $\phi$ at time $t$ , where $\mathbf{v}_{\text{ss}}(t) = (v_{\text{ss},\phi}(t))$

#### Symbols used in Chapter 4

$\boldsymbol{\alpha}$	PID weight vector for SOC compensator $\text{PID}_1$ , where $\boldsymbol{\alpha} = \{\alpha_P, \alpha_I, \alpha_D\}$ and $\boldsymbol{\alpha} \in \mathbb{R}^3$
$\boldsymbol{\beta}$	PID weight vector for MPC compensator $\text{PID}_2$ , where $\boldsymbol{\beta} = \{\beta_P, \beta_I, \beta_D\}$ and $\boldsymbol{\beta} \in \mathbb{R}^3$
$\Delta t$	Sub-half-hourly sample period, where $\Delta t \in \mathbb{Z}^{>0}$
$\eta$	Round-trip efficiency of power electronics, where $\eta \in (0, 1]$
$\hat{p}_{\text{net}}(t + \Delta t)$	Predicted next network power at sample $t$
$\mu$	Self-discharge losses of battery, where $\mu \in (0, 1]$
$\mathbf{a}$	Weight vector for compensator input regression of the AR model, where $\mathbf{a} = \mathbb{R}^N$

<b>b</b>	Weight vector for compensator output regression of the AR model, where $\mathbf{b} = \mathbb{R}^N$
<b>p</b>	ESMU power vector, where $\mathbf{p} = (p(t))$
$\mathbf{p}_{\text{for}}$	Half-hourly load forecast vector that is used for computing the ESMU schedule, where $\mathbf{p}_{\text{for}} = (p_{\text{for}}(k(t)))$
$\mathbf{p}_{\text{sch}}$	Half-hourly schedule vector that is generated from the load forecast, where $\mathbf{p}_{\text{sch}} = (p_{\text{sch}}(k(t)))$
$\mathbf{p}_{\text{bat}}$	Battery power vector, where $\mathbf{p}_{\text{bat}} = (p_{\text{bat}}(t))$
$\zeta(\mathbf{p})$	Global cost for a given power profile $\mathbf{p}$
$\zeta_{\text{MMD}}(\mathbf{p})$	Cost of a power profile $\mathbf{p}$ , based on the difference between minimum and maximum power, where $\zeta_{\text{MMD}}(\mathbf{p}) \in \mathbb{R}_{\geq 0}$
$\zeta_{\text{PAR}}(\mathbf{p})$	Cost of a power profile $\mathbf{p}$ , based on Peak-to-Average Ratio (PAR), where $\zeta_{\text{PAR}}(\mathbf{p}) \in \mathbb{R}_{\geq 0}$
$\zeta_{\text{TRA}}(\mathbf{p})$	Cost of a power profile $\mathbf{p}$ , based on largest power transient, where $\zeta_{\text{TRA}}(\mathbf{p}) \in \mathbb{R}_{\geq 0}$
$C_{\text{bat}}$	Battery capacity in kWh, where $C_{\text{bat}} \in \mathbb{Z}^{>0}$
$C_f$	Charge factor or “C-factor” of the battery, where $C_f \in \mathbb{Z}^{>0}$
$E_{\text{SOC}}(t)$	Error in state of charge at sample $t$ , where $E_{\text{SOC}}(t) \in \mathbb{R}$
$E_p(t)$	Difference between current and predicting network power at sample $t$ , where $E_p(t) \in \mathbb{R}$
$k(t)$	Sampling time conversion function, linking sub-half hourly samples $t$ at sampling period $\Delta r$ to half-hourly period $30\Delta t$
$N$	Number of regressors of the AR model, where $N \in \mathbb{Z}_{>0}$
$p(t)$	ESMU power at time $t$ , where $\mathbf{p} = (p(t))$ and $p(t) \in \mathbb{Z}$
$p_1(t)$	Corrective ESMU power components from PID <sub>1</sub> , where $p_1(t) \in \mathbb{R}$
$p_2(t)$	Corrective ESMU power components from PID <sub>2</sub> , where $p_2(t) \in \mathbb{R}$
$p_{\text{for}}(k(t))$	Half-hourly load forecast that is used for computing the ESMU schedule, where $p_{\text{for}}(k(t)) \in \mathbb{Z}$
$p_{\text{net}}(t)$	Most recent network demand at sample $t$ , where $\mathbf{p}_{\text{net}} = (p_{\text{net}}(t))$ and $p_{\text{net}}(t) \in \mathbb{R}$
$p_{\text{sch}}(k(t))$	Half-hourly schedule that is generated from the load forecast, where $p_{\text{sch}}(k(t)) \in \mathbb{Z}$

$P_{bat}$	ESMU power electronic rating, where $P_{bat} \in \mathbb{Z}^{>0}$
$p_{bat}(t)$	Battery power at time $t$ , which is derived from $p(t)$ , where $\mathbf{p}_{bat} = (p_{bat}(t))$ and $p(t) \in \mathbb{Z}$
$SOC(t)$	Scheduled state of charge at sample $t$
$SOC^*(t)$	Battery's state of charge at sample $t$ , where $SOC^*(t) \in [0, 1]$
$SOC_{tol}$	SOC tolerance, i.e. maximum deviation from the prescheduled SOC profile, where $SOC_{tol} \in [0, 0.5]$
$T$	Number of samples during the entire simulation, where $T \in \mathbb{Z}_{>0}$
$t$	Discrete sample of time, where $t \in \{0, \Delta t, \dots, T\Delta t\}$
$T_{sch}$	Length of scheduling horizon, where $T_{sch} \in \mathbb{Z}_{>0}$ and $T \geq T_{sch}$

### Symbols used in Chapter 5

$\beta$	Allocation parameter to assign a portion of the temporary energy demand, $\hat{E}_{u,n}$ , where $\beta \in (0, 1]$
$\Delta t$	Sample period for EV scheduling, where $\Delta t \in \mathbb{R}^{>0}$
$\hat{\mathbf{p}}_{u,n}^{\text{EV}}$	Temporary charging vector during iteration number $n$ , for EV $u$ , where $\hat{p}_{u,n}^{\text{EV}}(t) \in \hat{\mathbf{p}}_{u,n}^{\text{EV}}$
$\hat{\mathbf{p}}_{\text{base},n}$	Temporary demand vector, i.e. the aggregate of all EV charge vector and the base load vector, where $\hat{p}_n^{\text{base}}(t) \in \hat{\mathbf{p}}_{\text{base},n}$
$\hat{p}_n^{\text{base}}(t)$	Temporary demand at time $t$ , i.e. the aggregate of all EV charge vector and the base load vector, where $\hat{p}_n^{\text{base}}(t) \in \mathbb{Z}^{\geq 0}$
$\hat{p}_{u,n}^{\text{EV}}(t)$	Temporary charging power during iteration number $n$ , for EV $u$ , at time $t$ , where $\hat{p}_{u,n}^{\text{EV}}(t) \in \mathbb{Z}^{\geq 0}$
$\mathbf{p}_n^{\text{base}}$	Base load vector, where $p_n^{\text{base}}(t) \in \mathbf{p}_n^{\text{base}}$
$\mathbf{p}_{u,n}^{\text{EV}}$	Scheduled EV charging power vector, for EV $u$ at algorithm iteration $n$ , where $\mathbf{p}_{u,n}^{\text{EV}} = (p_{u,n}^{\text{EV}}(t))$
$N$	Number of algorithm iterations to schedule multiple EVs, where $N \in \mathbb{Z}^{>0}$
$n$	Iteration number of EV scheduling algorithm, where $N \in [1, \dots, N]$
$p_n^{\text{base}}(t)$	Base load at time $t$ , where $p_n^{\text{base}}(t) \in \mathbb{Z}^{\geq 0}$
$p_{u,n}^{\text{EV}}(t)$	Scheduled EV charging power, for EV $u$ at algorithm iteration $n$ for time $t$ , where $p_{u,n}^{\text{EV}}(t) \in \mathbb{R}^{\geq 0}$

$P_u^{\min}$	Maximum EV charging power
$P_u^{\max}$	Minimum EV charging power
$T^{\text{sch}}$	Scheduling horizon for EV charging, where $T^{\text{sch}} \in \mathbb{Z}^{>0}$
$U$	Number of EVs that need to be scheduled, where $U \in \mathbb{Z}^{>0}$
$u$	EV unit number, where $u \in [1, \dots, U]$

### Symbols used in Chapter 6

$\alpha$	Control parameter that regulates the additive increase, where $\alpha \in [0, 1]$
$\beta$	Control parameter that regulates the multiplicative decrease, where $\beta \in [0, 1]$
$\Delta t$	Sampling period, where $\Delta t \in \mathbb{Z}_{>0}$
$\Delta \text{SOC}(t)$	Change in SOC during time period $\Delta t$ , where $\Delta \text{SOC}(t) \in [-1, 1]$
$\delta^{**}(c)$	Scaling function for a current $c$ , which is used in the metric to quantify improvements in line utilisation for a case named <b>X</b> , where $\delta^{**}(c) \in \mathbb{R}$
$\delta^*(v)$	Scaling function for a voltage $v$ , which is used in the metric to quantify improvements in voltage levels for a case named <b>X</b> , where $\delta^*(v) \in \mathbb{R}$
$\eta$	Energy conversion efficiency, where $\eta \in (0, 1]$
$\hat{\eta}$	Direction dependent energy conversion efficiency, where $\hat{\eta} \in (0, 1]$
$\hat{n}_x(t)$	Predicted EV demand data, where $n_r(t) \in \mathbb{R}$
$\mu$	Self-discharge loss factor, where $\mu \in (0, 1]$
$\text{SOC}(t)$	Battery state of charge at time $t$ , where $\text{SOC}(t) \in [0, 1]$
$\text{SOC}_{\max}$	Maximum rated SOC for limited battery operation, where $\text{SOC}_{\min} < \text{SOC}_{\max}$ and $\text{SOC}_{\max} \in [0, 1]$
$\text{SOC}_{\min}$	Minimum rated SOC for limited battery operation, where $\text{SOC}_{\min} < \text{SOC}_{\max}$ and $\text{SOC}_{\min} \in [0, 1]$
$\zeta_{\mathbf{C}}^{***}$	Equality metric of using distributed BESS for <b>Case C</b>
$\zeta_{\mathbf{C}}^{**}$	Metric quantifying improvements in line utilisation for <b>Case C</b> , where $\zeta_{\mathbf{D}}^{**} \in \mathbb{R}$
$\zeta_{\mathbf{C}}^*$	Metric quantifying improvements in voltage levels for a <b>Case C</b> (i.e. AIMD), where $\zeta_{\mathbf{C}}^* \in \mathbb{R}$

$\zeta_{\mathbf{D}}^{***}$	Equality metric of using distributed BESS for <b>Case D</b>
$\zeta_{\mathbf{D}}^{**}$	Metric quantifying improvements in line utilisation for <b>Case D</b> , where $\zeta_{\mathbf{D}}^{**} \in \mathbb{R}$
$\zeta_{\mathbf{D}}^*$	Metric quantifying improvements in voltage levels for a <b>Case D</b> (i.e. AIMD+), where $\zeta_{\mathbf{D}}^* \in \mathbb{R}$
$C$	Battery capacity, where $C \in \mathbb{R}_{>0}$
$C_{\min}$	Minimum necessary line loading to take the changes into account, where $C_{\min} \in [0, 1)$
$n_s(t)$	Probability of starting a trip, where $n_s(t) \in [0, 1]$
$P_{\mathbf{B}}(c)$	Probability distribution of line utilisation for <b>Case B</b> (i.e. baseline case), where $P_{\mathbf{B}}(c) \in \mathbb{R}_{\geq 0}$
$P_{\mathbf{B}}(v)$	Probability distribution of voltage levels for case <b>Case B</b> (i.e. baseline case), where $P_{\mathbf{B}}(v) \in \mathbb{R}$
$P_{\mathbf{C}}(c)$	Probability distribution of line utilisation for <b>Case C</b> (i.e. AIMD), where $P_{\mathbf{C}}(c) \in \mathbb{R}_{\geq 0}$
$P_{\mathbf{C}}(v)$	Probability distribution of voltage levels for case <b>Case C</b> (i.e. AIMD), where $P_{\mathbf{C}}(v) \in \mathbb{R}$
$P_{\mathbf{D}}(c)$	Probability distribution of line utilisation for <b>Case D</b> (i.e. AIMD+), where $P_{\mathbf{D}}(c) \in \mathbb{R}_{\geq 0}$
$P_{\mathbf{D}}(v)$	Probability distribution of voltage levels for case <b>Case D</b> (i.e. AIMD+), where $P_{\mathbf{D}}(v) \in \mathbb{R}$
$p_{\text{bat}}(t)$	Battery power at time $t$ , where $p_{\text{bat}}(t) \in \mathbb{R}$
$P_{\max}$	Power rating of battery, where $P_{\max} \in \mathbb{R}_{>0}$
$U$	Number of BESS units in the network
$v_{\text{bat}}(t)$	The current BESS voltage at time $t$ , where $v_{\text{bat}}(t) \in \mathbb{R}$
$w_x(t)$	Trip distance probability for weekends ( $w_{we}(t)$ ) and week-days ( $w_{wd}(d)$ ), where $w_x(t) \in [0, 1]$

# Chapter 1

## Introduction

The aim of the work that is presented in this thesis is to make a contribution improving grid operation and reliance when using Battery Energy Storage Systems (BESS) in the UK Low-Voltage (LV) power distribution networks by adjusting sub-half-hourly operation and communication regimes of the BESS. In this context, grid operation performance is considering mainly peak power flow, but also includes voltage deviation, phase imbalance, distribution losses, and the magnitude of neutral currents.

Providing grid support is expected to become a vital necessity since the predicted increase in electricity demand and demand volatility will negatively effect the performance of the UK distribution networks. Due to the network's design and topology higher and more volatile demand is predicted to cause issues including voltage deviation, asset overloads, equipment damage and, in the worst case, service disruptions. As discussed in this thesis, BESS is a suitable alternative to traditional network reinforcements. However, to successfully combine fast system response capabilities (i.e. at sub-half-hourly resolution) with traditional operation schedules (i.e. at half-hourly resolution) to yield the best impact on network performance (e.g. peak-reduction) is still an open research question. Also, with the proliferation of household-connected BESS and Electric Vehicles (EVs), performance of algorithms that coordinate BESS

operation are an ongoing research topic, too.

In this chapter, Chapter 1, the background and motivation for the conducted research are presented. Then, on the basis of the identified challenges and opportunities for battery energy storage in the electricity distribution network, the problem statement and all research objectives are outlined. At the end of this chapter, all contributions and publications are summarised, and the structure of the rest of this thesis is presented.

## 1.1 Background and motivation

Today's society and economy are highly dependent on the continuous availability of energy or more specifically: electric energy. In the UK, demand for electricity has increased over the past decades, and this trend is expected to continue into the future [4]. This demand increase is only accelerated since a major focus of UK energy policies has been put on transitioning towards a low carbon economy [5]. Particularly the decarbonisation of heat and transport sectors are two areas of significant strategic focus and Low Carbon Technology (LCT) such as Photovoltaic (PV) installations, Electric Vehicles (EVs) and heat pumps are expected to contribute significantly to the energy mix of this transition.

As uptake of these LCTs continues and they start penetrating power distribution networks, stress on these networks will also continue to increase, resulting in operating issues that can eventually lead to additional service disruptions. Furthermore, the uptake of LCTs is not expected to progress evenly throughout the entire power network, and instead clusters of early adopters are predicted to form, leading to certain LV networks exceeding their operational constraints even at a relatively low national rate of LCT adaption [6]. The scale of this energy transition becomes becomes particularly apparent when referring to the UK's 2017 Future Energy Scenarios (FES)

that compare the predicted future load scenarios for the upcoming decades [1].

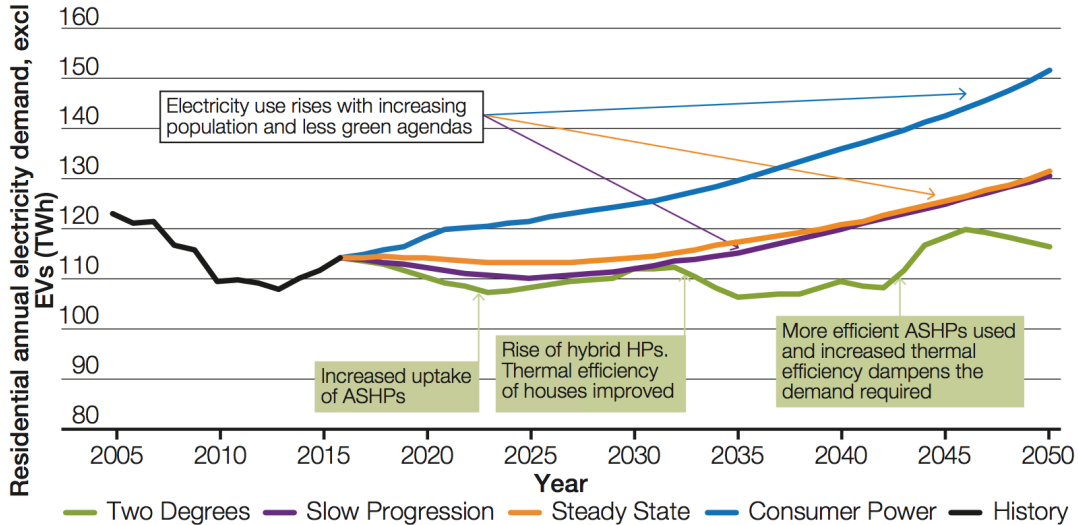


Figure 1.1: Change in residential annual electricity demand excluding electric vehicles from FES2017 [1]

Figure 1.1 shows the predicted increase in annual residential electricity demand; here the market driven scenario (i.e. “Consumer Power”) shows the largest increase until 2050. When putting more emphasis on environmental concerns, the “Two Degrees“ scenario emerges. This scenario refers to the intention of limiting global temperature increase to two degrees (previous FES reports referred to this scenario as “Gone Green“). According to the FES 2017 those two scenarios enable a continuing growth of the UK economy, but put very different emphasis on decarbonisation targets. Although the rise in demand for electricity is projected to differ by more than 30TWh in 2050 (i.e. if the “Two Degrees“ scenario is achieved), the aforementioned uptake of LCTs like EVs is expected to put additional load onto the power network in both scenarios.

When focusing on the electrification of personal transport (by introducing EVs into the electricity demand), Figure 1.2 shows that both the “Consumer Power” as well as the “Two Degrees” scenario will add more than 35TWh of annual energy demand by 2045. Since most of these EVs are expected to charge at home and (at

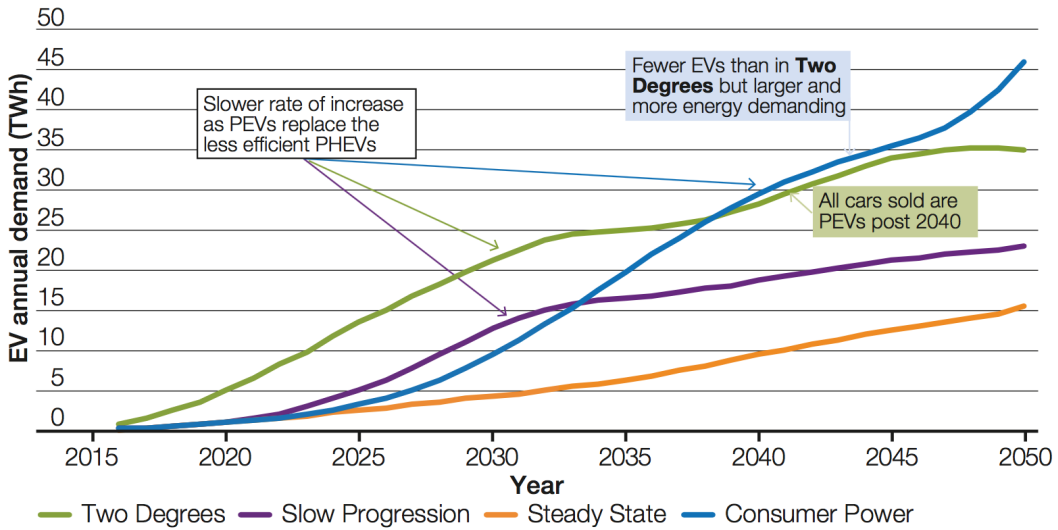


Figure 1.2: Rise in energy demand due to the uptake of electric vehicles as predicted by FES 2017 [1]

least initially) at similar times, aggregating effects are feared to not only exhaust national energy supply capabilities but also power distribution capacities.

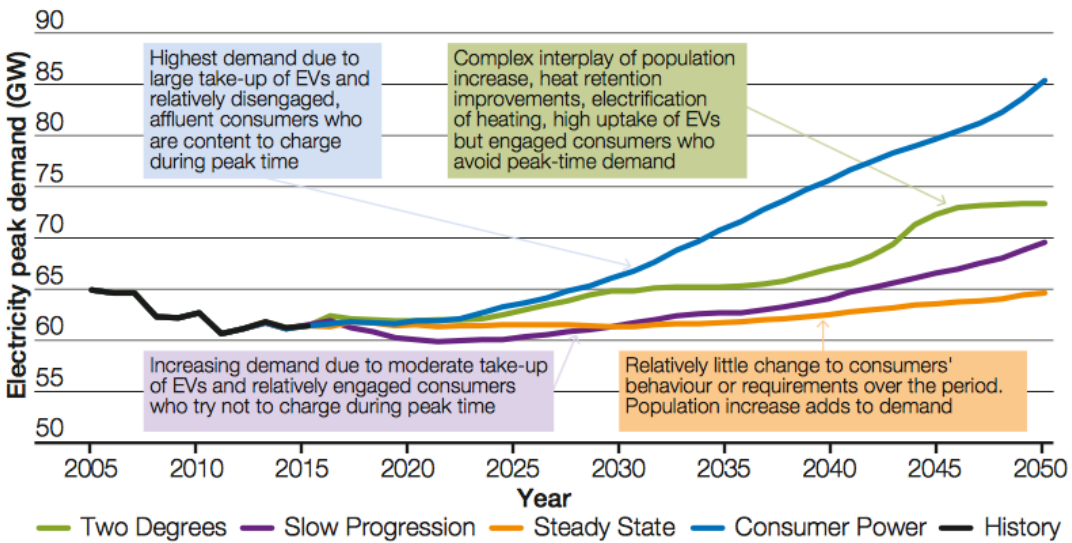


Figure 1.3: Change in annual peak power demand as predicted by FES2017 [1]

Figure 1.3 supports this fear since uncontrolled proliferation of LCTs and EVs (as shown in the “Consumer Power” scenario) will add more than 20GW of power demand onto today’s peak power levels. Such a rise in peak power would exceed today’s supply

capacities, especially since the new energy mix and decommissioning of fossil fuelled power plants have resulted in this year's winter capacity margin to only lie between 3.7GW and 4.9GW [7]. Although FES 2017 expects the "Two Degrees" scenario to also show an increase in peak power, better coordination and control is expected to mitigate half of the 20GW peak increase. From this point of view, today's narrow capacity margins could already cater for nearly half of the increase in peak demand that is expected to occur over the next 33 years, i.e. until 2050. Whilst UK power transmission networks are being upgraded and will therefore be capable of handling this increased power demand, the increasing stress on the distribution network still remains. This is due to the fact that loads in the residential and commercial sectors are typically situated at the network edge, i.e. in the LV distribution network, and reinforcing these networks can result in costly service disruptions.

### **1.1.1 Topology and challenges of the UK electricity network**

The UK electricity network in today's form has grown over the past century and is based on an interconnected high-voltage gird. Its largest part is also known as the transmission network, which connects remote power stations to distribution networks. Those distribution networks supply electricity to all loads across the mainland of the UK, including industrial, urban and rural customers<sup>1</sup>.

The entire structure of the electricity network is a three-phase Alternating Current (AC) system since this allows easy voltage level conversion with the use of transformers, i.e. without the need for power electronics. In the UK, the highest voltage level for generation and transmission is 400kV. Such a high voltage requires a relatively small current to transmit the generated bulk power, which in turn reduces conduction losses and maximises the efficiency of the high-voltage network. Regional supply

---

<sup>1</sup>Some small and remote UK islands like the Shetland islands are not connected to this national grid and have their separate electricity infrastructure. Therefore they are not considered as part of this thesis since the study of this kind of network lies outside the research scope.

points step-down this high voltage to 132kV<sup>2</sup> to deliver power to Distribution Network Operators (DNOs). From the primary level of the distribution network and onwards, this so called medium-voltage is stepped down to 33kV, then 11kV and finally 400V phase to phase (P2P), in order to cater for heavy industry, medium clients and household sized customers, respectively. In the UK, all households are connected to one of the three phases of the distribution network and therefore are supplied at a nominal voltage of 230V (phase to neutral - P2N). To achieve a balanced network, each customer's phase allocation is chosen at random.

This LV part of the electricity network is its weakest part, since its assets were designed to cater for small powers between 315kVA to 500kVA [8]. Despite this capacity limitation, DNOs aim to maintain distribution level voltages within their statutory operating bands, i.e. 230V +10% -6% for the LV network as specified by the Electricity Supply Quality and Continuity Regulation (ESQRC) [9] and Engineering Recommendation G59 [10]. Primary substations in the UK are equipped with regulation equipment, e.g. On-Line Tap-Changers (OLTC), to increase or decrease the voltage on the secondary transformer side depending on the current level of demand. Secondary transformers do not have such regulating equipment and instead apply a constant voltage conversion ratio which is set according to the network's typical demand.

A project based on the findings from *Electricity North West* (ENW) in [11] emphasises the issues that result from residential increase in demand for electricity; e.g. voltage deviation due to an uptake of LCTs. More specifically, in the ENW lead project 200 LV networks in the UK were monitored to assess the capacity for LCT adoption. Initial findings showed that even in today's distribution networks, 15% of all monitored substations experienced reverse power flow, 4.5% substations reported high voltages (i.e. above 253V), and only 2% substations reported occasional low

---

<sup>2</sup>In some cases regional supply points provide 127kV instead of 132kV.

voltages (i.e. below 216V). With the voltage drop assumption however, it was believed that customers in these network were still operating at BSEN50160 compliant voltage levels. Models to assess the LCT headroom indicated that the first issue is always voltage deviation and thermal or capacity limits are of second concern. This finding is based on the fact that LV networks are highly resistive and rarely managed in an active manner; hence as the number of PV installations is expected to grow the voltage deviation magnitude and frequency is also going to increase [12]. Since the expected voltage deviation was caused despite a relatively low adaptation of residential LCTs, strict precautionary regulation has been put in place to assure continuous operation without violating any operating constraints. Otherwise additional voltage deviation, unbalanced network operation or asset overloads could be the result.

Traditional network planning approaches that have been used by DNOs to expand and install network assets were designed to circumvent such issues in order to follow the aforementioned standards and regulations. The most common approach follows the commonly used practice of aggregating a large number of customers and designing the power delivery network to cater for their largest probable demand, i.e. the After Diversity Maximum Demand (ADMD) method [13]. This ADMD method has remained the same for many years and uses historical load analysis and standard growth assumptions that are both no longer valid in this unprecedented LCT uptake scenario [14]. To make things worse, LV networks in the UK are generally unmonitored once installed [14]. Distribution Network Operators (DNOs) have become aware of this issue and are developing updated planning strategies involving “smart” and “flexible” electricity grids [15]. However, in situ equipment that will become subject to the same adaptation of LCT needs to be managed actively via innovation in the use of existing and new technologies; otherwise both frequency of service disruptions and customer minutes lost will increase alongside the proliferation of LCTs [16]. One such innovative technology, which is the main focus of the presented thesis, is the

installation and management of battery storage [17]. The following section is going to introduce the two favoured solutions to address network issues and explain why battery energy storage was chosen as part of the presented research.

### **1.1.2 Solutions to mitigate impact of LCT**

The two most favoured solutions that allow DNOs to support LV network operation are: 1. the reinforcement of in situ network assets or 2. the deployment of network support equipment. Whilst network reinforcement would certainly address immediate issues of current network capacity constraints, this approach is also the more expensive and disruptive option. More specifically, customers will need to deal with outages during periods of asset upgrades (e.g. transformer upgrade and line re-conductoring after secondary transformers' tap settings have been adjusted). Therefore, alternatives to defer or avoid network reinforcements have been sought and assessed [18–21]. Most promising alternatives are to install flexible and controllable Distributed Energy Resources (DERs), or more specifically: Battery Energy Storage Solutions (BESS) [22]. BESS has not only seen significant advancements in technology, but also received increasing attention in both academic studies and industry trials [23].

Installing BESS on a strategic location in the LV network brings several advantages to DNOs' control over their network performance. Roles for and advantages of energy storage technology are extensively reviewed in Section 2.2. However, a few examples of potential benefits from BESS do include the regulation of voltages in order to operate within statutory voltage bands [24], shaving peak loads to relieve stress from the installed network assets [25], and reducing phase unbalance to increase network efficiency [26]. These three examples all implement a similar control paradigm where BESS is charged during periods of low demand and discharged at peak demand periods in order to achieve the best possible impact. Whilst the questions regarding locating and scaling of BESS have mostly been addressed, BESS control can still be

split into two complementing yet unmarried approaches:

1. “off-line” control, using load forecasts and BESS schedules [27–30], and
2. “on-line” control, using Set-Points Control (SPC), Model Predictive Control (MPC) or similar dynamic control methods [31–34].

These two control approaches are reviewed in detail in Section 2.4.1. Also, with the anticipated uptake of household BESSs and DERs, mechanisms to control and coordinate multiple storage systems have also grown in popularity [35–38]. An example in [38] that proposes to store solar energy in order to support charging of EVs is particularly interesting since it shows a well coordinated home system that does not impose any additional load onto the power distribution network. These results also highlight that without rooftop PV installations (or any co-located energy resource for that matter), distributed storage systems need to work in a cooperative manner to avoid adding network straining. Control methods that are capable of coordinating DERs by letting devices make intelligent control decisions have been summarised under the keyword “smart control”.

### 1.1.3 Smart control

As already mentioned in the previous section, Section 1.1.2, off-line and on-line control strategies exist to manage BESS. This traditional control often dealt with the dispatch of a single energy entity, but due to the distributed nature of the expected LCT uptake, methods to manage cooperative behaviour needed to be developed, too. With the penetration of smart meters and communication-enabled devices in e.g. the “Internet of Things“ (IoT), power systems have the potential of becoming interlinked networks of smart devices. Therefore “smart control” mechanisms can complement the traditional off-line and on-line control strategies and are of great research interest to enable the uptake of distributed LCTs since these strategies remove the single point

of failure, reduce computational burden from centralised controllers and allow individual devices to respond intelligently and quickly to local events like sudden voltage drops or capacity notifications.

For example the key term “smart charging” summarises EV charging mechanisms where the limited distribution network capacity causes multiple EVs to share the available resource amongst themselves [39–41]. However without any network load information EV coordination may still exhaust the network’s capacity, even when EVs are intelligently limiting their maximum charging rates. Limiting their charge rates based upon the current network demand as well as their own energy needs is a more sophisticated control option [42]. A similar key term is the “smart grid” where DER communicate and cooperate in order to e.g. shed load using Demand Side Response (DSR) or maintain microgrid operation in fault situations [43–45]. However, the fundamental requirement for the successful realisation of any such smart control method is the reliable exchange of information amongst the participating entities that physically operate within the power network.

Therefore smart control does not only require robust control mechanisms, but also a robust communications infrastructure. In Section 2.4.2, literature that reviews and compares centralised control methods with distributed control paradigms will show the implicit need to synchronise the coordination of multiple smart devices to achieve their promised benefits. It will be shown that all underlying control mechanisms dealing with the coordination of distributed energy resources either explicitly or implicitly assume a robust communication infrastructure where communication is synchronised. For instance, this requirement is assumed whenever messages are received and executed immediately and without delay after they have been dispatched or whenever a single control instruction result in the synchronised reaction of all controlled entities. In reality however, the strength of the communication link may vary with e.g. weather or current network traffic, and fixed message delays and exact device synchronisation

can no longer be guaranteed. Therefore, not only smart control algorithms, but also their sensitivity to the strength of the underlying communications infrastructure is of interest. As a result the research question can be risen whether communication desynchronisation can result in equal or better coordination performance; i.e. in reducing peak load.

The alternative to relying on telecommunication in order to coordinate DERs is to remove the requirement for device communication altogether. For instance, communication-less control of multiple power devices has been of particular interest in noisy environments like ships [46] or islanded power networks that do not have strong telecommunication capabilities [47]. Whilst these control methods support network operation they have not been designed to take device operation into account. More specifically, in a network where devices like household-connected BESS are no longer owned by DNOs, the interest of guaranteeing a certain lifetime may surpass the need to provide network support operation. Therefore distributed and communication-less control strategies need to assure a more equal device utilisation to spread the burden onto the entire collection of DERs. Otherwise, batteries situated at e.g. the end of the distribution network experience the largest voltage swing and are therefore likely to cycle more than those batteries located closer to the substation where voltages are more stable. Hence, following the review of several communication-less control methods in Section 2.4.3, an improved distributed and communication-less BESS control algorithm is proposed that takes this neglected network inequality into account.

## 1.2 Problem statement and research objectives

The focus of the research presented in this thesis is put on aiding DNOs to manage and operate their power distribution networks by installing energy storage into their

distribution networks in order to counteract the effects from electrification of heat and transport sectors as well as the decarbonisation of the grid itself. More specifically, BESS is the main focus since it is a rapidly improving technology that has the potential to defer or even mitigate costly network reinforcements. Modern battery technology allows the storage of electrical energy in ever-decreasing form factors, whilst power electronics technology becomes more efficient at integrating batteries into power networks. As shown in the literature review in Chapter 2, methods to control BESS, e.g. in order to optimise power flow, have been and still are of great research interest.

Therefore, the aim of this thesis is to present a contribution in BESS control to improve grid operation and reliance, when deploying it in the UK LV distribution network. Given the already established control approaches of “off-line” and “on-line” control, merging the two in order to take advantage of BESS schedules and real-time information is still an open research challenge. Subsequently, applying real-time corrections to BESS schedules in order to decrease peak demand whilst obeying to technical and operational constraints is also an identified research challenge. Since the expected uptake of distributed LCTs and DERs through proliferation of household-connected storage solutions (e.g. to support PV integration or to counteract EV impacts) requires “smart” coordination mechanisms. When requiring communication to implement this smart coordination, another challenge exists in developing algorithms that function despite communication disturbances (i.e. through message desynchronisation). Lastly, in the case where communication-less coordination of distributed devices is sought, the challenge of assuring equal device usage whilst providing network support (e.g. to guarantee a minimum lifetime) has also been identified.

These research challenges are extensively reviewed in the literature review in Chapter 2, and in accordance to these identified key challenges that motivate the conducted research, a set of objectives is presented in order to achieve the aim of contributing

to the existing field:

**Objective 1** Develop a control mechanism for a single BESS to further improve three-phase network operation without deviating from its predetermined BESS schedule.

**Objective 2** Develop a control mechanism that dynamically adjusts BESS schedules to reducing load peaks by combining both off-line and on-line control.

**Objective 3** Develop and compare operation of a charge scheduling algorithm for multiple entities in a synchronised and desynchronised communications environment.

**Objective 4** Develop a control strategy for distributed BESSs by individually assigning control parameters to an extended charge-discharge-algorithm.

### 1.3 Contributions to knowledge

The literature that is reviewed in Chapter 2 introduces the key contributions surrounding the control of energy storage in power distribution networks, and therefore supports the thesis problem statement that was presented in Section 1.2. This review concludes by identifying gaps in literature which are used as starting points to formulate the research objectives and resulting research contributions. Those contributions can be summarised as follows:

- An iterative closed-loop power adjustment method is presented that controls a DNO owned storage devices in such a way that its three-phase power flow improves LV network operation. This contribution is the result of **Objective 1** and is achieved by using the device's flexibility in assigning active power to the three phases, and by using the remaining capacity of power electronics to

inject or absorb reactive power. Meanwhile the BESS is obeying its underlying half-hourly schedule.

- A dynamic control method to merge off-line BESS scheduled control with an on-line power prediction mechanism (i.e. Model Predictive Control) is developed to minimises both the imminent sub-half-hourly load peaks as well as the day-ahead half-hourly load peaks. This contribution is the result of **Objective 2** and is achieved by merging schedules that are based on real load forecasts with an autoregressive model that is fed by real load data.
- A robust charge scheduling algorithm for multiple, distributed entities is developed to prevent charging spikes from adding excessive stress onto the distribution network which would otherwise experience capacity shortages. This contribution is the result of **Objective 3** and is achieved by implementing a “Multi-Agent System” (discussed in the literature review in Section 2.4.2) on a compute cluster to compare algorithm performance for both synchronised and desynchronised message exchange.
- A communication-less distributed control method is developed that improves the traditional Additive-Increase Multiplicative-Decrease (AIMD) algorithm to achieve cooperative behaviour of multiple BESSs in order to mitigate the impact of co-located “dumb-charging” EVs. This contribution is the result of **Objective 4** and is achieved by individually assigning control parameters to all BESS to infer the current network status whilst only using local voltage measurements.

## 1.4 Publications

- **First-authored publications:**

- M. J. Zangs, P. B. E. Adams, T. Yunusov, W. Holderbaum, and B. A. Potter, “Distributed energy storage control for dynamic load impact mitigation,” *Energies*, vol. 9, no. 8, 2016.
- M. J. Zangs, T. Yunusov, W. Holderbaum, and B. Potter, “On-line adjustment of battery schedules for supporting LV distribution network operation,” in 2016 International Energy and Sustainability Conference, IESC 2016, 2016.
- **Co-authored publications:**
  - T. Yunusov, M. J. Zangs, and W. Holderbaum, “Control of Energy Storage,” *Energies*, vol. 10, no. 7, p. 1010, 2017.
  - T. Yunusov, M. J. Zangs, and W. Holderbaum, “Online Control Algorithm for Sub-Half-Hourly Operation of LV-Connected Energy Storage Devices Owned by DNO”, in 24th International Conference & Exhibition on Electricity Distribution (CIRED), CIRED 2017, 2017
- **Unpublished papers:**
  - M. J. Zangs, T. Yunusov, W. Holderbaum, and B. Potter, “On Smart EV Charging with Asynchronous Multi-Agent System for Load Profile Optimisation” *IEEE Transactions of Smart Grid*
  - M. J. Zangs, T. Yunusov, W. Holderbaum, and B. Potter, “Battery control algorithm for peak load shaving in low-voltage power network with high demand volatility,” *Applied Energy*

## 1.5 Thesis structure

The structure of this thesis is organised as follows:

- **Chapter 2** carries out an extensive review of the literature surrounding the field in order to support the problem statement and proposed contribution.
- **Chapter 3** develops a BESS scheduling mechanism and identifies key network parameters that are used in their corresponding cost functions to improve network operation. Then, this chapter address **Objective 1** by presenting a method that assigns a BESS schedule to the three-phase power distribution network whilst minimising the aforementioned cost functions; therefore improving network operation. Results are compared against a “baseline” and a “normal” (or traditional) operation case by assessing them on a temporal and probabilistic level.
- **Chapter 4** then extends the work in Chapter 3 by presenting a dynamic control method that adjusts a half-hourly BESS schedule at sub-half-hourly temporal resolution in order to reduce both volatile and the daily load peak. This is achieved by combining two PID compensated control loops with a MPC and BESS schedule. Therefore, this chapter addresses **Objective 2**.
- **Chapter 5** addresses **Objective 3** by presenting a cooperative battery charging algorithm that is deployed on a Multi-Agent System and assessed in both a synchronised and desynchronised communications environment. In this chapter, both algorithm convergence and algorithm performance is compared between its implementation in the synchronised and desynchronised scenario.
- **Chapter 6** develops a stochastic EV demand model that is based on real vehicle mobility data, and it will develop a control algorithm for distributed BESS to mitigate the negative impact from the resulting EV demand. This chapter address **Objective 4**, the final research objective, by extending the Additive-Increase Multiplicative-Decrease algorithm to enable cooperating BESS operation under the absence of a shared communications infrastructure.

- **Chapter 7** presents a detailed conclusion that relates all findings back to the initial problem statement and the overarching aim of the presented PhD thesis. Also, this chapter highlights potential future work based on the findings from the conducted research.



# Chapter 2

## Literature Review

### 2.1 Overview

With the ongoing electrification and decarbonisation of the heat and transport sectors in the UK demand across the electricity network is expected to double by 2050 [48]. One contributor towards this increasing demand is the expected uptake of LCTs as they start penetrating power distribution networks. As discussed in Chapter 1 of this thesis, conventional reinforcement to upgrade the network's infrastructure in order to counteract capacity shortages is effective but costly. Instead, this PhD research focuses on the improvement of grid operation by controlling BESS in the LV distribution network, and together with recent availability of load information due to the distribution and installation of smart-meters, the opportunity arises for DNOs to develop energy storage control strategies in order to achieve the best possible performance and add most benefits to their distribution networks.

In fact, energy storage as an alternative to grid reinforcement has seen an increasing interest in industry since there are more than 1200 energy storage projects worldwide according to the Department of Energy's global energy storage database [49]. More specifically, as of 2016, 27 store projects were installed in the UK and they

accumulate to an energy storage capacity of 33GWh [50]. Out of all global energy storage projects, 61% use “electro-chemical energy storage technology” (i.e. rechargeable batteries) and 49% of those BESS are rated at less than 250kW. Their sizes and ratings make such BESS suitable for deployment in distribution networks, and the figures in the energy storage database indicate that worldwide 131 of these projects are indeed used for support of the secondary distribution network [49].

The range of applications for energy storage in the electricity grid has grown significantly over the past decades. Therefore, the first section of this chapter, Section 2.2, presents an extensive survey of roles for electrical energy storage solutions and narrows the focus on those roles that are applicable for the conducted PhD research. Section 2.3 then provides an extensive review of already conducted BESS research projects that support LV network operation; i.e. that are concerned with voltage control and power flow management. Next, Section 2.4 presents and reviews different control methods for grid connected energy resources that have either been used in the already discussed BESS research projects or that have been studied on a theoretical basis. Particular focus is put on comparing off-line and on-line control, centralised and distributed control and communication-less control. In the end of this chapter, in Section 2.5, the gaps and research opportunities are summarised to link to the research contributions and to support the problem statement of this thesis.

## 2.2 Role of energy storage - a survey

The idea of using energy storage in the electricity grid has been discussed for quite some time, and its important role in future energy systems has already been identified in the 70s [51]. As the name suggests electrical energy storage systems have the ability to consume, store and release electrical energy by converting it into a different form of energy. Depending on the rate at which energy can be consumed and released (i.e.

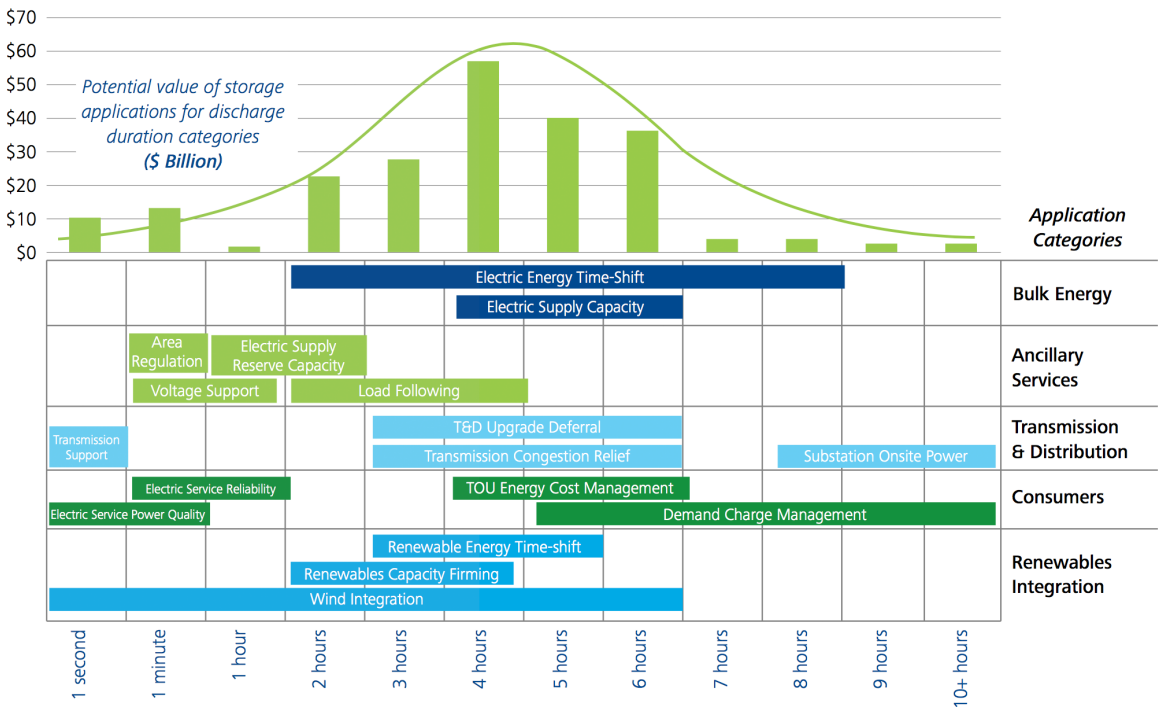


Figure 2.1: Energy storage applications and corresponding value for various discharge durations [2]

the system's power rating) as well as the amount of energy that can be stored (i.e. system's capacity) different functions can be provided. A Canadian and US based study for the Department Of Energy (DOE) showed that (when correctly exploited) these functions can yield direct financial benefits of \$157.56 billion on a national level over an estimated 10 year system lifecycle [52]. Figure 2.1 shows these benefits in relation to the storage system's typical discharge period, and links them to their associated functions, too. Here, Time Of Use (TOU) energy cost management yields the largest economic profit, yet from a historical point of view, bulk energy storage has played the most important role in the energy system.

Nowadays, storage can also tap into emerging revenue streams and perform additional functions. As identified in several review articles [17, 53, 54], the key roles and applications of energy storage systems, regardless of profitability in the current market situation, can be identified as follows:

- **Energy shifting - arbitrage:** This function uses the difference in energy price to yield revenue. More specifically, as energy pricing is expected to become more dynamic and responsive to current energy demand and generation, storage is controlled to charge when energy prices are low and discharge when energy prices are high [17, 55]. Such dynamic pricing schemes are expected to emerge due to significant changes in demand at morning and evening peaks [56]. However, for small storage may not be sufficient to justify energy shifting in LV networks.
- **Supply capacity:** In order to meet future energy demand, energy suppliers commit their resources in advance. Doing so allows them to plan for their operation and solve the economic dispatch problem. With increasing demand, the supply volume will have to increase, too. However, it is predicted that energy storage can defer or even avoid investments in power plants, assuming they are sized accordingly (i.e. several 100MW) [57]. Bulk energy storage was the first choice to support supply capacity. One example is pumped hydro-electric energy storage, which has seen a global growth of 127GW since 1979 [58–60].
- **Ancillary services:** These services are of interest to transmission and distribution system operators since they support the operation of their networks. For example, load following and frequency regulation are two complementing applications of that address the imbalance between demand and supply [61]. In case of a severe imbalance that resulted in network outage, black start is also a function that can be supplied by energy storage [62, 63]. Since modern energy storage systems can absorb and inject both active and reactive power, they can also provide voltage support [64].
- **Grid stability:** To make the grid more resilient to network faults (e.g. short-circuit or loss of a large generator), or to overcome scheduled network outages,

energy storage can be used as an intermittent energy source [65]. To provide optimal operation conditions for energy generators, storage can support rotor angle stability and voltage stability by injecting active and reactive power at the point of common coupling [66,67]. Furthermore, sub-synchronous resonance and harmonic interference can also be reduced [68]. This coupling resonance can occur between electrical and mechanical systems and can damage the mechanical structure due to repetitive stresses and strains.

- **Upgrade deferral:** As already stated in Section 1.1.2, both transmission and distribution systems would have to be upgraded unless energy storage could provide network-support functions. By deferring network upgrades, network assets will be used more efficiently, and customer disruptions will be avoided [52,69]. Furthermore, in areas where the expected load has already been met and growth has levelled out, deployed energy storage is flexible enough to provide alternative functions (unlike other network assets) [70].
- **Transmission charges:** In scenarios where generators are charged to use transmission systems (due to the capacity limitations of the transmission system), energy storage could take advantage of the price structure to maximise the profit from the generated energy [55,69].
- **Congestion relief:** High congestion at substations of heavily loaded transmission or distribution lines can be tackled by co-located energy storage units [64,71]. This can be achieved by e.g. shaving peak load or relaxing the energy requirements from distributed generation [72,73].
- **Service reliability:** In areas where a strong grid connection is needed to assure e.g. industry operations, an “uninterruptible power supply” may be required. Traditionally, these power supplies were diesel backup generators,

but modern energy storage technology can provide similar services at lower cost [74] (particularly when including alternative revenue streams).

- **Power quality:** Sub-cycle and harmonic distortions can severely deteriorate power quality, since they have unwanted effects on connected equipment (similar to the issue of sub-synchronous resonance at the generation side). Energy storage with modern power electronics could be capable of providing power filtering functions that suppress those distortion [75]. This feature could be of particular interest to LV networks in the UK, since customers are arbitrarily connected to a single phase of a three-phase network. Therefore, the discrepancy of power quality between the phases is even larger, yet available energy storage resources could even address this issue [76] (especially when considering household connected units).
- **Time-of-use energy charges:** A hurdle to DSM through flexible tariffs or TOU tariffs is the reason that consumers would have to adjust their energy consumption based on external price signals, which many are do not want to do. Energy storage could however decouple the consumer from these tariffs and allow them to continue with their normal lifestyle [77]. Additionally, when exploiting the energy price difference, storage could even supply arbitrage functions to some customers and reduce their electricity bill [78]. For customers with local generation, e.g. PV installation, their bill can be reduction even further. This would be done by storing the generated energy until a period of high energy prices arises. At this time energy storage could release the energy to maximise self-consumption [79].
- **Demand charges:** Larger customers, i.e. industrial and commercial loads, are not only charged for their total energy demand, but also their for their largest continuous power demand [80,81]. Therefore, a factory that may use a relatively

small amount of energy over a comparatively short amount of time, is billed accordingly. After all, the infrastructure to deliver the required power needs to be installed and maintained. In this scenario, energy storage could reduce the intermittent power demand without significantly increasing the total energy demand, and therefore reduce demand charges for larger customers [82].

- **Renewables integration:** Unlike traditional energy sources, renewables have are highly volatile and have limited availability. Since their availability, i.e. for solar PV, may not align with periods of high demand, i.e. during morning and evening, arbitrage functions may be provided to maximise the use of renewable generation - i.e. renewables “shifting” [83]. Furthermore, by discharging energy storage during times of low renewable generation, e.g. due to cloud cover or varying wind [84], a continuous supply of energy can be assured - i.e. renewables “smoothing”. And lastly, if a renewable resource was committed for longer periods of time, yet the associated energy forecasts overestimated its generation capacity, storage can supply the gap to avoid balancing charges - i.e. renewables “firming” [66].

This extensive list of possible applications for energy storage systems emphasises the potential for energy storage solutions in the future energy market. However, as also stated by Taylor et al. in [85]: “*The market for use [of electrical energy storage] is motivated by the need to increase the efficiency of the grid by the integration of RES*”. For this very reason, upgrade deferral, congestion relief, ancillary services (i.e. voltage support) and renewable integration are the key challenges that are of interest to DNOs. This finding is also supported by the motivation of research projects and field trials that were conducted with energy storage solutions in the LV distribution networks. These research projects are reviewed in the subsequent section, Section 2.3.

## 2.3 Energy storage research for LV application

The challenge for DNOs to manage their distribution networks is caused by the DER's and LCT's difficult predictability, their volatile nature, and the weakness of the network into which they are deployed. If left unmanaged, voltage fluctuations caused by e.g. PV systems [12,86] or capacity shortages due to additional loads like EVs [87,88] will threaten the power system's stability. Improved network management methods that are summarised under the term "smart grid" have thus become increasingly popular to counteract the negative impact from DERs and LCTs [89]. However, when deferring the reinforcement or retrofitting of network assets to construct such a smart grid, deployment of BESS can provide a significant contribution to the integration of DERs and LCTs. For instance, Grillo et al. in [90] showed how probabilistic price driven storage control successfully supports renewable integration. Their simulated and validated BESS model provides arbitrage functions through generation shifting and was able to achieve a daily gain of more than €130. But such an immediate financial benefit can only be achieved when their dynamic pricing is implemented and the repetitive discharge to 20% does not shorten the BESS lifetime. Focusing on grid support instead, Rowe et al. in [91] showed how a BESS schedule can maximise the peak reduction capability in order to free system resources. Since their BESS schedules were based on sometimes unreliable demand forecasts, they had to implement filtering operations to vary the forecast's peak magnitude, peak width and peak shape. This filtering maximised the resulting peak reduction performance to a median peak reduction between 5kW to 7kW (instead of 0kW when no forecast filtering was implemented). Similarly Hosseina et al. in [92] also used residential load forecasts to schedule BESS operation in order to level demand by shaving peak load. Their BESS was installed in the medium voltage distribution network since their redox flow-battery was significantly larger than the lithium-ion battery that was used by Rowe et al. (i.e. 34MWh instead of 25kWh). Apart from the difference in scale,

both pieces of research used residential load forecasts only whilst Li et al. solved a stochastic unit commitment and economic dispatch problem to maximise renewable integration in [93]. Unlike traditionally scheduled BESS operation, Li et al. also simulated real-time operation but assumed perfect demand and pricing knowledge at the time of operation. As a result they achieved a financial gain of more than \$34000, but did not guarantee the BESS impact on the underlying power distribution network.

Over the past decade electricity supplier branches from the Big Six (i.e. the UK's six major energy suppliers) begun trialling of BESS across their distribution network to better their understanding and potential contribution. This was done since the BESS benefits had only been estimated and not thoroughly studied through field trials. Showcase examples from some DNOs include: Scottish and Southern Electricity Networks (SSEN) in [94] where BESSs were deployed in Bracknell distribution networks to uphold voltage stability and power quality; EDF Energy Networks in [22] where BESS was installed in the 11kV distribution network for power flow management and to validate and improve system models; UK Power Networks (UKPN) in [95] where BESS was installed to shave load peaks and level supply volatility from an adjacent wind farm; E.ON UK in [96] where a 5MWh BESS was colocated with a combined heat and power plant to stabilise its energy supply; and Scottish Power in [97] where 1MWh of distributed batteries were installed in households to support grid operation through flexible tariffs. Nonetheless, from lessons learnt and aiming to meet statutory and physical restrictions under the future load changes, voltage control and the power flow problem have been identified as the two key challenges for DNOs [98, 99].

### 2.3.1 Voltage control

LV distribution networks in the UK operate at 230V Phase to Neutral (P2N) or 400V Phase to Phase (P2P) and have a statutory tolerance band of +10% and -

6%. But these voltages can deviate significantly due to the varying load on the network. Although todays deviation may infrequently exceed high-voltage or low-voltage thresholds, conduction losses and imperfect network conditions result in a lower overall system efficiency. Traditionally, On-Line Tap Changers (OLTCs) are used to raise and lower voltages across the entire LV distribution network in order to counteract voltage deviations [100]. However, such a hierarchical voltage control with OLTCs has its limited applicability, especially in cases where the voltage deviation significantly differs along individual branches of a feeding network [101]. More specifically, if voltages diverge along different branches or different phases of a feeder due to asymmetric loads then the adjustment of transformer taps will lead to high or low voltage violations regardless of the tap change direction. Installing a BESS at a strategic location (i.e. closer to the regions where voltage deviation takes place) and controlling the device to best suit the network's requirements is generally more applicable and commercially the more viable alternative [102].

As stated by Wade et al. [103], allocation of the BESS's limited storage capacity so it can solve the voltage problem most effectively is still a sophisticated challenge. Nonetheless, by installing a 200kWh unit that is rated at 600kW in a project that was carried out with *EDF Energy*, they showed the potential of BESS in a network to provide targeted voltage support [22]. Their results for a 0.4MWh BESS achieved a reduced voltage variation by 2.4% which resulted in a complete elimination of any “out-of-limit” voltage events, and a 70.96% reduction of all network events (including e.g. power events) over the annual simulation period. A demonstration project in Germany that was titled “More Microgrids” used four 180kWh batteries and demonstrated how both voltage stability as well as grid independence could be improved [104]. In this “More Microgrids” project a collection of holiday homes were fitted with a distributed PV system that is capable of generating a peak power of 315kW, and BESS was used to maximise the utility from this generation. How-

ever, due to the relatively small size of the network, due to the different behavioural patterns of holiday home occupants, and due to the different means of connecting customers to the German three-phase network, voltage deviation and phase unbalance issues were not as big as a concern as they are for UK distribution feeders. An equally sized German project entitled “GROWDERS” also used multiple BESS in the LV network, but instead of focusing at grid independent network operation, they mainly contributed to frequency and thermal constraints as well as voltage stability [105].

BESS that are sized between 100kWh to 200kWh (as those in the aforementioned projects [22, 103–105]) can easily address network issues, especially even when operating in a grid independent or “islanded” mode. Results from these early field trials show how BESS store the excess renewable power for usage during later times. But neither high nor low voltage events could be omitted once capacity limits were reached. An oversized BESS would be less likely to meet its operating limits, but the associated cost makes this oversizing unfeasible. Findings therefore indicate that not only the sizing, but also the BESS control method is of significant importance. Nonetheless, continuous voltage violations that require strong voltage support have not yet been encountered in any of these projects, and instead occasional violations accumulating to e.g. less than an average of 3.4 minutes per day are the norm [106]. Also, the majority of recorded low-voltage events on the UK distribution networks (i.e. when voltage levels fall below 216.2V) are caused by anomalous network events or are due to failures of the measurement equipment [107]. Therefore the complementing task of choosing correct control methods to optimally manage the network’s power flow is also important.

### 2.3.2 Power flow management

Interest in BESS control for power flow management has grown since improved measurement equipments in LV substations is more reliable and precise than traditional smart meter readings, but also since excessive power flow is the main cause for operational issues which do eventually lead to system overloads and outages<sup>1</sup> [110, 111]. To prevent future power flow from exceeding the system's capacity, BESS has been proposed to function as an instantaneous reserve [112, 113]. Resulting methods like BESS droop control use local voltage and frequency measurements to infer the latest loading and stress on the network to issue corresponding BESS control instructions [114]. The initial simulations in [114] showed how droop control can effectively remove reactive power demand and thus free the corresponding resource. Conventional droop control was designed to inject reactive power into high voltage transmission lines to counteract voltage drops and inject active power to counteract phase shift [115]. This control mechanism works since the impedance of high voltage transmission networks is more inductive than resistive. LV distribution networks on the other hand are more resistive in nature. Droop control for the LV applications is therefore founded on the assumption that network frequency will drop as demand begins to exceed supply, and that voltages along the distribution feeder drop more significantly when load is increased. Yet as already stated in Section 1.1.1, reversed power flow can raise voltage levels which makes such droop control methods less reliable and potentially unsuitable for LV network support. This problem was also encountered by Riffonneau et al. in [116], where they control BESS to solve an optimal power flow problem for grid connected PV systems. Ultimately, they were able to achieve a 13% reduction of electricity bills by implementing a rule-based dynamic programming optimiser,

---

<sup>1</sup>In fact, according to the UK energy regulator *OFGEM*, on average 45% of all customers experienced service disruptions in the period 2015-16 [108]. Unanticipated outages due to severe winter weather did lead to £39 million worth of damages. Whilst the resulting planned outages (i.e. for network repairs and upgrades to prevent future failures) also took place, unanticipated outages do still make up the larger amount of customer interruptions and customer minutes lost [109].

and they reduced peak power by successfully integrating PV. However, they do not consider reactive power within their power management method although it could free additional network resources and yield benefits to the distribution network, e.g. better voltage control and lower phase imbalance. The reason behind excluding it from their study was due to the potential conflicts that may arise with the proposed voltage control method which heavily relies on voltage measurements. Using BESS to reallocate PV generation for maximised self-consumption [117] or to achieve “peak-shaving” behaviour [25, 118] has seen continued interest in the field of BESS power flow management.

Aiming to address both voltage and power flow problems, *Scottish and Southern Electricity Networks* (SSEN) became the first UK network operator to trial street-level BESS deployment in the LV network, and they installed 500kWh worth of storage in Bracknell, UK [119]. This capacity was achieved by 25 Energy Storage Management Units (ESMUs), like those pictured in Figure 2.2. Each ESMU had cascadable 12.5kWh Energy Storage Units (ESUs), and the ESUs were connected to the distribution network via a three-phase 36kW Power Electronic Unit (PEU) to both manage the batteries and perform filtering operations. The aim of this so called *New Thames Valley Vision* (NTVV) project was to understand potential benefits, practicalities and costs of installing street-level BESS. In the beginning the main problem of finding an optimal deployment location for the ESMUs to achieve their best possible impact on system voltages had to be addressed. Yunusov et al. and Rowe et al. worked in collaboration with *SSEN*, and they assessed different BESS locations in several networks [14, 91, 120]. They found that a location 4/7 to 2/3 down the feeder yields the best overall impact on voltage levels and power flow. However, their findings also show that this location can vary significantly when not focusing on voltage support exclusively; i.e. proximity to the feeding substation was of greater importance when reducing the system’s overloads or distribution losses. Also, the chosen control sys-



Figure 2.2: Energy Storage Management Unit overview: (a) 12.5kWh Energy Storage Unit, (b) Power Electronics Unit, (c) deployed 12.5kWh system, (d) deployed 25kWh system - pictures are taken from the NTVV close down report [3]

tem had significant impact on the BESS performance, which is why more emphasis has been put on BESS control instead of locating or constructing BESS. Therefore, a review of BESS control methods including those that are implemented in the NTVV project are presented in the next section, Section 2.4.

## 2.4 Control of energy storage and its applications

Installing BESS at a strategic location in the LV network brings several advantages to DNOs' control over the network's performance. Regulating voltages to stay within statutory operating bands [24], improving power quality by optimising its power factor [121], shaving peak load to relieve stress from the installed network assets [25] or reducing phase unbalance to increase network efficiency [26] are only a few examples of recent research in this field. Whilst the questions regarding locating and scaling of BESS have mostly been addressed, BESS control still remains an open question and can be split into two complementing yet unmarried approaches:

1. “off-line” control, using load forecasts and BESS schedules; and
2. “on-line” control, using Set-Points Control (SPC), Model Predictive Control (MPC) or similar dynamic control methods.

These two control approaches have evolved from two different fields of active network management. Nonetheless, both approaches hold significant benefits to the operational performance of power distribution networks and neither of the two can be neglected. Therefore, Section 2.4.1 addresses and discusses the two control approaches and their missing link.

The current form of the NTVV project focuses on controlling a single BESS in the LV distribution network. However, the uptake of household connected BESS will increase the number of distributed systems, which need to be managed cooperatively. Therefore, Section 2.4.2 reviews and discusses different control approaches

for distributed BESS since the control of multiple single-phase storage units in a three-phase network is inherently more challenging than controlling one three-phase device.

### 2.4.1 Off-line and on-line control

Off-line control uses historic data to predict future load patterns which are used to schedule BESS operation accordingly. Early approaches, e.g. by Oudalov et al. [80], who used dynamic programming to generate BESS schedules had relatively high forecast errors due to the inherent difficulty of predicting future loads. These errors ultimately limit the ability of any given BESS schedule to e.g. effectively reduce peaks. This is why recent research has begun including uncertainty, like the work done by Baker et al. [122] where uncertainty of wind power was taken into account when scheduling and sizing BESS. Other work frequently re-evaluates BESS schedules to control and adjust its schedules after completing individual decision epochs [123]. Nonetheless, load forecasting remains a key component for BESS scheduling despite those load forecasts (and the resulting BESS schedules) being imperfect. This fact was emphasised by Rowe et al. in [91], and they developed a filtering mechanism for scheduling algorithms to reduce peak load in LV networks due to the presence of forecast errors. They also highlight the fact that most day-ahead load forecast only predict at a temporal resolution down to half-hourly periods which makes estimating errors at higher temporal resolution less dominant. The reason behind choosing this half-hourly forecasting period was pointed out by Haben et al. in [6, 124], as they argue that forecasts at half-hourly resolution yield the best compromise between high accuracy and high temporal resolution. Therefore, half-hourly forecasts have become the standard for generating any resource commitment and resource operation schedules. However, sub-half-hourly load volatility imposes the biggest stress on the network and it is this volatility that cannot be addressed when relying on half-hourly

forecast alone. In conclusion, on-line control has been considered as an alternative to off-line control.

One flavour of on-line control is the Set-Point Control (SPC) which is a robust technique that can immediately respond to network changes. SPC achieves this behaviour by measuring some properties of the power system (e.g. voltage level or frequency) and comparing those values to an internal target value, i.e. the set-point. Droop control, as mentioned in Section 2.3.2, was one of the first control methods that followed the SPC paradigm. A single set-point is however not suitable for a network that changes dynamically which is why droop control was extended to become adaptive as done by Tayab et al. in [115]. Their research shows how conventional droop control runs the risk of allowing system frequency to drop to 48.4Hz (from a nominal 50Hz), whereas adaptive droop was capable of frequency restoration with little to no observable frequency variation. However, their solution only injected reactive power into the system, yet BESS in LV distribution networks needs to provide active power from its limited energy resource. Conventional droop control does therefore run the risk of reaching energy shortage or surplus if the set-points and system dynamics are chosen too low or high. Modifications like hysteresis control and ramp-rate control were proposed to yield an adaptive SPC [125–128]. Hysteresis control prevents the device from oscillating between different power states even when small changes in the network are detected and would otherwise trigger an SPC change. When implementing a dead-band around the controller’s set-point as well as utilising a ramp-rate control, as done by Such et al. in [128], BESS can correct its internal energy state and therefore prevent hitting its operational limits. Furthermore, Such et al. showed how reverse power flow can be completely omitted through the use of on-line BESS control. However, this kind of on-line control is less effective when addressing daily demand peaks since pure SPC can only react to present network demand and does not respond to general trends or upcoming load events.

In order to address these shortcomings SPC has been extended by using short-term load predictions through the implementation of Model Predictive Control (MPC) [129,130]. Some MPC examples include Auto-Regressive (AR) models [131,132], fuzzy logic models [133, 134], genetic algorithms [135, 136] or Artificial Neural Networks (ANN) [72, 137–142]. Advancements in computational power allowed ANN to gain traction, and as shown in the study by Quan et al. in [138] ANN is becoming a promising method to generate load forecasts. In fact, in their study, Quan et al. proved how ANN can outperform AR and fuzzy logic models given that the ANN was optimally trained. Therefore, MPC can yield a acceptable prediction performance for linear systems when its complexity is sufficiently increased. For instance, Reihani et al. in [72] use the most recent 20 minutes of load information with a complex-valued ANN to predict the next 20 minutes of minutely load variations. Since their raw forecasts were more erratic than the actual load profile, a Kalman filter was implemented to smoothen the MPC’s output, yet this step introduced significant discrepancies between the actual and the forecasted load. Therefore they increased MPC complexity even further by taking into account parallel time-series, i.e. they considered the same 20 minutes from previous days in the prediction mechanism. This addition produced significantly better results and they shaved daily peaks by around 300kW in the medium-voltage network. Implementing such increasingly complex MPC to support on-line control is therefore a promising research trend, however the computational burden to deliver real-time solutions makes deployment of such systems costly or difficult.

Therefore, finding a way of combining both off-line control (i.e. scheduled BESS operation which is executed at half-hourly resolution) with on-line control (i.e. a mechanism that is responsive to power system changes) allows application of real-time corrections to the BESS schedule. Since this is still an open and ongoing research problem that has not yet been solved, **Objective 1** and **Objective 2**, as outlined in

Section 1.2, aim to develop and present a control mechanism that utilises the benefits from scheduled and real-time control. The objectives' corresponding chapters are, respectively, Chapter 3 and Chapter 4, and they address this research problem in two stages. At first the problem is addressed by developing a framework to apply scheduled BESS operation to a three-phase network in a sub-half-hourly manner but without modifying its underlying half-hourly schedule. Secondly, this hard constraint is removed by developing and implementing a dynamic controller that allows an operational tolerance around the pre-computed BESS schedule in order to guide BESS operation without violating its energy storage limits whilst maximising its flexibility to respond to sudden system changes. This a control system does however rely on a communications infrastructure in order to be implemented and deployed in reality. These infrastructures and their underlying control either follow a centralised or distributed networking paradigm. Both paradigms entail their specific costs and benefits which are addressed in the subsequent section, Section 2.4.2.

#### 2.4.2 Centralised and distributed control

It is important to understand the topology of an on-line control system since most of them have to gather power system information from multiple locations in order to make intelligent control decisions. This is particularly true if the control system consists of multiple entities that are distributed across the power network. The monitoring and control of such a distributed system (and hence of any power network) includes four systems that are inherently linked [143]:

1. The *managed system* itself, i.e. power network, that needs to be controlled;
2. a *monitoring system* that generates data through sensors and measuring equipment that is installed in the *managed system*;
3. a *decision making system* that uses the provided data to generate certain aims,

e.g. to improve the system state; and

4. a *control system* to generate control actions for the *managed system*.

In traditional power system control, systems 1 and 2 are grouped into the distributed measuring system and systems 3 and 4 are grouped into a centralised controller [144]. Therefore a bidirectional flow of information must exist in order to control and assure operation of the underlying physical network. Supervisory Control And Data Acquisition (SCADA) is the typical control architecture that enables the implementation of this bidirectional information flow. Tokyo is a showcase of successfully implementing such a centralised control system on a very large scale. In 1990, *Tokyo Electric Power Co.* (TEPCO) and *Toshiba* presented their latest installation of a centrally managed power distribution network that could deliver 43GW of power to the entire city of Tokyo [145]. All control instructions were generated from TEPCO’s central dispatching centre, which took into account measurements from a network of 819 nodes and 938 branches. Since Tokyo has grown significantly over the past decades, computational burden to relay data and act upon the information has increased, too. The UK power network is also a centrally managed system that has seen an increase in complexity, yet “*the network is 99.9999% reliable - a statistic we're proud of*“ [146].

But with the deployment of smart meters, network enabled appliances and controllable LCTs that can be part of the so called “Internet of Things” (IoT) system complexity is expected to increase beyond the capabilities of a single central management centre. This reason is why research began focusing on distributed control mechanisms [147–156]. For example, Vovos et al. in [147] compared centralised and distributed systems for voltage control and showed how they can yield a 86% gain (using centralised control) and 72% gain (using distributed control) in connectible capacity. Adding distributed BESS into the energy mix, Toledo et al. in [150] evaluated its impact on the IEEE-14 bus network when subjected to PV energy injection.

Their developed voltage index showed how voltages can deviate from nominal levels. In their results this index was 0.074%, 2.823%, and 3.471% for a release of system capacity of 500kW, 1000kW, and 1500kW, respectively. In their work a higher index represents a larger voltage deviation in comparison to a predefined base case without PV or BESS. To counteract this voltage rise, research like that by Marra et al. in [151] used coordinated EV charging to maximise self-consumption and thus alleviate grid power injection by PV. Focusing on the LV network's voltage issues, Marra et al. showed how high voltage incidents are completely avoided by charging at strategic times throughout the day, and at relatively low charging powers of 3.5kW. In fact, the majority of existing literature that uses BESS in distribution networks focuses on voltage security [35, 106, 150, 151, 154], power flow management [148, 156] and management of flexible loads [152, 153]. For instance, the approach used by Mokhtari et al. in [35] relies on bus voltage and network load measurements to prevent system overloads, and Marra et al. in [151] go even further and use information sharing between PV and BESS in order to limit voltage deviation. Both research teams were able to stabilise the network, and Marras et al. even increased the voltage margin by an additional 6.1V. The reasons why the usage of distributed and hierarchical control systems have become this attractive include lighter computational load for all control systems through abstraction at higher control levels and improved system stability, security and redundancy [157, 158].

Approaches and topologies to manage the flow of information within these control systems are classified by Bidram et al. in [149] where they separate the real network (i.e. the *physical layer*) from Information and Communication Technology (ITC) (i.e. the *cyber communication layer*). This separation allowed them to represent any distributed power system as a system of multiple cooperating entities, i.e. intelligent agents that form a so called Multi-Agent System (MAS). The technology of MAS comes from computer science and is well established in theory and practice of

intelligent agents [159]. As stated by Wooldridge et al. in [160] intelligent agents are flexible and autonomous entities that are defined by three fundamental properties:

1. *Reactivity*, which allows an agent to respond to changes in its observed environment,
2. *Pro-activeness*, which makes an agent act to meet its own or a collaborative goal, and
3. *Social-ability*, which enables the agent to coordinate its action with other agents.

Computer scientists would describe an agent as a component that gathers and collaboratively reacts to information about its environment. But distributed control systems in power distribution networks share the same characteristics. For this very reason MAS has seen increasing attention in the power and energy engineering disciplines. Some MAS applications are focusing on integration of DERs [161–165], matching of demand and supply [166], restoring the power distribution network [167], reconfiguring the network to reduce unbalance [168], integration of EVs [42, 169–171] and providing voltage support [172]. For example, Dou et al. in [163] proposed a MAS that coordinates DERs in as a so called Virtual Power Source (VPS). This VPS is an aggregate of all distributed entities and responds to voltage events throughout the LV distribution systems. In the case where generation increase would raise voltage levels beyond their statutory limits their VPS control could maximise power sharing and thus limit voltage overshoot to stay within voltage tolerance. This VPS is typically referred to as a Virtual Power Plant (VPP), which has also been implemented as a MAS by Vasirani et al. in [164]. In their work Vasirani et al. propose a distributed control strategy that utilises EVs as an energy storage medium to maximise profits from operating distributed renewable energy sources. Their findings suggest that when providing 12kWh of the EV’s energy storage capacity for renewable integration an annual EV profit of more than €250 (at 40% depth of discharge) can be achieved.

However, research involving MAS or any distributed control for that matter does require strong and standardised communication mechanisms.

A standard for MAS was established by the Foundation for Intelligent Physical Agents (FIPA) since the underlying versatility of different MAS would otherwise make integration very challenging. This challenge was also raised by Catterson et al. in [173], where they tried to merge the Condition Monitoring Multi-agent System (COMMAS) [174] with the Protection Engineering Diagnostic Agents (PEDA) system [175]. They showed the inherent difficulty of combining different ontologies despite the similar underlying goals. Also, as the number of independent elements becomes ubiquitous requirements for a strong telecommunications infrastructure become equally important [130]. So far synchronisation amongst agents has been taken for granted, yet MAS on multilayer networks may not automatically be synchronised [176]. The impact of desynchronised information exchange on the performance of a MAS driven energy scheduling algorithm still remains an open research question. Therefore, assessing the impact of introducing such a desynchronisation has become part of the research that is presented in this thesis, and **Objective 3** as outlined in Section 1.2 aims to answer this research question. Regardless of the synchronised or desynchronised nature of the distributed control, they both do however require some kind of communications infrastructure which may not always be present. Therefore, the next section, Section 2.4.3, introduces control mechanisms where communication between devices is no longer a strong requirement.

### 2.4.3 Communication-less control

Lastly, developing control methods for distributed system that do not rely on a communications infrastructure is also an important research topic since this infrastructure may not always be available; despite this being a common assumption [130]. So called communication-less systems are typically collections of multiple “dumb” devices that

follow their own control instructions without any external inputs. The current procedure of charging EVs is a perfect example of such a system since their charging commences immediately after they have been plugged into the grid. At the current rate of EV uptake so called “dumb charging” (or any “dumb action” for that matter) has high potential of causing significant network issues [177, 178]; i.e. voltage deviations, equipment overloads, asset damage and system outages. This issue is amplified since the EV uptake is anticipated to increase as driving range increases, cost of purchase reduces and the emphasis on leading an environmentally-friendly lifestyle is favoured more [179]. ICT reliant distributed control methods aim to circumvent these issues by using Demand Side Management (DSM) strategies. In [180] for example, Mohsenian-Rad et al. based developed a DSM mechanism that was based on game theory where multiple users engaged in the energy market to minimise the Peak-to-Average Ratio (PAR) of the resulting demand profile. Their results show that both minimising financial cost or the PAR of the resulting demand profile resulted in a 21.9% reduction in PAR when compared to a scenario without scheduling the energy consumer. But minimising PAR resulted in only a 7.31% reduction in energy cost, whilst minimising cost directly lead to a 19.6% reduction, despite the similar improvements in demand profile. However, this approach highly relies on ICT, as do similar DSM approaches that use e.g. time-of-use tariffs [181, 182] or other pricing signals [183]. None of them can be implemented without ICT and instead an indirect method must be sought.

A communication-less form of controlling Distributed Energy Resources (DERs) is the already mentioned Set-Point Control (SPC) [184]. Using traditional SPC on multiple identically-configured DERs can provide an optimal operation conditions, if each DER’s control parameters (e.g., bus voltage) were shared [185]. But in a communication-less environment this requirement cannot be satisfied which is why DER control algorithms have to be improved to prevent e.g. devices located furthest

from the substation from being used more frequently than others. The algorithm that is to be extended to control several BESS in a LV network is the Additive Increase Multiplicative Decrease (AIMD) algorithm. Unlike traditional SPC or hysteresis control like in [186], where a fuel-cell’s bus voltage was used as input to a ramp control for active power sharing, AIMD (like MAS) has its roots in computer science. Originally, AIMD algorithms were applied to congestion management in communications networks using the TCP protocol [187] to maximise utilisation while ensuring a fair allocation of data throughput amongst a number of competing users [188]. The same AIMD-type algorithms have previously been applied to power sharing scenarios in low voltage distribution networks where the limited resource is the availability of power throughput capacity of the substation’s transformer. One of the first proposed implementations for DER management was by Stüdli et al. [189], yet their system still required a one-way communications infrastructure to broadcast a so called “capacity event” [190, 191]. Later their work was extended to include Vehicle to Grid (V2G) applications with reactive power support [192], but this work still relied on a functioning and robust ICT infrastructure. Therefore, the question whether a truly communication-less dynamic control method can be developed (i.e. mitigating voltage deviation and capacity limitations) is still a remaining research problem. More specifically, this control method should not only avoid to impose any ICT requirements, but it should also aim to equalise the utilisation of all controlled devices which is not guaranteed by the traditional AIMD algorithm. **Objective 4**, as outlined in Section 1.2 aims to solve this research problem by extending AIMD to AIMD+, where natural voltage drops are taken into account to correctly skew the algorithm’s control decisions for individual control entities. Previous research is therefore extended since previous work has only utilised common SPC thresholds for controlling each of the DERs or previous work relied still on some form of communications infrastructure. In strong contrast to the former objectives of this thesis where substation monitoring

was used, the proposed AIMD+ algorithm does not require this information or any communication infrastructure for that matter.

## 2.5 Summary of gaps in literature

In this chapter, Chapter 2, the current and future roles for energy storage have been laid out. When focusing on BESS applications that support DNO owned networks, i.e. to enable the integration of LCTs and DERs within the LV distribution network without the need for network reinforcements, two key functions have emerged: 1. limiting voltage deviation to within statutory regulations, and 2. avoid thermal constraints by solving the power flow problem. Since DNOs had little experience with using BESS in their LV networks, several research projects and field trials were undertaken over the past decade. So far this research has already focused on sizing, locating and operating BESS. From the presented literature BESS control methods can be split into two categories that still remain unlinked: off-line control (e.g. scheduled or forecast driven control) and on-line control (e.g. SPC or MPC). Whereas off-line control takes into account daily load trends (i.e. at half-hourly resolution) it cannot compensate for load volatility due to DERs and LTCs (i.e. at sub-half-hourly resolution). On-line control methods on the other hand are designed to react quickly when system changes occur (i.e. at sub-half-hourly resolution), but they cannot efficiently include daily or weekly load patterns (i.e. at half-hourly resolution) due to the increase in model complexity. On the basis of the gaps in literature, as highlighted in the literature review, Chapter 2, and the problem statement of this thesis which is stated in Section 1.2 research **Objective 1** and **Objective 2** were derived. Furthermore, as the number of DERs increases throughout the grid methods to manage them need to become more sophisticated, too. However, all developed algorithms to control DERs either explicitly or implicitly assume synchronisation amongst all controlled entities

which need not be the case in reality. Assessing how information desynchronisation impacts the performance of a distributed algorithm is still an open research question that is addressed by **Objective 3**. **Objective 4** then aims to extend a distributed control algorithm by developing a method that no longer depends on communication systems. To summarise, the problems that arises from the identified gaps in literature are:

- how to assign pre-scheduled BESS half-hourly power profiles to a three-phase network at sub-half-hourly resolution in order to yield the largest positive impact for the underlying power distribution system (**Objective 1**),
- how to adjust a half-hourly BESS schedule (derived from a realistic but erroneous load forecast) based on sub-half-hourly load variations to minimise daily peak demands at both temporal resolutions (**Objective 2**),
- how large the impact will be on the performance of a scheduling and control algorithm when information exchange or message passing amongst the distributed control entities becomes desynchronised (**Objective 3**), and
- how multiple BESS can be coordinated in a communication-less environment to circumvent the need for ICT whilst contributing to voltage stability and thermal constraints without allocating their energy resources unevenly (**Objective 4**).

Despite some of the literature including aspects of the proposed research, none of them answer the research questions that are identified above. The novelty of the research in this thesis consists of combining on-line and off-line control, as well as to assess and extend the control of distributed BESS. All contributions, corresponding publications and draft papers, as outlined in Section 1.3 and Section 1.4, reflect upon the novelty of the presented research against the objectives as well as their aim and gaps in literature upon which they are founded.



# **Chapter 3**

## **Improving network performance by adjusting battery operation at sub-half-hourly resolution**

*M. J. Zangs, et al., “On-line adjustment of battery schedules for supporting LV distribution network operation,” 2016 International Energy and Sustainability Conference (IESC), Cologne, Germany, 2016, pp. 1-6.*

— Available: <http://dx.doi.org/10.1109/IESC.2016.7569485>

### **3.1 Overview**

Due to the trends in energy demand, future network load is expected to increase in both magnitude and volatility. As a result, DNOs have two choices to address the issues that are expected to result from increased network stress. They can either invest in network reinforcement or install network support equipment. For several reasons, e.g. decommissioning cost, installation cost, service disruption, etc., which have been outlined in Chapter 1, the installation of network support equipment was favoured. As also mentioned in Chapter 1, SSEN deployed and trialled an Energy Storage Management Unit (ESMU) in some of their Low-Voltage (LV) power distribution

networks. Within the scope of their trials, ESMU had to be controlled to benefit the network, without exceeding or violating any operational constraints. In order to achieve this kind of operation, ESMU operation had to be scheduled. During this kind of operation, the system either consumes or injects power, according to a predetermined plan that changes at regular intervals. For historic reasons and system compliance, this interval was chosen to be of 30 minutes, i.e. at half-hourly period.

Since the ESMU schedule was generated based upon a demand forecast, any resulting impact on the LV network operation is therefore based upon two factors:

1. quality of the underlying forecast that is used to generate ESMU schedules, and
2. network parameters that are used to quantify the improvements that would have been expected, when the half-hourly schedule is applied.

The previous research that was conducted by the Energy Research Laboratory (ERL) at the University of Reading (UoR) focused on improving half-hourly network operation to e.g. reduce peak load [91, 193]. However, in that research, sub-half-hourly demand variability has not been taken into account. Therefore, previously used performance parameters, and the corresponding measure of success, did not effectively quantify the ESMU's capability at mitigating negative impacts from this sub-half-hourly demand.

Therefore, this chapter addresses **Objective 1** of this thesis (which is outlined in Section 1.2), and a closed-loop optimisation method is proposed that adjusts the ESMU's phase powers at a sub-half-hourly resolution in order to improve network operation, whilst maintaining the charging and discharging profile during the corresponding half-hourly period. Unlike previous work in the field, this approach makes the ESMU follow its predetermined ESMU schedule, as well as allowing it to respond to high-resolution variations in three-phase network load.

In order to investigate how network operation may be improved, a collection of

commonly used parameters are evaluated in a set of corresponding cost functions. Initially, these cost functions are minimised on an individual basis to inspect their separate impact on network performance. Then, all cost functions are combined as a weighted sum to form a global cost function, which is used in the final analysis. For each optimisation approach, power flow simulations are run on a standardised UK power distribution feeder model in the simulation environment OpenDSS. This chapter therefore addresses the research question, whether sub-half-hourly adjustments to scheduled ESMU operation can significantly improve measured key network parameters.

The obtainment of key network parameters and their corresponding measure of improvement is explained next, in Section 3.2. All acquired data and the power network models used for this piece of work are shown in Section 3.3. Subsequently, the closed-loop optimisation method is presented in Section 3.4. At the end of this chapter, all results are presented and discussed in Section 3.5, and a concluding summary is presented in Section 3.6.

## 3.2 Key network parameters and derived cost functions

Two distinct approaches have emerged to quantitatively improve the performance of a system: either “cost” is reduced or “utility” is maximised. Both approaches rely on a mathematical explanation of underlying features that relate to performance of the system. The choice for this piece of work was to associate a cost to each key network parameter, for the reason that cost functions can be minimised towards a finite value, i.e. zero. Utility maximisation on the other hand is a theoretically unbound problem that can only reach a maximum, if its maximum can be estimated in advance. In other words, solutions to a cost function where the resulting cost is zero, are by definition

part of the set of optimal solutions. Determining the set of optimal solutions for the maximisation of a utility function is however more difficult.

With this in mind, the key network parameters are defined and their corresponding cost functions are introduced. In this chapter, Chapter 3, of work, power flow simulations are run at discrete times,  $t$ , which are separated by a sampling period  $\Delta t$ . The model used for these simulations is the IEEE LV Test Case, i.e. a network consisting of 906 three phase buses which resulting in a total of 2718 observable nodes. For each node, complex currents and voltages can be obtained, making the number of parameters to chose from nearly inexhaustible. In reality however, a power distribution network can only be observed at a limited number of measuring points. For the NTVV project, these points were at the substation and the ESMU's Point of Common Coupling (PCC). Therefore, all derived network parameters that could be obtained in reality are seen as “realistic parameters”, despite the fact that all key network parameters are extracted from power flow simulations. The remaining key network parameters, i.e. those that could not easily be obtained in reality, are therefore referred to as “theoretical parameters”<sup>1</sup>.

Due to the high number of these theoretical parameters, only a subset of them is used. The choice of parameters is based on their importance, role and impact on the actual network operation. A list of all key network parameters is presented below, and in this list all theoretical key network parameters are marked with a dagger ( $\dagger$ ).

- Voltages at substation transformer's secondary winding, i.e.  $\mathbf{v}_{ss}(t)$
- Voltages at ESMU's PCC, i.e.  $\mathbf{v}_{\text{ESMU}}(t)$
- Voltages at customer lateral <sup>$\dagger$</sup> , i.e.  $\mathbf{v}_{\text{load}}(t)$

---

<sup>1</sup>In literature, parameters are usually referred to as being “observable” or “unobservable”. From a technical perspective however all simulated parameters are observable. Therefore a parallel to real life observability and unobservability is drawn with the keywords “realistic” and “theoretical”, respectively.

- Total power flow, i.e.  $s_{\text{net}}(t)$
- Substation line utilisation, i.e.  $\mathbf{i}_{ss}(t)$
- Maximum line utilisation<sup>†</sup>, i.e.  $\mathbf{i}_{\text{line}}(t)$
- Distribution losses<sup>†</sup>, i.e.  $\mathbf{s}_{\text{losses}}(t)$

The following three subsections cover all key network parameters, by detailing the cost functions relating to: voltages, powers and currents.

### 3.2.1 Voltage related cost functions

In the UK, LV networks operate at a nominal voltage of 230V Phase-to-Neutral (P2N) or 400V Phase-to-Phase (P2P). Substations supply electricity to a three-phase cable, i.e. the feeder, and link to MV distribution networks, which operate at 11kV P2P. In an ideal case the voltage measured at the substation transformer's secondary winding remains constant as load changes. But in reality, internal losses (e.g. conductive losses and magnetic leakage) lead to a dropping voltage level, when load increases. Therefore, any deviation from the substation's nominal voltage can be seen as an indication of suboptimal network operation.

The “voltage deviation cost function”  $\zeta_{\text{voltage}}(\mathbf{v}(t))$  captures this suboptimal operation. This cost function is defined for a multi-phase complex voltage vector as  $\mathbf{v}(t)$  where  $\mathbf{v}(t) = (v_\phi(t))$ , where  $\phi$  is the phase number and where  $t$  the time at which the measurement was taken. Both phase and time are discrete, i.e.  $\phi \in \{1, \dots, \Phi\}$  where  $\Phi \in \mathbb{Z}_{>0}$  and  $t \in \mathbb{Z}_{\geq 0}$ . When using the three-phase substation voltage vector,  $\mathbf{v}_{ss}(t)$  (where  $\mathbf{v}_{ss}(t) = (v_{ss,\phi}(t))$ ), with this cost function, any drop in transformer voltage results in a positive cost.

$$\zeta_{\text{voltage}}(\mathbf{v}(t)) := \sum_{\phi=1}^{\Phi} \begin{cases} \zeta_h(v_\phi(t)) & \text{if } V_{ss} \leq v_\phi \\ \zeta_l(v_\phi(t)) & \text{otherwise} \end{cases} \quad (3.1)$$

where  $\Phi \in \mathbb{Z}_{>0}$

In this voltage cost function,  $\Phi$  represents the number of phases (i.e.  $\Phi = 3$ ), and  $\zeta_h(v_\phi)$  and  $\zeta_l(v_\phi)$  are two functions that convert a single voltage value, i.e.  $v_\phi$ , into a normalised positive cost based upon the direction of voltage deviation. High and low voltage thresholds, respectively  $V_h$  and  $V_l$ , are introduced in order to define these two functions. When choosing these two thresholds, then they must also satisfy the following inequality:

$$V_l < V_{ss} < V_h \quad (3.2)$$

For the work presented here, these two thresholds are based on the UK's nominal LV voltage range of +10% -6% around  $V_n$ , i.e. 230V P2N. As a result, the following upper and lower threshold functions are defined, in order to form a continuously differentiable cost function with a single zero tangent.

$$\zeta_h(v_\phi) := \left( \frac{v_\phi - V_{ss}}{V_h - V_{ss}} \right)^2 \quad (3.3)$$

$$\zeta_l(v_\phi) := \left( \frac{V_{ss} - v_\phi}{V_{ss} - V_l} \right)^2 \quad (3.4)$$

Substations may raise the voltage above the nominal LV voltage level, since voltage levels drop continuously along a purely consumptive feeder. The impact on the cost function  $\zeta_{\text{voltage}}(\mathbf{v})$  when  $V_{ss}$  is increased is shown in Figure 3.1 (for simplicity a single-phase voltage vector is shown, i.e.  $\Phi = 1$ ).

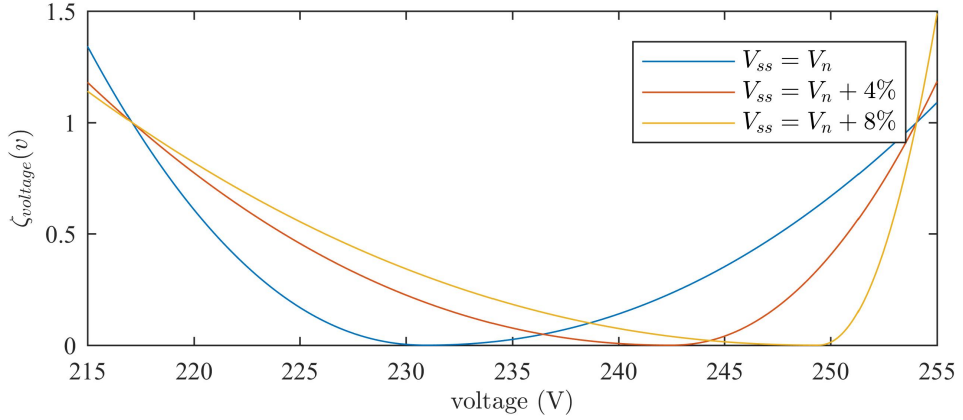


Figure 3.1: Cost function  $\zeta_{\text{voltage}}(v_\phi)$  values for different substation voltages

In this figure, it can be seen that  $\zeta_{\text{voltage}}(\mathbf{v})$  at the thresholds  $V_l$  and  $V_h$  equates to one, and to zero at the set substation voltage, even when this voltage is risen. This intentional feature is demonstrated by raising  $V_{ss}$  from  $V_n$  by +4% and +8%. At the ESMU's Point of Common Coupling (PCC), the device has access to all three phases of the feeder. One can assume that the line voltage along a purely consumptive feeder will drop continuously. Reasons behind this voltage drop are the resistive and inductive losses in the distribution lines, which are amplified with proximity to the substation, due to aggregated load currents from "down stream" customers. Under heavy load conditions, this voltage is likely drop below the statutory operation limit. Since this limit is an operational constraint for DNOs, it must not be violated.

To mitigate this voltage drop, power is injected into the feeder at the ESMU's PCC. Doing so increases the voltage at its PCC and surrounding nodes, since the portion of load current that would normally be supplied by the substation is now delivered by the ESMU. This effect when injecting power is sketched in the Figure 3.2 below.

In this figure, the expected voltage drop along the entire feeder is sketched. It can be seen how the voltage of the feeder's tailing section can potentially drop below  $V_l$ , but ESMU's intervention can alleviate some load and bring voltages back within

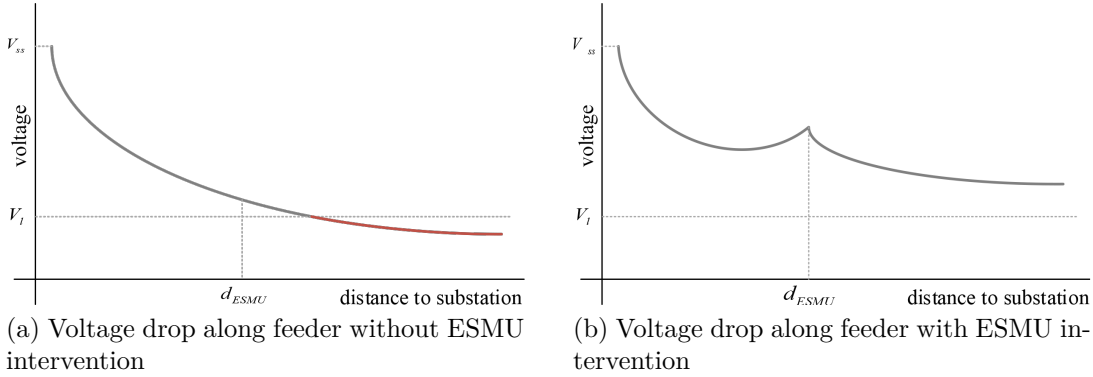


Figure 3.2: Sketch of the benefits that occur when ESMU injects power into the feeder in order to mitigate the voltage drop along the cable

operational bounds. The three-phase ESMU voltage,  $\mathbf{v}_{ESMU}(t)$  (where  $\mathbf{v}_{ESMU}(t) = (v_{ESMU,\phi}(t))$ ) is seen as a realistic key network parameter, which is also used in combination with a cost function. In fact,  $\mathbf{v}_{ESMU}(t)$  is used with cost function,  $\zeta_{\text{voltage}}(\mathbf{v}(t))$ , which was defined in Equation 3.1. This is the same cost function (i.e.  $\zeta_{\text{voltage}}(\mathbf{v})$ ) that was used to asses the deviation in transformer voltage. Therefore, the resulting cost can be formulated as  $\zeta_{\text{voltage}}(\mathbf{v}_{ESMU}(t))$ . The Electricity Safety, Quality and Continuity Regulations (ESQCR) define the statutory voltage range at UK electricity customers. However, monitoring those voltages to assure they lie within limits is unfeasible, since the installation of synchronised voltage measurement equipment at all loads implies significant cost. Therefore, in reality, these voltages are unknown. Nonetheless, in simulations all load voltages can easily be extracted, and since ESMU can impact all voltage levels to some degree, they are treated as theoretical key network parameters.

To illustrate this load voltage drop, a snapshot OpenDSS simulation was run on the used network model with all load consuming 8kW of power<sup>2</sup>. Figure 3.3 then shows all load bus voltages against their distances to the substation.

In this figure, two observations can be made.

---

<sup>2</sup>Whilst historic and recent loads may reach values of this magnitude quite infrequently, future customer demand with the aggregated effect home-charging of EVs is expected to yield extreme scenarios like this.

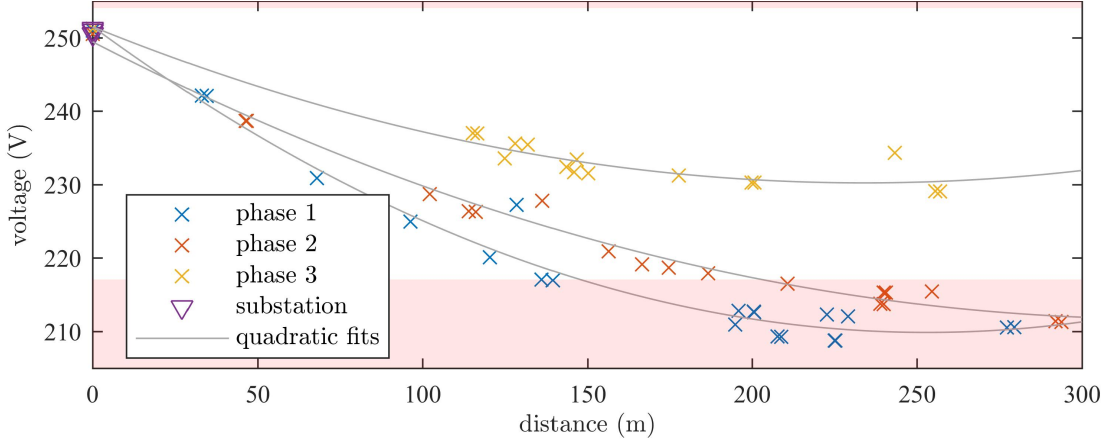


Figure 3.3: Voltage at the loads in the IEEE LV Test Case network for a total load of 440kVA against distance between the corresponding load and substation: for the quadratic fit  $R^2 = 58.76\%$

1. It can be seen that phases are significantly unbalanced.
2. Customers further than 200m from the substation are likely to experience low-voltage events.

Although ESMU can reduce the number of such low-voltage events, including a cost for each load would add significant difficulty to the minimisation problem. Therefore, to solve this problem more efficiently, the previously defined voltage cost function (i.e. Equation 3.1) is expanded to only return a single value from all customer voltages. More specifically, only the cost deviation is used. By reducing this number to the worst case, any implemented solver only focuses on the edges of the problem. This focus is of particular importance, especially if the impact of the ESMU on some customer voltages is comparatively low. An aggregated voltage deviation cost would potentially obfuscate this impact and prevent the solver from effectively targeting the worst cases. Therefore, the customer (or load) voltage is defined as  $\mathbf{v}_{\text{load}}(t)$ , where  $\mathbf{v}_{\text{load}}(t) = (v_{\text{load},i,\phi}(t))$ , and used in the new cost function,  $\zeta_{\text{load voltage}}(\mathbf{v}_{\text{load}}(t))$ , which is defined as:

$$\zeta_{\text{load voltage}}(\mathbf{v}(t)) := \max_{i,\phi} (\zeta_{\text{voltage}}(v_{i,p}(t))) \quad (3.5)$$

where  $i \in \{1, \dots, I\}$  and  $\phi \in \{1, \dots, \Phi\}$  and  $I \in \mathbb{Z}_{>0}$  and  $\Phi \in \mathbb{Z}_{>0}$

Here,  $i$  represents the customer number out of a total customer count  $I$ , and  $\phi$  represents the phase, out of the phase count  $\Phi$ , to which the customer is connected.

### 3.2.2 Power related cost functions

Beside meeting voltage constraints, DNOs need to assure that their distribution networks operates both in an efficient and hence ideal manner. How ideal a three-phase network operates is indicated by its phase unbalance. This disturbance due to unbalanced phase load may not have an immediate impact, but negative long term effects (e.g. asymmetric load on transformers, rotating machines and increased neutral current) do weaken network assets and cannot be neglected. The approach by which UK customers are connected to the feeder increases the problem of phase unbalance even more, because the single phase allocation is performed arbitrarily. Randomly assigning customers' phases was intended to distribute load evenly across all three phases, which in theory should balance the three-phase network load. In reality however this is not the case. Even in the unlikely case where the number of customers per phase is the same, the probability that all their loads match is very low. Therefore, the probability that LV distribution feeders in the UK are unbalanced is very high.

Substation monitoring is capable of providing reliable three-phase power measurements. Hence, they can be used as realistic key network parameters to determine the network's phase unbalance. The American National Standards Institute's (ANSI) definition of Unbalance Factor (UF) is used to calculate the phase unbalance [194]:

$$\text{UF}(\mathbf{x}) := \frac{\max_n |\bar{\mathbf{x}} - x_n|}{\bar{\mathbf{x}}} \text{ where } \mathbf{x} = (x_n) \quad (3.6)$$

and  $n \in \mathbb{Z}_{>0}$

Here,  $\mathbf{x}$  can be an arbitrary vector, consisting of scalar values  $x_n$  (e.g.  $x_n$  may be voltage, current or power measurement per phase  $n$ ). In this context,  $x_n$  is chosen to be the power flow into one of the network's phases. For clarity, the notation of  $\bar{\mathbf{x}}$  is used to define the mean of the given vector, i.e.:

$$\bar{\mathbf{x}} := \frac{1}{N} \sum_n^N x_i \quad (3.7)$$

Substituting the three-phase substation power vector,  $\mathbf{s}_{ss}(t)$  (where  $\mathbf{s}_{ss} = (s_{ss,\phi})$ ), for  $\mathbf{x}$ , allows the formulation of another cost, i.e. the “unbalance” cost,  $\zeta_{\text{unbalance}}(\mathbf{s}_{ss}(t))$ , which is defined as:

$$\begin{aligned} \zeta_{\text{unbalance}}(\mathbf{s}(t)) &:= \text{UF}(\mathbf{s}(t)) - 1 \\ &= \frac{\max_\phi \left| \bar{\mathbf{s}}(t) - s_\phi(t) \right|}{\bar{\mathbf{s}}(t)} - 1 \end{aligned} \quad (3.8)$$

where  $\phi \in \{1, \dots, \Phi\}$  and  $\Phi \in \mathbb{Z}_{>0}$

Since the lowest value of  $\text{UF}(\mathbf{x})$  is one, the corresponding cost function had to be adjusted in order to reach a minimum value of zero instead. A sample illustration, showing how this cost behaves as phase unbalance increases, is included in the Figure 3.4.

Here, it can be seen how  $\zeta_{\text{unbalance}}(\mathbf{s}(t))$  rises with an increasing separation of the three-phase power values. Additionally, to assess the effective utilisation of the power distribution network, deviation from a unity Power Factor (PF) is also formulated

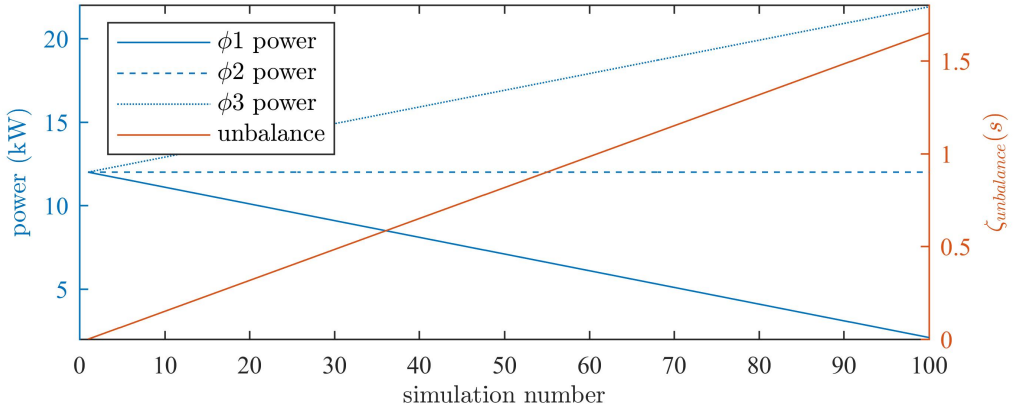


Figure 3.4: Sample network imbalance for different phase loadings as defined in ANSI/NEMA MG 1-2011

as a cost. PF is the ratio between active ( $p$ ) and apparent power ( $s$ ), and gives an indication of how much “good” power is being consumed by the system<sup>3</sup>. Experts would agree that keeping PF of a system close to unity indicates that it only requires active power to operate, which implies that uses the lowest possible amount of power transmission resources. In order to indicate the proximity to unity PF, a corresponding cost,  $\zeta_{\text{PF}}(\mathbf{s}_{ss}(t))$ , is used, which is defined as:

$$\zeta_{\text{PF}}(\mathbf{s}(t)) := \Phi - \sum_{\phi=1}^{\Phi} \frac{\text{Re}(s_{\phi}(t))}{|s_{\phi}(t)|} \text{ where } \mathbf{s}(t) = (s_{\phi}(t)) \text{ and } \Phi \in \mathbb{Z}_{>0} \quad (3.9)$$

Any deviation from a unity PF per phase increases the associated cost, whilst achieving a perfect PF for each phase results in a total cost of zero. In perfectly balanced systems that operate at unity PF, all three phases are  $120^\circ$  out of phase, and the sum of their instantaneous powers should equate to zero. This zero-sum also indicates, that no neutral current is flowing in the system. However, in an unbalanced system that operates at non-unity PF, the power transmitted through the neutral conductor can significantly deviate from zero. The negative impact of

---

<sup>3</sup>Reactive power is used to maintain magnetic fields in rotating machines, yet this can be supplied by local reactive power compensators and thus need not occupy otherwise free power transmission resources.

transmitting power through the neutral conductor is further amplified, since typical power distribution cables often use neutral conductors with significantly smaller cross-section areas than those used as line conductors. Results of any such additional power flow in the neutral conductor are further deviation of neutral voltages from ground, increased losses, and quicker exhaustion of the neutral conductor's power carrying capability (making the system become more prone to failures). To address this last point, a “neutral load” cost,  $\zeta_{\text{neutral load}}(\mathbf{s}_{ss}(t))$ , is defined as follows:

$$\zeta_{\text{neutral load}}(\mathbf{s}(t)) := \left| \sum_{\phi=1}^{\Phi} s_{\phi}(t) e^{\frac{j2\pi\phi}{\Phi}} \right| \quad \text{where } \mathbf{s}(t) = (s_{\phi}(t)) \text{ and } \Phi \in \mathbb{Z}_{>0} \quad (3.10)$$

Equation 3.10, superimposes the three-phase network powers whilst rotating each power vector by an integer multiple of  $120^\circ$  (i.e.  $e^{\frac{j2\pi\phi}{3}}$  where  $\phi = \{1, 2, 3\}$ ) in the complex plane. In a perfectly balanced scenario, the summation results in no neutral power, i.e. a value of zero, but for an unbalanced network, the magnitude value will be greater than zero. Therefore this magnitude of the neutral's apparent power vector is computed, which is then used as the resultant cost. Power losses have already been mentioned. In comparison to the losses of the entire electricity grid, losses in a LV distribution network are negligibly small. Nonetheless, the aggregate effect of reducing those losses could have a noticeable impact on both network efficiency and maximising profit margins (after all, nobody pays for undelivered energy). For example, in the high load scenario that was simulated in Section 3.2.1, distribution losses were calculated as 58kW. This equates to 12% of the total network power, however, losses would be noticeably lower during normal network operation, e.g. a maximum of 5%. The rising proportion of losses, as uniform network load is continuously increased, is shown in Figure 3.5.

In Figure 3.5, the region where losses exceed 5% of the total network power is

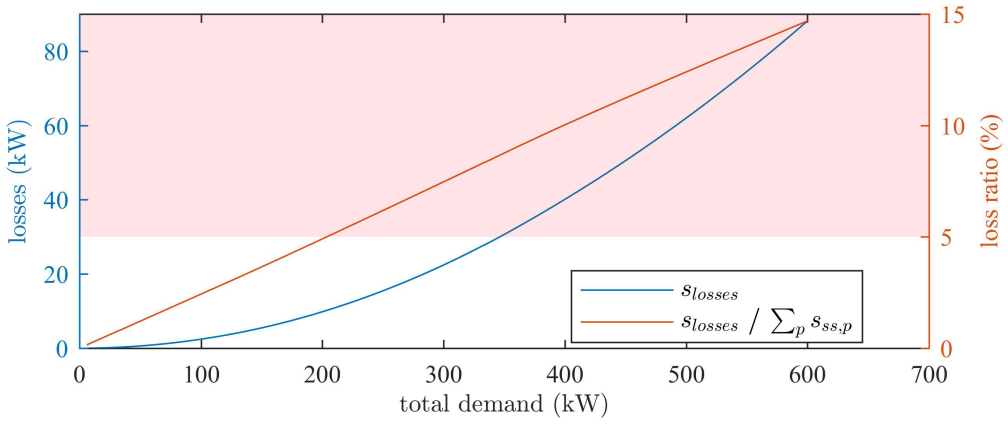


Figure 3.5: Losses against increasing power demand

highlighted in red. Whilst these losses are easily obtained from power flow simulations, in reality, distribution losses cannot be determined with such ease. Therefore, the network losses,  $s_{losses}(t)$ , are seen as theoretical key network parameters and they are used in the final power related cost,  $\zeta_{losses}(s(t))$ , which is defined as follows:

$$\zeta_{losses}(s(t)) := |s(t)| \quad (3.11)$$

### 3.2.3 Current related cost functions

Having addressed voltage deviation and inefficient network operation, physical network limits have not yet been taken into account: i.e. the current carrying capabilities of the cables. Heat, i.e. losses that are caused by the line's impedance, deteriorates the cable over time. Therefore, cables have an assigned thermal rating which should not be exceeded in order to minimise permanent cable damage and mitigate possible network failure. At substation level, to prevent over-currents, fuses or reclosers are installed that will disconnect the network under fault or high current conditions. To quantify whether the substation fuse is approaching its tripping point, its nominal fuse rating,  $I_{fuse}$ , is used. For the context of this work,  $I_{fuse}$ , is a static value which must not be exceeded. Using the three-phase current vector,  $\mathbf{i}_{ss}(t)$  (obtained via sub-

station monitoring, where  $\mathbf{i}_{ss}(t) = (i_{ss,\phi}(t))$  a cost,  $\zeta_{\text{fuse utilisation}}(\mathbf{i}_{ss}(t))$ , is formulated, and defined as follows:

$$\zeta_{\text{fuse utilisation}}(\mathbf{i}(t)) := \left( \frac{\sum_{\phi=1}^{\Phi} i_{\phi}(t)}{I_{\text{fuse}}} \right)^2 \quad \text{where } \phi \in \{1, \dots, \Phi\} \text{ and } \Phi \in \mathbb{Z}_{>0} \quad (3.12)$$

In the Figure 3.6, a plot has been included to illustrate how this quadratic cost behaves as substation current increases. For this simple case, the substation line rating was set as  $i_{\text{fuse}} = 400\text{A}$ , and the total substation current is the sum of all three phase currents. The red area indicates the region where current exceeds the fuse's nominal rating.

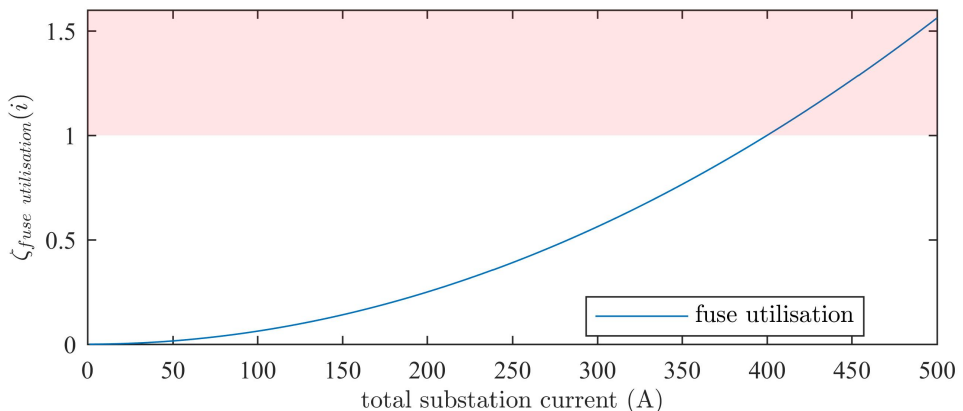


Figure 3.6: Cost of line or fuse utilisation against network current

In addition to the currents flowing through the substation's fuse, currents flowing through all lines in the network may also be considered. Just like voltage levels at each customer, line currents are also seen as theoretical key network parameters, since they cannot easily be obtained. Generally, as the distance to the substation increases fewer “down stream” customers are connected to a radially expanding feeder, and therefore cables can be scaled down, i.e. to save cost. However with the expected uptake of LCTs, feeders are expected to deliver increasingly larger currents throughout all lines. For smaller lines at the network edge, these currents may increase to a magnitude

larger than their nominal ratings. Therefore, the fuse current cost is expanded to take into account all line currents,  $i_{\text{line},l,\phi}(t)$ , and their nominal ratings,  $I_{\text{nom},l}$ . Here  $l$  represents the line number and  $\phi$  the phase of that line. Collecting them in  $\mathbf{i}_{\text{line}}(t)$  (where  $\mathbf{i}_{\text{line}}(t) = (i_{\text{line},l,\phi}(t))$ ) allows the formulation of an extended line utilisation cost,  $\zeta_{\text{line utilisation}}(\mathbf{i}_{\text{line}}(t))$ , which is defined as follows:

$$\zeta_{\text{line utilisation}}(\mathbf{i}(t)) := \max_l \left( \frac{\sum_{\phi=1}^P i_{l,\phi}(t)}{I_{\text{nom},l}} \right)^2 \quad (3.13)$$

where  $l \in \{1, \dots, L\}$  and  $\phi \in \{1, \dots, \Phi\}$  and  $L \in \mathbb{Z}_{>0}$  and  $\Phi \in \mathbb{Z}_{>0}$

Similar to Equation 3.5, this cost function only considers the maximum line utilisation in order to reduce computational burden without decreasing any parameter sensitivity.

### 3.3 Data, models and storage scheduling

In this section the used power data is presented first. Then the network model, from which all aforementioned key network parameters are extracted, and the battery model are explained. In the end, the scheduling procedure is detailed.

#### 3.3.1 Load profiles

Alongside the LV Test Case model, the IEEE published 100 minutely demand profiles; each profile lasting 24h. Therefore, by assigning one load profile to each customer, a series of 1440 snapshot simulations could be run in OpenDSS in order to simulate the variation and volatility in demand over the entire day. A standardised power factor of 0.95 was used for all loads to calculate their reactive component. The apparent network power,  $s_{\text{net}}(t)$ , is therefore defined for each time-step,  $t$ , as the aggregate of all load apparent powers,  $\mathbf{s}_{\text{load}}(t)$ :

$$s_{\text{net}}(t) := \sum_{i=1}^I s_{\text{load},i}(t) \text{ where } I \in \mathbb{Z}_{\geq 0} \quad (3.14)$$

However, this demand profile does not take into account the distribution losses, since they are only known after performing the power flow simulations. Nonetheless, it functions as a simple time-series to schedule ESMU operation, which is detailed in Section 3.3.4.

### 3.3.2 Network model

The IEEE Power and Energy Society (IEEE-PES) provides several multi-node test cases. These test cases used to be limited to distribution networks in the United States. In 2015 however, they published a standardised model of a LV distribution network for the UK power network. This model is called the “European Low Voltage Test Feeder” [195]. Within the context of this work, this feeder is referred to as the “LV Test Case” and a network plot of this feeder has been included for reference.

A substation (triangle in north west) provides power to the feeder, and the power magnitude is visualised by the thickness of the feeder’s lines. In total, there are 55 single-phase households connected to the substation, which represents a medium-sized, unbalanced UK feeder.

### 3.3.3 Battery model

The ESMU systems that were deployed throughout the NTVV project consisted of two parts: the Power Management Unit (PMU) and the Energy Storage Unit (ESU). The PMU controls three-phase powers and links the ESU to the grid. Each PMU’s single-phase power rating,  $S_{\text{rating}}$ , is 12kVA and can also perform filtering functions beside battery charging and discharging, e.g. compensating for harmonic distortion, reactive power and phase unbalance. The ESU is a modular container of 12.5kWh

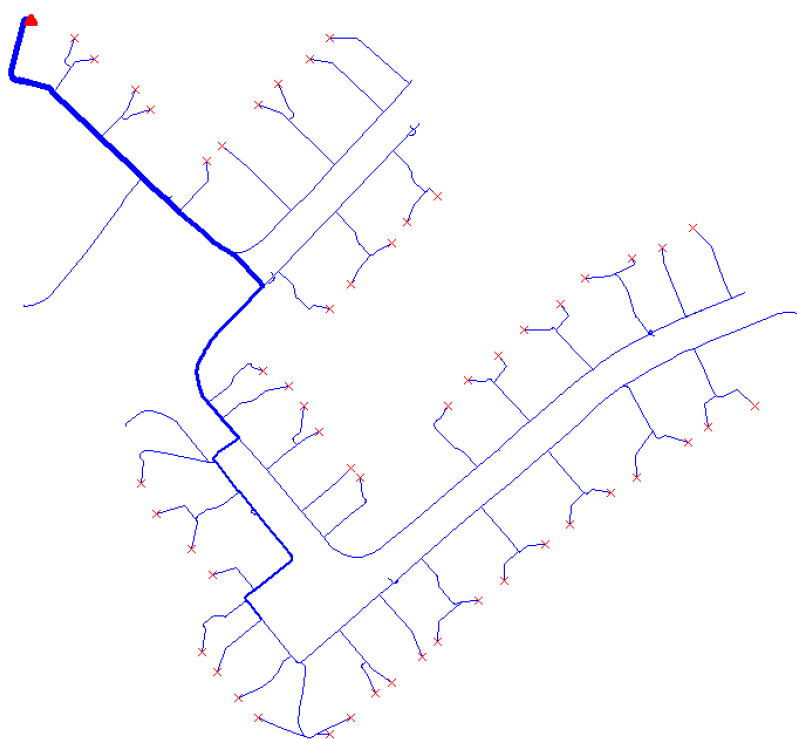


Figure 3.7: A power flow plot of the IEEE-PES European Test Case Feeder, i.e. a LV distribution network in the UK.

of Li-Ion energy storage that can be aggregated to increase the total energy storage capacity. All battery monitoring, conditioning and regulation is performed within the ESU and hence lies outside the scope of this work. However, control instructions that are sent to the ESMU system should not request the device to operate outside its own specifications, i.e. avoid under- or over-charge.

In order to simulate this ESMU system and its energy storing behaviour, in this section, Section 3.3.3, an energy model is developed from the given device specifications. This model includes an charge-discharge efficiency,  $\eta$ , and standby losses,  $\mu$ .  $\eta$  is related to the efficiency of the PMU's power converters, which are quoted to have a round trip efficiency of 98%, i.e.  $\eta = 0.98$ .  $\mu$  on the other hand is linked to the nominal power drawn by the battery's control system as well as the battery's self-discharge rate. With the charge-discharge efficiency,  $\eta$ , the battery charge-discharge power,  $p_{\text{bat}}(t)$ , can be calculated for any given ESMU power,  $\mathbf{s}_{\text{ESMU}}(t)$  (where  $\mathbf{s}_{\text{ESMU}}(t) = (s_{\text{ESMU},\phi}(t))$ ).

$$p_{\text{bat}}(t) := \begin{cases} \eta \text{Re} \left\{ \sum_{\phi=1}^{\Phi} s_{\text{ESMU},\phi}(t) \right\} & \text{if } \text{Re} \left\{ \sum_{\phi=1}^{\Phi} s_{\text{ESMU},\phi}(t) \right\} \geq 0 \\ \frac{1}{\eta} \text{Re} \left\{ \sum_{\phi=1}^{\Phi} s_{\text{ESMU},\phi}(t) \right\} & \text{otherwise} \end{cases} \quad (3.15)$$

where  $\phi \in \{1, \dots, \Phi\}$  and  $\Phi \in \mathbb{Z}_{>0}$

Although the ESMU's PSU rating,  $S_{\text{rating}}$ , may allow for a maximum power consumption of 36kVA (i.e.  $= 3 \times 12\text{kVA}$ ), the charging power is internally limited, by a charging factor,  $C_f$ . This factor is the ratio between the battery's maximum discharge power and its total capacity (i.e.  $\max_t(p_{\text{bat}}(t)) \leq C_f \cdot C_{\text{bat}}$ ). In accordance to the ESMU's specification,  $C_f$  was fixed as 1.6. With those restrictions in mind, a charge-discharge power can be applied to charge or discharge the battery. Assuming that this power remains constant during a predefined sample period,  $\Delta t$ , then the

change in stored energy can be defined as follows.

$$\Delta E_{\text{bat}}(t) = p_{\text{bat}}(t)\Delta t \quad (3.16)$$

The battery's dynamics can therefore be modelled as the change in energy level from time  $t$  to time  $t + \Delta t$ . Taking into account the standby losses,  $\mu$ , the next energy level  $E_{\text{bat}}(t + \Delta t)$  is defined as:

$$E_{\text{bat}}(t + \Delta t) := \mu (\Delta E_{\text{bat}}(t) + E_{\text{bat}}(t)) \quad (3.17)$$

In an ideal case,  $\mu = 1$ , where no energy would be lost in the storage system. However, to model energy storage dynamics, it became common practice to assess the energy storage's charge level as the State of Charge (SOC) instead of using the actual charge stored. This SOC is defined as the actual energy stored in the ESU,  $E_{\text{bat}}(t)$ , divided by the total capacity of the system,  $C_{\text{bat}}$ . i.e.:

$$SOC(t) := \frac{E_{\text{bat}}(t)}{C_{\text{bat}}} \quad (3.18)$$

Similar to the energy dynamics, the SOC dynamics can therefore be defined as:

$$SOC(t + \Delta t) := \mu \left( \frac{p_{\text{bat}}(t)\Delta t}{C_{\text{bat}}} + SOC(t) \right) \quad (3.19)$$

When summarising  $\hat{s}_{\text{ESMU}}(t) = \text{Re} \left\{ \sum_{\phi=1}^{\Phi} s_{\text{ESMU},\phi}(t) \right\}$  and combining Equation 3.15 with Equation 3.19, then the battery model's full dynamics can be defined as:

$$SOC(t + \Delta t) := \begin{cases} \mu \left( \frac{\eta \hat{s}_{\text{ESMU}}(t)\Delta t}{C_{\text{bat}}} + SOC(t) \right) & \text{if } \hat{s}_{\text{ESMU}}(t) \geq 0 \\ \mu \left( \frac{\hat{s}_{\text{ESMU}}(t)\Delta t}{\eta C_{\text{bat}}} + SOC(t) \right) & \text{otherwise} \end{cases} \quad (3.20)$$

A flowchart to visually represent the developed battery model, is included in Figure 3.8. In this figure, all green and blue fields indicate, respectively, model inputs

and results. The white states represent operations applied onto those inputs and results and in the end yield the output, i.e. the yellow field.

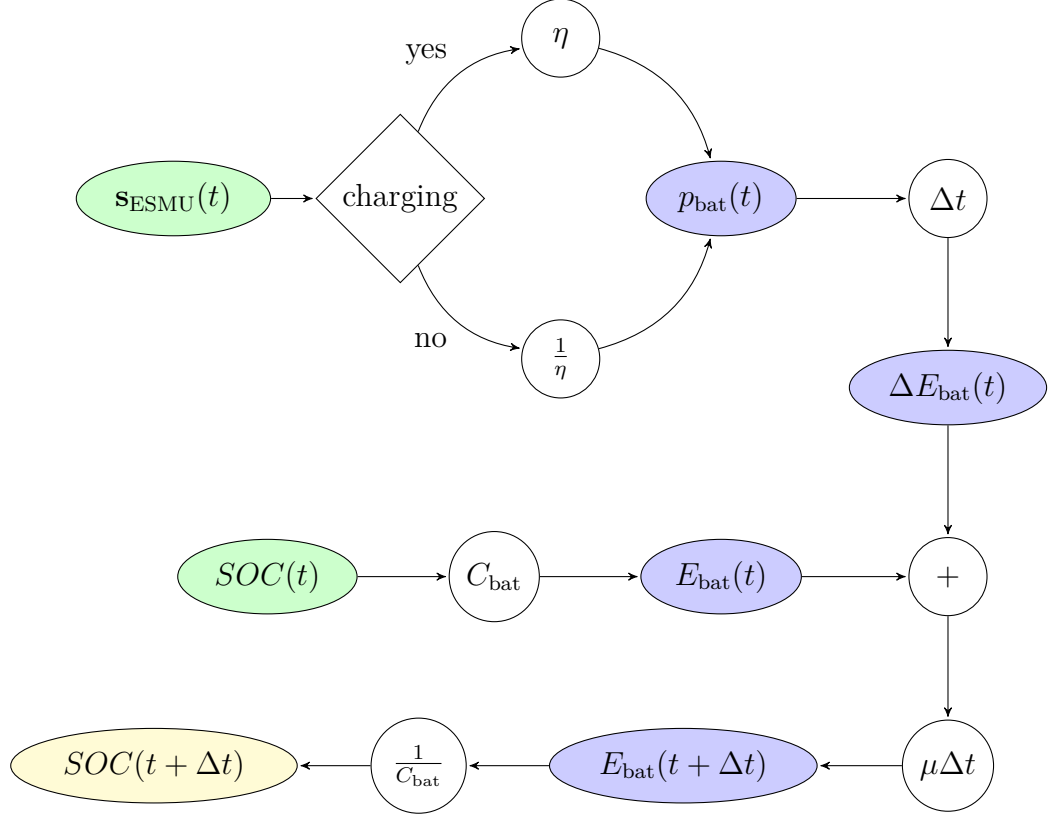


Figure 3.8: Flowchart to calculate the next SOC (i.e.  $SOC(t + \Delta t)$ ) based on current ESMU power (i.e.  $s_{ESMU}(t)$  which is predefined) and current SOC (i.e.  $SOC(t)$  which is predefined).

### 3.3.4 ESMU scheduling

Computing the ESMU's daily schedule at the dataset's temporal resolution, i.e. sub-half-hourly, is ineffective and slow. Doing so is ineffective, because demand variability due to behavioural unpredictability makes forecasting at high temporal resolution unfeasible, and the large number of search parameters makes finding a solutions very computationally demanding. Therefore, forecasting and scheduling is generally performed at half-hourly temporal resolution. To obtain such a half-hourly profile, the sub-half-hourly profile had to be down-sampled and synchronised. This is done with

the synchronisation function  $k(t)$ , which links the original sub-half-hourly demand to a half-hourly time-series and is defined as follows:

$$k(t) := \left\lfloor \frac{t-1}{K\Delta t} \right\rfloor + 1 \quad (3.21)$$

Here,  $\Delta t$  is the sub-half-hourly sampling period of the simulation, and  $K$  is the duration of the half-hourly time-slot, i.e. number of sub-half-hourly periods within the half-hourly slot. It should be noted that the integer multiple of  $K$  has to equate to the scheduling horizon's length,  $T_{\text{sch}}$ ; i.e.  $a := \frac{K}{T_{\text{sch}}}$  where  $a \in \mathbb{Z}_{>0}$ . Otherwise, the sub-half-hourly profile cannot be divided into a set of equal length time-slots, where each time-slot is of length  $K\Delta t$ . Therefore, the resulting half-hourly network load,  $s_{\text{net}}^*(t)$  (where  $\mathbf{s}_{\text{net}}^* = (s_{\text{net}}^*(t))$ ), is defined as follows:

$$s_{\text{net}}^*(t) = \frac{1}{K} \sum_{\tau=\alpha(t)}^{\beta(t)} s_{\text{net}}(\tau) \text{ where } K \in \mathbb{Z}_{>0} \quad (3.22)$$

where  $\alpha(t) := k(t)K$  and  $\beta(t) := (k(t) + 1)K - 1$

Now, over the period from  $\alpha(t)$  to  $\beta(t)$ , are power values are equal. To illustrate the difference between the original sub-half-hourly network load and the resulting half-hourly demand, both profiles are plotted in Figure 3.9. In this figure, it can be observed how the high variability and volatility in power is removed in the half-hourly profile. When generating ESMU schedules these variations are neglected and thus the unwanted peak power demands cannot be sufficiently compensated.

The main goals when scheduling battery operation are to achieve “valley-filling” and “peak-shaving” behaviour. As shown in the literature review in Chapter 2, the Peak-to-Average Ratio (PAR), the min-max-difference (MMD) and the power transients (TRA) are good indicators of such a behaviour. Therefore, three half-hourly costs regarding are used as,  $\zeta_{\text{PAR}}(\mathbf{s}_{\text{ESMU}}^* + \mathbf{s}_{\text{net}}^*)$ ,  $\zeta_{\text{MMD}}(\mathbf{s}_{\text{ESMU}}^* + \mathbf{s}_{\text{net}}^*)$ , and

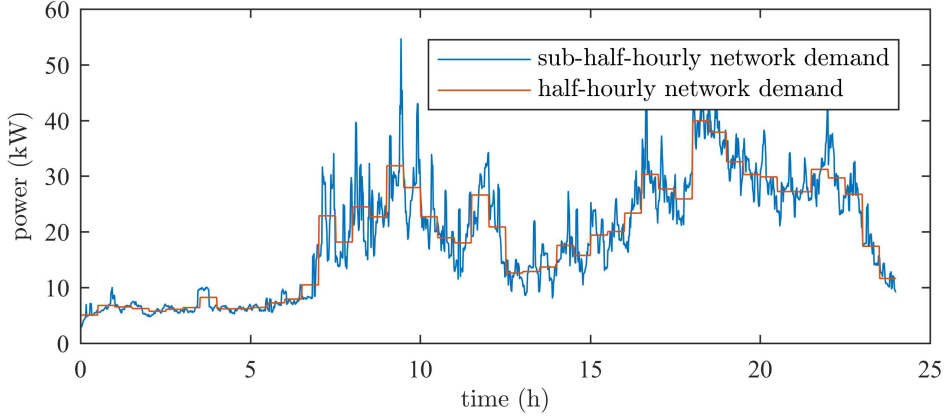


Figure 3.9: Highly variable and volatile demand profile vs half-hourly demand (i.e. a forecast under perfect foresight conditions)

$\zeta_{\text{TRA}}(\mathbf{s}_{\text{ESMU}}^* + \mathbf{s}_{\text{net}}^*)$  are defined as follows:

$$\zeta_{\text{PAR}}(\mathbf{s}) := \frac{\max_t |\mathbf{s}|}{\frac{1}{K} \sum_{t=1}^a s(t)} - 1 \text{ where } \mathbf{s} = (s(t)) \quad (3.23)$$

$$\zeta_{\text{MMD}}(\mathbf{s}) := \frac{\max_t (\mathbf{s}) - \min_t (\mathbf{s})}{\frac{1}{K} \sum_{t=1}^a s(t)} \text{ where } \mathbf{s} = (s(t)) \quad (3.24)$$

$$\zeta_{\text{TRA}}(\mathbf{s}) := \max_t |s(t + \Delta t) - s(t)| \text{ where } \mathbf{s} = (s(t)) \quad (3.25)$$

The half-hourly cost in Equation 3.23 computes the ratio between the maximum network power and the mean network power. To normalise this value with a minimum value of zero, one is subtracted. Equation 3.24 returns the difference between the largest and smallest network power, and Equation 3.25 computes the change in network power over time. All three costs functions assess the sum of the half-hourly ESMU schedule,  $\mathbf{s}_{\text{ESMU}}^*$ , and the half-hourly network load profile,  $\mathbf{s}_{\text{net}}^*$ , and when they reach a value of zero, then a perfectly flat, i.e. valley-filled and peak-shaved profile is obtained. Combined with all underlying model constraints, the following minimisation problem is defined to aim and obtain such a flat power profile:

$$\begin{aligned}
& \min_{\mathbf{s}_{\text{ESMU}}^*} \{ \zeta_{\text{PAR}}(\mathbf{s}_{\text{ESMU}}^* + \mathbf{s}_{\text{net}}^*) + \zeta_{\text{MMD}}(\mathbf{s}_{\text{ESMU}}^* + \mathbf{s}_{\text{net}}^*) + \zeta_{\text{TRA}}(\mathbf{s}_{\text{ESMU}}^* + \mathbf{s}_{\text{net}}^*) \} \\
\text{s.t. } & \begin{cases} p_{\text{bat}}(t) \leq C_f \times C_{\text{bat}} \\ |s_{\text{ESMU},\phi}(t)| \leq S_{\text{rating}} \forall \phi \\ 0 \leq SOC(t) \leq 1 \end{cases} \tag{3.26}
\end{aligned}$$

To solve this minimisation problem, a Sequential Quadratic Programming (SQP) approach was chosen. The resulting half-hourly ESMU power,  $\mathbf{s}_{\text{ESMU}}^*$ , could then be extrapolated using the same synchronisation function,  $k(t)$ , to yield a sub-half-hourly ESMU schedule.

For the work presented in this chapter, the supplied half-hourly network load (or forecast) was obtained from sub-half-hourly data. Treating it as a forecast with perfect foresight does not skew the already imperfect schedule performance, which is obtained when applying the resulting half-hourly schedule to sub-half-hourly load. Figure 3.10 shows a sample day, where the impact of this half-hourly ESMU schedule becomes apparent.

This figure shows the positive impact on the half-hourly profile (i.e. in Figure 3.10a), which is particularly dominant during the evening peak load. However, the impact on the actual sub-half-hourly demand (i.e. in Figure 3.10b) has a much larger demand spike during the morning hours, which is not that strongly addressed. When compared, the ideal peak power shaving dropped from 9.46kW to only 6.36kW. Nonetheless, the overall improvement yielded by the ESMU schedule can still be noticed. The method of how to adjust the ESMU's phase powers to mitigate the impact of such volatile load spikes is addressed in the following section.

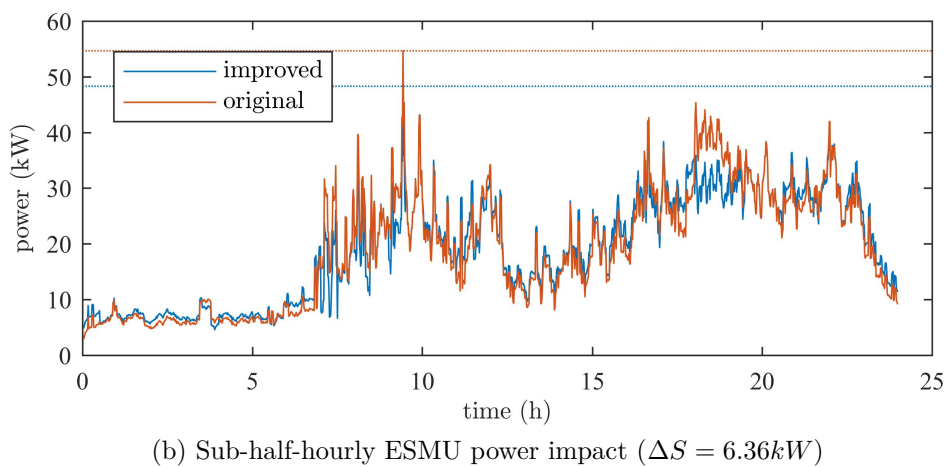
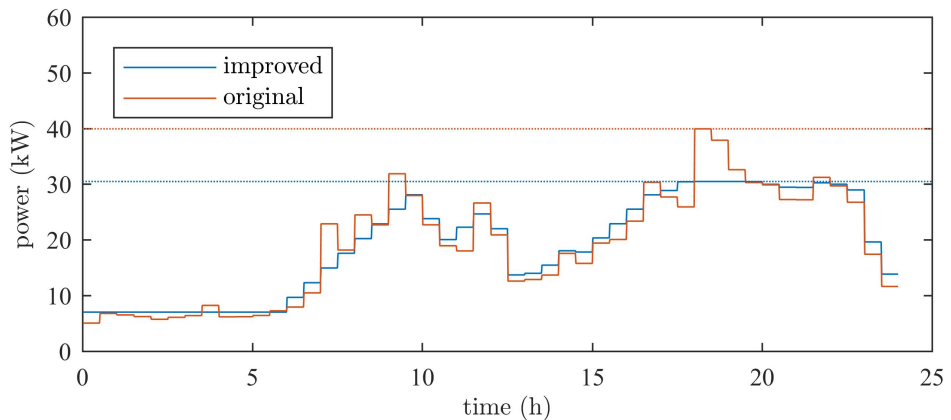


Figure 3.10: Impact of half-hourly ESMU schedule on sub-half-hourly power profile

## 3.4 Optimisation method

Previously, in Section 3.2, the key network parameters and associated cost functions have been established, and the data, models and schedule generation is explained in Section 3.3. A summary of all key network parameters that are used in this work is listed below, but the full notation is defined in the nomenclature of this thesis:

- substation phase voltages,  $\mathbf{v}_{ss}(t) = (v_{ss,\phi}(t))$ ,
- ESMU phase voltages,  $\mathbf{v}_{ESMU}(t) = (v_{ESMU,\phi}(t))$ ,
- all load voltages,  $\mathbf{v}_{load}(t) = (v_{load,i}(t))$ ,
- substation apparent phase power,  $\mathbf{s}_{ss}(t) = (s_{ss,\phi}(t))$ ,
- substation phase currents,  $\mathbf{i}_{ss}(t) = (i_{ss,\phi}(t))$ ,
- all line currents,  $\mathbf{i}_{line}(t) = (i_{line,l,\phi}(t))$ , and
- all network losses,  $s_{losses}(t)$ .

In this section, the method of adjusting the predetermined ESMU schedule on a sub-half-hourly basis is presented. This method is designed to improve network performance, which in turn is indicated by the aforementioned key network parameters. After detailing the method itself, the generation and assessment of all results are explained.

### 3.4.1 Closed-loop schedule adjustment

A global cost function is generated to summarise and combine all eight costs that were derived from the key network parameters, and that were defined in Equations 3.1, 3.5, 3.8, 3.9, 3.10, 3.11, 3.12, and 3.13. This cost function is defined as follows:

$$\begin{aligned}
\zeta(\mathbf{v}_{ss}(t), \mathbf{v}_{ESMU}(t), \mathbf{v}_{load}(t), \mathbf{s}_{ss}(t), \mathbf{i}_{ss}(t), \mathbf{i}_{line}(t), s_{losses}(t), \boldsymbol{\alpha}) := \\
\alpha_1 \sum_{\phi=1}^{\Phi} \zeta_{\text{voltage}}(v_{ss,\phi}(t)) + \alpha_2 \sum_{\phi=1}^{\Phi} \zeta_{\text{voltage}}(v_{ESMU,\phi}(t)) + \alpha_3 \zeta_{\text{load voltage}}(\mathbf{v}_{load}(t)) \\
+ \alpha_4 \zeta_{\text{unbalance}}(\mathbf{s}_{ss}(t)) + \alpha_5 \zeta_{\text{PF}}(\mathbf{s}_{ss}(t)) + \alpha_6 \zeta_{\text{neutral load}}(\mathbf{s}_{ss}(t)) \\
+ \alpha_7 \zeta_{\text{fuse utilisation}}(\mathbf{i}_{ss}(t)) + \alpha_8 \zeta_{\text{line utilisation}}(\mathbf{i}_{line}(t)) + \alpha_9 \zeta_{\text{losses}}(s_{losses}(t))
\end{aligned}$$

where  $\phi \in \{1, \dots, \Phi\}$  and  $\Phi \in \mathbb{Z}_{>0}$

and  $\boldsymbol{\alpha} = \{\alpha_1, \dots, \alpha_9\}$  and  $\alpha_n \in \{0, 1\}$  (3.27)

Here,  $\boldsymbol{\alpha}$  is a binary choice vector, with which the weight of the global cost function can easily be adjusted. In other words, this vector allows the global cost to target any specific key network improvement, which is based on a specific cost. To simplify the notation, and since all key network parameters are outputs of the power flow simulations and not directly adjustable, the global cost function is shortened to  $\zeta(\boldsymbol{\alpha})$ .

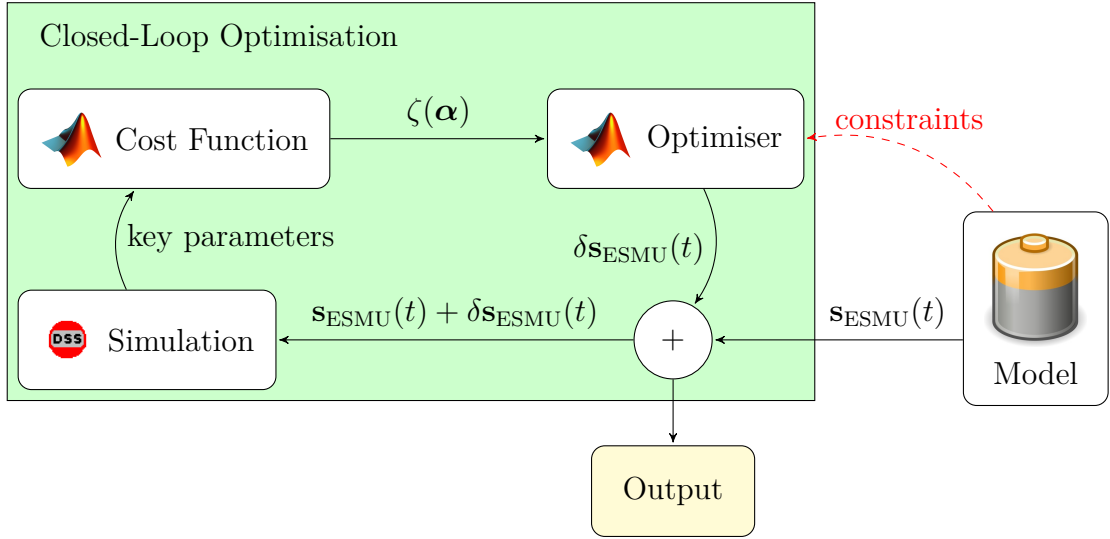


Figure 3.11: ESMU schedule adjustment flow diagram

The underlying method that performs the proposed closed-loop optimisation is shown in Figure 3.11. For each time-slot,  $t$ , the pre-scheduled ESMU power vector,

$\mathbf{s}_{\text{ESMU}}(t)$ , is extracted and adjusted by an offset vector,  $\delta\mathbf{s}_{\text{ESMU}}(t)$ . An optimal offset vector is found through iterative optimisation to minimise the global cost function,  $\zeta(\boldsymbol{\alpha})$ . This minimisation is achieved by repetitively running power flow simulations of the IEEE distribution feeder and adjusting  $\delta\mathbf{s}_{\text{ESMU}}(t)$ . Once the adjusted ESMU schedule (i.e.  $\mathbf{s}_{\text{ESMU}}(t) + \delta\mathbf{s}_{\text{ESMU}}(t)$ ) has converged and a solution has been found, then the closed-loop optimisation process terminates and the simulation begins optimisation during the next time slot (i.e.  $t + \Delta t$ ). Since  $\delta\mathbf{s}_{\text{ESMU}}(t)$  must not impact the underlying half-hourly ESMU schedule, one more constraint is defined. This constraint assures that the sum of all phase powers in the adjustment vector equates to zero, hence keeping the internal battery's charging-discharge power the same. Including the previously mentioned battery system constraints, which ensure that the ESMU operates within its technical limitations, the minimisation problem for the closed-loop optimisation mechanism is formulated as follows:

$$\min_{\delta\mathbf{s}_{\text{ESMU}}(t)} \zeta(\boldsymbol{\alpha}) \text{ s.t.} \begin{cases} \sum_{\phi=1}^{\Phi} \text{Re}(s_{\text{ESMU},\phi}(t)) = 0 \\ p_{\text{bat}}(t) \leq C_f \times C_{\text{bat}} \\ |s_{\text{ESMU},\phi}(t)| \leq S_{\text{rating}} \forall \phi \\ 0 \leq SOC(t) \leq 1 \end{cases} \quad (3.28)$$

where  $\mathbf{s}_{\text{ESMU}}(t) = (s_{\text{ESMU},\phi}(t))$  and  $\Phi \in \mathbb{Z}_{>0}$

### 3.4.2 Execution and result assessment procedure

Being able to focus the global cost function in Equation 3.27 on improving a particular key network parameter by adjusting the binary choice vector  $\boldsymbol{\alpha}$ , and after having established how the closed-loop optimising method aims to achieve these improvements, the performance assessment procedure is introduced. The complete evaluation procedure and assessment is summarised in Figure 3.12.

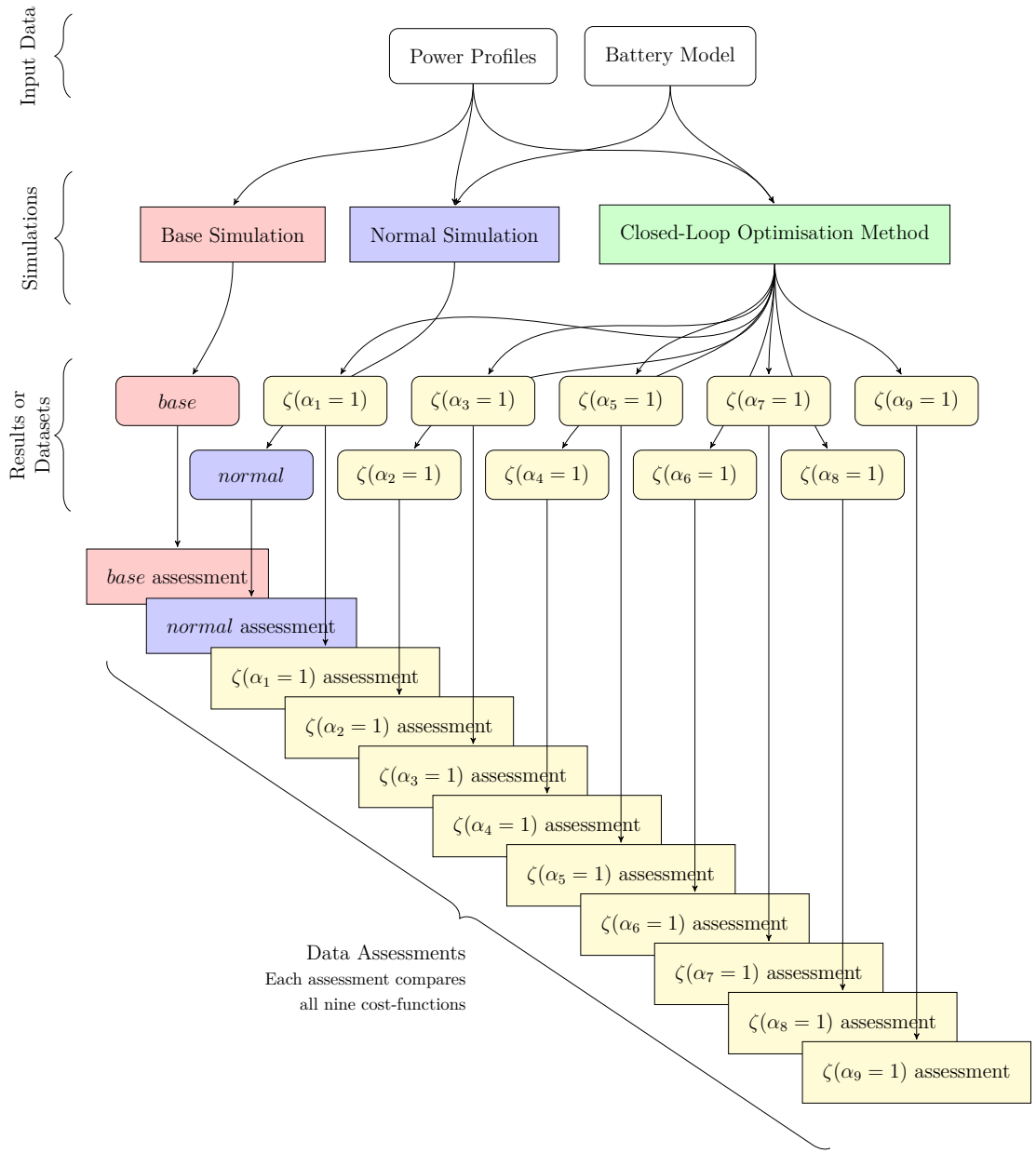


Figure 3.12: Method execution and results assessment flowchart

Since the global cost function can be focused in nine distinct ways using  $\alpha$ , eleven datasets of simulation results can be assessed and compared. These additional two results are obtained from a *base* simulation, and a *normal* simulation (and nine cost driven i.e. *optimisation* simulations). For the *base* simulation, the outcome is generated by applying just the daily power profiles without any ESMU intervention. Therefore, this case represents the baseline of network performance, which should be improved by any ESMU intervention. The *normal* simulation is the simplest of all ESMU interventions, since the ESMU executes its normal (or traditional) half-hourly schedule without any additional modifications. Comparing results from the *base* and *normal* simulations does show the direct impact of the traditional ESMU operation on network performance. The remaining nine datasets are results of the nine different cost driven simulations, where the ESMU schedule is adjusted on a sub-half-hourly level for each simulation. This adjustment is designed to minimise one underlying cost-function, whilst conforming to the ESMU's overall half-hourly charging and discharging profile. In order to treat each cost-function separately  $\alpha$  is set to focus on each cost independently, e.g. by setting  $\alpha_1 = 1$  and  $\alpha_2 = \alpha_3 = \dots = \alpha_9 = 0$ . For simplicity, the flowchart in Figure 3.12 abbreviates the specific costs by only indicating which entry in the  $\alpha$  vector is set to 1, e.g.  $\zeta(\alpha_1 = 1)$ .

Once all eleven simulations have completed, their corresponding datasets are assessed in an identical manner, so that their impact on network performance can be compared. This comparison is broken into three parts for all dataset:

1. **Time Series Analysis** - The underlying profiles are plotted and compared against their respective counterpart cases, in order to link the immediate network impacts to their physical meaning. Here the used performance metric is the cost that is calculated from the simulation specific cost function. For the same profiles, their corresponding cost profiles are calculated and plotted in the results section. This is done to highlight how the profiles are interpreted by

the cost-functions in terms of improvement (i.e. lower cost) or worsening (i.e. increased cost).

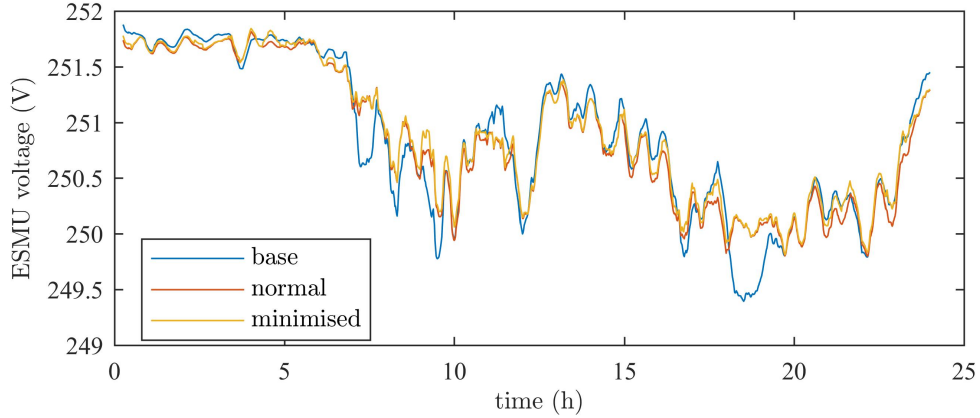
2. **Difference Analysis** - The difference in cost profiles, compared to the respective *base* or *normal* case, is calculated and boxplots of these differences are presented in the results section to show the statistical spread of improvements or worsening. For these plots, a generally positive boxplot indicates a general improvement of the underlying network parameters, whilst a generally negative boxplot does indicate worse performance in regards to the underlying network parameters.
3. **Probability Density Analysis** - A set of Probability Density Functions (PDF) is derived for each cost profile using the well established kernel density estimation. These PDFs indicate the probability that a certain cost value occurs. An improvement is noted when the PDF is shifted towards the lower cost values, whereas a shift towards higher cost values worsened the network performance.

## 3.5 Results and Discussion

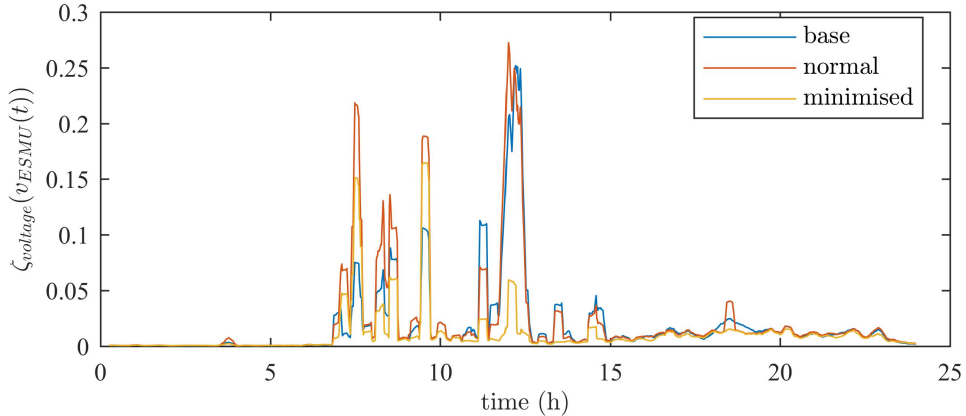
In this section, all results are presented and discussed. Each of the three assessments in this section focuses on improvements in voltage level, improvements in network efficiency (i.e. power quality and network losses), and improvements in resource utilisation. Hence, only a subset of all results is included, but the complete set of results has been appended to this Thesis in Appendix A.1. Data is used and collected in this section as per Section 3.3.1.

### 3.5.1 Time Series Analysis

The ESMU's largest impact on network voltage levels can be noticed at the ESMU's PCC. Consequently, any adjustments to the ESMU powers should become noticeable. This impact can clearly be observed in Figure 3.13.



(a) Voltage levels at ESMU's PCC when minimising its voltage deviation (nominal substation voltage included for reference)



(b) Cost associated with the minimisation of the ESMU's PCC voltage deviation

Figure 3.13: Voltage level modifications as noted at the ESMU's PCC by adjusting its schedule

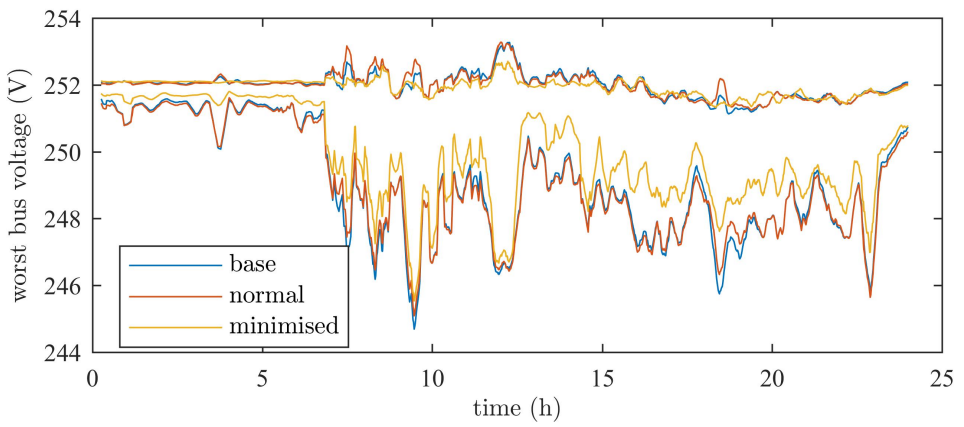
In this figure, the *base* and *normal* case's voltage profiles are plotted alongside the *minimisation* case, for which voltage deviation is minimised. The plot shows that during the night's light load (i.e. from 0:00 to 6:00), ESMU was able to boost its voltage towards the nominal feeder voltage. This is also the case during the lighter

load in the afternoon (i.e. between 12:00-14:00). But during the rest of the day when network load increases, the ESMU is unable to reduce voltage deviation to match its PCC voltage with the network's nominal substation voltage. The reason behind this behaviour is that the ESMU has allocated its resources to serve for the underlying half-hourly ESMU schedule. Therefore, the remaining resources that could provide voltage support during periods of low demand become limited during periods of high demand. Combined with the fact that the LV distribution networks are more resistive than inductive (i.e. unlike HV transmission networks), adjusting only being able to adjust the ESMU's reactive powers to stabilise voltage levels, has an even smaller impact. Nonetheless, due to some continuous yet small availability of power resource, ESMU is able to boost voltages to some extent at all times. In Figure 3.13b, this can be seen since the associated cost has always been reduced in comparison to the *base* and *normal* cases.

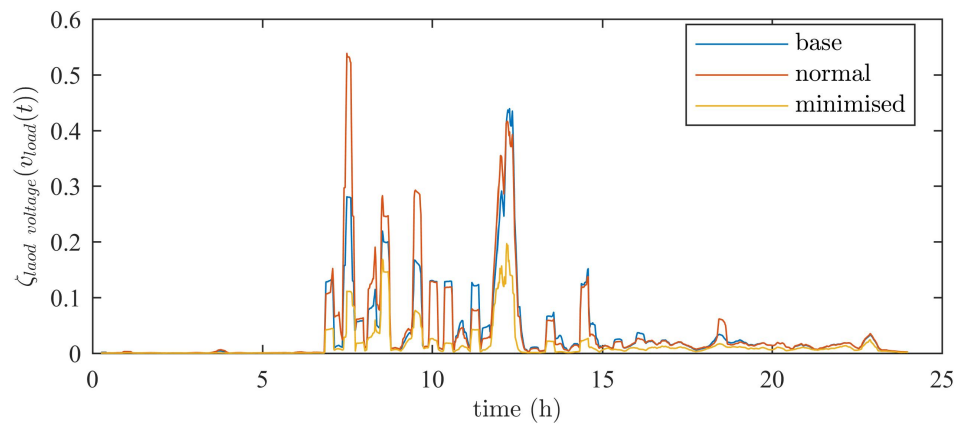
The ability to support voltage levels at the ESMU's PCC is interesting, yet supporting voltage levels at all buses throughout the network is more relevant since some of these buses are linked to customers, for which it is essential to maintain a constant voltage level. Therefore, the results assess both the highest and lowest voltage level that is recorded throughout the network.

In Figure 3.14a, despite no voltage violations taking place due to the already boosted substation voltage, the ESMU's positive impact can be observed. Here, the difference between highest and lowest voltage in the network is noticeably reduced at all times, and their average voltage is brought closer to a nominal voltage level. The ESMU's function to support the network in providing more stable voltage levels at customer endpoints is therefore met. This fact is also supported by the associated cost plot in Figure 3.14b, where a reduction in cost can be observed throughout the entire simulated day.

Beside providing stable voltage levels, power quality should also be upheld to as-

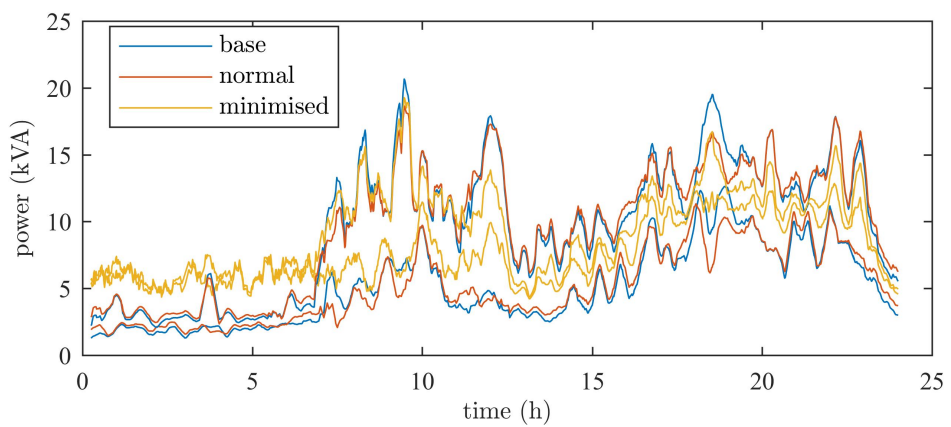


(a) Highest and lowest voltage levels that were recorded throughout the network when minimising the worst voltage deviation (nominal substation voltage included for reference)

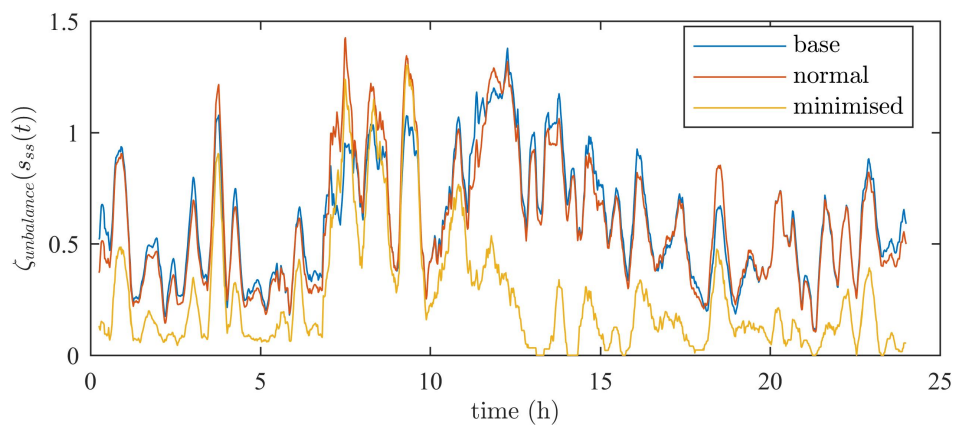


(b) Cost associated with the worst voltage deviation throughout the entire network

Figure 3.14: Voltage level improvements at all buses in the entire distribution network due to the ESMU schedule adjustment.



(a) Network's highest and lowest phase power demand when phase unbalance was minimised



(b) Cost associated with the network's phase unbalance

Figure 3.15: Reduction of the network's phase unbalance due to the adjustment of the ESMU schedule.

sure that distribution networks operate as efficient as possible. The first power related parameter that indicates network efficiency is phase unbalance. In Figure 3.15a, the power value of the highest and lowest loaded corresponding phases is plotted over time. At all times, the sub-half-hourly adjustments of the ESMU's schedule did reduce the underlying phase imbalance. This is achieved by redistributing power from the most loaded phase to the least loaded phases; hence utilising the unused capacity of the lighter loaded phases. As expected, the associated cost has been noticeably lowered in comparison to the *base* and *normal* cases. It should however be noted, that phase balancing during the morning hours is predominantly achieved by using reactive power injection and absorption. This can be seen by the similar yet increased phase loadings between 0:00 and 7:00. Therefore, the tradeoff between adding additional strain onto the network, versus balancing phases has to be taken into account. One such strain that is being put onto the network, is increased neutral power flow due to phasor misalignment.

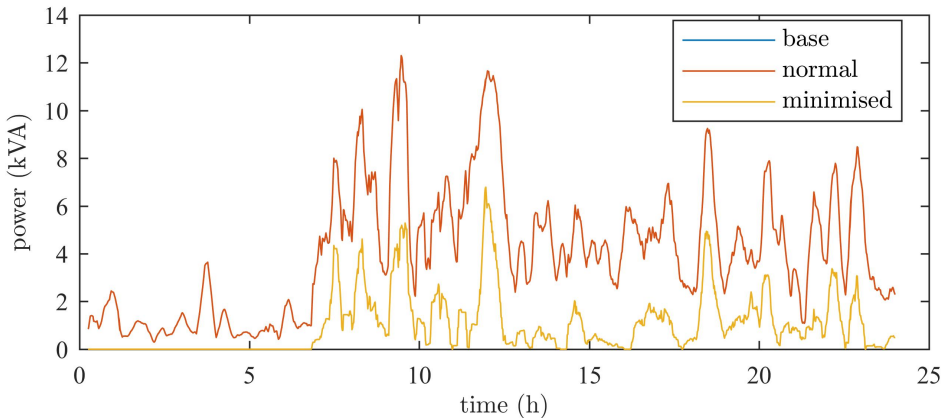


Figure 3.16: Neutral power reduction due to the ESMU schedule adjustments

For the results that are plotted in Figure 3.16, neutral power flow is minimised through the adjustment of ESMU powers. It can be seen, that for the *normal* case, neutral power is not affected at all. Reason for this result is the choice of evenly assigning the scheduled ESMU power to all three phases. Therefore, neither phase

unbalance nor loading of the neutral conductor is being taken into account. For the *minimisation* case however, loading of the neutral conductor is successfully reduced in comparison to both the *normal* and *base* case.

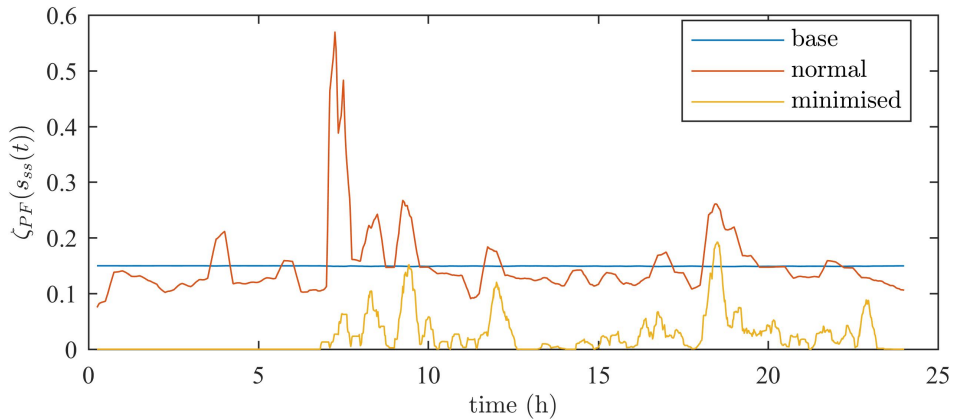


Figure 3.17: Power factor cost improvements due to the adjustment of the ESMU schedule

Unlike neutral phase unbalance and neutral loading, power factor on the other hand is impacted just by introducing the half-hourly ESMU schedule, as shown in Figure 3.17. Whilst the choice of a static power factor for all loads in the *normal* case resulted in a constant power throughout the day, half-hourly ESMU intervention in the *base* case results in a noticeable power factor variation. This variation is however successfully reduced throughout the entire day for the *minimisation* case, in comparison to the *normal* cases.

The final parameter that indicates system efficiency are the distribution losses. Figure 3.18 shows the reduction in distribution losses that were achieved when adjusting the ESMU powers accordingly. In fact, an additional 6.42% energy savings is achieved, simply by adjusting the ESMU's power injection and absorption behaviour, when comparing the *base* and *minimisation* cases. Although this amount of energy may seem negligibly small, these saving can amount to a noticeable level of savings on a national scale, which can potentially benefit the entire power network. Nonetheless, measuring losses is difficult and costly, which is why attempting to do so will likely

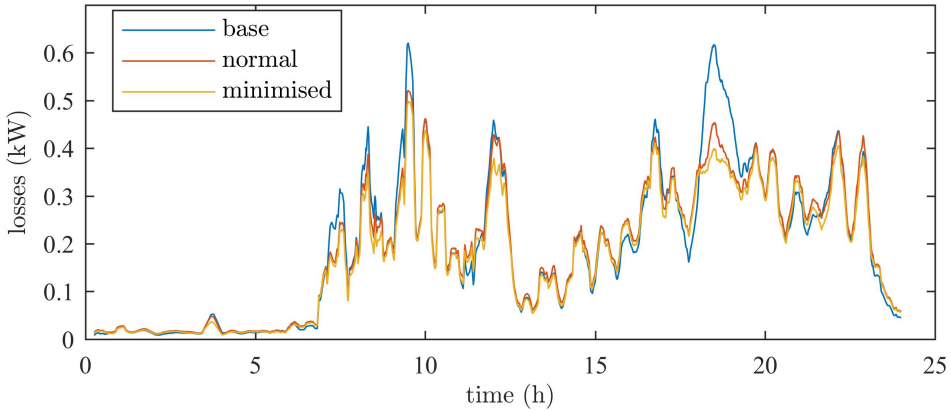


Figure 3.18: Instantaneous losses of the distribution network when adjusting the ESMU schedule in order to reduce the former (energy lost: 75.9Wh for base; 74.7Wh for normal; 69.9Wh for minimised).

outweigh the benefits.

Instead, a better way of relieving stress from the power network is to minimise its assets utilisation by mitigating demand spikes that were taken into account in Equation 3.26. However, since the ESMU was constraint to not deviate from its underlying half-hourly schedule, only phase related demand differences can be addressed, and the impact of correcting those phase differences is barely noticeable, which can be seen in Figure 3.19.

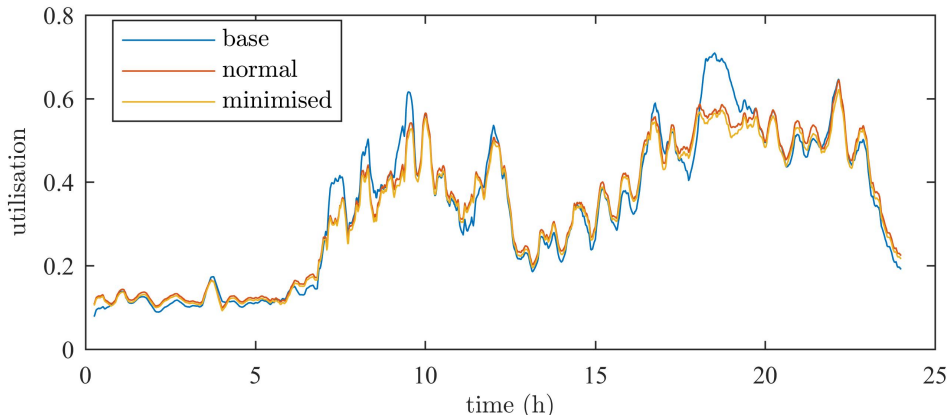


Figure 3.19: Improvement of the worst line utilisation across the entire network when adjusting the ESMU schedule correspondingly.

Whilst the *normal* case noticeably lowered some of the daily demand, power spikes

after e.g. 9pm were not addressed at all. Even the *minimisation* case could barely reduce those spikes, due to the constraining half-hourly schedule. Nonetheless, throughout the entire day, ESMU was still able to reduce line utilisation at the substation level; despite those improvements being relatively small in comparison to the impact in the *normal* case.

### 3.5.2 Difference Analysis

In order to gage whether the sub-half-hourly ESMU power adjustment results in a statistical difference in network performance, a box-plot was generated to compare each *minimisation* with the corresponding *normal* case. Hence, the underlying data for each box-plot represents the difference between the *minimisation* case's costs and the *normal* case's costs, i.e. when operating without adjusting ESMU powers. Therefore, any positive difference in cost indicates an improvement to the system's performance, whilst a negative difference would imply a worsening. All cases are compared and plotted in Figure 3.20, and the complete set of box-plots (showing the “cross-cost difference”) is included in Appendix A.1.2.

This figure shows the how the reduction in cost (defined in Equation 3.27) is distributed. In this case, the cost reduction, i.e.  $-\delta\zeta(\boldsymbol{\alpha})$ , is the change in cost from the *normal* ESMU operation case to *minimisation* operation cases, e.g. for “phase unbalance”  $\delta\zeta(\boldsymbol{\alpha}) = \zeta(\alpha_1 = 1) - \zeta(\alpha_6 = 1)$ ). Due to the different scales however, the improvements are difficult to observe. Therefore, this cost reduction has been normalised in regards to the *normal* ESMU operation case and is replotted in Figure 3.21.

In this figure, it can be seen that the most significant cost related impact on the network is yielded, when improving voltage deviation, phase unbalance and power factor costs. Reason for this noticeably larger impact is due to ESMU being able to assign its scheduled active power to all three phases in an optimal manner, as long

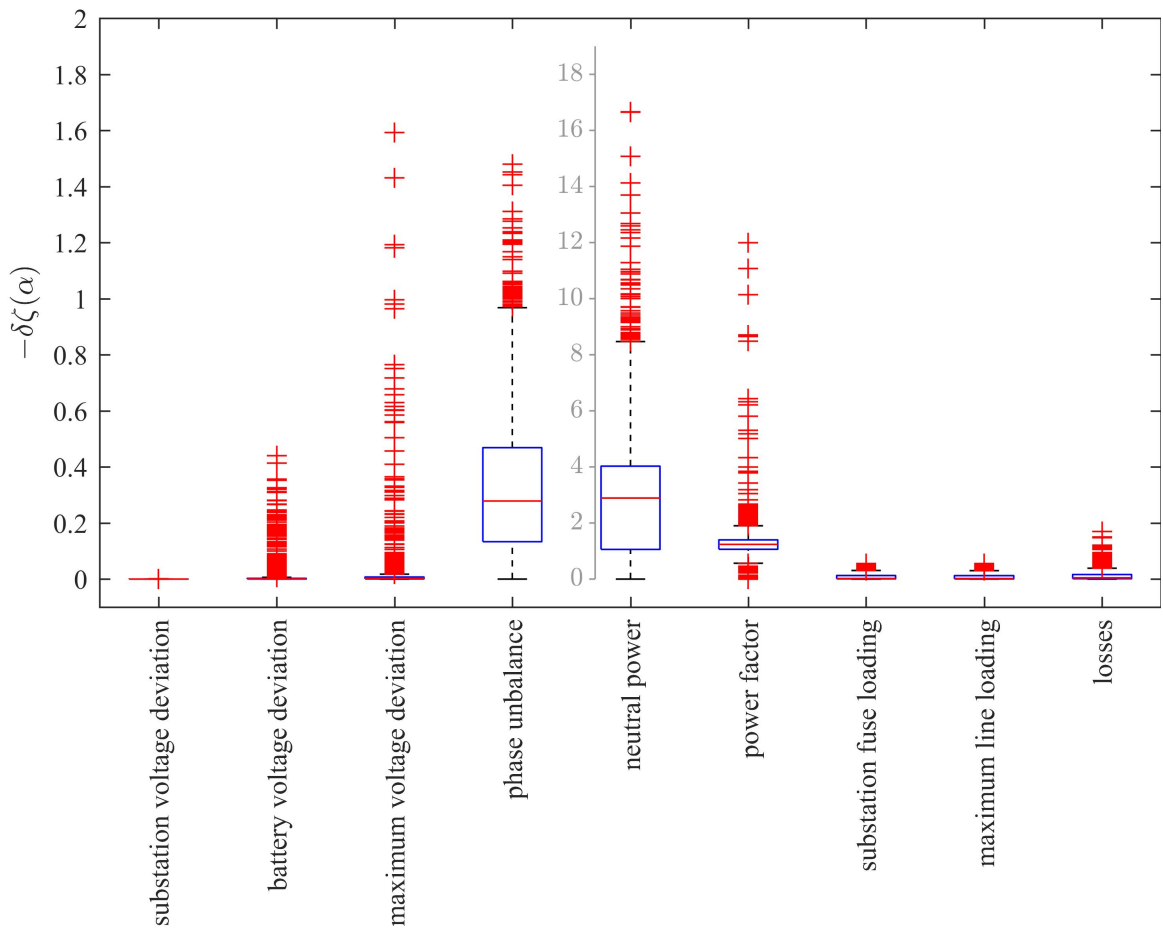


Figure 3.20: Cost improvement spread, when comparing against the *normal* ESMU operation case and when optimising for the underlying cost (a separate y-axis is introduced for the optimisation of “neutral power”).

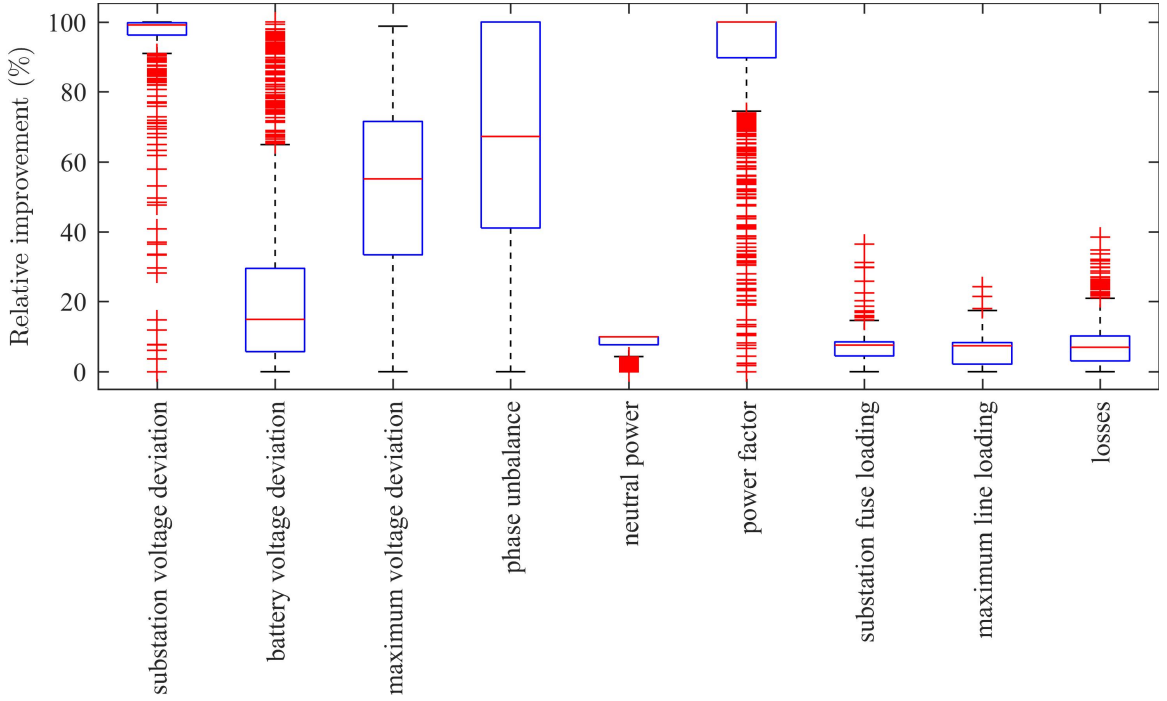


Figure 3.21: Relative cost improvement spread, when comparing against the *normal* ESMU operation case and when optimising for the underlying cost.

as the predetermined half-hourly schedule is obeyed. It is this obedience constraint, that limits the extend by which all other key network parameters can be impacted. Reactive power on the other hand is only indirectly constrained by the ESMU schedule. The only limit that applies to the ESMU's reactive power injection capabilities is the remaining PMU capacity after committing the scheduled active power. Also, unlike active power, reactive power has a smaller impact on the LV network due to its physical property, i.e. being more resistive than inductive. Nonetheless, when each key network parameters became subject to their corresponding cost minimisation, all of them were impacted positively.

In addition to the box-plots, the cost improvements (whose box-plots are presented in the Appendix A.1.2), are calculated and tabulated in Table 3.1. This table shows the cumulative difference in  $-\delta\zeta(\boldsymbol{\alpha})$  between the *normal* case and the *minimisation* case, i.e. where  $\delta\zeta(\boldsymbol{\alpha}) = \zeta(\alpha_1 = 1) - \zeta(\alpha_2 = 1)$ . However, instead of only presenting the cost reduction that is yielded when minimising it, this table also includes all other

resulting costs; i.e. the daily aggregated cost to be precise. This value is defined as the “cumulative cost difference”, i.e.  $\sum_t \delta\zeta(\boldsymbol{\alpha})$ . In addition to the comparison between *minimisation* and *normal* cases, the *normal* case is compared to the *base* case for reference. For convenience, all positive cost reductions (i.e. network improvements) have been highlighted.

As expected, all entries along the diagonal are positive in cross-cost difference, i.e. where the evaluated cost is also the cost that was minimised. But beside this fact, one can also observe which cost minimisation has an impact on different costs. For example, adjusting the ESMU schedule to achieve the largest reduction in distribution losses (i.e. far right column) improves nearly all key network parameters, apart from substation voltage deviation. Furthermore, Table 3.1 indicates that reducing battery voltage deviation, maximum voltage deviation, phase unbalance and neutral power (respectively, columns 3, 4, 5 and 6) have a noticeable impact on each other. Minimising any of these four costs does however not impact power factor, loading and losses (apart from reducing battery voltage deviation).

Although the impact on network improvements for some costs is easily determined and explained with the underlying physical properties of distribution systems, other impacts of minimising cost do not share this transparency. For example, minimising power factor (column 7) has a greater impact on reducing line loadings than directly minimising substation or maximum line loading (column 8 and 9, respectively). The reason behind this effect is due to instantaneous apparent power contributing to the line current. This means, that maximising the network’s power factor minimises reactive load, which in turn lowers the total line current. Since the solving algorithm does not know which cost to minimise first, the task of finding a global minimum becomes more difficult. To improve the performance of adjusting ESMU powers, one could propose to concatenate several cost minimisation procedures in a sequential series. Doing so would focus the search for global minima for each iteration of the

	minimisation cases					
	normal			losses		
substation voltage deviation	0.00	0.08	-2.49	-1.39	-4.89	-8.72
battery voltage deviation	-5.01	-0.40	15.52	17.04	9.14	14.93
maximum voltage deviation	-6.83	-1.15	28.22	36.42	24.66	33.05
phase unbalance	12.15	40.93	284.87	380.57	490.22	351.35
neutral power	-0.83	-96.72	2303.70	1642.37	2698.78	4415.85
neutral power	-0.27	159.42	-7.63	-37.25	-633.30	-314.11
power factor	5.14	13.34	-0.43	-8.69	-51.76	-72.68
substation fuse loading	4.53	12.88	-6.17	-10.04	-80.41	-97.30
maximum line loading	4.34	7.22	13.38	-4.46	-46.37	-66.32
losses						
maximum line loading						
substation fuse loading						
maximum voltage deviation						
battery voltage deviation						
phase unbalance						
neutral power						
neutral power						
power factor						
substation fuse loading						
maximum line loading						
losses						

Table 3.1: Cross-cost improvements due to adjustments to the original ESMU schedule.

sequence, yet this lies outside the scope of this Thesis and may be sought in future research.

### 3.5.3 Probability Density Analysis

The final part of analysing the results is to determine, whether the cumulative cross-cost differences are statistically significant. To do so, the probability density functions (PDF) of the cross-cost differences is analysed using a null hypothesis test. The underlying data is conditioned in order to meet all prerequisites that are necessary to perform the null hypothesis test, e.g. the standard  $t$ -test. These prerequisites include stationarity, low auto-correlation and high gaussianity of the underlying time-series. The procedure to meet these prerequisites is carried out without falsifying the data, which means that all applied conditioning operations were restricted to time-series division and linear transformation. Details on the exact data conditioning steps are outside the scope of this chapter, but for completeness they are included in Appendix A.1.3.

Table 3.2 presents the results from this analysis, where  $p$ -values have been tabulated and those cells with a value below 0.05 have been highlighted. A similar pattern to that in the previous table can be seen (i.e. Table 3.1). In this table however, instead of just comparing cross-cost reductions, statistical indications to support the significance of the findings is presented. In combination with the preceding table, one can therefore determine that e.g. the impact of optimising operation based on maximum voltage deviation has little to no significant impact on improvements in power factor, whilst adjusting ESMU powers to improve the network's power factor has the most significant statistical impact on the chosen key network parameters.

	minimisation cases		losses	
	normal	substation voltage deviation	neutral power	power factor
substation voltage deviation	0.851	< 0.001	0.999	1.000
battery voltage deviation	0.899	< 0.001	< 0.001	< 0.001
maximum voltage deviation	0.718	0.000	< 0.001	< 0.001
phase unbalance	0.331	< 0.001	< 0.001	< 0.001
neutral power	0.940	0.999	< 0.001	< 0.001
power factor	0.488	< 0.001	0.020	0.999
substation fuse loading	0.777	< 0.001	0.929	0.999
maximum line loading	0.846	< 0.001	0.996	0.999
losses	0.881	< 0.001	0.637	0.910
maximum line loading			< 0.001	< 0.001
substation fuse loading			< 0.001	< 0.001
phase unbalance			< 0.001	< 0.001
neutral power			< 0.001	< 0.001
battery voltage deviation			< 0.001	< 0.001
maximum voltage deviation			< 0.001	< 0.001
phase unbalance			< 0.001	< 0.001
neutral power			< 0.001	< 0.001
power factor			< 0.001	< 0.001
substation fuse loading			< 0.001	< 0.001
maximum line loading			< 0.001	< 0.001
losses			< 0.001	< 0.001

Table 3.2:  $p$ -values for statistical evidence of cross-cost improvements based on statistical two-sample single-tailed  $t$ -test.

## 3.6 Summary

In this chapter, a method to adjust three-phase ESMU powers on a sub-half-hourly basis to support network operation, whilst following a pre-determined half-hourly schedule, is proposed and tested. The ESMU schedule is tailored to result in a “peak-shaving” and “valley-filling” behaviour and uses a realistic ESMU model to meet any operational constraints. A set of key network parameters to indicate the performance of the network, were used in a corresponding set of cost functions. By adjusting the ESMU’s active and reactive powers, each cost could be minimised and therefore network operation is improved.

Results indicate that when explicitly focusing on the improvement of certain key network parameters, then the derived cost reduces for every single case. The scale by which the cost was reduced, and network performance was improved, became apparent for the time-series assessments in Section 3.5.1. During periods of low demand and low ESMU powers, reactive power injection provided the largest benefits (i.e. before 7am). Active power that is dictated by the underlying ESMU schedule, did however provide peak reduction and thermal constraint functions for the remaining time of the day. Nonetheless, any cost minimisation always had an effect on different costs (e.g. loss minimisation positively impacted nearly all other costs).

Using cumulative cross-cost differences in Section 3.5.2, it is shown that a net cost reduction is achieved simply by implementing the proposed ESMU power adjustment method top of the normal execution of a half-hourly schedule. Although the impact with which different costs reduced is not as large as the impact on the cost that is currently focused on, all costs did experience some kind of cross-cost impact. Since the units of this assessment were cost specific, a true assessment of the correlation between costs cannot be performed.

Therefore, Section 3.5.3 focused on the statistical sensitivity of the cost reduction. Using the two-paired  $t$ -test, the aforementioned fact that costs do indeed impact each

other is supported too. Hence there is strong evidence that those power adjustments do have a positive impact on the distribution network's operation, and the first objective of this thesis, which is outlined in Section 1.2, has been met.

The main limitation of the proposed method is however the battery's half-hourly schedule. It dictates the active power that has to be injected into or absorbed from the distribution network. Also, this schedule inadvertently dictates the remaining overhead in reactive power that may be compensated for on each phase. Therefore, the next chapter in this thesis presents a method of dynamically adjusting this scheduled power profile in real-time without violating any physical constraints.



# Chapter 4

## Real-Time Adjustment of Battery Operation using MPC Guided Schedule Deviation

*M. J. Zangs, et al., “Battery control algorithm for peak load shaving in low-voltage power network with high demand volatility,” Applied Energy*

— Unpublished

### 4.1 Overview

In the preceding chapter, Chapter 3, an Energy Storage Management Unit (ESMU) is used to improve network operation. This improvement is achieved by optimally adjusting the device’s scheduled three-phase powers. Any improvement is indicated by a cost reduction, where the underlying cost functions are tied to changes in key network parameters. The extend to which ESMU is able to improve network operation is then shown by focusing on the minimisation of different cost functions and repetitively optimising and simulating the distribution network. However, this network improvement is limited by the constraint of having to obey the underlying

half-hourly ESMU schedule, despite applying adjustments at a sub-half-hourly level.

In the subsequent chapter, Chapter 4, research **Objective 2** is addressed (it is outlined in Section 1.2) by removing these limiting constraint and proposing a corresponding sub-half-hourly ESMU schedule adjustment method. This method unifies the benefits from sub-half-hourly demand measurements and half-hourly demand forecasts. Unlike previous work in the field, the proposed approach reverses the traditional control paradigm to compensate for schedule inaccuracies. Put differently: traditional approaches implemented on-line control mechanisms like Set-Point Control (SPC) in combination with prediction models in order to adjust and prepare ESMU for future load trends. In this chapter however, forecast driven schedules are adjusted using on-line measurements instead of supporting on-line control with real-time load predictions. This is achieved by first scheduling ESMU operation at half-hourly resolution, i.e. by following a “peak-shaving” and “valley-filling” behaviour which has been explained in Chapter 3, and then modifying this schedule using MPC. In this case, MPC is comprised of a lightweight AR model to assure real-time deployability. These two control signals are unified using two Proportional Integral Derivative (PID) compensators that are tuned to assure system robustness regardless of the forecast’s erroneousness. All ESMU schedules are generated under the constraints of a realistic ESMU model, and all demand measurements and corresponding forecasts that are used in this work are based on real data that is provided by the project partner and DNO: *Scottish and Southern Energy Networks* (SSEN). Results are generated from this realistic (i.e. provided) network load with their corresponding load forecasts, and cases are compared against the original and a baseline load case (i.e. traditional off-line control). It is shown that the proposed schedule adjustment method can successfully reduce sub-half-hourly peaks, even under these imperfect forecast conditions. In fact, whilst the probability distribution of the baseline case sat around an average of 1.78kW peak reduction, the proposed method could increase the reduction to

5.24kW. Since this proposed control method is the natural extension of our previous work in [101], it is hereon referred to as “dynamic control”.

The chapter is organised as follows: In Section 4.2, all constituent system components including ESMU model, forecast acquisition and ESMU schedule generation are explained. Section 4.3 presents the dynamic control, including the dual PID setup and MPC. Section 4.4 outlines the different case studies that were used to compare the performance of the dynamic control. In Section 4.5, all results from these case studies are presented and discussed. Finally, conclusion and the future work are described in Section 4.6.

## 4.2 System Explanation

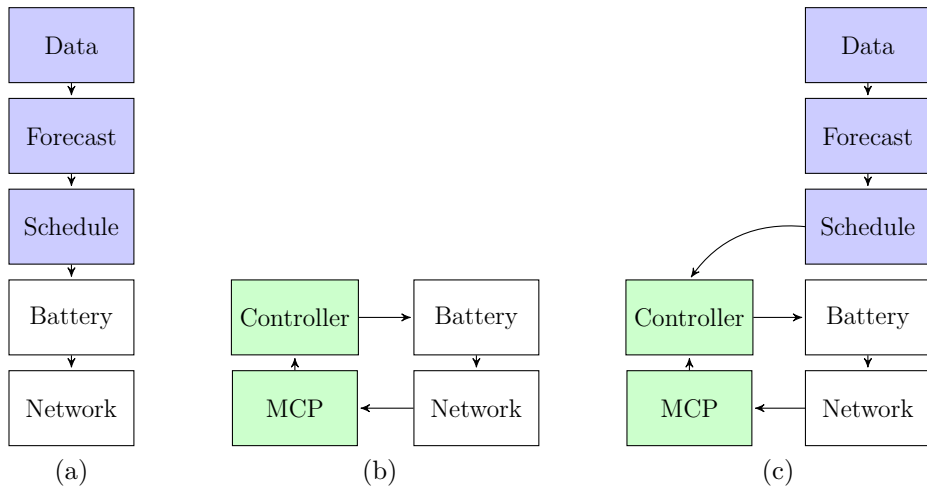


Figure 4.1: (4.1a) Traditional forecast driven BESS control; (4.1b) Traditional on-line system; (4.1c) Proposed dynamic control system

The presented work is part of the *New Thames Valley Vision* (NTVV) research project, and was conducted in collaboration with the British DNO *Scottish and Southern Energy Networks* (SSEN) [94]. From the findings of this research project, the diagram in Figure 4.1 was generated, showing two well established ESMU control approaches and the proposed dynamic control approach. This figure includes all

constituent systems that were used during the ESMU street-level deployment. The two traditional systems are off-line and on-line ESMU control, which are shown in Figure 4.1a and 4.1b, respectively. Alongside these two control approaches is the proposed dynamic control system that is shown in Figure 4.1c. This control approach entails the benefits from both the traditional half-hourly forecast driven and the sub-half-hourly ESMU control system, and can therefore be seen as the hybrid of the two traditional systems. Unlike previous work, this hybrid system does not rely on Set-Point Control (SPC) which is adjusted by a MPC to compensate for trends in the load profile. Instead, it operates by executing a predetermined half-hourly ESMU schedule which is adjusted at sub-half-hourly intervals. Therefore the necessity of relying on a stable SPC is removed and replaced by a robust schedule execution. Nonetheless, flexibility is provided by allowing the aforementioned schedule adjustments. The preceding work by Rowe et al. in [120] inspired this hybrid system and used a similar approach, emphasising these benefits of using a hybrid system. Unlike the work by Rowe et al. in [120] however, the proposed hybrid system operates at a higher temporal resolution (it uses a light weight deterministic adjustment method in the form of MPC), and it does not rely on a long forecasting horizon since it recomputes the power adjustments for every single time-step. As already mentioned, those adjustments are based on MPC-guided instructions, and details about this dynamic control are outlined in Section 4.3.

In this section however the battery model, which is used in this work, is reminded first. Also the load data acquisition, forecasting and ESMU schedule generation are outlined, where scheduling is performed in accordance to the ESMU model's constraints.

### 4.2.1 ESMU model

The ESMU model is based on the physical system that was deployed by SSEN during the NTVV project. Since this model is the same model as the one used in the preceding chapter, which has been explained in detail in Section 3.3.3, only the model's final equation (as well as all used parameters) are detailed, hence foregoing the re-deriving of the same battery storage model. This ESMU model equation is as follows:

$$SOC(t + \Delta t) = \begin{cases} \mu \left( SOC(t) + \frac{\eta \Delta tp(t)}{C_{bat}(3.6 \times 10^6)} \right) & \text{if } p(t) \geq 0 \\ \mu \left( SOC(t) + \frac{\Delta tp(t)}{\eta C_{bat}(3.6 \times 10^6)} \right) & \text{otherwise} \end{cases} \quad (4.1)$$

Here, the next State of Charge,  $SOC(t + \Delta t)$ , is computed from the current State of Charge,  $SOC(t)$ , and the current battery power,  $p(t)$ . This is done by calculating the current change in SOC as the added energy  $\Delta tp(t)$ , divided by the total battery capacity  $C_{bat}$ . Dynamic properties of the model also take into account the energy conversion efficiency,  $\eta$ , and the self-discharge factor,  $\mu$ .

For the purpose of the simulation, it is assumed that the battery is initially charged up to 50%. Hence, the initial conditions of this model are defined as  $SOC(0) = 0.5$ , which makes the model valid for a time span of  $t \geq 0$ , where  $t \in \mathbb{Z}_{\geq 0}$ .

### 4.2.2 Load data and ESMU scheduling

Having established the ESMU model, the procedure to generate a corresponding schedule is explained in this subsection. This procedure follows the same practice as outlined in the previous chapter, in Section 3.3.4, where an ESMU schedule is generated at half-hourly temporal resolution. Therefore, the same synchronisation function,  $k(t)$ , is used that links the native sampling period of  $\Delta t$ , to the schedule's half-hourly period. Since the sub-half-hourly operation was at a minutely period, and the generated schedule is at half-hourly period, this fixed conversion function is

defined as:

$$k(t) := \left\lfloor \frac{t-1}{30\Delta t} \right\rfloor + 1 \quad (4.2)$$

Having established a means of synchronising the two sampling periods, the shape of the ESMU schedule that would “smoothen” the underlying power profile is defined next. For simplicity linear forwarding was chosen, which means that the power assigned at e.g.  $t = 1$  remains constant over the scheduling period of  $30\Delta t$ , until  $t = 31$ . With this assumption, the ESMU’s SOC can be calculated for each  $t$  despite the scheduled power profile only having been defined for every 30<sup>th</sup>  $t$ . Furthermore, with this second assumption, not only every sub-half-hourly ESMU power can be derived from its half-hourly schedule, but it also enables the calculation of every SOC, i.e.  $SOC(t)$  is well defined.

For the generation of the ESMU schedule a load forecast,  $\mathbf{p}_{\text{for}}$ , was required; here  $\mathbf{p}_{\text{for}} = (p_{\text{for}}(k(t)))$ . Just like the ESMU forecast, this forecast is also produced at half-hourly temporal resolution and it was provided by SSEN as part of the NTVV research project. The task at hand is to find a half-hourly ESMU schedule,  $\mathbf{p}_{\text{sch}}$ , where  $\mathbf{p}_{\text{sch}} = (p_{\text{sch}}(k(t)))$ , that improves the shape of the underlying forecast, e.g. by reducing load peaks. In order to generate this optimised ESMU schedule, a performance metric quantifying improvements had to be defined first. The remaining task is to now compute a half-hourly schedule,  $\mathbf{p}_{\text{sch}}$ , that yields the best performance. This computation is done by minimising several cost-functions.

In Chapter 3, several cost functions have been defined. Here however, three shape dependent cost-functions are used that quantify the profile improvements that are yielded by  $\mathbf{p}_{\text{sch}}$ . These costs entailed the Peak-to-Average Ratio (PAR), the difference between the resulting power profile’s maximum and minimum (MMD) load, and the magnitude of all power transients (TRA) [180, 196]. Although these costs and their benefits have already been presented in Section 3.3.4 of this thesis, they are reminded

for convenience. Before however detailing each of these three cost functions, a notation that simplifies power as,  $\mathbf{p}$ , is introduced:

$$p(t) = p_{\text{for}}(k(t)) + p_{\text{sch}}(k(t)) \quad (4.3)$$

where  $\mathbf{p} = (p(t))$

Within this section, the vector  $\mathbf{p}$  represents the power profile as it would be measured at the substation when both forecast,  $p_{\text{for}}(t)$ , and scheduled,  $p_{\text{sch}}(t)$ , power were applied. The first cost function that is used in this chapter addresses the minimisation of PAR and is defined as follows:

$$\zeta_{\text{PAR}}(\mathbf{p}) := \left( \frac{\max_t |\mathbf{p}|}{\bar{\mathbf{p}}} \right)^2 - 1 \quad (4.4)$$

Here,  $\bar{\mathbf{p}}$  represents the mean power, i.e.  $\bar{\mathbf{p}} = \frac{\Delta t}{T_{\text{sch}}} \sum_{t=1}^{T_{\text{sch}}} p(t)$  and  $\bar{\mathbf{p}} \in \mathbb{R}$ , where  $T_{\text{sch}}$  is the length of the scheduling horizon in regards to the sampling period  $\Delta t$ . If the profile  $\mathbf{p}$  had a lot of spikes, then the ratio between its maximum and its mean value is greater than one (or with the  $-1$  term greater than zero). A perfectly flat power profile would however result in cost of zero. However, due to limited battery capacity, achieving such a cost of zero is unlikely. This is why a solution to minimise this cost needs to be found together with the previously explained ESMU model. To not only increase the mean power or reduce peak power, the second cost function of this chapter is defined as the difference between minimum and maximum power of  $\mathbf{p}$ :

$$\zeta_{\text{MMD}}(\mathbf{p}) := (\max_t(\mathbf{p}) - \min_t(\mathbf{p}))^2 \quad (4.5)$$

Similar to the PAR, this cost also reduces to zero when the resulting power profile is perfectly flat. Unlike the PAR, this cost does not incentivise an increase of mean power. Minimising PAR by itself may result in unnecessary and potentially damaging

battery cycling, when trying to elevate the power profile's mean, yet this is avoided when  $\zeta_{\text{MMD}}$  is included alongside  $\zeta_{\text{PAR}}$ . However,  $\zeta_{\text{PAR}}$  and  $\zeta_{\text{MMD}}$  only impact the fringes of the resulting half-hourly power profile. The final cost therefore addresses the interim power volatility by aiming to minimise the largest possible power transient:

$$\zeta_{\text{TRA}}(\mathbf{p}) := \max_t (p(t + \Delta t) - p(t))^2 \quad (4.6)$$

Minimising this final cost has a smoothening effect on the improved half-hourly power profile, since a profile with no transients is by definition a flat smooth profile. Since all three cost functions are normalised, they are summaries into a single global cost function. In this cost function only the half-hourly ESMU schedule,  $\mathbf{p}_{\text{sch}}$ , is used as an input and the forecast,  $\mathbf{p}_{\text{for}}$ , is kept as constant:

$$\begin{aligned} \zeta(\mathbf{p}_{\text{sch}}) := & \zeta_{\text{PAR}}(\mathbf{p}_{\text{sch}} + \mathbf{p}_{\text{for}}) \\ & + \zeta_{\text{MMD}}(\mathbf{p}_{\text{sch}} + \mathbf{p}_{\text{for}}) \\ & + \zeta_{\text{TRA}}(\mathbf{p}_{\text{sch}} + \mathbf{p}_{\text{for}}) \end{aligned} \quad (4.7)$$

Subject to ESMU constraints, this global cost function is minimised using a standard solver (i.e. Sequential Quadratic Programming - SQP) to yield a ESMU schedule that is optimised for the given forecast:

$$\min_{\mathbf{p}_{\text{sch}}} \zeta(\mathbf{p}_{\text{sch}}) \text{ s.t. } \begin{cases} SOC_{\text{tol}} \leq SOC(t) \\ SOC(t) \leq 1 - SOC_{\text{tol}} \\ |p_{\text{bat}}(t)| \leq C_{\text{bat}} \cdot C_f \end{cases} \quad (4.8)$$

In order to limit the control's flexibility, a State Of Charge tolerance,  $SOC_{\text{tol}}$ , is included in this minimisation problem.  $SOC_{\text{tol}}$  defines the maximum allowed deviation from the computed SOC profile without hitting operational limits, i.e. SOC of

one or zero, and may take values in the form of  $SOC_{tol} \in [0, 0.5]$ , where 0 implies no tolerance and 0.5 implies complete flexibility. For the work at hand, a value of 0.1 was chosen.

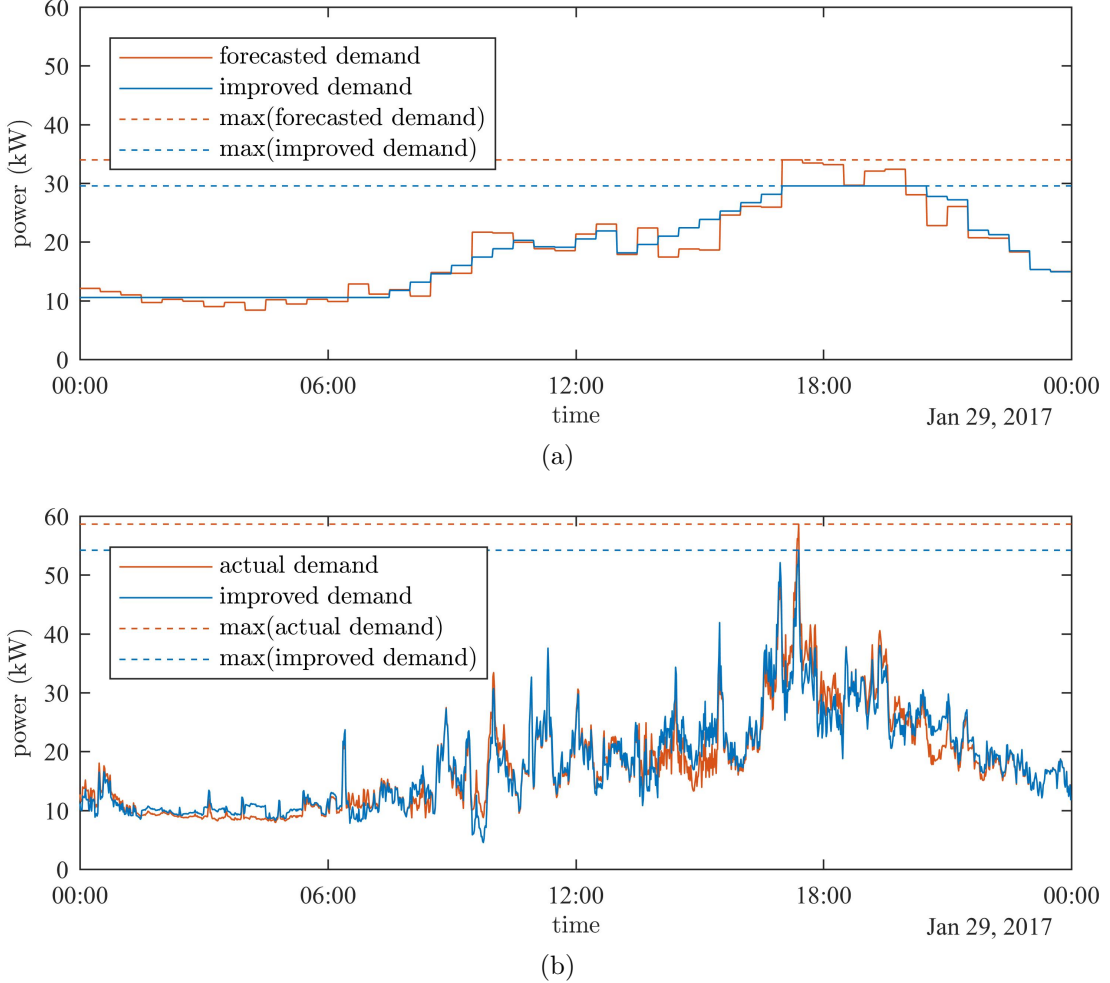


Figure 4.2: An example of applying a half-hourly ESMU schedule to its half-hourly schedule (Subfig. 4.2a) and the actual, sub-half-hourly daily load (Subfig. 4.2b).

As repetitively mentioned, the ESMU operation that results from this scheduling mechanism is at half-hourly resolution and has therefore limited impact on sub-half-hourly load variation. To visualise this limitation, a single day's ESMU schedule was generated from its corresponding forecast as defined in Equation 4.8, and plotted in Figure 4.2. In this simple comparison, the noticeable discrepancy between the half-hourly ESMU schedule and the actual, sub-half-hourly demand can be observed.

Furthermore, noticeable disparity in peak duration, magnitude and volatility can be noted. This discrepancy and disparity emphasise the incompatibility issues between half-hourly ESMU schedules and the actual sub-half-hourly load. As previously discussed, benefits of ESMU were intended to mitigate sub-half-hourly load volatility, yet this cannot be achieved when solely applying half-hourly ESMU schedules in an off-line manner. Therefore, in the next section, the control strategy to add an on-line component is explained.

### 4.3 Control of ESMU

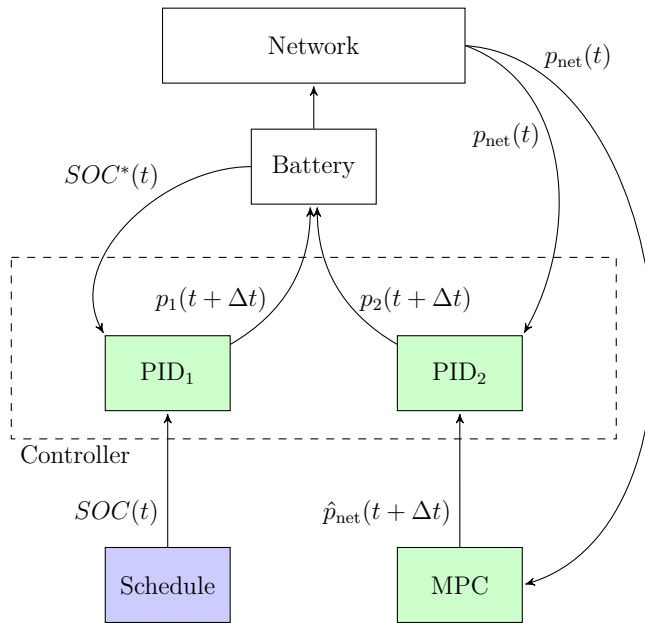


Figure 4.3: Dynamic controller breakdown as previously shown in Figure 4.1c.

This section explains the dynamic control (i.e. the controller block that is shown in Figure 4.1c), which contains the two PID compensators. The first PID compensator is fed by the ESMU schedule, and the other is fed by the MPC load estimations. After the control system is detailed in this section, the auto-regressive models, which were used during the course of this research, are explained, too.

### 4.3.1 Dynamic control

The content of the dynamic control procedure is shown in Figure 4.3. Here, two reference signals are used as inputs to the dynamic control. The first reference signal is the SOC profile derived from the ESMU scheduled,  $SOC(t)$ , and the second is an estimated future network power,  $\hat{p}_{\text{net}}(t + \Delta t)$ . These two inputs are fed into compensator PID<sub>1</sub> and compensator PID<sub>2</sub>, respectively. The output of each compensator is a corrective battery power component that, when summed, yields the next ESMU power, i.e.  $p_1(t + \Delta t)$  and  $p_2(t + \Delta t)$ , which is applied to the ESMU model. Each PID compensator also receives a feedback signal to compute the internal error states. More specifically, PID<sub>1</sub> receives the most recent SOC value that is obtained from the ESMU model,  $SOC^*(t)$ , and PID<sub>2</sub> receives the network's most recent power demand,  $p_{\text{net}}(t)$  (e.g. through measurements by substation monitoring).

Inside the PID<sub>1</sub> component, a SOC error term,  $E_{\text{SOC}}(t)$ , is computed. This term is the difference between the scheduled SOC profile,  $SOC(t)$ , and the actual (or simulated) SOC values,  $SOC^*(t)$ . The following equation captures this error term.

$$E_{\text{SOC}}(t) := SOC^*(t) - SOC(t) \quad (4.9)$$

Applying a standard, linearly weighted dynamic gain vector,  $\boldsymbol{\alpha}$ , to the SOC error, allows the calculation of a corrective ESMU power component dynamically. Here,  $\boldsymbol{\alpha} = \{\alpha_P, \alpha_I, \alpha_D\}$ , where being the P, I and D weights, respectively. How to determine the values of  $\boldsymbol{\alpha}$  is explained later in this section. This corrective power is denoted as  $p_1(t + \Delta t)$ , and is defined as follows:

$$\begin{aligned}
p_1(t + \Delta t) &:= \alpha_P E_{\text{SOC}}(t) \\
&\quad + \alpha_I \sum_{i=0}^{\infty} E_{\text{SOC}}(t - i\Delta t) \\
&\quad + \alpha_D \frac{E_{\text{SOC}}(t) - E_{\text{SOC}}(t - \Delta t)}{\Delta t}
\end{aligned} \tag{4.10}$$

Here, the integral component removes steady-state error and the instantaneous error differential prevents overshooting. All in all, this compensator uses present and past values to issue a corrective future ESMU instruction. Compensator  $\text{PID}_2$  on the other hand uses values from the present, past and future in order to minimise the power transient and load peaks.

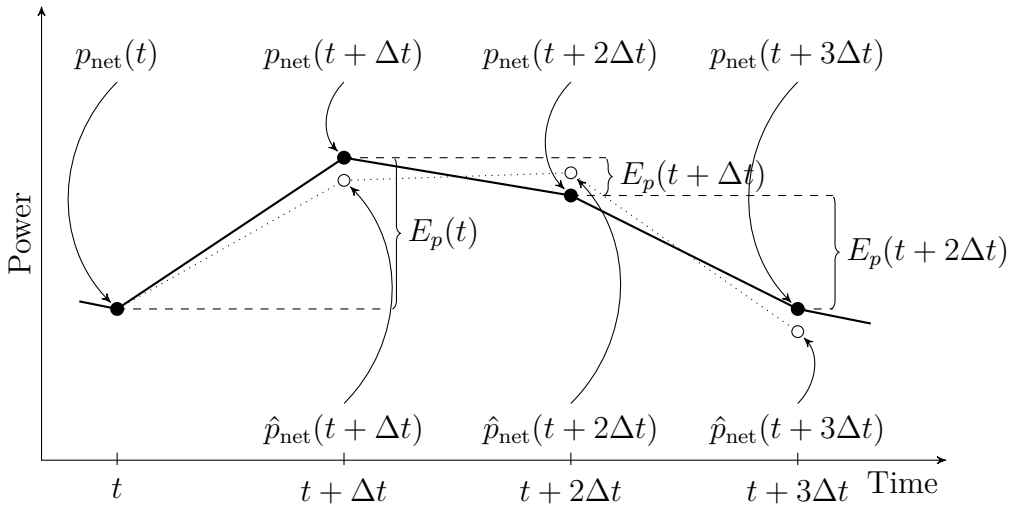


Figure 4.4: Underlying time-series based compensation strategy for compensator  $\text{PID}_2$ .

Figure 4.4 summarises the time series computations for each power sample at times  $t$ ,  $t + \Delta t$ , etc. Ideally,  $\text{PID}_2$  uses present power readings,  $p_{\text{net}}(t)$ , and a power value of the immediate future, i.e.  $p_{\text{net}}(t + \Delta t)$ , to compute a power error signal, which is to be reduced to a smallest possible value. This error signal is defined as:

$$E_p(t) := p_{\text{net}}(t + \Delta t) - p_{\text{net}}(t) \tag{4.11}$$

However, since the future network power is unknown an “estimated next power”,  $\hat{p}_{\text{net}}(t + \Delta t)$ , is used instead. This value is the  $\text{PID}_2$ ’s input from the MPC and results in an “estimated power error signal”:

$$\hat{E}_p(t) = \hat{p}_{\text{net}}(t + \Delta t) - p_{\text{net}}(t) \quad (4.12)$$

Similarly to  $\text{PID}_1$ ,  $\text{PID}_2$  produces a corrective ESMU power component,  $p_2(t)$  that smoothens the resulting power profile. This corrective ESMU power is also computed using a standard linear weighted dynamic vector  $\beta$ , with  $\beta = \{\beta_P, \beta_I, \beta_D\}$ , being the P, I and D weight, respectively (similar to  $\alpha$  how to determine the values of  $\beta$  is explained later in this section):

$$\begin{aligned} p_2(t + \Delta t) := & \beta_P E_p(t) \\ & + \beta_I \sum_{i=0}^{\infty} E_p(t - i\Delta t) \\ & + \beta_D \frac{E_p(t) - E_p(t - \Delta t)}{\Delta t} \end{aligned} \quad (4.13)$$

Finally, the “next ESMU power” can be deduced by adding the two corrective ESMU power components, as shown in the equation below.

$$p(t + \Delta t) = p_1(t + \Delta t) + p_2(t + \Delta t) \quad (4.14)$$

Both PID compensators do however depend on correctly chosen weights for  $\alpha$  and  $\beta$ . Therefore they need to be tuned prior to executing the dynamic control. For this work a minimisation problem was formulated, based on a cost function,  $\zeta^*(\alpha, \beta)$ , to deduce the two weight vectors as follows:

$$\begin{aligned} & \min_{\alpha, \beta} \zeta^*(\alpha, \beta) \\ \text{s.t. } & \begin{cases} SOC(t) - SOC_{tol} \leq 0 \\ -SOC(t) \leq 0 \\ SOC(t) - 1 \leq 0 \end{cases} \end{aligned} \tag{4.15}$$

Here,  $\zeta^*(\alpha, \beta)$  is defined as:

$$\begin{aligned} \zeta^*(\alpha, \beta) &:= \max_t (\mathbf{p}_{net} + \mathbf{p}) \\ \text{where } \mathbf{p}_{net} &= (p_{net}(t)) \text{ and } \mathbf{p} = (p(t)) \end{aligned} \tag{4.16}$$

In Equation 4.15 and Equation 4.16,  $\zeta^*(\alpha, \beta)$  represents the sub-half-hourly peak load during a day, when ESMU schedules are adjusted with the corresponding  $\alpha$  and  $\beta$  weights. Also, the same SOC tolerance that was used to generate the SOC schedule, i.e.  $SOC_{tol}$ , is included to prevent the solution from deviating off the prescheduled SOC profile. To generalise this solution for all load cases, a minimisation problem was formulated to solve multiple daily load profiles in order to find ideal  $\alpha$  and  $\beta$  weights. This resulting set of  $\alpha$  and  $\beta$  weights, therefore guaranteed a convergent and stable solutions for the provided data. The details concerning these case studies themselves, are however outlined in Section 4.4.

### 4.3.2 Model predictive control

As explained in the literature review in Chapter 2, Model Predictive Control (MPC) is favoured over Set-Point Control (SPC), since it takes into account time-series to produce a behaviour. With this knowledge, MPC can be used to not only react to recent changes but also to counteract foreseen trends. Different approaches exist to

obtain these foreseen trends and these approaches highly vary in accuracy, computational burden and robustness. Equally, the characteristics of underlying data which is used to train these models impacts their performances. For the presented work, an efficient and robust approach is required, since potential ESMU deployment with SSEN demands these functional requirements. Prediction accuracy on the other hand is an optional requirement which becomes important only when the predicting model can issue predictions in real-time and does (for the predicting horizon) remain stationary and bounded.

The simplest form of producing a prediction, is to assume that the currently observed trending load will also occur in the future. This kind of prediction does however not take into account demand dynamics. An AR model on the other hand uses a series of past observations and their individual contribution to predict the next power. But the further into the future these predictions are made the less accurate they become. This accuracy loss is however circumvented since the hybrid system was designed to only apply corrections based on load predictions of the immediate future, i.e. next sample time at  $t + \Delta t$  (not  $t + 2\Delta t$  or similar). This simplification also reduces computational burden and guarantees real-time operation, especially when choosing the simplest dynamic model, i.e. an Auto-Regressive (AR) model instead of e.g. deep artificial neural networks. Since external forces can and often do impact the behaviour of the model, the AR model is treated as an exogenous model, with a time-series of input powers,  $\mathbf{p} = (p(t))$ , a time-series of predicted “next powers”,  $\hat{\mathbf{p}} = (\hat{p}(t))$ , and an internal delay function  $t - \Delta t$ .

Figure 4.5 graphically captures the standard AR model’s function tree, which is equivalently represented mathematically in the following equation:

$$\hat{p}(t + \Delta t) = p(t) + \sum_{i=1}^N a_i p(t - i\Delta t) + \sum_{i=1}^N b_i \hat{p}(t - (i - 1)\Delta t) \quad (4.17)$$

Values of the two weight vectors  $\mathbf{a}$  and  $\mathbf{b}$ , where  $\mathbf{a} = (a_i)$  and  $\mathbf{b} = (b_i)$ , are

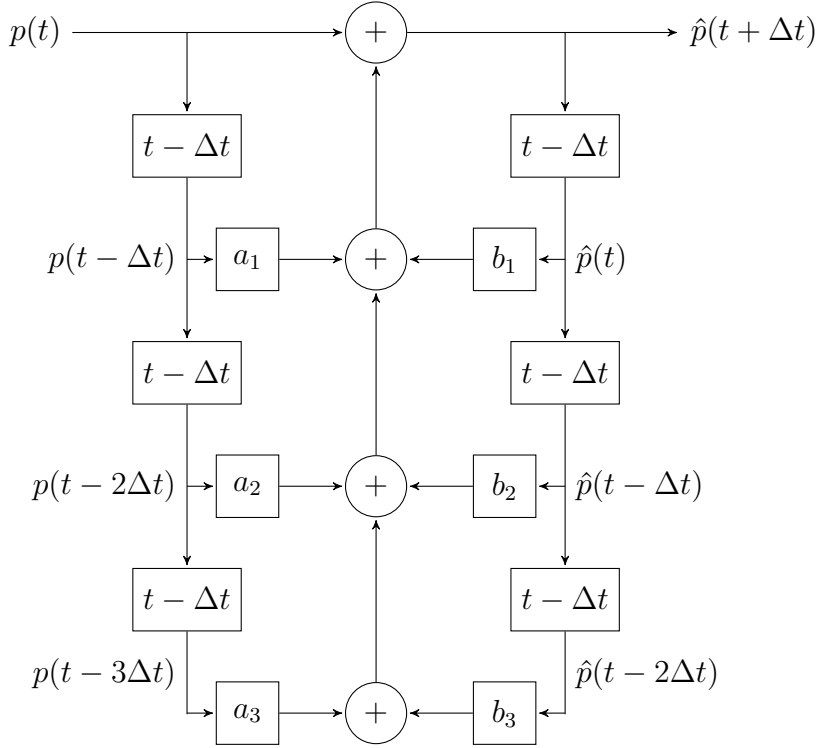


Figure 4.5: Example of exogenous auto-regressive model that is used for model predictive control. Here,  $t - \Delta t$  indicates the time delay by one sample period.

determined during runtime using the standard adaptive least squares algorithm, i.e.:

$$\min_{\mathbf{a}, \mathbf{b}} (p(t) - \hat{p}(t))^2 \quad (4.18)$$

Or:

$$\min_{\mathbf{a}, \mathbf{b}} \left( p(t) - p(t - \Delta t) + \sum_{i=2}^N a_i p(t - i\Delta t) + \sum_{i=2}^N b_i \hat{p}(t - (i-1)\Delta t) \right)^2 \quad (4.19)$$

Therefore, the proposed algorithm adjusts **a** and **b** to minimise the prediction error at each time-step. Beside finding optimised values for **a** and **b**, the model's number of regressors,  $N$ , is also expected to impact the model's performance ( $N$  is also referred to as the "model length"). The example in Figure 4.5 represents a symmetric model where  $N = 3$ . This short length however is most likely insufficient in predicting  $p(t + \Delta t)$ , which is why several models of increasing lengths are assessed

and compared. From this comparison, the impact of  $N$  on the models' resulting values of  $\hat{p}(t + \Delta t)$ , and correspondingly on the performance of the dynamic controller can be discussed. Details about the cases for different model length are presented in the case studies in Section 4.4.

## 4.4 Case studies

All cases that are used to demonstrate the operation of the proposed hybrid control use 27 days of uninterrupted historical demand data. In total, five cases are assessed. Two special cases, respectively case **O** and case **B**, assess the performance of the original case, i.e. where no ESMU operation takes place, against a baseline case, i.e. where traditional off-line ESMU operation that only uses predetermined half-hourly ESMU schedules is referred to as the benchmark case. The remaining remaining cases, which are explained below, capture different implementations of the dynamic control. These three case studies are defined: cases **I**, **II** and **III**. This group of three case studies evaluates the impact of the proposed dynamic control when subjected to realistic (i.e. imperfect) half-hourly load forecasts. In each of the three cases, a different mechanisms is used to predict the power volatility. More specifically:

- case **I** represents an ideal scenario where perfect foresight is assumed and the exact next load can be estimated,
- case **II** uses the aforementioned MPC, and performance of different AR model lengths is compared, and
- case **III** is the third and final case and implements the simplest prediction mechanism, i.e. it is assumed that the current power measurements repeats.

For clarity, all three cases, numbered **I** to **III**, are summarised and tabulated in Table 4.1.

estimation method	real forecast
perfect foresight	<b>I</b>
MPC (AR/ARX)	<b>II</b>
power repetition	<b>III</b>

Table 4.1: Three cases and their dynamic control input assumptions

Results from all ESMU cases (**B**, **I**, **II** and **III**) are first compared against the original, i.e. uncompensated, network load case (**O**). Here, by using a sample day, the assessment of load profile improvements are made clear. Once it is clear how the day's peak is reduced by the algorithm, the daily peak reduction capability from all cases' results are compared. Rather than assessing the underlying load profile from a time-series perspective, focus is only put on any additional reductions of peak load. However, the number of days may make it difficult to spot trends and improvements in the data. Therefore, from the daily peak reduction results, a Probability Density Function (PDF) is derived, which is based on kernel density estimation. The PDF shows the stochastic improvement of each case in comparison to the original case, i.e. case **O**. Finally, to assess the AR model's impact on the peak reduction performance, the simulations are re-run using different AR model lengths ( $N$ ) are and the results are compared using the same PDF comparison method.

## 4.5 Results and discussion

All proposed cases are used to control power flow of the ESMU using 27 days of uninterrupted sub-half-hourly load record. In this section, the time-series improvements are presented at first, where a day's peak reduction due to the sub-half-hourly schedule adjustment are highlighted. Then, the daily peak reduction across the entire dataset is presented, following by a probability density plot to better compare these findings. In the end, the ARX model's impact on the peak reduction performance is assessed.

#### 4.5.1 Time-series analysis

A single day was plotted in Figure 4.6, which shows the time-series improvements, yielded by the ESMU operation. For visual clarity, Figure 4.6a and 4.6b show, respectively, the entire day and a zoomed in version that focuses on the period of interest where the ESMU impact is most apparent. It can be observed, that the unmodified demand profile, i.e. the original case (case **O**), and the case where scheduled half-hourly ESMU operation is applied, i.e. the baseline case (**B**), result in noticeably higher load peaks than any of the three adjustment cases. More specifically, the original peak reduction (which is equal to the scheduled ESMU power) was 1.8kW (3.9% reduction). The average peak reduction when applying adjustments to the ESMU operation was 9.6kW (20.6% reduction). Although it is too early to conclude on any overall performance improvements, this time-series modification does show the physical impact of the ESMU schedule adjustments on the network's load profile. Furthermore, figure 4.6a highlights the volatility of the underlying data, which would be neglected for half-hourly ESMU schedules.

Interestingly, both the standard AR and the exogenous AR estimation models, that were used in case **II**, performed very similar and show little to no significant difference in peak reduction performance. Equally noteworthy is the fact that the simplest prediction methods of them all in case **III**(i.e. the method of assuming a power repetition occurs) yields peak power reductions, too. However, case **I** slightly outperformed all other cases since perfect knowledge would also imply best results. Nonetheless, only a small improvement was possible due to the imperfect underlying half-hourly ESMU schedule. The amount by which the three cases were able to reduce the daily peak load is also indicated by horizontal dashed lines and dots located at the point of peak load for each profile. These initial findings show that every single version of dynamic control reduces peak load when compared to the baseline case **B**. This finding is also tabulated in Table 4.2, and it suggests that the prediction

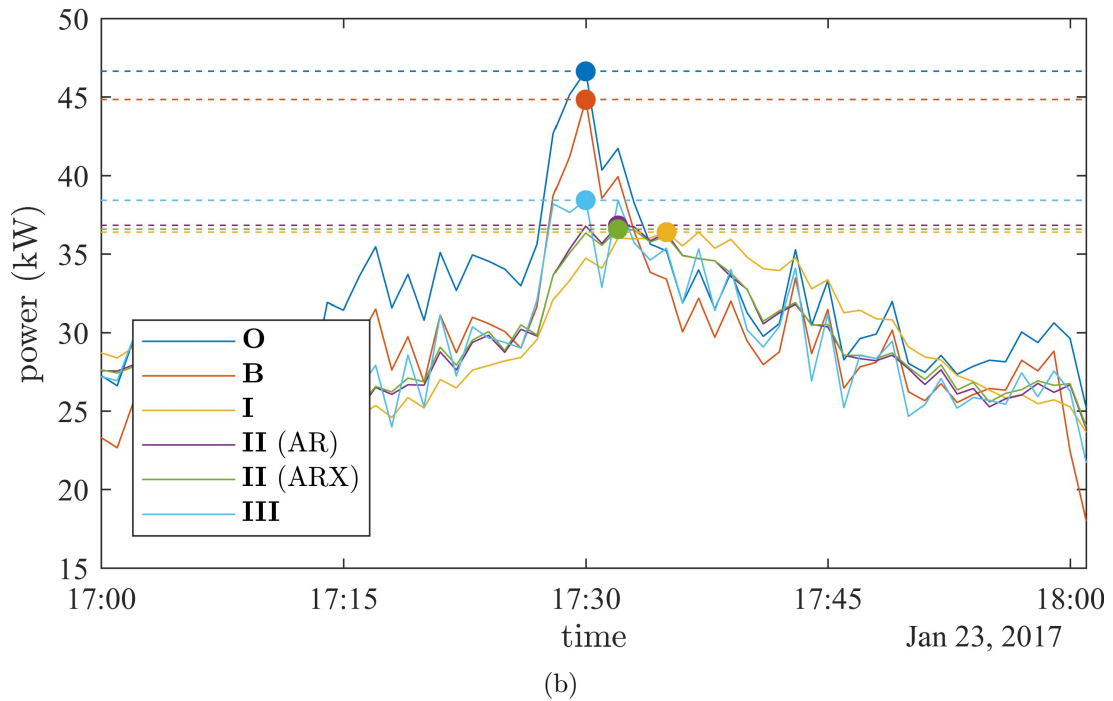
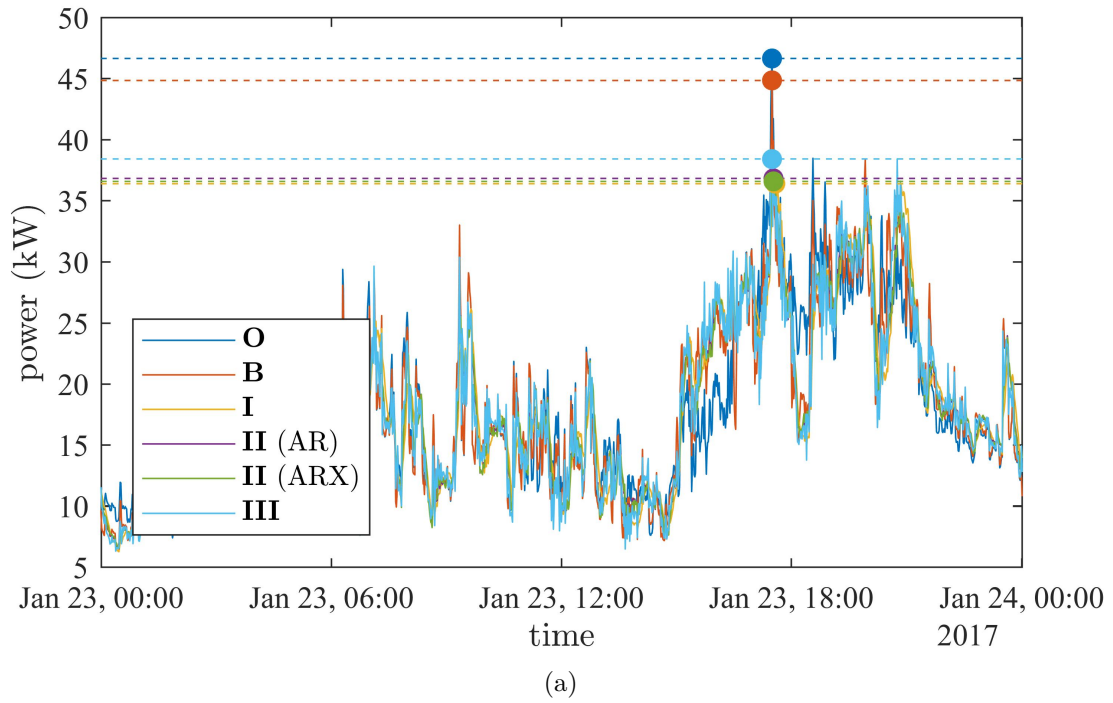


Figure 4.6: Time series performance over a single day when using realistic load forecasts: (4.6a) total day; (4.6b) zoomed in on critical period

mechanism by itself did play some role when compensating for demand volatility.

case	<b>O</b>	<b>B</b>	<b>I</b>	<b>II</b> (AR)	<b>II</b> (ARX)	<b>III</b>
peak (kW)	46.6	44.8	36.4	36.8	36.6	38.4

Table 4.2: Peak reduction in time-series sample

However, the general magnitude of peak reduction performance can only be assessed if the complete dataset is evaluated. Hence, the next section compares the daily peak load reduction from the application of each case.

### 4.5.2 Daily peak reduction

In Figure 4.7, every day's power peak was extracted in a similar way to the procedure that was used for Figure 4.6. Here, the actual power peaks were plotted in Figure 4.7a, and the relative power improvements (i.e. ratio to the baseline power peaks) were plotted in Figure 4.7b. From both plots, it can be seen that controlling ESMU using the proposed dynamic control lowers peak load. This is true even when the underlying ESMU schedule originally worsened and increased peak load. Such a behaviour can be observed clearly during e.g. days 6 and 25, where the half-hourly ESMU schedule increased the actual load peak by 2.8kW and 2.5kW, respectively. The ESMU schedule adjustment mechanisms however compensated for this error, but in those two cases the compensation was not enough to reduce peak power below the original value. Day 26 on the other hand experienced a similar increase in peak power during the baseline case (i.e. case **B**) by 1.2kW, but the power adjustment mechanism corrected this forecast error and reduced the final peak power below the original value.

Nonetheless, the sensitivity to the underlying power prediction approaches becomes apparent when having this larger set of peak reduction results to compare the dynamic control's performance against its baseline cases. As seen in Figure 4.7b, the scenario with perfect foresight (i.e. case **I**) frequently outperformed all other cases

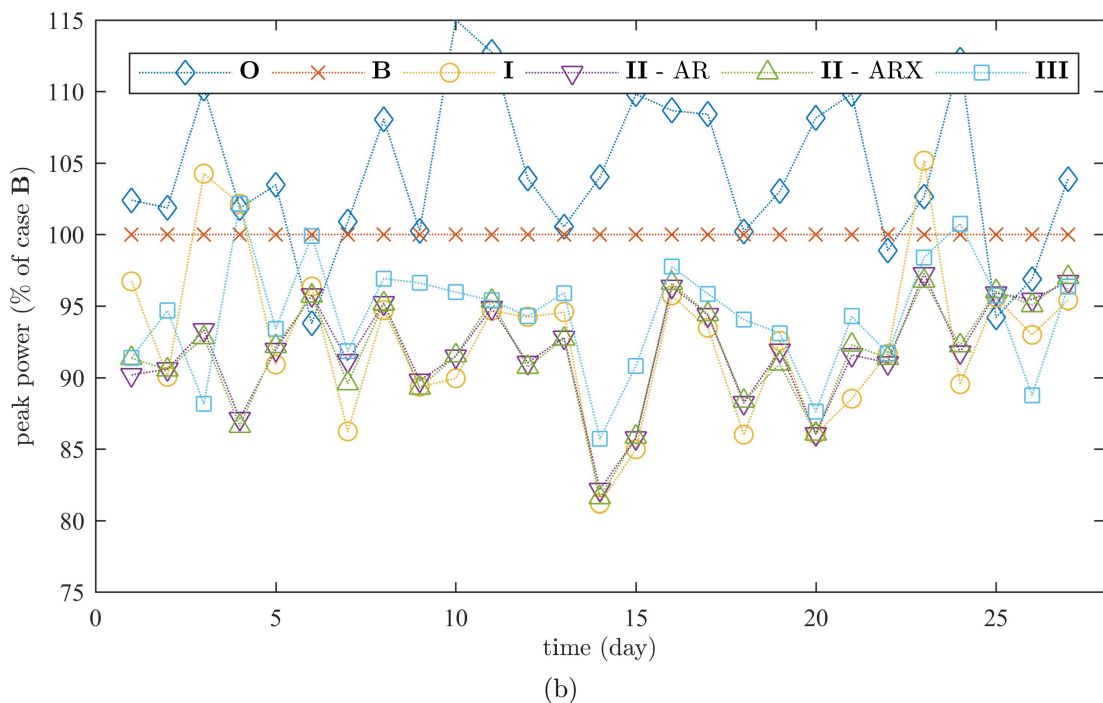
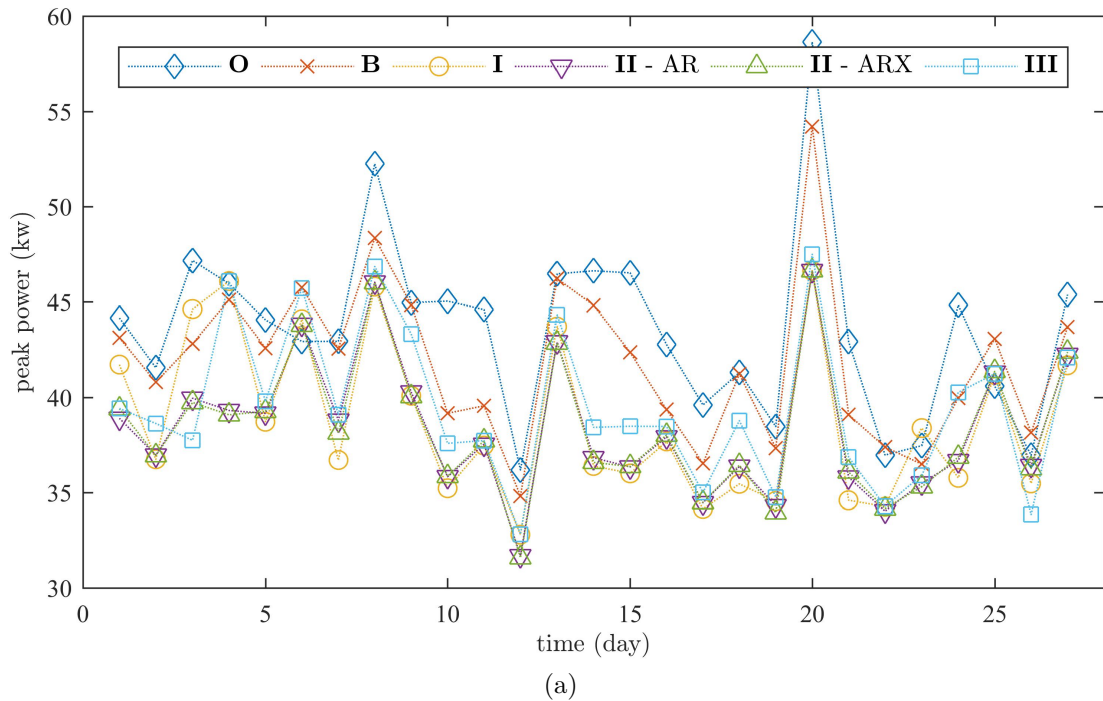


Figure 4.7: Daily peak reduction when using realistic forecasts as: (4.7a) peak power values; (4.7b) percentage of original case **B**.

since it appears to achieve largest peak power reduction from the baseline case. During some days however (i.e. day 3, 4 and 24) the compensators reached the SOC tolerance before the daily peak and could not correctly compensate despite the perfect forecasts. This fact resulted in the two instances of significant worsening of the daily peak. The simplest of all cases on the other hand (i.e. case **III**) yielded a constant but small reduction when compared to the baseline case. Case **II** seems to perform similar, but slightly worse than case **I**. With those daily peak demand reductions between 80% and Whether this assumption holds can however not be said with the presented analysis and instead, in order to obtain a more general picture of the overall peak reduction performance, the Probability Density Function had to be estimated for all cases. This is done in the following section.

#### 4.5.3 Probability of peak reduction

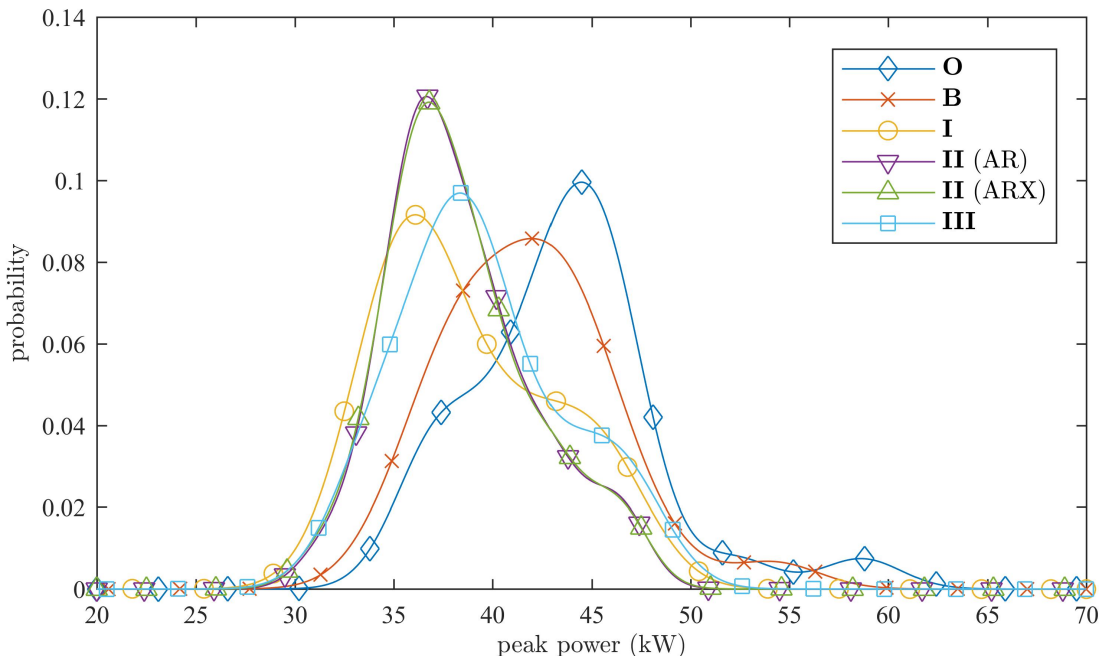


Figure 4.8: Peak load probability for different prediction mechanisms.

With the use of the standard kernel density estimation, the PDF is plotted in Figure 4.8. The data used to generate these plots is the same data shown in Figure 4.7.

Now, the probability of a peak power occurring is linked to the magnitude of this peak. It can be seen that case **O** has the highest probability around a load peak of 45kW, whilst case **B** has its highest probability around a load peak of 42kW. This indicates that even there is a high probability of the half-hourly ESMU schedule having a positive impact on the load peaks. When adjusting this schedule by using of the proposed dynamic control this peak was lowered further. Case **I** performed best by having a most probable peak power of 36.1kW. Case **II** achieve the second best values at 36.7kW and 36.8kW (for AR and ARX case, respectively) whilst the simplest prediction mechanism has its peak power probability maximised at 38.4kW.

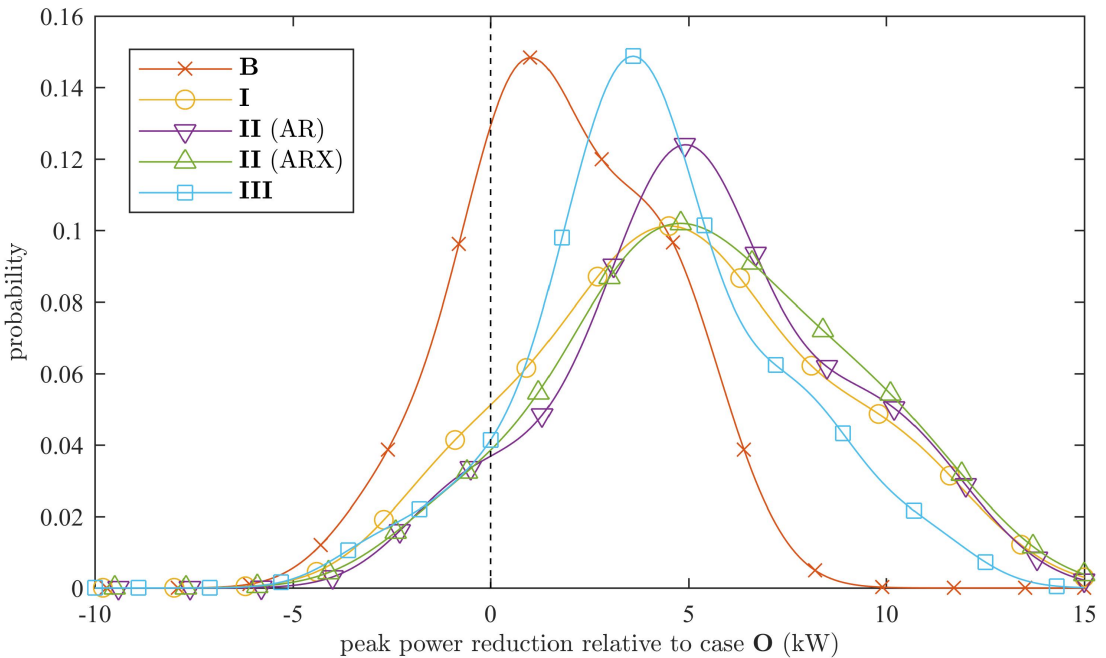


Figure 4.9: Probability of peak load reduction for different prediction mechanisms.

Figure 4.9 takes this analysis even further, where only the difference in peak load to the original case (i.e. case **O**) is plotted. Now, ESMU impact can easily be seen since a high probability of positive peak load reduction indicates a beneficial impact of the ESMU operation. A negative peak load reduction (i.e. increased peak load) would therefore indicate a worse performance. As expected, case **B** has a slight positive impact on the system, whilst a cumulative probability of more than 25%

(i.e. area under curve of case **O** to the left of 0kW) suggests that the peak might be worsened one in four times. The dynamic control with its simplest prediction method however (i.e. case **III**) lowered this probability to only 11.8%, the perfect foresight model (i.e. case **I**) performing best at only 7.4%, and the MPC based cases (i.e. case **II**) achieved an average of 8.0% worsening probability.

Beside the reduced probability of missing or worsening peak load, the probability of having a larger positive impact is also increased when using the dynamic control. Whilst the probability of reducing load peaks by 1.7kW or more was at 50% for case **B**, case **III** increased this probability to 77.7%, case **II** to 84.5 5% (AR) / 83.1% (ARX), and case **I** to 79.8%. The reason why this perfect foresight case achieved a slightly lower value than the AR/ARX cases was due to aforementioned issues with the chosen SOC tolerance. Nonetheless, when comparing the three dynamic control cases with each other as done in Figure 4.9, then it can be seen that case **II** using an AR model for MPC performed best at reducing peak loads for the used dataset.

#### 4.5.4 Impact of varying the model's length

The subsequent results are intended to show whether the length of the AR/ARX model impacted the peak reduction performance. To do so, the same procedure was used as shown in Section 4.5.3, but the length of the AR and ARX models was varied from five minutes to two hours. Therefore, the MPC of the dynamic control took into account a longer power history to potentially improve the prediction of the next power.

Similar to Figure 4.9, Figure 4.10 shows the probability for the difference in peak power between the original case (**O**) and all other cases. In this plot however, all PDFs for the different model lengths have been included (whilst the previous study only showed the inter-model means). It can be seen, that both the AR and ARX case, **II**, performed noticeably better than the baseline case, **B**. Despite the varying model

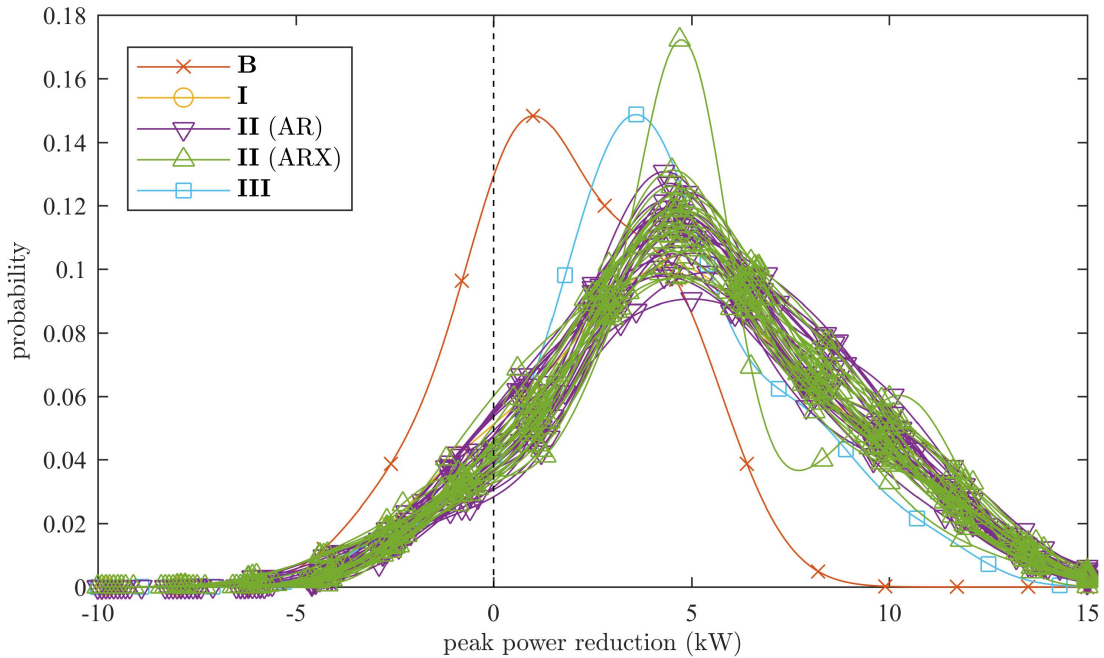


Figure 4.10: Probability of peak load reduction for different prediction mechanisms and different AR/ARX model lengths.

length, all PDFs appear to peak around a reduction performance of 5kW. Therefore, one may assume that the length of the chosen models does not significantly impact the results.

This assumption is supported by the boxplots in Figure 4.11, where the peak power distributions are visualised for all different model lengths and the six different case studies. It can be seen, that the different AR/ARX model lengths, **II**, outperforms both the original and baseline cases, **O** and **B**, respectively. Also, a certain variation in peak reduction performance can be observed, but no apparent trend. Therefore, the assumption that the model length impacts the performance of the dynamic control is true but, for the used data, the assumption that a longer model generally yields better results is not.

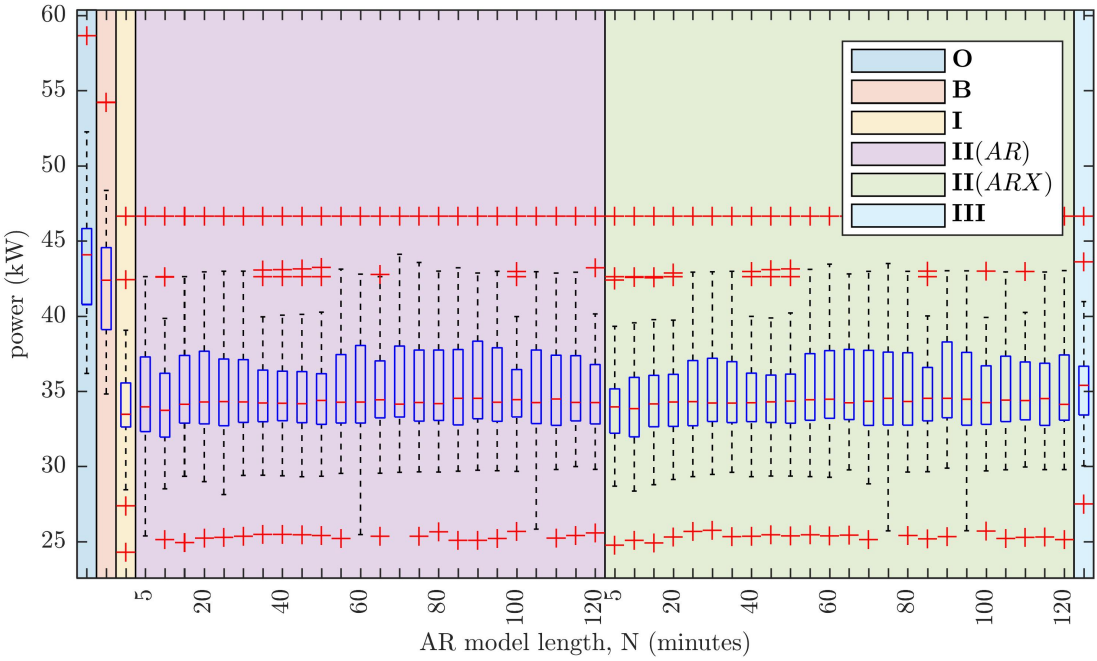


Figure 4.11: Visualisation of the peak power distribution for different AR/ARX model lengths.

## 4.6 Summary

In this chapter a dynamic control method is proposed to address **Objective 2** in the objective list, which is presented in Section 1.2. The proposed method adjusts half-hourly Energy Storage Management Unit (ESMU) schedules on a sub-half-hourly basis in order to minimise otherwise neglected sub-half-hourly power spikes without risking a shortage or surplus of ESMU stored energy. Reason behind this were, that traditional load forecasts usually lack in accuracy and temporal resolution, making it hard to schedule ESMU in an optimal manner. Recent research implements derivatives of Set-Point Control (SPC), which is typically guided by a short-term Model Predictive Control (MPC) mechanisms to address both load volatility and to prepare ESMU for upcoming load spikes. However, those approaches do not utilise the information, quality and operational certainty that would be provided by load forecasts and ESMU schedules. The proposed dynamic control addresses this shortcoming by approaching the problem from the opposite direction: i.e. it adjusts a predetermined

ESMU schedule based on two linked PID compensators.

The first compensator was designed to minimise the deviation from the pre-scheduled ESMU's State Of Charge (SOC) profile, and the second compensator was designed to minimise the load volatility. For the second compensator to operate however, a short-term predictive model was used to estimate the load power in the immediate future, i.e. the next time step. Different light weight and well established mechanisms were used to implement this predictive model in order to assure real-time operation and robustness of the system.

Simulating these different models to guide schedule adjustments yielded positive results for each test case that used dynamic control. In fact, dynamic control outperformed the baseline case in nearly every case, where the baseline case is the scenario of applying a traditional half-hourly ESMU schedule in an off-line manner. Whilst this baseline operation did also increase peak load under severe forecast errors, the best performing dynamic control case was able to reduce the probability of increasing peak loads by a factor of 3.12. Also, the length of the underlying prediction models was varied from 5 minutes to 2 hours in order to assess the impact of this variation on the performance of the dynamic control. It was determined that there is no linear correlation between the models' lengths and the performance of the dynamic control. Instead, the dynamic control performed with slight performance variations, yet always outperformed the original and baseline cases. Those performance gains were achieved despite the fact that all cases used the same underlying ESMU schedule that were generated from realistic (hence imperfect and erroneous) load forecasts.

The work presented here, demonstrates how imperfect ESMU schedules may still be used to yield more beneficial impacts. With future deployment of ESMU throughout Low-Voltage power distribution networks, advanced ESMU control is necessary to assure their impact is in accordance to volatile demand. Control, like the one proposed here, can take into account the complete range of demand volatility and,

when implemented correctly, defers or avoid network reinforcement altogether. This is particularly true since ongoing electrification of UK heat and transport sectors change consumers' electricity consumption and increase stress on power distribution networks.



# Chapter 5

## Effects of Desynchronising Information Propagation when Distributing Smart-Charging

*M. J. Zangs, T. Yunusov, W. Holderbaum, and B. Potter, “On Smart EV Charging with Asynchronous Multi-Agent System for Load Profile Optimisation“ IEEE Transactions of Smart Grid*

— Unpublished

### 5.1 Overview

In previous chapters the the question regarding how one can optimally control a single battery energy storage has been addressed. It was shown that half-hourly forecasts can be used to predict demand based on customers' behaviours. With this knowledge, Battery Energy Storage Systems (BESS) can be scheduled to shave half-hourly peak loads on a daily basis, in order to avoid overloading the power distribution system. Yet sub-half-hourly issues could not be addressed by traditional BESS schedules, which is why two successive sub-half-hourly power adjustment methods were proposed and developed as BESS control methods. The first method in Chapter 3 focused on improv-

ing network operation by considering the underlying three-phase network properties, whilst strictly following the underlying half-hourly operating schedule. The second method on the other hand, which was presented in Chapter 4, alleviated this constraint by adjusting the total power flow instead. Benefits like preparing the storage for a day-ahead peak can be exploited by using BESS schedules and complementing them with dynamic feedback. As shown in the previous two chapters, Chapter 3 and Chapter 4, together these two methods yield improved system operation as well as a reduction in both daily and sub-half-hourly peak load.

The next step would be to take such control methods and apply them to multiple, distributed batteries. To prevent the negative impact from e.g. simultaneous battery charging, particularly when dealing with the home-charging of Electric Vehicles (EVs), their energy consumption needs to be coordinated. As already discussed in the literature review in Chapter 2, multiple control methods that can also be used to coordinate Distributed Energy Resources (DER), including EV charge scheduling methods (i.e. [35, 106, 143, 147–158]). Those approaches propose demand prioritisation, multi-tariff environments and even game theory based methods to maximise utility or to operating reduce cost. In the context of EV charging, reacting to other EV's changes in charging plans becomes a vital requirement when scheduling and coordination their own charging profiles. For this very reason has research predominantly focused on improving so called smart-charging algorithm improvements, but in a distributed system this scheduling assumption of perfect knowledge exchange may not always hold: In fact, during distributed EV scheduling, control instructions that may be broadcasted by one EV to inform all other scheduling EVs of e.g. an updated charging schedule, need not or cannot be received and responded to at the exact same time unless some synchronisation amongst all EVs is emplaced. A method to develop smart-charging algorithms that explicitly function in both synchronised and desynchronised environments does not yet exist, to the best of the author's knowl-

edge. Therefore, this chapter, Chapter 5, first develops a smart-charging method for a synchronised fleet of EVs and then introduces message desynchronisation to assess the performance difference between the two environments. By doing so, Chapter 5 addresses **Objective 3** of this thesis, which was outlined in Section 1.2, which aims to develop an EV scheduling method that is immune to message desynchronisation.

It should be noted, that the charging of EVs is explicitly assessed instead of managing a collection of BESSs, since storage is able to release energy and thus provide grid support. Traditional EVs on the other hand do not have such capabilities<sup>1</sup> and need to be coordinated in order to avoid home-charging related load spikes. To achieve this coordination, Chapter 5 implements a Multi-Agent System (MAS) to enable the distributed scheduling using the Foundation for Intelligent Physical Agents (FIPA) compliant agents as communication entities [197]. A smart-charging algorithm is developed and implemented in each agent, where communication is assumed to be synchronised. Results show how EV scheduling in a synchronised environment leads to the expected outcomes, some of which have also been established in literature (e.g. load oscillation like in [42]). However, adding jitter to message broadcasting significantly changes the algorithm's behaviour. Differences regarding rate of convergence and criteria for stability are most noticeable. Scheduling performance on the other hand does not deteriorate. The structure of this chapter is as follows: First, the EV demand and scheduling mechanism to coordinate the synchronised and desynchronised smart-charging is explained in Section 5.2. Next, in Section 5.3, the distributed control system for the chosen MAS is presented, alongside the two cases for synchronised and desynchronised information propagation. Section 5.4 presents and discusses the results from these two cases, upon which a conclusion is drawn in Section 5.5.

---

<sup>1</sup>Research delving into Vehicle-to-Grid (V2G) support do consider reverse energy flow, yet this is not included in the work presented in this thesis.

## 5.2 Coordination of EV charging

In this section, an algorithm for EV charging is presented, which is implemented in both a synchronised and desynchronised case. The Irish load dataset [198] is used in combination with EV energy demand to test the proposed smart-charging algorithm. Performance of the algorithm at preventing new power spikes from occurring is then assessed with the use of standard performance metrics. Finally, to study the convergence of the algorithm, a convergence criteria as well as rate of convergence are presented, too.

### 5.2.1 EV Demand

In order to simulate the fleet of  $U$  charging EVs, where  $U \in \mathbb{Z}^{>0}$ , each EV,  $u$  where  $u \in \{1, \dots, U\}$ , is modelled as a load that needs to consume a certain amount of energy,  $E_u$ , over the course of a scheduling horizon,  $T^{\text{sch}}$  where  $T^{\text{sch}} \in \mathbb{Z}^{>0}$ . Unlike typical load profiles (e.g. household load profiles), EVs are modelled to not have a predetermined load profile, but are flexible in order to schedule their own demand,  $p_{u,n}^{\text{EV}}(t)$ , at any moment time  $t$ , where  $\mathbf{p}_{u,n}^{\text{EV}} = (p_{u,n}^{\text{EV}}(t))$  and  $t \in \mathbb{Z}^{\geq 0}$ . In other words, EVs can autonomously assign their own charging plan over the predetermined number of future time-slots,  $T^{\text{sch}}$ . Due to limitations in on-board power electronics, each EV's maximum charge rate,  $P_u^{\max}$ , is restricted and may not be exceeded. Equally, in order to meet the EV's charging demand over the scheduling horizon,  $T^{\text{sch}}$ , a soft minimum charging power,  $P_u^{\min}$  is also introduced:

$$P_{\min,u} := \frac{E_u}{T^{\text{sch}}} \quad (5.1)$$

Although the upper limit represents a technical restrictions, this lower limit is a necessity to assure the demanded energy is charged over the entire charging period, and this limit is used to initiate the scheduling procedure itself. This charging pro-

cedure is explained in Section 5.2.3. Using MAS, EVs utilise their agent systems to purchase energy quantities for each time-slot,  $t$ , and also sell or “undo” some of the already acquired energy quantities if it helps lowering a potential load spike.

### 5.2.2 Base Load

To represent real power consumption in simulations, historic customer load profiles were used in this work [198]. This dataset consisted of 7392 demand readings for 543 loads, which were sampled at half-hourly period, i.e.  $\Delta t = 0.5$  hours. A single scheduling horizon was defined as one day, therefore  $T^{\text{sch}} = 48$  samples.

In this context, each household dispatches its agents once to acquire the household’s half-hourly energy demand for the entire day; making the assumption that some demand foresight is available. After having acquired or reserved the daily demand by issued an energy request, the entire network demand is known to the energy supplier and can be relayed to all EV agents when they query for it. This ability is exploited when scheduling and negotiating the unknown EV charging profiles. More specifically, all EV’s agents communicate with the supplier’s agent to optimally embed their charging profiles,  $p_{u,n}^{\text{EV}}(t)$ , within this aggregated base load.

### 5.2.3 Scheduling Algorithm

For the EV charging coordination strategy, an algorithm was designed that generates charging profiles for each EV so that the network power is optimised. Here, an optimal network power,  $p^{\text{net}}(t)$  implies that when adding all aggregated charging profiles to the network’s base demand,  $p^{\text{base}}(t)$ , no additional power spikes occur in the resulting power profile, i.e.  $p^{\text{net}}(t) = p^{\text{base}}(t) + \sum_{u=1}^U p_{\text{EV},u,N}(t)$ . The charging profiles are generated by repetitively querying energy supplies for the network’s base load, adjusting individual EV charging profiles, and resubmitting the adjusted charging profile. As already stated, the common assumption when designing such a scheduling algorithm

is that all scheduling entities are synchronised, i.e. wait for each other, before querying for the network's base load. For visualisation, the message exchange between two loads and a supplier including a synchronisation time is shown in Figure 5.1.

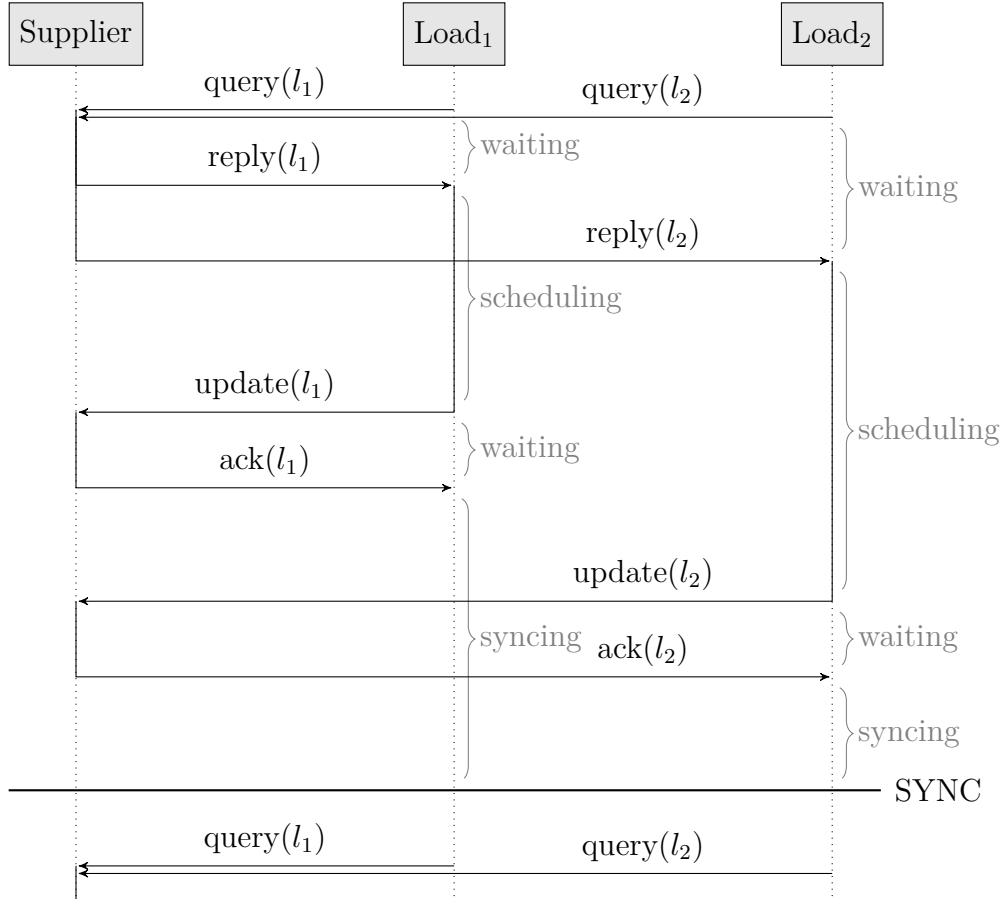


Figure 5.1: Example of agent synchronisation process before re-scheduling their EVs charging profile.

In this figure, the horizontal arrows indicate messages being sent from loads (i.e. EV agents) to a supplier and vertical lines indicate processing or idle time. Shown within Figure 5.1 is a single scheduling iteration, which can be broken into the sub-processes of: querying, scheduling, updating and synchronising. From top to bottom, the sequential execution of these sub-processes is as follows:

First, both  $load_1$  and  $load_2$  query the supplier for the currently known network load (i.e.  $query(l_1)$  and  $query(l_2)$ ). This network load is used to schedule their power

profiles to “fill valleys”, i.e. only charge EVs during periods of low demand. Upon receipt of a reply from the energy supplier (i.e.  $\text{reply}(l_1)$  and  $\text{reply}(l_2)$ ), both loads immediately start scheduling their profiles. In the example above,  $\text{load}_1$  found a solution before  $\text{load}_2$  and can therefore inform the supplier about its intended load profile sooner, by sending an update (i.e.  $\text{update}(l_1)$ ) to the supplier. Subsequently querying the supplier for an updated network load would be premature, since the other load (i.e.  $\text{load}_2$ ) has not yet generated and updated its load profile. Therefore, a synchronisation mechanism had to be used, forcing  $\text{load}_1$  to wait until all loads have sent updates to the supplier. Here,  $\text{load}_1$  waits until  $\text{load}_2$  has sent an update and the corresponding profile was acknowledged by the supplier (i.e.  $\text{ack}(l_2)$ ). Only after this had happened, a synchronisation event would be triggered (i.e.  $\text{SYNC}$  event). After this synchronisation event, the next algorithm iteration is initiated and the procedure repeats. Since all subsequent iterations are similar to the one shown in Figure 5.1, only the two querying messages of the second iteration are shown.

Although timing and message exchange has been defined, the mechanism to allocate and reallocate charging powers in order to achieve a valley filling behaviour has not yet been defined. This behaviour is shown in Figure 5.2, where several iterations numbered  $n$  are shown, and for each subsequent iteration, some amount of prescheduled power is reallocated to different time-slots.

For every iteration,  $n$  where  $n \in \mathbb{Z}^{>0}$ , in Figure 5.2, charging profiles are added onto a base network load,  $\mathbf{p}_n^{\text{base}}$ , where  $p_n^{\text{base}}(t) \in \mathbf{p}_n^{\text{base}}$ . This base load is shown as the bold black line and does not change throughout EV scheduling. For any iteration, the charging profile during iteration number  $n$ , for EV  $u$ , is defined as  $\mathbf{p}_n$ , where  $\mathbf{p}_n = (p_{u,n}(t))$ . During the first iteration however, i.e. Figure 5.2a where  $n = 1$ , this charging profile is determined by assigning the maximum EV charging power to the time-slots of lowest load, until the total EV energy demand is met, i.e. at time-slot  $t = \text{argmin}(\mathbf{p}^{\text{base}})$ . Since all EVs schedule their profiles based upon the

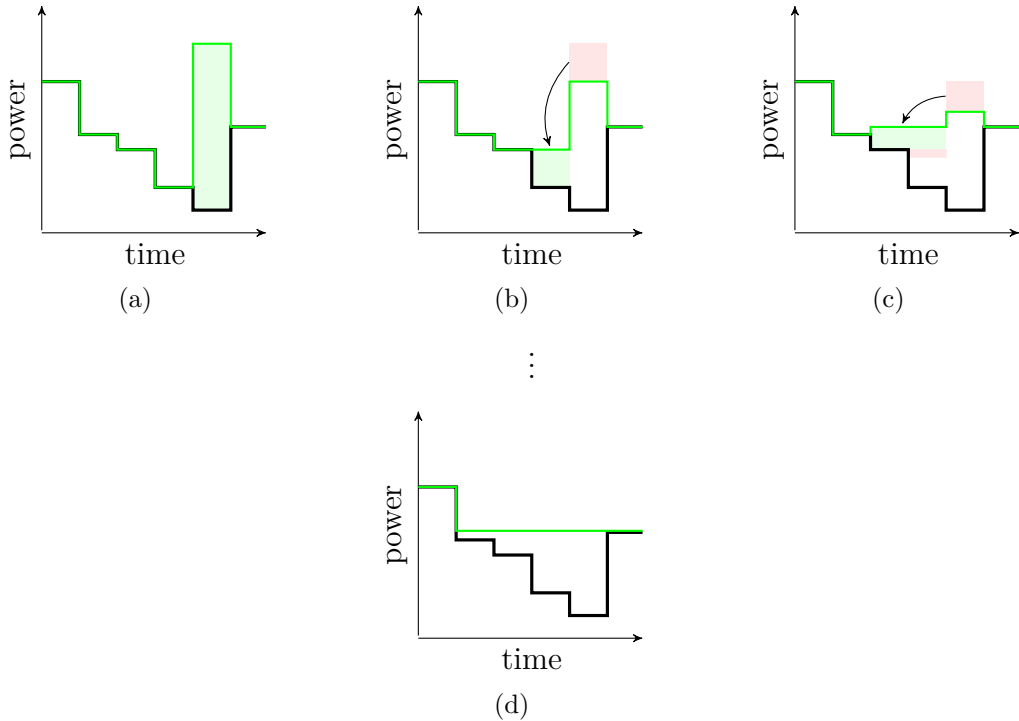


Figure 5.2: Charging power (green line) allocation on top of base network load (black line) for valley-filling behaviour. Here  $n = 1$  for Fig. 5.2a,  $n = 2$  for Fig. 5.2b,  $n = 3$  for Fig. 5.2c, and  $n = N$  for Fig. 5.2d.

same knowledge of  $\mathbf{p}_n^{\text{base}}$ , the aggregated charging power is likely to generate a new spike. This spike is seen on an updated or temporary demand profile,  $\hat{\mathbf{p}}_n^{\text{base}}$ , where  $\hat{\mathbf{p}}_n^{\text{base}} = (\hat{p}_n^{\text{base}}(t))$ , is defined as:

$$\hat{p}_n^{\text{base}}(t) := p_n^{\text{base}}(t) + \sum_{u=1}^U p_{u,n}(t) \forall t, n \quad (5.2)$$

For the next iteration  $n + 1$ , i.e. Figure 5.2b where  $n = 2$ , a proportion of the previously scheduled power vector  $\mathbf{p}_{n-1}^{\text{EV}}$  is “undone”. Subsequently, the spike in the resulting  $\hat{\mathbf{p}}_n^{\text{base}}$  is reduced, yet the energy that has been undone needs to be reallocated. The amount by which  $\mathbf{p}_{n-1}^{\text{EV}}$  is reduced is determined by the “undoing” parameter  $\alpha$ , where  $\alpha \in [0, 1]$ . A new reduced or temporary charging vector  $\hat{p}_{u,n}^{\text{EV}}(t)$  is therefore defined as:

$$\hat{p}_{u,n}^{\text{EV}}(t) := p_{u,n-1}^{\text{EV}}(t)(1 - \alpha) \quad (5.3)$$

Using this temporary charging power, the regained or temporary energy demand,  $\hat{E}_{u,n}$ , that needs to be reallocated, can also be defined by including the sampling period  $\Delta t$ :

$$\hat{E}_{u,n} := E_u - \sum_{t=1}^{T^{\text{scl}}} \hat{p}_{u,n}^{\text{EV}}(t) \Delta t \forall u, n \quad (5.4)$$

To include the first iteration of the algorithm, Equation 5.4 needs to be expanded to redefine  $\hat{E}_{u,n}$  for all possible algorithm iterations  $n$ :

$$\hat{E}_{u,n} := \begin{cases} E_u & \text{if } n = 1 \\ E_u - \sum_{t=1}^{T^{\text{scl}}} \hat{p}_{u,n}^{\text{EV}}(t) \Delta t & \text{otherwise} \end{cases} \quad \forall u, n \quad (5.5)$$

Following the similar procedure as for the first iteration,  $\hat{E}_{u,n}$  is then allocated to different time-slots where the rule of performing the power allocation  $p_{u,n}^{\text{EV}}(t)$  based on  $p_{u,n-1}^{\text{EV}}(t)$ , is defined as follows.

$$p_{u,n}^{\text{EV}}(t) = \begin{cases} \hat{p}_{u,n-1}^{\text{EV}}(t) + \frac{\hat{E}_{u,n}}{\Delta t} \beta & \text{if } \hat{p}_{u,n-1}^{\text{EV}}(t) + \frac{\hat{E}_{u,n}}{\Delta t} \beta \leq P_u^{\max} \\ P_n^{\max} & \text{otherwise} \end{cases} \quad \forall u \quad (5.6)$$

where  $t = \text{argmin}(\hat{\mathbf{p}}_{\text{base},n})$

$$\text{and } \hat{p}_{u,n-1}^{\text{EV}} + \frac{\hat{E}_{u,n}}{\Delta t} \beta \geq P_{\min,u}$$

Here,  $\beta$  is the maximum “allocation” parameter, where  $\beta \in (0, 1]$ , and this parameter limits the power that may be allocated to any successive time-slot,  $t$ . To not exceed the EV’s maximum charging power, any value in the charging vector,  $\mathbf{p}_{u,n}^{\text{EV}}$ , is capped to  $P_u^{\max}$ . If  $\beta$  is chosen as one, then the undone energy is allocated as quickly

as possible. For smaller values of  $\beta$  on the other hand, the undone charge is reallocated in smaller portions. Since EV scheduling takes place over a finite scheduling horizon,  $T^{\text{sch}}$ , a constraint was added in Equation 5.6. This was done to assure that the temporary energy demand equates after some charging power was assigned to every time-slot of  $\mathbf{p}_{u,n}^{\text{EV}}$ .

In any following algorithm iteration, i.e.  $n > 2$  as shown in Figure 5.2c, each EV's charging profile is adjusted and spread further over the base load,  $\mathbf{p}^{\text{base}}$ . In the end, i.e. when  $n = N$ , the ideal EV charging profiles add to the base load in such a way, that the resulting network load has an optimally filled valley. This valley filling behaviour is achieved with the “undoing” and “allocation” of EV charging power from one algorithm iteration to the next. Regardless of the final network load’s shape, the algorithm terminates when the final iteration is reached, i.e.  $n = N$ . Rate of convergence of the algorithm differs based upon the choice of  $\alpha$  and  $\beta$  values. However, convergence is in fact guaranteed when selecting values of  $\alpha < 1$  and  $\beta < 1$ , since, in those cases, the algorithm satisfies the D’Alembert Criterion; the criterion requires a continuous but not necessarily regular reduction in output.

To summarise this section, the complete EV scheduling algorithm was developed by: 1. defining the message exchange and synchronisation mechanism, which is shown in Figure 5.1; 2. formulating the initial and successive “undoing” of charging power, as shown in Equation 5.3; and 3. defining the iterative update and “allocation” of the temporary energy demand, as defined in Equation 5.5. For clarity, the this smart charging algorithm’s pseudocode, performing the complete valley filling procedure, has been included in Algorithm 1.

```

1 // Input data, i.e. initial conditions
Data:  $p_{base,n}$ ,  $E_u$ ,  $P_{max,u}$ ,  $P_{min,u}$ ,  $\Delta t$ ,  $T_{sch}$ 
Result:  $p_{EV,u,n}$ 
2 for  $n \leftarrow 1$  to  $N$  do
3   // Query for base load
4    $p_{base,n} \leftarrow \text{query}();$ 
5   // Forward and undo previous schedule
6   if  $n > 1$  then
7     |  $p_{EV,u,n} \leftarrow p_{EV,u,n-1}(1 - \alpha);$ 
8   else
9     |  $p_{EV,u,n} \leftarrow [0, 0, \dots, 0];$ 
10  end
11 // Determine unallocated energy
12  $\hat{E}_{u,n} = E_u - \sum_{\tau=1}^{T_{sch}} p_{EV,u,n}(\tau) \Delta t;$ 
13 // Fill valley
14 for  $\tau \leftarrow \text{argmin}(p_{base,n})$  to  $\text{argmax}(p_{base,n})$  do
15   if  $p_{EV,u,n}(\tau) + \frac{\hat{E}_{u,n}}{\Delta t} \beta \leq P_{max,u}$  then
16     |  $p_{EV,u,n}(\tau) \leftarrow p_{EV,u,n}(\tau) + \frac{\hat{E}_{u,n}}{\Delta t} \beta;$ 
17   else
18     |  $p_{EV,u,n}(\tau) \leftarrow P_{max,u};$ 
19   end
20    $\hat{E}_{u,n} = E_u - \sum_{\tau=1}^{T_{sch}} p_{EV,u,n}(\tau) \Delta t;$ 
21   // Once EV profile is found, send update
22   if  $\hat{E}_{u,n} = 0$  then
23     |  $\text{update}(p_{EV,u,n});$ 
24     |  $\text{break}();$ 
25   end
26 end
27 synchronising();
28 end

```

**Algorithm 1:** Robust valley filling algorithm for a single EV in

## 5.3 Distributed Systems

As discussed in the literature review in Chapter 2, several mechanisms exist to decentralise control of DERs. For their reactivity, pro-activeness, social ability and flexibility however, the Multi Agent System (MAS) distinguished itself from traditional software and hardware systems, which is why it was also chosen for the coordination of smart EV charging. Several agent package implementations exist, each following different interaction paradigms. Some of these paradigms include “Belief, Desire and Intention” (BDI), neutral behaviour or other specialised functionality [199]. From the catalogue of MAS paradigms, the Java Agent Development Framework (JADE) was chosen, since it natively implements the Foundation for Intelligent Physical Agent (FIPA) specification [200, 201]. Furthermore, JADE is an application independent package that has become quite popular, as seen by the increasing number of publications [42, 202–205].

In this work, multiple virtual trading agents are used to negotiate their corresponding EV charging profile with other trading agents. Tying virtual agents to a physical entity is not new [162, 206–208], and allows a clear decoupling of the data storing and interacting entities. In previous work however, physical agents directly controlled the virtual entities whilst the agents in the presented work negotiate schedules that will be applied after schedule ratification. Therefore, the physical agent is never notified of any intermediate charging profile and only receives the final schedule. Scheduling and inter-agent communication is achieved by so called “broker” agents that follow the Brokering Interaction Protocol (BIP) to serve the final charging profile when requested. It is those broker agents that communicate and negotiate with each other by following the Contact-Net Protocol (CNP). All these FIPA protocols are based on the FIPA Agent Communication Language (ACL) that is required to communicate over a shared telecommunications infrastructure since it standardises the communication ontology and schemas. Following this standard also opens the

possibility of including different agent packages into the scheduling mechanism, but this lies outside the work's scope. Explanations of all protocols that were used in this implementation of FIPA agents are included in Appendix B. In this work, each broker is linked to a single EV and negotiates its charging profile over the aforementioned scheduling horizon,  $T_{\text{sch}}$ . This link is shown in Figure 5.3.

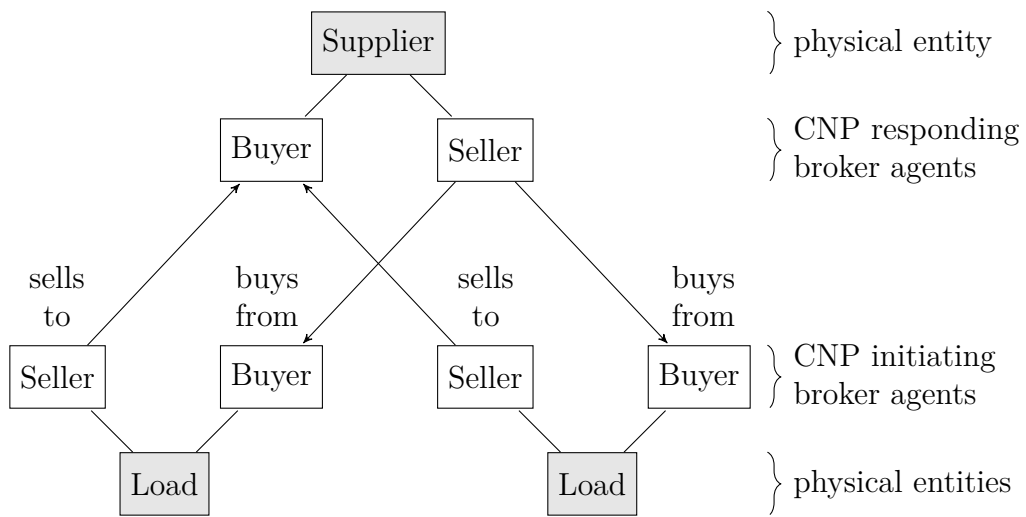


Figure 5.3: A simplified MAS structure containing virtual seller and buyer agents (white), that negotiate power/charging profiles for physical entities (grey).

The example in Figure 5.3 shows the structure of a MAS with three physical agents and six virtual agents. A supplier and two loads are the physical agents and two charging EVs, respectively, which dispatch two brokers each. One of the brokers is for buying energy, i.e. “allocating” energy, and the other one for selling energy, i.e. “undoing” energy. With this kind of system architecture, the scheduling algorithm can be executed to mitigate potential charging spikes.

How this MAS is implemented, synchronised and desynchronised is explained in the following sections, Section 5.3.1 and Section 5.3.2, respectively. Subsequently, in Section 5.3.3, all case studies and performance metrics that are used to assess the MAS performance are outlined.

### 5.3.1 MAS Implementation

The MAS is implemented in Java and runs on a parallel compute cluster (i.e. the *HTCondor* cluster at the former *School of Systems Engineering* at the *University of Reading*). How the compute cluster was used to realise multiple agents is shown in Figure 5.4.

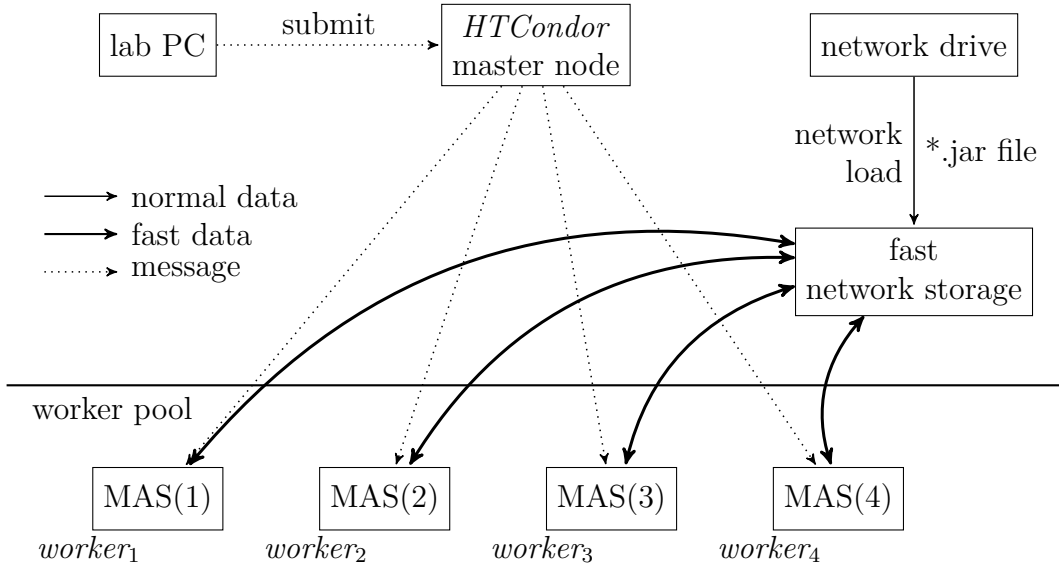


Figure 5.4: The implementation of FIPA on *HTCondor*.

In this figure, Figure 5.4, at the laboratory workstation, a collection of MAS simulations is compiled in order to extensively cover the algorithm's operating spectrum. More specifically, 10000 repetitions of the scheduling algorithm are queued for a single base load, but with different  $\alpha$  and  $\beta$  parameters. Therefore, the algorithm's parameter sensitivity is probed at a resolution of 0.01 for both  $\alpha$  and  $\beta$ , i.e.  $\alpha \in \{0.01, 0.02, \dots, 1.00\}$  and  $\beta \in \{0.01, 0.02, \dots, 1.00\}$ . This queue of 10000 simulations is then submitted to the *HTCondor* master node, which schedules the execution of each simulation to its pool of workers. Each worker internally simulates an instance of the MAS and stores its outputs to a fast networked storage, which also serves as the worker's data source Given the 1540 load profiles from the Irish dataset and assuming a typical distribution network of 55 customers, a theoretical

limit of  $6.11 \times 10^{101}$  simulations would exist. Due to the limited time and size of the available worker pool (ca. 200 workers), a total number of  $1.5 \times 10^7$  MAS simulations is chosen to yield a sufficiently accurate estimate of the algorithm’s performance. For all submitted simulations a relatively high EV uptake of 20% was chosen in order to maximise the effect of badly scheduled EV charging, and in order to give the algorithm a larger energy volume when adjusting the EV charging schedules. Also, in the diagram in Figure 5.4, all bold arrows indicate data transmissions that are faster than the lab PC connection (this connection is used to acquire and store the datasets that are used for each MAS simulation), solid arrow indicates the loading of simulation data, and the dotted arrows indicate the software messages to submit and launch the MAS simulations.

### 5.3.2 MAS Desynchronisation

Originally, the smart-charging algorithm was intended to run in a synchronised MAS environment, as shown in Figure 5.1. However, when aiming to desynchronise this operation, two distinct ways exist: Either, any idle state that is interrupted by the synchronising signal (which is shown in Figure 5.1) is removed and agent execution continues immediately, or agents are launched with a random jitter and operate in an execution loop with a fixed time delay. Although the first approach would result in the quickest simulation execution, it still would require a synchronised start since one agent would already finish all algorithm iterations by the time a second agent joins the MAS. Therefore, only the second way yields a truly desynchronised agent execution that still guarantees that all agents partake in the scheduling process. Furthermore, using this jitter and therefore extending the execution time of each simulation makes the algorithm compliant with the compute cluster’s terms of usage, since it would otherwise threaten to overload *HTCondor* at managing the submission and data transfer between all workers.

In order to implement the second way of desynchronising agents, each agent is equipped with its individual loop timer that regulates its execution behaviour. All agents are launched in quick succession and immediately begin their enumeration and scheduling tasks. Desynchronisation amongst all agents is then achieved by introducing a jitter to both the agents' loop timers and the period between successive agent launches. The resulting MAS then consisted of a completely desynchronised collection of agents, i.e. none of the agent's loop execution is aligned or dependent on any other agent's loop execution. An example of this desynchronisation mechanism is presented in Figure 5.5.

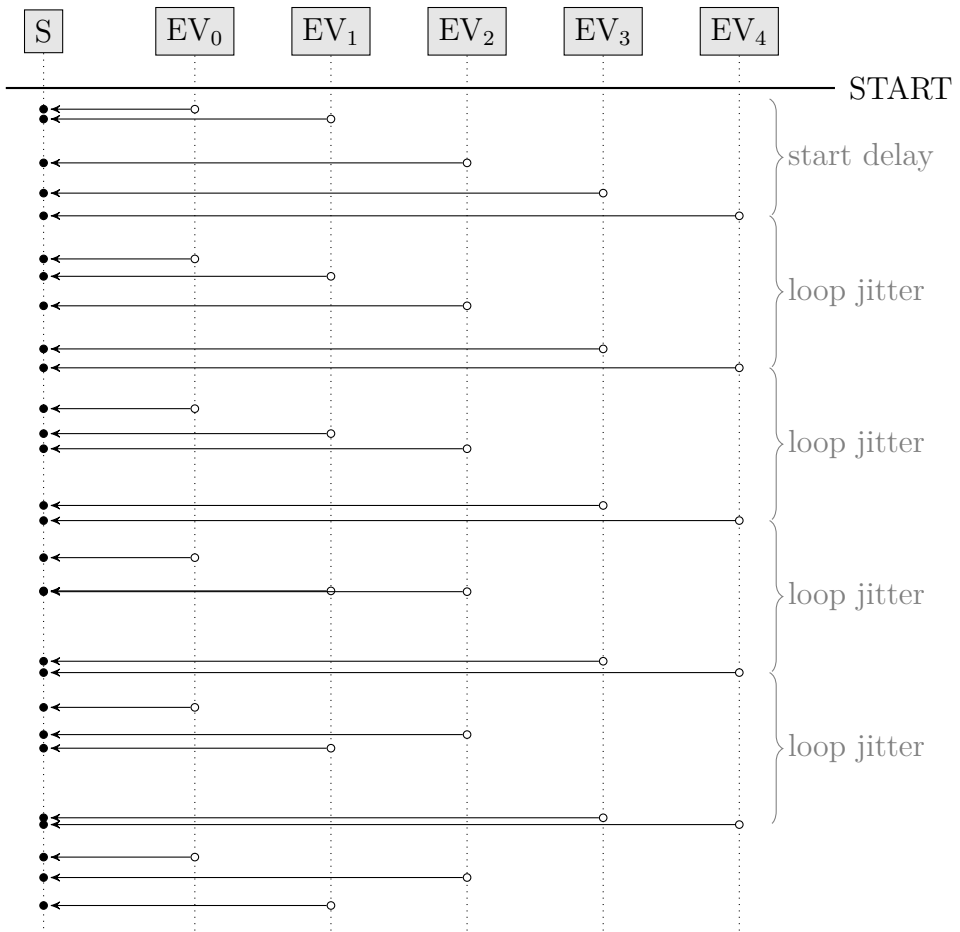


Figure 5.5: Example of agent desynchronisation when running through algorithm iterations in their respective execution loop. Here, communication events may be in quick succession, but are never at the exact same time.

From Figure 5.5, the successful desynchronisation can be observed since the supplier never receives more than one message at a time. Whilst the synchronised and desynchronised algorithm implementation do not differ in the scheduling method, their updating procedure does distinguish them. More specifically, for the synchronised implementation, the algorithm obtains the complete demand (i.e. Equ. 5.2) after all EVs have sent their updated charging profiles. The desynchronised implementation on the other hand receives intermittent updates of the network demand. To investigate the difference in performance a set of cases and performance metrics are defined in the following section, Section 5.3.3.

### 5.3.3 Cases and Performance Metrics

A set of load profiles is assessed with three different configurations:

1. Synchronised algorithm execution
2. Desynchronised algorithm execution with regular loop delays
3. Desynchronised algorithm execution with irregular loop delays

For each load profile, 10000 MASs are simulated to cover a high range of  $\alpha$  and  $\beta$  parameter pairs. In this context each simulation is seen as an individual case study. Therefore each case study executes up to 100 iterations after which the smart-charging algorithm terminates. Throughout the progress of executing the algorithm, every EV's charging profile is recorded for each iteration. Also, when the simulation terminates, the final aggregated charging profile is also recorded. Therefore, an information on the development of the total demand profile can be obtained for every single algorithm iteration. The performance of the algorithm is then determined by assessing the shape of the resulting demand profile by using the Peak-to-Average Ratio (PAR) and the Transient power metric (TRA).

Similar to the previous chapters, Chapter 3 and Chapter 4, the PAR and TRA values are used as performance metrics for the demand profile. There two metrics, respectively  $\zeta^{\text{PAR}}(\mathbf{p}_n^{\text{net}})$  and  $\zeta^{\text{TRA}}(\mathbf{p}_n^{\text{net}})$ , have already been defined in those preceding chapters. Here,  $\mathbf{p}_n^{\text{net}}$  denotes the total network demand, i.e.  $\mathbf{p}_n^{\text{net}} = \mathbf{p}^{\text{base}} + \sum_{u=1}^U \mathbf{p}_{u,n}^{\text{EV}}$ , for algorithm iteration  $n$ , and for convenience, the two parameter definitions are included in Equation 5.7 and Equation 5.8.

$$\zeta^{\text{PAR}}(\mathbf{p}_n^{\text{net}}) := \left( \frac{\max_t(\mathbf{p}_n^{\text{net}})}{\frac{1}{T} \sum_{t=0}^T p_n^{\text{net}}(t)} \right)^2 \text{ where } \mathbf{p}_n^{\text{net}} = (p_n^{\text{net}}(t)) \quad (5.7)$$

$$\zeta^{\text{TRA}}(\mathbf{p}_n^{\text{net}}) := \sqrt{\frac{1}{N-1} \sum_{n=1}^{N-1} (p_{n+1}^{\text{net}} - p_n^{\text{net}})^2} \text{ where } \mathbf{p}_n^{\text{net}} = (p_n^{\text{net}}(t)) \quad (5.8)$$

If the proposed scheduling algorithm successfully fills valleys and avoid adding new charging peaks, then the gap between mean and maximum demand reduces and  $\zeta^{\text{PAR}}$  in Equation 5.7 tends towards one. At this point, one might assume a perfectly flat demand profile. However, if the total charging power of all EVs constructively superimposes at the same time, and if this additional power does not increase the daily demand peak, then  $\zeta^{\text{PAR}}$  would still decrease despite the unwanted demand shape. Therefore, the change in power, i.e. the mean transient, is also taken into account in Equation 5.8 with  $\zeta^{\text{TRA}}$ . This value is only lowered when the change in power between consecutive time-steps is reduced and thus the profile becomes smooth.

When the scheduling algorithm was detailed in Section 5.2.3, convergence for the synchronised case was guaranteed since the algorithm follows the D'Alembert Criterion. This criterion holds if the ratio between the metrics for the current and previous algorithm outputs (i.e. from Algorithm 1) is less than one or; as long as these values are decreasing for every successive algorithm iteration. Formally, this criterion is satisfied when

$$\lim_{n \rightarrow \infty} \frac{|\zeta^{\text{PAR}}(\mathbf{p}_n^{\text{net}})|}{|\zeta^{\text{PAR}}(\mathbf{p}_{n-1}^{\text{net}})|} < 1 \text{ where } n \geq 2 \text{ and } \zeta^{\text{PAR}}(\mathbf{p}_n^{\text{net}}) \neq 0 \quad (5.9)$$

and

$$\lim_{n \rightarrow \infty} \frac{|\zeta^{\text{TRA}}(\mathbf{p}_n^{\text{net}})|}{|\zeta^{\text{TRA}}(\mathbf{p}_{n-1}^{\text{net}})|} < 1 \text{ where } n \geq 2 \text{ and } \zeta^{\text{TRA}}(\mathbf{p}_n^{\text{net}}) \neq 0 \quad (5.10)$$

These two convergence criteria in Equation 5.9 and Equation 5.10 are limited to values of  $\zeta^{\text{PAR}}$  and  $\zeta^{\text{TRA}}$  greater than zero. Whilst the ratio between maximum and mean can only reduce to a value of one,  $\zeta^{\text{PAR}}$  satisfies this criterium.  $\zeta^{\text{PAR}}$  on the other hand may reduce to a value of zero. To prevent this from happening, the number of EVs and their total demand are limited to a value that could not fully “fill” the network demand’s valleys and lead to a perfectly flat demand profile.

Although the chosen D’Alembert Criterion can be used to check whether the smart-charging algorithm converges, it cannot produce the rate of convergence. Similar to Laplace, the rate of convergence is determined by an exponential decay function. Since the underlying mathematical function is unknown, an estimated exponential is used instead. The estimate is obtained by fitting an exponential function to the series of  $\zeta^{\text{PAR}}$  and  $\zeta^{\text{TRA}}$  values over all iterations, and by using the following definition of a simple exponential function:

$$f_n(a, b) = ae^{-bn} \quad (5.11)$$

In Equation 5.7,  $a$  is the zero-crossing point of this function and  $b$  the rate of convergence. For the scope of this chapter,  $n$  is limited to  $n \geq 0$ . The size of  $b$  indicates how fast the values converged, which is why  $b$  is used as a convergence indicator. Values for  $a$  and  $b$  are found by reducing the error between the exponential function and the series of  $\zeta^{\text{PAR}}$  or  $\zeta^{\text{TRA}}$  values, i.e.:

$$\min_{a,b} \sum_{n=1}^N \left| (\zeta_{\text{PAR}}(\mathbf{p}_n) - \min(\zeta^{\text{PAR}}(\mathbf{p}))) - f(n, a, b) \right| \quad (5.12)$$

and

$$\min_{a,b} \sum_{n=1}^N \left| (\zeta_{\text{TRA}}(\mathbf{p}_n) - \min(\zeta^{\text{TRA}}(\mathbf{p}))) - f(n, a, b) \right| \quad (5.13)$$

It is however worth mentioning, that the condition is not satisfied when  $\alpha = 1$  and  $\beta = 1$ . In this case, an algorithm behaviour is expected where each EV's demand is oscillating between a set of profile troughs. A similar behaviour has already been observed by Karfopoulos et al. in [42], which is why the main part of the results in this chapter study values where  $\alpha$  and  $\beta$  are not one at the same time.

Results are split into three parts. In the first part, results are presented for the time-series evolution when using the algorithm in a synchronised MAS. Different  $\alpha$  and  $\beta$  values are used to explore and show the sensitivity of the algorithm. With this in mind the corresponding  $\zeta^{\text{PAR}}$  and  $\zeta^{\text{TRA}}$  values are presented to show their link to the underlying load profile's shape, and their convergence values, i.e.  $b$  is also presented. Finally, a complete set of final  $\zeta^{\text{PAR}}$  and  $\zeta^{\text{TRA}}$  values, as well as their convergence values,  $b$ , are plotted for the entire spectrum of  $\alpha$  and  $\beta$  pairs. This is to show the sensitivity of the algorithm for the complete range of  $\alpha$  and  $\beta$ . The second step is then to introduce algorithm desynchronisation, but with regular loop delays, and repeat the complete analysis to compare it with the results in the first part. In the third and last part, the algorithm desynchronisation is changed so that the algorithm's loop delays are irregular. All results are once again compared to the preceding two parts of the results by following the same analysis.

## 5.4 Results and Discussion

### 5.4.1 Algorithm performance for synchronised operation

The objective of the smart-charging algorithm is to distribute the charging demand of a fleet of EVs over the underlying base demand in such a way that no additional demand spikes are produced. After assigning each EV's energy demand to its initially known demand trough, the algorithm produces a new demand spike since all EVs are charging simultaneously. Through repetitive iterations and reallocating a portion of the assigned energy to different demand troughs, the algorithm is then able to spread all EVs' demands to form a flat demand profile in the end. This process is shown in Figure 5.6.

Here, the first algorithm iteration is shown in Figure 5.6a, where allocated power profile produces two new morning spikes of around 200kW and subsequently 110kW. The second iteration however reduces these spikes by the factor  $\alpha$  (i.e 0.2) and redistributes the undone charging powers over the new power profile. Figure 5.6b shows this reduction and reallocation. Figure 5.6c is the third iteration that reduces and redistributes the peaks even further. In the end, i.e. when  $n = N$ , the resulting power profile becomes as flat as possible, which is shown in Figure 5.6d. Throughout these iterations, it can be observed how the peak load in the total power, i.e.  $\mathbf{p}_n$ , reduces and it can be observed how the changes in charging power, i.e.  $\mathbf{p}_{n+1} - \mathbf{p}_n$ , reduce in variance, which indicates that the algorithm works for the chosen parameters of  $\alpha$  and  $\beta$ . However, different parameters of  $\alpha$  and  $\beta$  do impact the performance of this synchronised algorithm execution, as shown in Figure 5.7.

Whereas the  $\alpha$  and  $\beta$  parameters used to produce the results in Figure 5.6 reduced the power spike, those parameters in 5.7 did not, where  $\alpha = \beta = 1.0$ . In fact, an oscillating behaviour can be observed since the initially applied power profile is completely undone and completely reassigned onto a different demand trough. Since

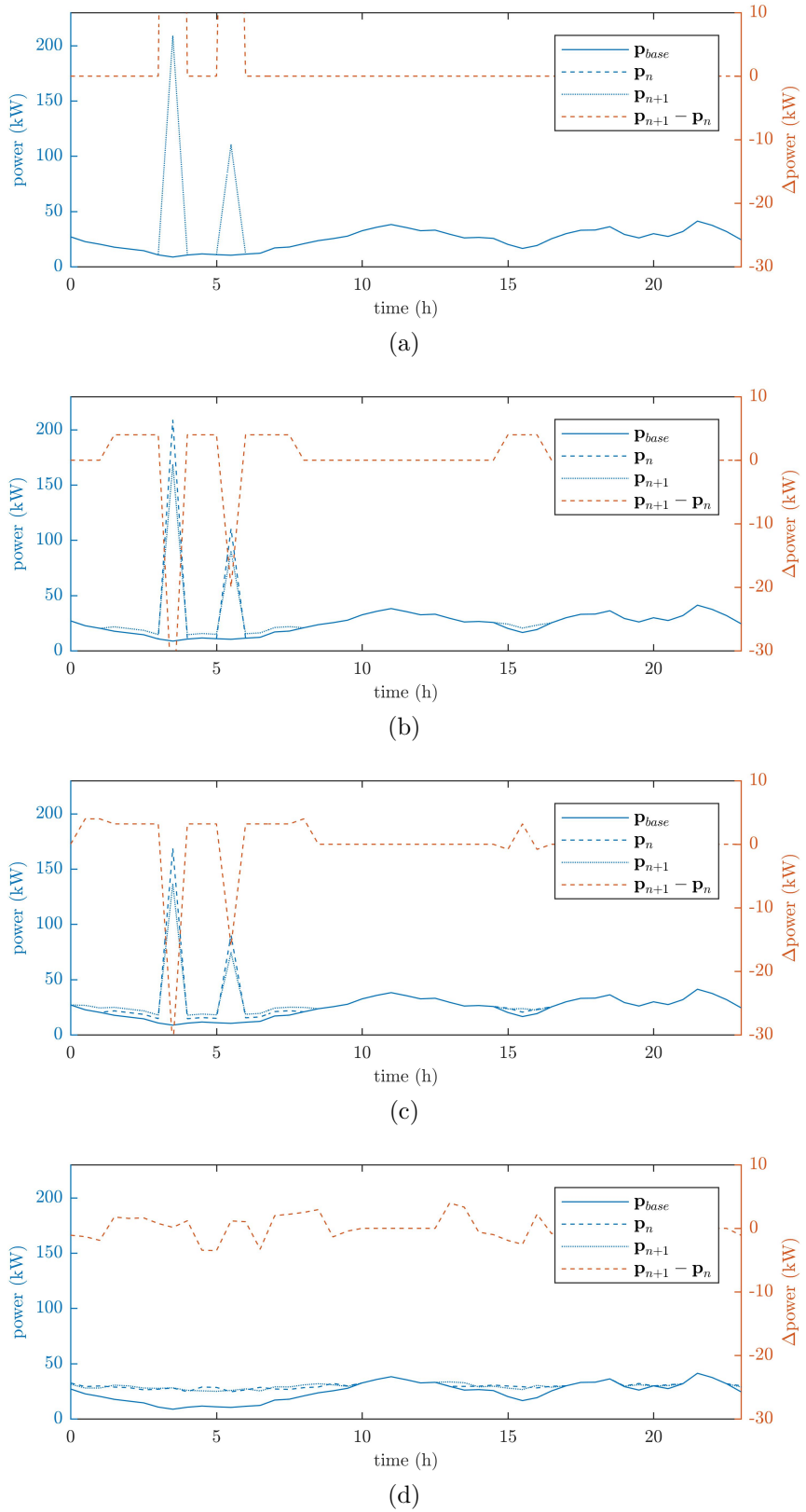


Figure 5.6: Synchronised time series evolution for  $\alpha = 0.02$  and  $\beta = 0.20$ , where (a) is at  $n = 1$ , (b) is at  $n = 2$ , (c) is at  $n = 3$ , and (d) is at  $n = N - 1$ .

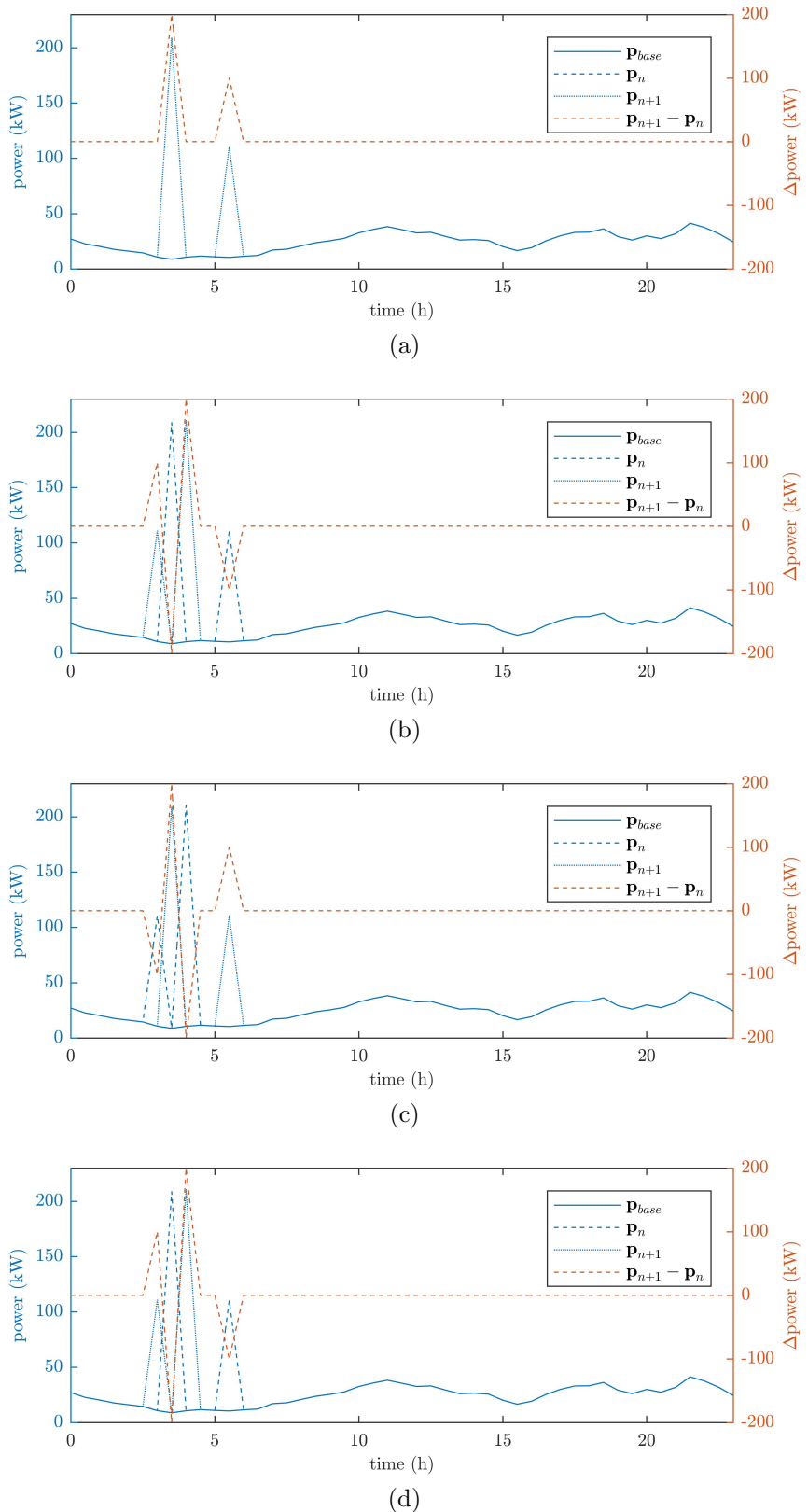


Figure 5.7: Synchronised time series evolution for  $\alpha = 1.00$  and  $\beta = 1.00$ , where (a) is at  $n = 1$ , (b) is at  $n = 2$ , (c) is at  $n = 3$ , and (d) is at  $n = N - 1$ .

iteration ( $n$ )	$\alpha = 0.02$ and $\beta = 0.20$		$\alpha = 1.00$ and $\beta = 1.00$	
	$\zeta_{\text{PAR}}$	$\zeta_{\text{TRA}}$	$\zeta_{\text{PAR}}$	$\zeta_{\text{TRA}}$
1	46.84	45.86	46.84	45.86
2	30.61	35.54	47.66	46.26
3	20.10	27.31	46.84	45.86
4	13.28	20.75	47.66	46.26
5	8.83	15.56	46.84	45.86
6	5.93	11.41	47.66	46.26
7	4.02	8.20	46.84	45.86
8	2.76	5.83	47.66	46.26
9	1.92	4.24	46.84	45.86
10	1.83	3.22	47.66	46.26
:	:	:	:	:
100	1.83	2.72	47.66	46.26
convergence ( $b$ )	0.47	0.32	0.00	0.00

Table 5.1: Comparison of  $\zeta^{\text{PAR}}$  and  $\zeta^{\text{TRA}}$  for two  $\alpha$  and  $\beta$  parameter pairs. Each value per iteration  $n$  and the convergence  $b$  is shown.

this produces similar peaks, the same procedure repeats and reassigns the complete power profile back to the original demand troughs. In the end, these charging spikes could never be fully mitigated and the algorithm did not smoothen the total demand. The resulting charging spike of more than 200kW could therefore cause significant issues if e.g. the underlying physical network was not been scaled appropriately. This longevity of issue becomes more evident when comparing the  $\zeta^{\text{PAR}}$  and  $\zeta^{\text{TRA}}$  values for both parameter pairs. The evolution of  $\zeta^{\text{PAR}}$  and  $\zeta^{\text{TRA}}$ , as tabulated in Table 5.1, shows this difference in performance and convergence of the algorithm when subjected to different values of  $\alpha$  and  $\beta$ . Therefore, multiple parameter pairs across the entire range of  $\alpha$  and  $\beta$  are studied to determine how the algorithm performs for each given pair. The results for the synchronised algorithm performance are plotted in Figure 5.8.

Figure 5.8a and Figure 5.8c show how the final values for both  $\zeta^{\text{PAR}}$  and  $\zeta^{\text{TRA}}$  were lowest when either  $\alpha$  or  $\beta$  was chosen closer to zero. This result coincides with the finding that hard reduction and reallocation lead to an oscillating behaviour of

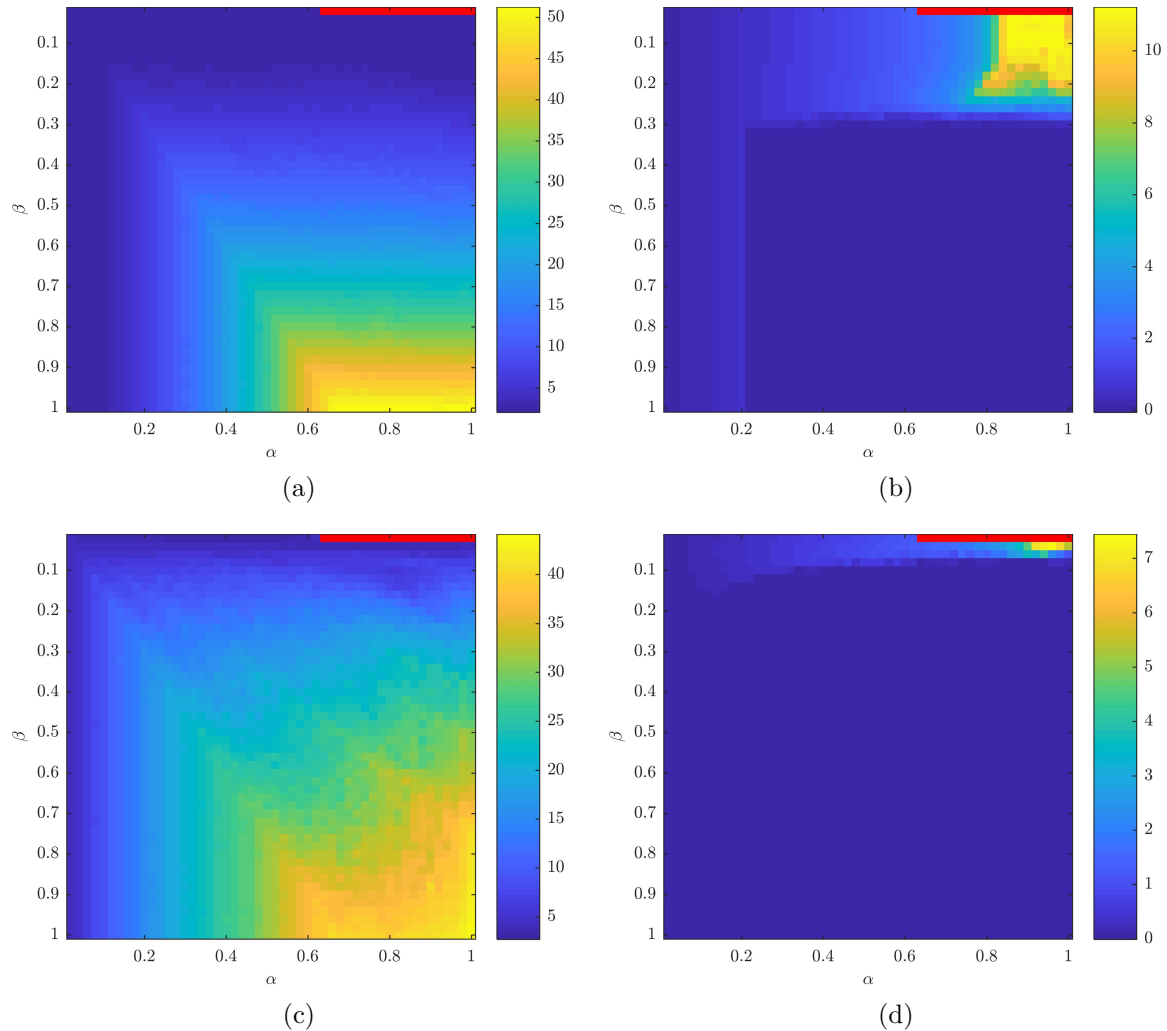


Figure 5.8: Full range analysis of  $\alpha$  and  $\beta$  for the synchronised MAS where, (a) shows the final  $\zeta_{\text{PAR}}$ , (b) shows the convergence,  $b$ , for  $\zeta_{\text{PAR}}$ , (c) shows the final  $\zeta_{\text{TRA}}$ , and (d) shows the convergence,  $b$ , for  $\zeta_{\text{TRA}}$  (red indicates missing data).

the algorithm. Similarly, the convergence of those two performance metrics, as shown in Figure 5.8b and Figure 5.8d, was best when  $\alpha$  approached one and  $\beta$  approached zero. This behaviour is by design, since a larger value of  $\alpha$  increases the rate at which the currently applied peak is reduced, whilst a smaller value of  $\beta$  limits the amount that can be reallocated for each time slot. Such clear behavioural differences for different pairs of  $\alpha$  and  $\beta$  indicate an optimal operation region of the algorithm within the north-east quadrant of the plot. Whether the algorithm still performs in this way when introducing desynchronisation is answered in the subsequent section, Section 5.4.2.

### **5.4.2 Algorithm performance for desynchronised operation with regular timing**

Looking at the evolution of the time-series when desynchronising the algorithm's execution shows significant differences already. Figure 5.9 shows this evolution for the same parameters as those chosen for Figure 5.6. The difference is however, that the assignment of charging powers lead to a significantly lower demand spike at the very beginning of executing the algorithm. Subsequent iterations then reduce this spike much broader than it has been the case when executing the algorithm in a synchronised manner. Therefore, more demand troughs are filled and a smoother profile is obtained much quicker, when compared to the synchronised case.

This behaviour becomes particularly apparent when looking at the full range of  $\alpha$  and  $\beta$  values. Figure 5.10 shows the same full range analysis as the figure in the previous section did, i.e. Figure 5.8. When comparing them at the same scale,  $\zeta^{\text{PAR}}$  and  $\zeta^{\text{TRA}}$  values (plotted in Figure 5.10a and Figure 5.10c, respectively) have significantly lowered in magnitude. This indicates a much better performance of the algorithm across the entire range of  $\alpha$  and  $\beta$  parameters. Convergence rates (plotted in Figure 5.10b and Figure 5.10d, respectively) were however not impacted to the same

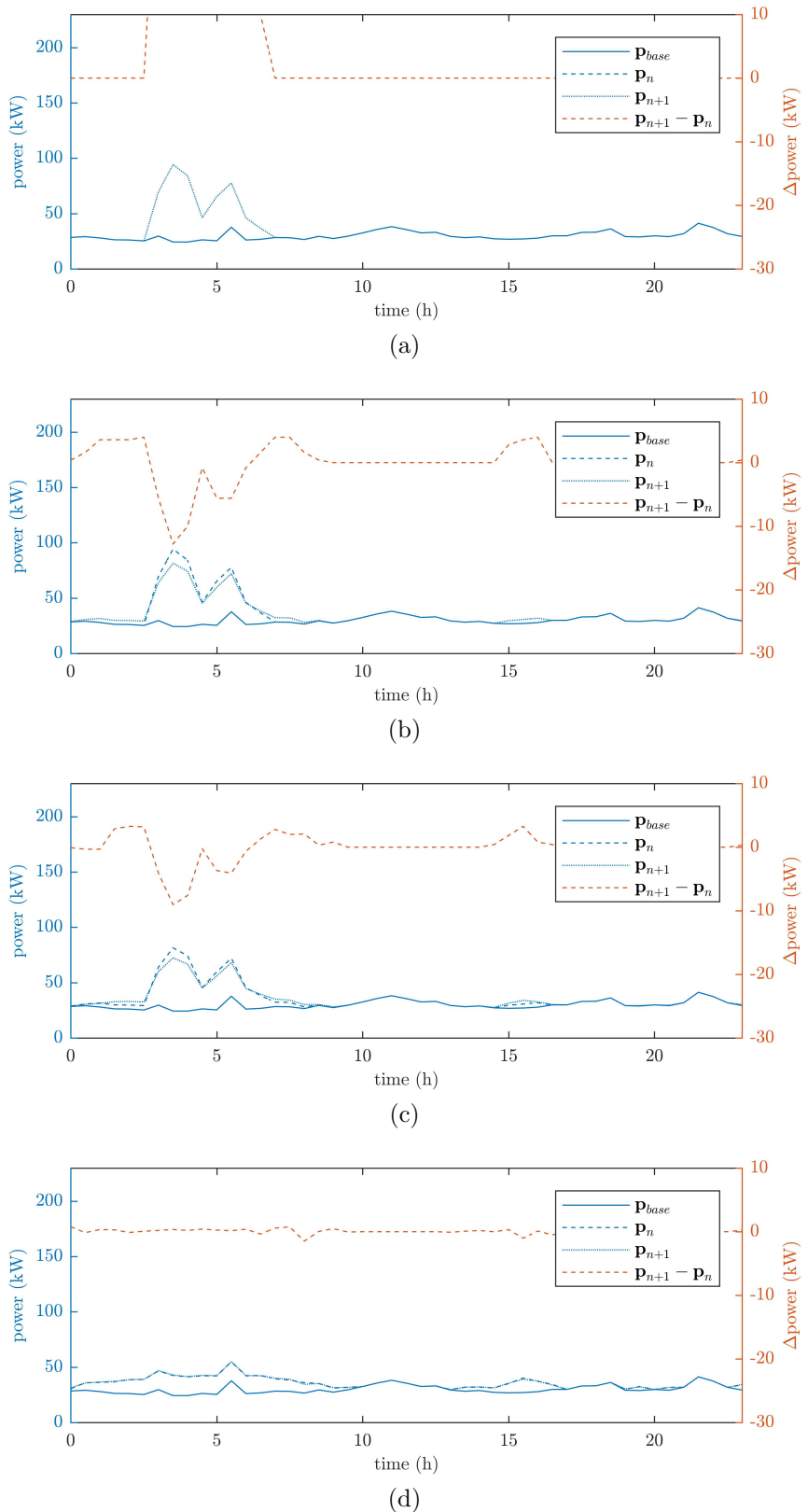


Figure 5.9: Desynchronised time series evolution for  $\alpha = 0.02$  and  $\beta = 0.20$ , where (a) is at  $n = 1$ , (b) is at  $n = 2$ , (c) is at  $n = 3$ , and (d) is at  $n = N - 1$ .

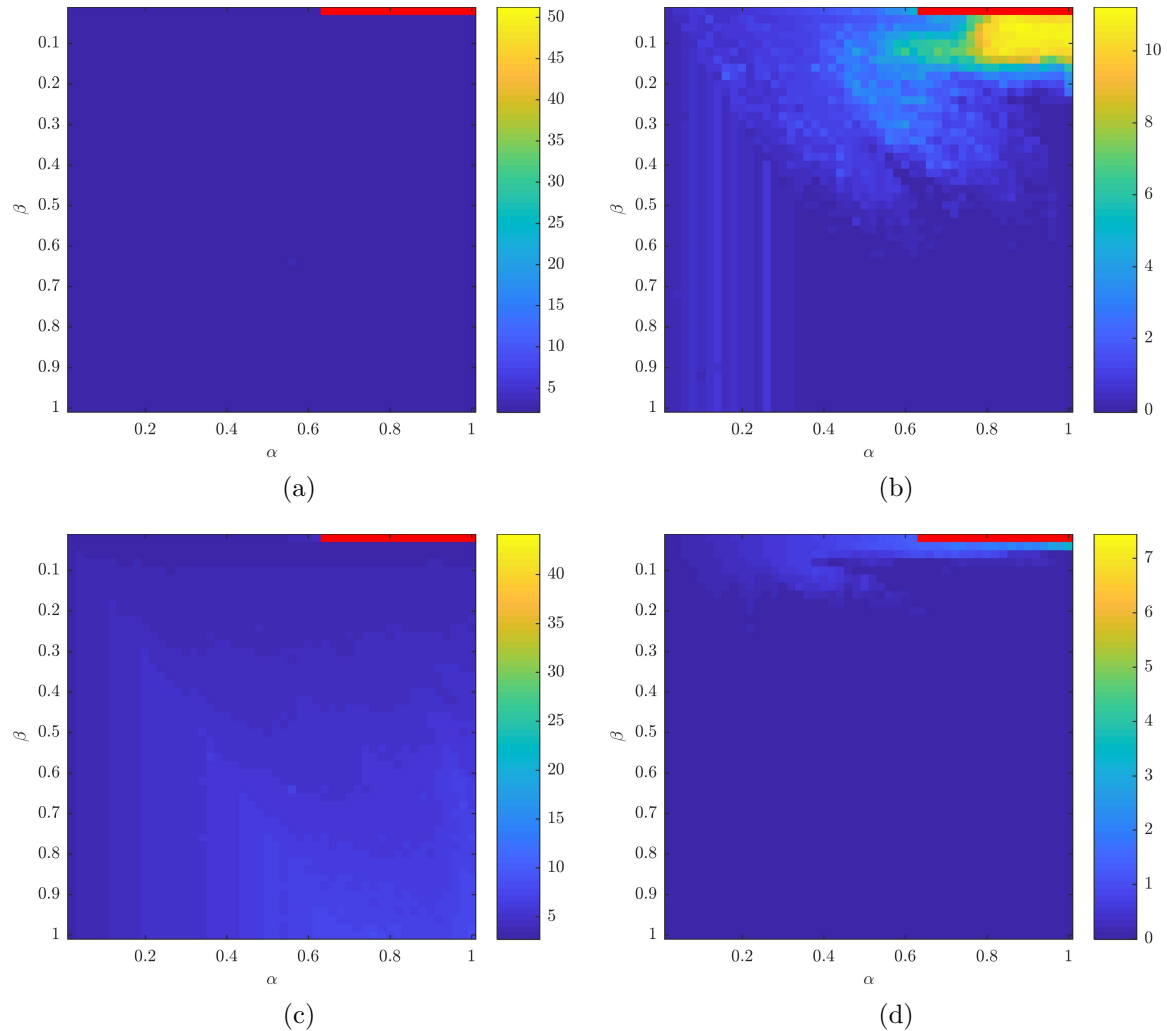


Figure 5.10: Full range analysis of  $\alpha$  and  $\beta$  for the desynchronised MAS where, (a) shows the final  $\zeta^{\text{PAR}}$ , (b) shows the convergence,  $b$ , for  $\zeta^{\text{PAR}}$ , (c) shows the final  $\zeta^{\text{TRA}}$ , and (d) shows the convergence,  $b$ , for  $\zeta^{\text{TRA}}$  (red indicates missing data).

extend. This indicates that the underlying execution of the algorithm still performs as intended, but the interplay between the agents that implement this algorithm changes the outcome of the aggregated result. The next step is to assess whether desynchronising the algorithm’s execution by randomising the loop delays yields any further changes in algorithm performance and behaviour. Results from that step are presented in the following section, Section 5.4.3.

### 5.4.3 Algorithm performance for desynchronised operation with irregular timing

As shown in Figure 5.11, the difference between regular and irregular loop delays when executing the smart-charging algorithm is barely noticeable. The interlaced querying still causes each agent to react to a slightly different network demand profile, which results in a varied power profile allocation. A functioning peak reduction behaviour is therefore a positive sign, since this irregular algorithm desynchronisation, as introduced in Section 5.3.2, represents the worst algorithm deployment scenario. Performance and convergence do however need to be inspected for the complete range of  $\alpha$  and  $\beta$  values.

Figure 5.12 shows the results for this range of  $\alpha$  and  $\beta$  valued, when executing the algorithm on a desynchronised MAS with irregular loop delays. The values for  $\zeta^{\text{PAR}}$  and  $\zeta^{\text{TRA}}$  are still significantly lower than they were for the synchronised case, and do not differ much from the regular desynchronisation case. The same is true when comparing convergence, which indicates that the algorithm’s underlying execution still performs as intended.

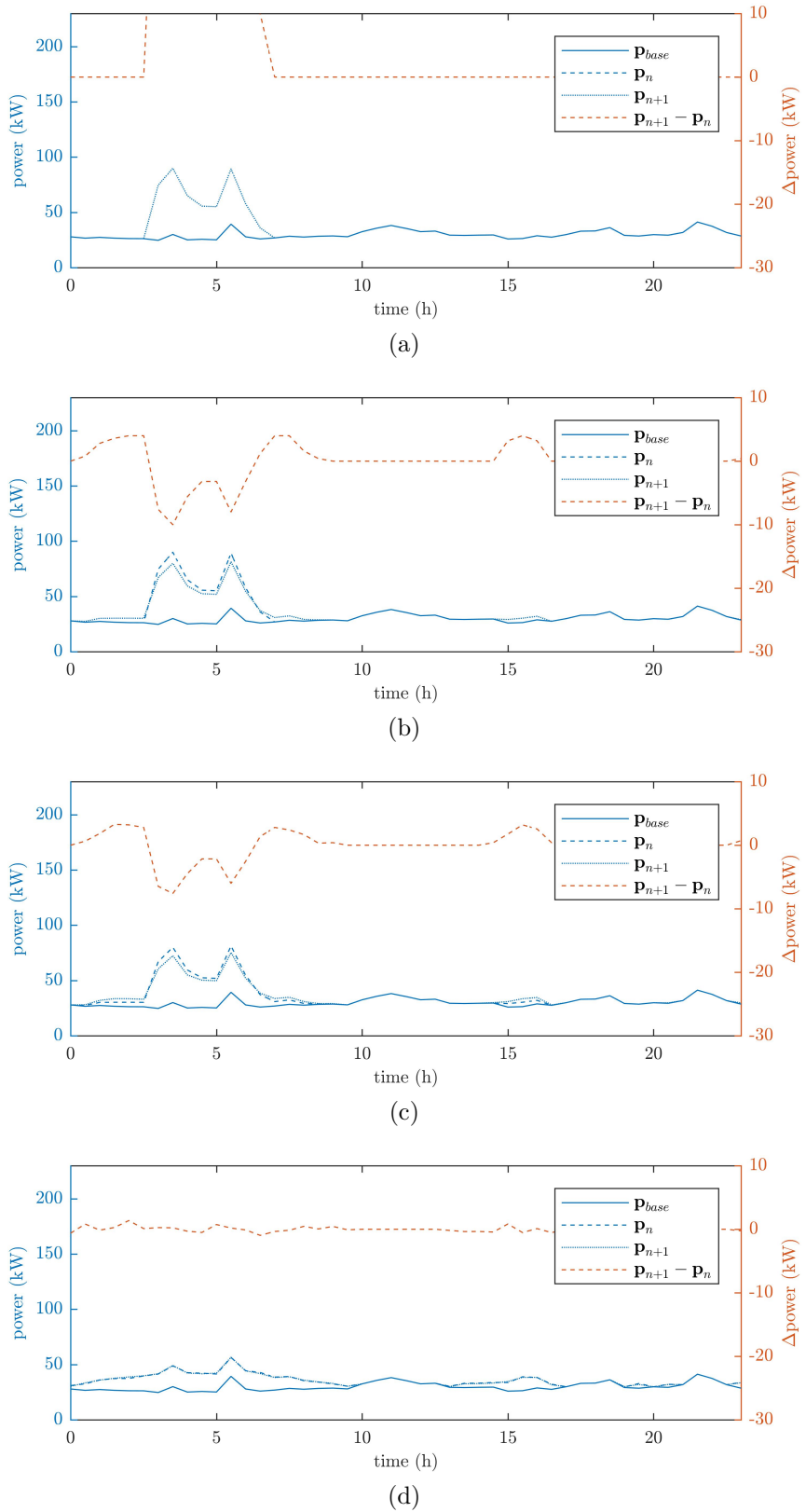


Figure 5.11: Desynchronised time series evolution when using irregular loop delays for  $\alpha = 0.02$  and  $\beta = 0.20$ , where (a) is at  $n = 1$ , (b) is at  $n = 2$ , (c) is at  $n = 3$ , and (d) is at  $n = N - 1$ .

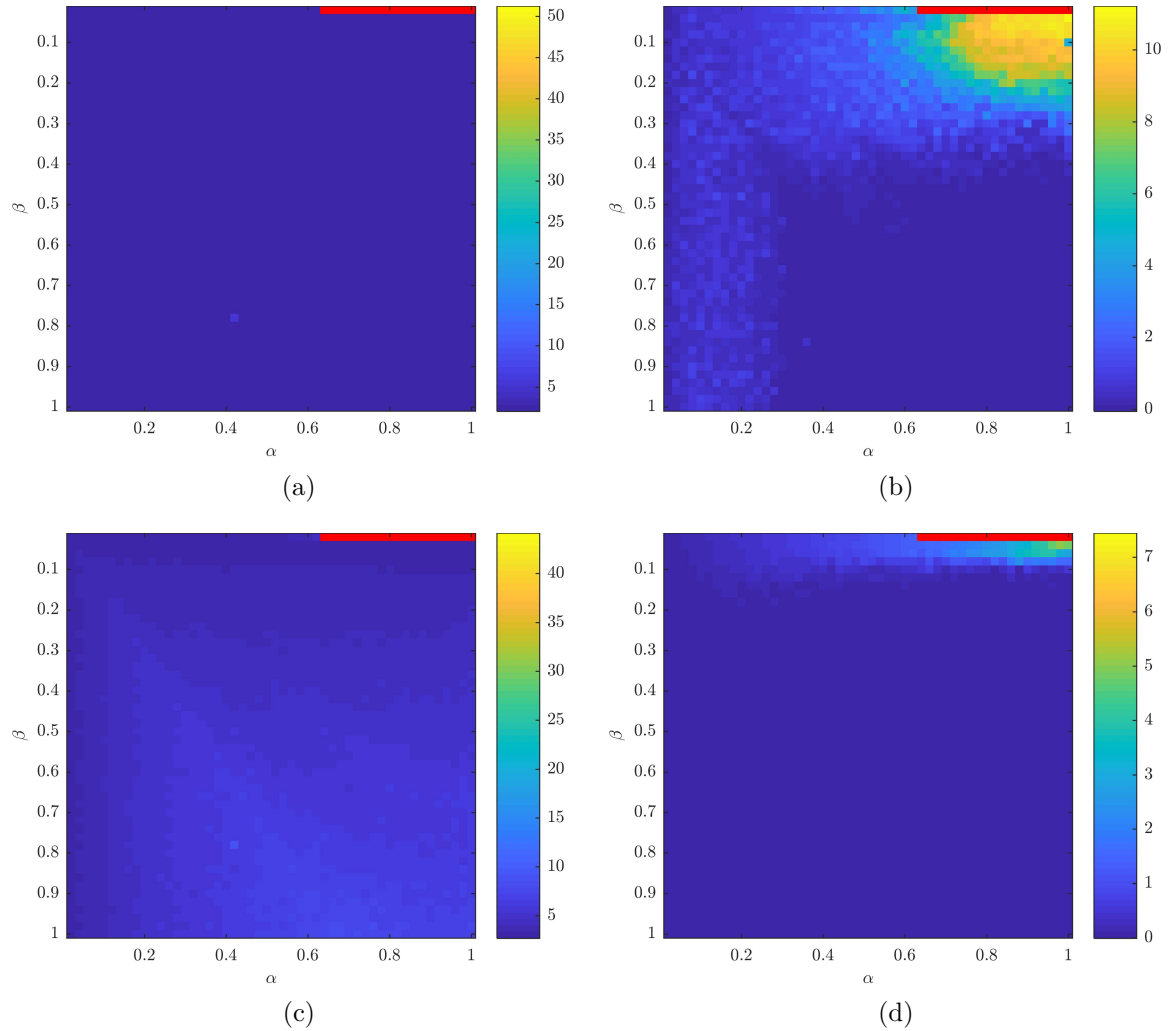


Figure 5.12: Full range analysis of  $\alpha$  and  $\beta$  for the desynchronised MAS with irregular loop delays where, (a) shows the final  $\zeta^{\text{PAR}}$ , (b) shows the convergence,  $b$ , for  $\zeta^{\text{PAR}}$ , (c) shows the final  $\zeta^{\text{TRA}}$ , and (d) shows the convergence,  $b$ , for  $\zeta^{\text{TRA}}$  (red indicates missing data).

## 5.5 Summary

When designing a smart-charging algorithm to distribute the EV load over the entire day and thus avoid new demand spikes, coordination between EVs is usually achieved by the means of ICT. In this chapter, Chapter 5, such an algorithm was developed to assure that the coordinated charging of an EV fleet does not add a new demand spike onto the base power profile. This algorithm was then deployed on a MAS and controlled using two parameters, i.e.  $\alpha$  and  $\beta$ , that allowed each agent to, respectively, undo and reassign an amount of its charging profile. By repeating this behaviour of undoing and reassigning fractions of the charging profile, agents were able to respond to each other and avoid simultaneous charging. Two performance metrics, i.e.  $\zeta^{\text{PAR}}$  and  $\zeta^{\text{TRA}}$ , indicated, respectively, the spikiness and volatility of the final power profile. Reducing these metrics is therefore the key function of the smart-charging algorithm, despite the algorithm not being metric dependent.

Originally however, the presented smart-charging algorithm was designed for synchronised MAS execution, which means that all agents obtain a network update and update their charging profile at exactly the same time. By desynchronising the agent communication, the output's parameter dependence significantly changed when compared to the synchronised execution of the algorithm. In fact regular and irregular desynchronisation yielded much lower values for  $\zeta^{\text{PAR}}$  and  $\zeta^{\text{TRA}}$ , as seen in Section 5.4.2 and Section 5.4.3. Convergence towards the final values on the other hand, did remain similar to the synchronised algorithm execution despite the difference in MAS execution. Therefore, the algorithm's valley-filling behaviour was still upheld, yet the interplay between agents that implement this algorithm significantly changed the outcome of the aggregated result. This work thus completes **Objective 3** of this thesis, which was outlined in Section 1.2, since it shows the capabilities of a smart-charging algorithm and highlights the importance of considering agent de/synchronisation when developing a multi-controller DSM network. Such

findings are especially relevant due to the inherent difficulty and cost associated with the synchronisation of a distributed control system. More specifically, synchronisation becomes particularly difficult when the network size and number of controllers increases. With lightweight algorithms like the one proposed in this chapter, Chapter 5, synchronisation can be neglected without sacrificing algorithm performance. Nonetheless, this finding is true for any smart algorithm, as long as the algorithm is studied in both a synchronised and desynchronised test environment; which is however done very seldom. This inherent difficulty of designing and implementing any smart algorithm with ICT, would thus raise the question if it is possible to design a cooperative algorithm that does not rely on ICT. The subsequent chapter, Chapter 6, intends to answer this question.



# Chapter 6

## Cooperative Battery Operation of without Communications Infrastructure Needs

*M. J. Zangs, P. Adams, et al., “Distributed Energy Storage Control for Dynamic Load Impact Mitigation,” Energies, vol. 9, no. 8, p. 647, August 2016*

— Available: <https://dx.doi.org/10.3390/en9080647>

*T. Yunusov, M. J. Zangs, et al., “Control of Energy Storage,” Energies, vol. 7, no 10, p. 1010, July 2017*

— Available: <https://doi.org/10.3390/en10071010>

### 6.1 Overview

In the past three chapters of this thesis, on-line control methods have been developed to optimally control power injection into the LV network, and to shave or prevent load peaks. Chapter 3 and Chapter 4 showed how such an on-line control can be tuned to maximise BESS impact on a three-phase LV network, and how it can also minimise both daily (i.e. half-hourly) and intermittent (i.e. sub-half-hourly) demand peaks.

In Chapter 5, a smart-charging algorithm was developed to mitigate charging peaks from an EV fleet. By analysing the communications requirements of the algorithm, it was executed in different MAS environments, where its distributed control was run in both a synchronised and desynchronise system. It was found that control methods that rely on such information exchange also rely on a stable ICT infrastructure, otherwise the global performance significantly deviates from the algorithm's expected smart-charging behaviour. To continue contributing towards the aim of this thesis, in this chapter, Chapter 6, the impact of charging an EV fleet is mitigated in a different, communication-less approach. More specifically, this chapter addresses **Objective 4** of this thesis (which is outlined in Section 1.2), and proposes an individually tuned control algorithm for multiple household connected BESSs in order to mitigate the impact from charging EVs. As already discussed in the literature review, in Chapter 2, although the adoption of EVs is often seen as the potential solution to decarbonise future transport networks, conventional charging, i.e. "dumb-charging", is expected to dominate the domestic charging demand [179]. This kind of charging behaviour is expected to put the most significant burden on the power distribution network, and this burden is aimed to be mitigated by the distributed BESS control that is proposed in this chapter, Chapter 6. More specifically, the proposed algorithm uses an individualised Set-Point Control (SPC) to regulate bi-directional battery power flow and, for stability, is built upon the traditional Additive-Increase Multiplicative-Decrease (AIMD) algorithm [187]. As a result, the developed battery control method reduces voltage deviation, it reduces over-currents and it reduces the otherwise uneven usage of deployed batteries. Reducing this uneven battery usage leads to a more homogeneous operation of all of the distributed BESSs and e.g. prevents unequal degradation rates and potentially unfair device utilisation.

The remainder of Chapter 6 is organised as follows: Section 6.2 gives some background to related work on AIMD algorithms on which this research is based. Sec-

tion 6.3 outlines the EV, network and storage models used in this research. Additionally, it explains the assumptions that accommodate and justify these models. Section 6.4 elaborates on the proposed AIMD control algorithm (AIMD+). Next, Section 6.5 details the implementation and scenarios used for a set of test cases. For later comparison, this section also outlines a set of comparison metrics. Section 6.6 presents and discusses the results, followed by a chapter summary in Section 6.7.

## 6.2 Related Work

The main body of existing literature on communication-less control has already been covered in Section 2.4.3. Within this literature the main usage of BESS in LV distribution networks is to assure voltage security and was addressed in [35, 106, 150, 151, 154]. However, as also identified by Hatziargyriou et al. in [130], the underlying requirement for a communication infrastructure to relay network information and control instructions still remains. Therefore, in the presented chapter, a control algorithm is proposed that removes the need for any such BESS communication, by only using local voltage measurements and individually tuned control to infer the network operation. In order to prevent conflicting device behaviour, the underlying coordination mechanism is of particular importance. The AIMD algorithm is perfectly suited for such coordinated control, although it originated from a different research area. In this section, Section 6.2, the origin and current usage of AIMD are explained to emphasise the algorithm's suitability and room for improvements.

Originally, AIMD algorithms were applied to congestion management in communications networks using the TCP protocol [187], to maximise utilisation while ensuring a fair allocation of data throughput amongst a number of competing users [188]. Later, AIMD-type algorithms have also been applied to power sharing scenarios in LV distribution networks, where the limited resource is the availability of power from

the substation’s transformer. For EV charging, one such an algorithm was initially proposed by Stüdli et al. in [189], yet this algorithm still required a one-way communications infrastructure to broadcast a “capacity event” [190, 191]. Later, their work was extended to include vehicle-to-grid applications with reactive power support [192], yet the ICT requirements were still not addressed. The battery control algorithm proposed in this chapter builds upon the algorithm used by Mareels et al. [209], where EV charging was organised by including bidirectional power flow and the use of a reference voltage profile derived from network models. Similar to the work by Xia et al. [210], who utilised local voltage measurements to adjust the charging rate, the work presented in this chapter only uses voltage measurements at the batteries’ connection sites in order to control the batteries’ operations.

By developing the bi-directional and individually tuned BESS AIMD control algorithm, previous research is extended since it has only utilised common set-point thresholds for controlling each of the DERs. The approach proposed in this chapter ensures that unavoidable voltage drops along the feeder do not skew the global control decisions, and that voltage oscillations caused by demand variation are taken into control considerations. In contrast to previous work, where substation monitoring was used to inform control units of the transformer’s present operational capacity, the proposed algorithm does not require this information and does not require such any extensive ICT infrastructure.

### 6.3 System Modelling

In this section, Section 6.3, the underlying assumptions to validate the research are presented. Then, the EV charging model and a BESS model are explained. In the end of this section, the network models that are used to simulate the power distribution networks are presented.

### 6.3.1 Assumptions

For this work, several underlying assumption were made to obtain the models:

1. The uptake of EVs is assumed to increase and, hence, to have a significant impact on the normal operation of the low voltage distribution network. This assumption is based on a well-established prediction that the majority of EV charging will take place at home [211].
2. The transition from internal combustion engine-powered vehicles to EVs is assumed to not impact the users' driving behaviour, apart from the introduction of home-charging. Similar to [212], this assumption allows the utilisation of recent vehicle mobility data [213] to generate leaving, driving and arriving probabilities, from which the EV charging demand can be determined and the resulting energy demand can be determined.
3. The transition to low carbon technologies will increase the variability of electricity demand, and therefore, grid-supporting devices, such as BESS, are anticipated to play a more important role [214]. Hence, alongside a high uptake of EVs, an increased adoption of distributed BESS devices is assumed.
4. It is assumed that BESS solutions, or more specifically battery energy storage solutions, start the simulations at 50% SOC and are not 100% efficient at storing and releasing electrical energy, as in [91]. Additionally, its utilisation will degrade the energy storage capability and performance over time, as shown in [215]. Therefore, the requirements for equal and fair storage usage is of high importance.
5. It is assumed that the load profiles provided by the IEEE Power and Energy Society (PES) are sufficient as base load profiles for all simulations.

### 6.3.2 EV charging behaviour

From publicly-available car mobility data in [212, 213] an empirical model was developed to capture the underlying driving behaviour. This data contained three parts: the probability of starting a trip,  $n_s(t)$ , the probability of a weekday trip being of a certain distance,  $w_{wd}(t)$ , and the probability of a weekend trip being of a certain distance,  $w_{we}(t)$ . Both probabilities are at a 15-min period. The probability of starting a trip,  $n_s(t)$ , is approximated by three continuous normal distribution functions since it is assumed that driver behaviour is distributed normally around key times. Each distribution is based on the subsequent equation:

$$\hat{n}_x(t) := \beta_x \frac{1}{\sigma_x \sqrt{2\pi}} \exp \left[ -\frac{(t/24 - \mu_x)^2}{2\sigma_x^2} \right] \text{ where } t \in [0, 24] \quad (6.1)$$

From Equation 6.1, a probability distribution is denoted  $\hat{n}_m(t)$  represent the probability of a vehicle leaving in the morning,  $\hat{n}_l(t)$  represents the probability of it leaving during lunch time, and  $\hat{n}_e(t)$  represents the probability of it leaving during the evening. It is assumed that vehicles perform a round trip from their home to a certain location and back. In order to represent this symmetric commuting behaviour, i.e. vehicles departing in the morning return during the evening, an equality amongst the three probabilities was defined as follows:

$$0 = \int_0^{24} \hat{n}_m(t) + \hat{n}_l(t) - \hat{n}_e(t) dt \quad (6.2)$$

To approximate the original probability of starting a trip, the difference between these three probability functions' aggregate and the original distribution,  $n_s(t)$ , needed to be minimised. This minimisation problem is defined as follows:

$$\begin{aligned}
& \min_{\mu, \sigma, \beta} \int_0^{24} (\hat{n}_m(t) + \hat{n}_l(t) + \hat{n}_e(t) - n_s(t))^2 dt \\
& \text{s.t. } \begin{cases} 0 = \int_0^{24} \hat{n}_m(t) + \hat{n}_l(t) - \hat{n}_e(t) dt \\ 1 = \int_0^{24} \hat{n}_m(t) dt = \int_0^{24} \hat{n}_l(t) dt = \int_0^{24} \hat{n}_e(t) dt \end{cases} \quad (6.3)
\end{aligned}$$

This minimisation problem was solved using a Generalised Reduced Gradient (GRG) algorithm, and the obtained parameters fit the three functions to the original data. The resulting parameters from the GRG fitting of the three distribution functions are tabulated in Table 6.1. Additionally, the resulting departure probabilities, as well as the original data,  $n_s(t)$ , are shown in Figure 6.1.

Equation $\hat{n}_x(t)$	$\mu_x$ (Mean)	$\sigma_x$ (SD)	$\beta_x$ (Weight)
$\hat{n}_m(t)$	0.3049	0.0488	0.00206
$\hat{n}_l(t)$	0.4666	0.0829	0.00314
$\hat{n}_e(t)$	0.7042	0.0970	0.00521

Table 6.1: Parameters for normal distributions.

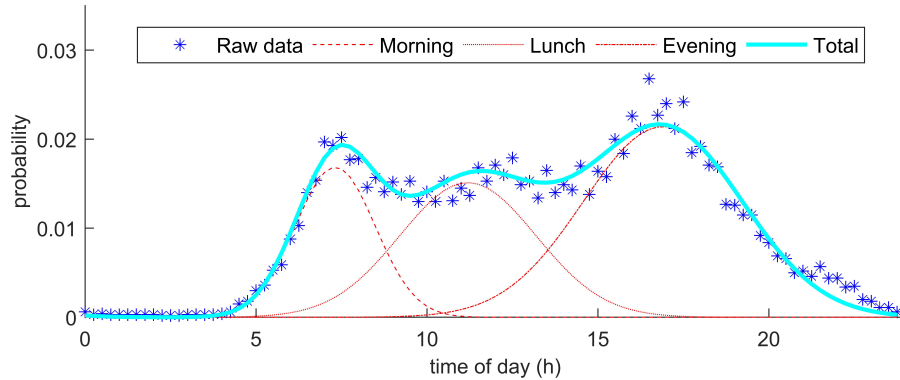


Figure 6.1: The probability of starting a trip at a particular time during a weekday, extrapolated into three normal distributions (RMS error: 9.482%).

The second statistical data, i.e. the data capturing the probability distribution of a trip being of a certain distance, was also extracted from the dataset and approximated. This was done for both the weekdays  $w_{wd}(d)$  and weekends  $w_{we}(d)$ . The Weibull

function was chosen to fit these probability distributions to the original data since it best suited the underlying data distribution, and it is defined as follows:

$$\hat{w}_x(d) := \begin{cases} \frac{k_x}{\gamma_x} \left(\frac{d}{\gamma_x}\right)^{k_x-1} \exp\left[-\left(\frac{d}{\gamma_x}\right)^{k_x}\right] & \text{if } d \geq 0 \\ 0 & \text{if } d < 0 \end{cases} \quad (6.4)$$

Similar to the approximation of the probability of starting a trip, a minimisation problem was designed to fit the two probability distributions to their original data.

$$\begin{aligned} & \min_{\gamma, k} \int (\hat{w}_x(d) - w_x(d))^2 dd \\ & \text{s.t.} 1 = \int \hat{w}_x(d) dd \end{aligned} \quad (6.5)$$

This problem was also solved using the same GRG algorithm. As a result, the weekday trip distance distribution,  $\hat{w}_{wd}(d)$ , and the weekend trip distribution,  $\hat{w}_{we}(d)$ , could be estimated. The computed function parameters for these two estimated distribution functions are tabulated in Table 6.2. Their resulting probability distributions are plotted for comparison against the real data,  $w_{wd}(d)$  and  $w_{we}(d)$ , in Figure 6.2.

Equation $\hat{w}_x(d)$	$\gamma_x$ (Scale)	$k_x$ (Shape)
$\hat{w}_{wd}(t)$	15.462	0.6182
$\hat{w}_{we}(t)$	38.406	0.4653

Table 6.2: Parameters for Weibull distributions.

In addition to these probabilities, an average driving speed of 56 kmh (35 mph) and an average driving energy efficiency of 0.1305 kWh/kmh (0.21 kWh/mph) are taken from [216]. Using the predicted driving distance and average driving speed with the driving energy efficiency, it is possible to estimate an EV's energy demand upon arrival. Starting to charge from this arrival time until the energy demand has been met allows the generation of an estimated charging profile of a single EV. To do

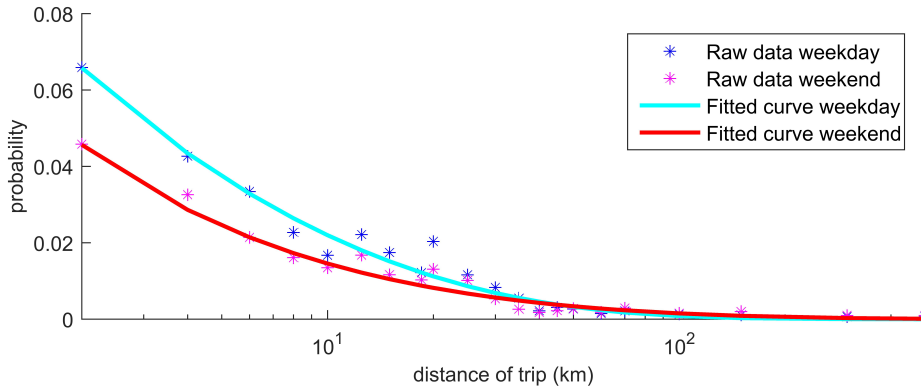


Figure 6.2: The probability of a trip being of a particular distance during a weekday, extrapolated into a Weibull distribution (RMS error: 3.791%).

this, a maximum charging power of the U.K.'s average household circuit rating (i.e., 7.4 kW) and an immediate disconnection of the EV upon charge completion were assumed [217].

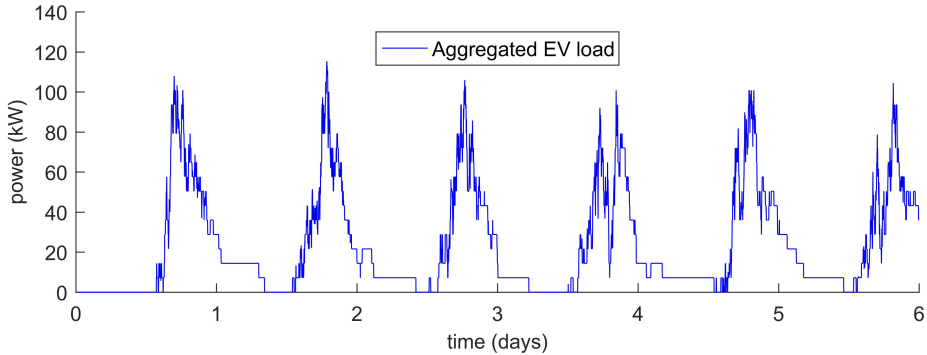


Figure 6.3: Excerpt from the aggregated 50 EVs; charging powers that were each generated from the empirical models.

Generating several of those charging profiles and aggregating them produces an estimated charging demand for an entire fleet of EVs. To provide an example, charge demand profiles for 50 EVs were generated, aggregated and plotted in Figure 6.3. This plot shows the expected magnitude and variability in energy demand that is required to charge several EVs at consumers' homes based on the vehicles' daily usage.

This model's EV charging behaviour has been implemented to reflect EV demand if applied today without widespread smart charging infrastructure. It does therefore reflect the worst assumable charging scenario. This model's data is used to simulate

additional demand in the power network, which are detailed in the next section.

### 6.3.3 Battery Modelling

In this chapter a similar BESS model is used as the one that has already been introduced in Chapter 3 and in Chapter 4 of this thesis (i.e. see Section 3.3.3 and Section 4.2.1). The following paragraphs are however used as a reminder of this model for convenience. This battery model consists of a self-discharge loss,  $\mu$  where  $\mu \in (0, 1]$ , that is dependent on the current State Of Charge (SOC) and an energy conversion efficiency,  $\eta$  where  $\eta \in (0, 1]$ , to compute the amount of energy that is lost when charging or discharging this battery.

When an ideal battery charges or discharges, the change in SOC is determined by the battery power,  $p_{\text{bat}}(t)$ . By sampling battery operation at a regular period,  $\Delta t$ , the energy transferred into the battery can be described as  $p_{\text{bat}}(t)\Delta t$ . The change in SOC for this ideal battery is therefore defined as:

$$\Delta \text{SOC}(t) := \frac{p_{\text{bat}}(t)\Delta t}{C} = \text{SOC}(t) - \text{SOC}(t - \Delta t) \quad (6.6)$$

The self-discharge loss is determined by  $\mu$  and is included in this ideal battery model to represent the continual loss of energy in the battery, which is typical for chemical energy storage. This loss,  $\Delta \text{SOC}_{\text{self-discharge}}$ , is defined as a proportion of the current SOC and is determined using the self-discharge loss factor,  $\mu$ , as follows:

$$\Delta \text{SOC}_{\text{self-discharge}}(t) := \mu \text{SOC}(t) \quad (6.7)$$

Additionally, to represent the losses in the power electronics and energy conversion process, an energy conversion loss,  $\Delta \text{SOC}_{\text{conversion}}(t)$ , is defined. This loss is proportional to the rate at which the battery's SOC changes, and since a difference is made between charging and discharging BESS, a “direction dependent energy conversion

efficiency”,  $\hat{\eta}$ , is used that is derived from  $\eta$ :

$$\Delta\text{SOC}_{\text{conversion}}(t) := \hat{\eta}\Delta\text{SOC}(t) \text{ where } \hat{\eta} \in (0, 1] \quad (6.8)$$

Here, the conversion losses in the power electronics are reflected as an asymmetric efficiency, which depends on the direction of the flow of energy. This is done by charging the battery at a lower power when consuming energy and discharging it more quickly when releasing energy. Mathematically, this can be represented as:

$$\hat{\eta} = \begin{cases} \eta & \text{if } \Delta\text{SOC}(t) \geq 0 \\ \frac{1}{\eta} & \text{if } \Delta\text{SOC}(t) < 0 \end{cases} \text{ where } \eta \in (0, 1] \quad (6.9)$$

When substituting the self-discharge loss from Equation 6.7,  $\Delta\text{SOC}_{\text{self-discharge}}$ , and conversion losses from Equation 6.8,  $\Delta\text{SOC}_{\text{conversion}}$ , into the SOC evolution equation, the full battery model, i.e. the transition from  $\text{SOC}(t)$  to  $\text{SOC}(t + \Delta t)$ , can be summarised as follows:

$$\begin{aligned} \text{SOC}(t + \Delta t) &:= \Delta\text{SOC}(t) - \Delta\text{SOC}_{\text{self-discharge}}(t) - \Delta\text{SOC}_{\text{conversion}}(t) \\ &= (1 - \mu)\Delta\text{SOC}(t) - \hat{\eta}\Delta\text{SOC}(t) \end{aligned} \quad (6.10)$$

In addition, both the SOC and the battery power,  $p_{\text{bat}}(t)$ , are constrained due to the device’s maximum and minimum energy storage capabilities, respectively  $\text{SOC}_{\text{max}}$  and  $\text{SOC}_{\text{min}}$ , and maximum charge and discharge rate,  $P_{\text{max}}$ . These limitations are captured in Equations 6.11 and Equation 6.12, respectively.

$$\text{SOC}_{\text{min}} \leq \text{SOC}(t) \leq \text{SOC}_{\text{max}} \quad (6.11)$$

$$|p_{\text{bat}}(t)| \leq P_{\text{max}} \quad (6.12)$$

### 6.3.4 Network Models

Similar to Chapter 3 of this thesis, the Open Distribution System Simulator (OpenDSS), developed by the Electronic Power Research Institute (EPRI), was used in order to simulate the LV energy distribution networks. It requires element-based network models, including line, load and transformer information, and generates realistic power flow results.

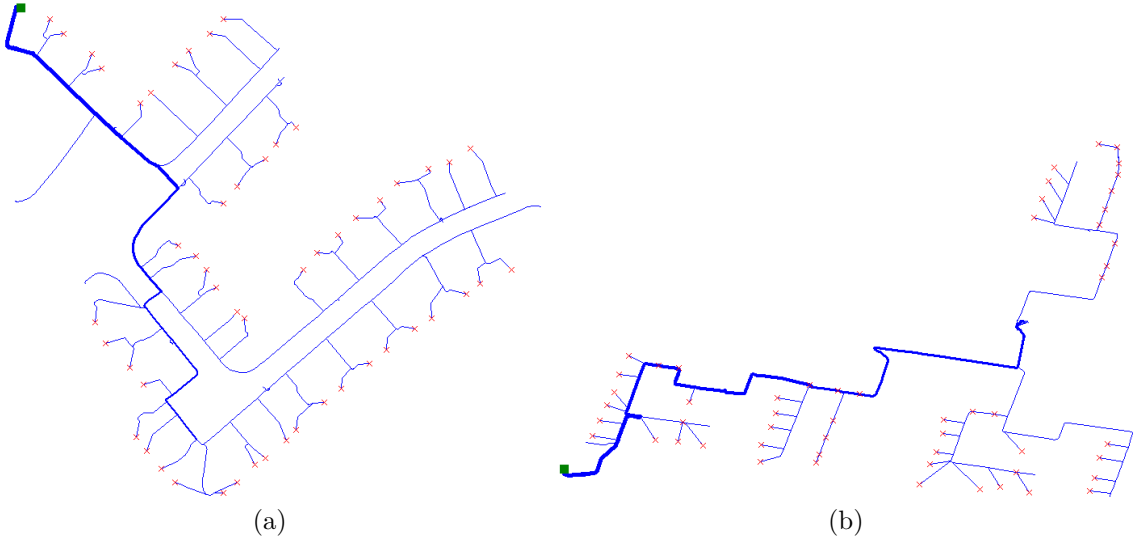


Figure 6.4: Sample OpenDSS power networks, where consumers are indicated as red crosses and 11/0.416-kV substations are marked with a green square. Here, (a) is the IEEE PES EU LV test feeder, and (b) is a SSEN Common Information Model (CIM) based feeder

Simulations were conducted using the IEEE's European Low Voltage Test Feeder [218] and six detailed U.K. feeder models, that are based on real power distribution networks and provided by Scottish and Southern Electricity Networks (SSEN). The SSEN circuit models were provided as Common Information Models (CIM) during the collaboration on the New Thames Valley Vision Project Project (NTVV) [94]. An example of the IEEE EU LV Test feeder and a UK feeder provided by SSE-PDEN are shown in Figure 6.4b and Figure 6.4b, respectively. A summary of these model's parameters is given in the Table 6.3.

Throughout the remainder of this chapter, all excerpt and time series results were

Parameter	IEEE Feeder	SSEN Feeders					
		1	2	3	4	5	6
network No.	1	55	56	53	91	59	88
no. of customers	227	227	231	241	224	237	237
mean customer load (VA)	16.8	16.8	16.8	19.5	16.8	19.5	16.8
max. customer load (kVA)	24.4	24.9	23.9	41.9	25.6	38.9	16.3
mean net. load (kVA)	72.6	72.7	72.2	92.9	73.5	89.6	60.5
max. net. load (kVA)							

Table 6.3: Network model parameters [94].

extracted from experiments with the IEEE EU LV Test feeder (i.e., Network No. 1). Any further results are then based on an aggregation of all networks to include their network diversity in the analysis.

The same model-derived EV data and IEEE EU LV Test feeder consumer demand profiles were used for all simulations. The resulting demand profiles therefore represent the total daily electricity demand of households with connected EVs. These profiles were sampled at  $\Delta t = 1$  min. The OpenDSS simulation environment was controlled using MATLAB, achieved through OpenDSS's Common Object Model (COM) interface and accessible using Microsoft's ActiveX server bridge.

## 6.4 Storage Control

In this section, the control of the energy storage system is explained. More specifically, all parameters that are used in the Additive-Increase Multiplicative-Decrease (AIMD) algorithm are explained first. Secondly, the structure of the BESS based AIMD algorithm is presented, where its decision mechanism is explained in full. In the end, the voltage referencing that is used to extend AIMD to AIMD+ is detailed.

### 6.4.1 Algorithm Parameters

The proposed distributed battery storage control is shown in Algorithm 2. This algorithm takes the current voltage reading,  $v_{\text{bat}}(t)$ , current BESS power,  $p_{\text{bat}}(t)$ , and the

**Data:**  $p_{\text{bat}}(t)$ , SOC( $t$ ),  $v_{\text{bat}}(t)$ ,  $V_{\text{thr}}$ ,  $V_{\text{max}}$ ,  $V_{\text{min}}$ , SOC<sub>max</sub>, SOC<sub>min</sub>,  $\alpha$ ,  $\beta$

**Result:**  $p(t + \Delta t)$

```

1 for  $t \leftarrow 1$  to  $T$  do
2   // Define the rate for the recent voltage reading
3    $r(t) = (v_{\text{bat}}(t) - V_{\text{thr}});$ 
4   if  $v_{\text{bat}}(t) \geq V_{\text{thr}}$  then
5     // If voltage levels are above a threshold and...
6     if  $SOC(t) \leq SOC_{\text{max}}$  then
7       // ...SOC is not at max.: increase charging power
8        $p(t + \Delta t) = p_{\text{bat}}(t) + \alpha P_{\text{max}}r(t)$ 
9     else
10      // ...SOC is at max.: shut off
11       $p(t + \Delta t) = 0;$ 
12    end
13    // If the battery has been discharging...
14    if  $p_{\text{bat}}(t) < 0$  then
15      // ...reduce discharging power by  $\beta$ 
16       $p(t + \Delta t) = \beta p_{\text{bat}}(t);$ 
17    end
18  else
19    // If voltage levels are below a threshold and...
20    if  $SOC(t) \geq SOC_{\text{min}}$  then
21      // ...SOC is not at min.: increase discharging power
22       $p(t + \Delta t) = p_{\text{bat}}(t) - \alpha P_{\text{max}}r(t)$ 
23    else
24      // ...SOC is at min.: shut off
25       $p(t + \Delta t) = 0;$ 
26    end
27    // If the battery has been charging...
28    if  $p_{\text{bat}}(t) > 0$  then
29      // ...reduce charging power by  $\beta$ 
30       $p(t + \Delta t) = \beta p_{\text{bat}}(t);$ 
31    end
32  end
33  // Restrict power to BESS limits
34   $p_{\text{bat}}(t + \Delta t) = \text{signum}(p_{\text{bat}}(t))\min(|p_{\text{bat}}(t)|, P_{\text{max}});$ 
35 end

```

**Algorithm 2:** Compute battery power

current state of charge,  $\text{SOC}(t)$ , as variable inputs. Using a set of reference parameters that include the nominal voltage threshold,  $V_{\text{thr}}$ , the minimum voltage level  $V_{\text{min}}$ , the maximum voltage level,  $V_{\text{max}}$ , the minimum allowable state of charge,  $\text{SOC}_{\text{min}}$ , the maximum allowable state of charge,  $\text{SOC}_{\text{max}}$ , and the two control parameters,  $\alpha$  and  $\beta$ , this Algorithm 2 computes the next BESS power  $p_{\text{bat}}(t + \Delta t)$ . The last two parameters, i.e.  $\alpha$  (where  $\alpha \in [0, 1]$ ) and  $\beta$  (where  $\beta \in [0, 1]$ ), respectively control the size of the power's additive increase step and the size of the multiplicative decrease. In traditional Internet base applications of AIMD algorithms,  $\alpha$  is set to a value that slowly increases the number of sent messages (e.g. 0.1) and  $\beta$  is set to a larger value (e.g. 0.5) to quickly decrease throughput if congestion is noticed. The constants  $V_{\text{max}}$ ,  $V_{\text{min}}$  and  $V_{\text{thr}}$  are the maximum and minimum historic voltage values and the set-point threshold that is used to regulate the BESS operation. In the case when the total demand is too high, the local voltages will fall below  $V_{\text{thr}}$ , and the batteries reduce their charging power and eventually start discharging. This behaviour raises overall voltage levels since the total demand on the feeder is reduces. For the simulations in this chapter,  $V_{\text{max}}$  is set to the nominal voltage of the substation transformer, i.e., 240 V, and  $V_{\text{thr}}$  is set to a value below  $V_{\text{max}}$ , which was found by solving a balanced power flow analysis of the underlying network. For each BESS,  $V_{\text{min}}$  is then chosen as the value below  $V_{\text{thr}}$  so that  $V_{\text{thr}}$  lies equidistant to  $V_{\text{max}}$  and  $V_{\text{min}}$ . The variable  $v_{\text{bat}}(t)$  is the battery's local bus voltage and is used to trigger control actions. This value is obtained by solving the power flow of the underlying network and adjusts the battery power,  $p_{\text{bat}}(t)$ , in as defined in by the algorithm. To stay within operational limits,  $P_{\text{max}}$  is set as the maximum charging/discharging power of the battery. The charging and discharging power of the batteries is increased in proportion to the available headroom on the network (which is inferred from the local voltage measurement  $v_{\text{bat}}(t)$ ) to avoid any sudden overloading of the substation transformer.

### 6.4.2 AIMD Algorithm Structure

The algorithm itself, as shown in Algorithm 2, contains two decision levels. The first level (lines 4-17) determines whether the network is underloaded by comparing the local bus voltage,  $v_{\text{bat}}(t)$ , to the battery's set-point threshold,  $V_{\text{thr}}$ . If the network is under low load, i.e. when  $v_{\text{bat}}(t) \geq V_{\text{thr}}$ , then the BESS is triggered to decrease its power injection until it begins charging. In this case, the battery's SOC is compared to its operation limit to check whether the battery can charge, i.e.,  $\text{SOC} < \text{SOC}_{\max}$ . If there is enough charging capacity left, then the battery's charging power is linearly increased using  $\alpha$  (lines 6-8). Otherwise, i.e. if the BESS is fully charged by reaching its highest charge level of  $\text{SOC}_{\max}$ , the charging process is turned off (lines 9-11). If the battery was previously discharging however, the related discharging power is multiplicatively reduced (lines 14-17) to begin reducing voltage levels.

The second decision level (lines 18-32) is entered when the network is overloaded. If the network is under high load, i.e. when  $v_{\text{bat}}(t) < V_{\text{thr}}$ , then the BESS is triggered to decrease its charging power until it begins to inject energy into the network. In this case, the discharging power is linearly increased if the battery has enough energy stored, i.e.  $\text{SOC} > \text{SOC}_{\min}$  (lines 20-22). Otherwise, i.e. if the BESS has discharged to its low charge level of  $\text{SOC}_{\min}$ , the discharging process is turned off (lines 23-25). However, if the battery was previously charging, then its charging power is multiplicatively reduced (line 28-31) to begin increasing voltage levels.

The direction of the charging/discharging power adjustment is determined by the first decision level, as well as the threshold proximity ratio  $r(t)$ . As the battery's bus voltage,  $v_{\text{bat}}(t)$ , approaches the threshold voltage,  $V_{\text{thr}}$ , this ratio tends to zero and thus stops the battery operation. Therefore, oscillatory hunting is effectively mitigated. The last step of the algorithm (lines 33-34) assures that the battery's charge/discharge power stays within the device's ratings.

### 6.4.3 Reference Voltage Profile

The difference in the location and load of each customer results in the over-utilisation of the batteries that are located at the feeder end. This is particularly true when using a fixed voltage threshold. To individualise the voltage thresholds, a reference voltage profile is generated by performing a power flow analysis of the network model by subjecting it to its maximum power demand. This approach is comparable to the procedure by Papaioannou et al. in [219] who generated profiles for the control of EV charging. In this chapter however, bi-directional power flow of BESS is controlled. An example of a fixed threshold and reference voltage profile is shown in Figure 6.5.

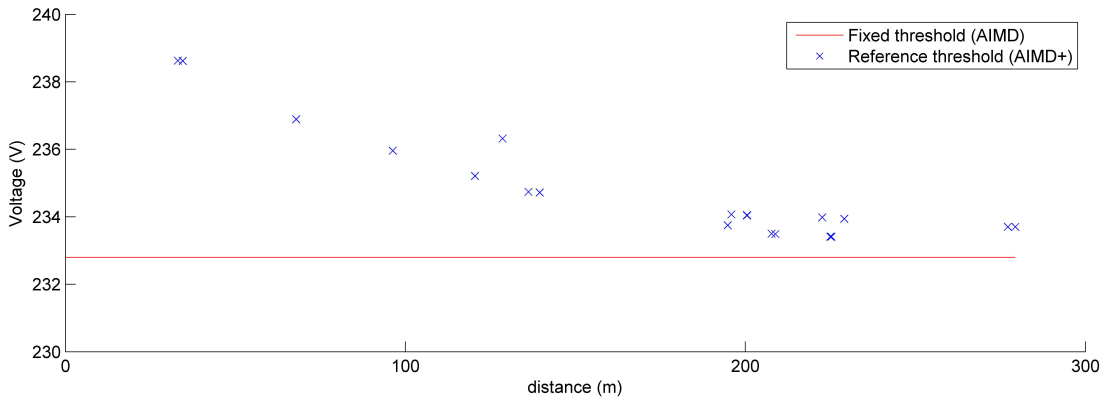


Figure 6.5: An example plot showing the difference between the fixed voltage threshold (AIMD) and the reference voltage profile (AIMD+) against the load's distance to its feeding substation.

Therefore, in the AIMD+, consumers located at the head of the feeder are allocated a higher voltage threshold than those towards the end of the feeder. However, customers with lower thresholds are allocated a voltage threshold similar to that of the fixed threshold control. This allocation takes into account the expected voltage drop, that occurs along the length of the feeder, and hence results in a better tuned utilisation of all battery storage units, regardless of their distance to the substation. For the work presented in this chapter, the voltage threshold is set in such a way as to limit the maximum voltage drop to 3% at the end of the feeder.

## 6.5 Scenarios and Comparison Metrics

This section covers several scenarios that were used to test the performance of the battery control algorithm. Following that is the definition of three comparison metrics. These metrics quantify the improvements caused by the different algorithms in comparison to the worst case scenario.

### 6.5.1 Test Cases and Scenarios

In all simulations, the EVs plug-in on arrival and charge at their nominal charging rate until fully charged. The BESS devices were chosen to have a capacity of 7 kWh with a maximum power rating of 2 kW (battery specifications are based on the Tesla Powerwall [220]). Four excerpt cases were defined with different levels of EV and storage uptakes. The detail of these cases are as follows:

**Case A** A normal scenario, where only household demand is used.

**Case B** A baseline or worst case scenario, in which EV uptake is 100% and no BESS is used.

**Case C** An AIMD scenario, in which EV uptake is 100% and each household has a battery energy storage device. Here, each battery was controlled using the AIMD algorithm using a fixed voltage threshold.

**Case D** An AIMD+ scenario, in which EV uptake is 100%, and each household has a battery energy storage device. Here, each battery was controlled using the AIMD+ algorithm using the optimised reference voltage profile.

A storage uptake of 100% was adopted to represent the worst case scenario. In addition to the four defined scenarios, a full set of simulations was performed with EV and storage uptake combinations of 0% to 100% in steps of 10%.

## 6.5.2 Performance Metric Definition

In order to compare the network's performance during execution of the predefined cases, three performance metrics, i.e.  $\zeta^*$ ,  $\zeta^{**}$  and  $\zeta^{***}$ , are defined. These metrics capture, respectively, the improvements in voltage violation mitigation, line overload reduction and the equality of battery usage. They are derived from the Probability Distribution (PD) of the underlying measurements and thus allow an comparison of the four scenarios. In the following sections, all metrics' subscripts are used to indicate which scenario they represent, e.g.  $\zeta_{\mathbf{C}}^{**}$  represents **Case C** and  $\zeta_{\mathbf{D}}^*$  represents **Case D**. For reproducibility, all excerpts to showcase the performance metrics were generated from simulations based on the IEEE EU LV Test feeder.

### 6.5.2.1 Parameter for Voltage Improvement

Metric  $\zeta^*$  is designed to assess the changes in voltage PD. For instance, a narrow voltage PD around the nominal voltage (i.e.  $V_{ss}$ ) would indicate a stable voltage at all nodes of the network. A wider or even shifted PD would however indicate that the voltage deviation has increased, and that voltage levels are not stable at all nodes. In order to compare the AIMD and AIMD+ cases (i.e. respectively **Case C** and **Case D**), the two voltage PD dependent performance metrics are defined:

$$\zeta_{\mathbf{C}}^* := \sum_{v=V_{\min}}^{V_{\max}} \delta^*(v) [P_{\mathbf{B}}(v) - P_{\mathbf{C}}(v)] \quad (6.13)$$

$$\zeta_{\mathbf{D}}^* := \sum_{v=V_{\min}}^{V_{\max}} \delta^*(v) [P_{\mathbf{B}}(v) - P_{\mathbf{D}}(v)] \quad (6.14)$$

$$\delta^*(v) := \begin{cases} \frac{V_{ss}-v}{V_{ss}-V_{low}} & \text{if } v \leq V_{ss} \\ \frac{v-V_{ss}}{V_{high}-V_{ss}} & \text{otherwise} \end{cases} \quad (6.15)$$

where  $V_{low} < V_{ss} < V_{high}$

Together with their scaling function,  $\delta^*$ , in Equation 6.15, Equation 6.13 and Equation 6.14 define the performance metrics  $\zeta_C^*$  and  $\zeta_D^*$ , respectively. In these equations,  $P_B(v)$  represents the probability distribution of all voltages for **Case B** (the baseline case). The two metric specific PDs, i.e.  $P_C(v)$  and  $P_D(v)$ , represent the voltage PDs for **Case C** and **Case D**. By computing the weighted difference, a reduction in probabilistic voltage deviation is found. The weighting is necessary to emphasise changes in PD that make voltages tend towards the nominal substation voltage,  $V_{ss}$ .  $V_{high}$  and  $V_{low}$  are also used in Equation 6.15 to normalise the deviation at the upper and lower voltage bounds (these constants are also used in the AIMD+ algorithm in Section 6.4). With  $\delta^*(v)$ , regions outside the nominal operating band are thus weighted higher than those within and surrounding the nominal voltage level. In summary, the proposed voltage comparison parameters,  $\zeta_C^*$  and  $\zeta_D^*$ , show an improvement in voltage PD when they are negative, whereas a positive value implies a voltage PD with higher deviation from the nominal level,  $V_{ss}$ .

### 6.5.2.2 Parameter for Line Overload Reduction

Similar to measuring the voltage level improvements, all line utilisation PDs are also compared with the base case, **Case B**. This follows a similar approach as in Equations 6.13 to 6.15, but the line utilisation PD uses a different scaling factor. The two line utilisation performance metrics,  $\zeta_C^{**}$  and  $\zeta_D^{**}$ , for assessing, respectively, **Case C** and **Case D** are defined as follows:

$$\zeta_{\mathbf{C}}^{**} := \sum_{c=0}^{C_{\max}} \delta^{**}(c) [P_{\mathbf{C}}(c) - P_{\mathbf{B}}(c)] \quad (6.16)$$

$$\zeta_{\mathbf{D}}^{**} := \sum_{c=0}^{C_{\max}} \delta^{**}(c) [P_{\mathbf{D}}(c) - P_{\mathbf{B}}(c)] \quad (6.17)$$

$$\delta^{**}(c) := \begin{cases} \left(\frac{c}{1-C_{\min}}\right)^2 & \text{if } c \geq C_{\min} \\ 0 & \text{otherwise} \end{cases} \quad (6.18)$$

where  $C_{\min} \in [0, 1)$

Here,  $P_{\mathbf{B}}(c)$  represents the baseline PD (i.e. **Case B**),  $P_{\mathbf{C}}(c)$  represents the line utilisation PD for the AIMD scenario (i.e. **Case C**), and  $P_{\mathbf{D}}(c)$  represents the line utilisation PD for the AIMD+ scenario (i.e. **Case D**). Line utilisation is computed as the ratio between the simulated current in each line and the nominal rating of this line. A value of one would therefore indicate a fully loaded line. To scale the comparison with the baseline case correctly, a corresponding scaling function  $\delta^{**}(c)$  in Equation 6.18, is defined. This function is a quadratic function since the relationship between line current and resistive losses is also quadratic. A minimum load,  $C_{\min}$ , is however used to neglect those probabilities where lines are only lightly loaded. The resulting scaling effect thus amplifies the impact of line current reduction beyond the line's nominal rating and reduces the weight on those improvements within the line's thermal constraints. For the work presented in this chapter, the value for this modifier is set to 0.5 since only line utilisation improvements above 0.5 p.u. are considered noteworthy. In summary, a reduction in line overloads would give a negative  $\zeta_{\mathbf{C}}^{**}$  or  $\zeta_{\mathbf{D}}^{**}$ , whereas a positive value implies a higher line utilisation, i.e. worse results.

### 6.5.2.3 Parameter for the Improvement of Battery Cycling

The final metric,  $\zeta^{***}$ , gives an indication of the inequality of battery cycling. Here, one battery cycle is defined as a full discharge and charge of the BESS at its maximum operating power. Since BESS at the bottom of the feeder are more likely to partake in voltage correcting functions than a BESS located closer to the substation, higher degradation can be expected. To assess the difference in cycling between different BESSs, the ratio between the peak and mean battery cycling is used. Previous chapters used this so called Peak-to-Average Ratio (PAR) to assess smoothness of load profiles (see Section 3.3.4, Section 4.2.2 and Section 5.3.3 of this thesis). In this chapter however, PAR is used to quantify the maximum deviation in battery cycling from the mean battery cycling. The metrics to determine the PAR for **Case C** and **Case D** are defined as follows:

$$\zeta_{\mathbf{C}}^{***} := \frac{\max |\mathbf{c}_{\mathbf{C}}|}{U^{-1} \sum_{u=1}^U |c_{\mathbf{C}}^u|} \text{ where } \mathbf{c}_{\mathbf{C}} = (c_{\mathbf{C}}^u) \quad (6.19)$$

$$\zeta_{\mathbf{D}}^{***} := \frac{\max |\mathbf{c}_{\mathbf{D}}|}{U^{-1} \sum_{u=1}^U |c_{\mathbf{D}}^u|} \text{ where } \mathbf{c}_{\mathbf{D}} = (c_{\mathbf{D}}^u) \quad (6.20)$$

In Equation 6.19 and Equation 6.20,  $c^u$  is the total cycling of a BESS unit,  $u$ , out of a total number of units  $U$ . For simplicity, a BESS cycling vector,  $\mathbf{c}$ , is used to combine the cycling of all devices, where  $\mathbf{c} = (c^u)$ . To differentiate between **Case C** and **Case D**,  $\mathbf{c}_{\mathbf{C}}$  (where  $\mathbf{c}_{\mathbf{C}} = (c_{\mathbf{C}}^u)$ ) and  $\mathbf{c}_{\mathbf{D}}$  (where  $\mathbf{c}_{\mathbf{D}} = (c_{\mathbf{D}}^u)$ ) are used to indicate the total cycling of each BESS unit for the AIMD and AIM+ case, respectively. In the event of a perfectly equal cycling of all batteries,  $\zeta_{\mathbf{C}}^{***}$  and  $\zeta_{\mathbf{D}}^{***}$  will have a value of one. Yet, as batteries are more likely to operate differently, these values are expected to be greater than one. Therefore, values closer to one imply a more equal and therefore fairer utilisation of the deployed batteries, whilst values deviating further from one imply the opposite.

## 6.6 Results and Discussion

In this section, all presented results were generated from the simulation of the different cases. In each of the following three subsections, the performances of the AIMD and AIMD+ algorithm are compared against each other and the baseline cases. To do so, the performance metrics that were outlined in Section 6.5.2 are used. Results from the four test cases, which have been defined as **Case A**, **Case B**, **Case C** and **Case D** in Section 6.5.1, are explained first. Then the results from the full analysis over the large range of EV and battery storage uptake is presented.

### 6.6.1 Voltage Violation Analysis

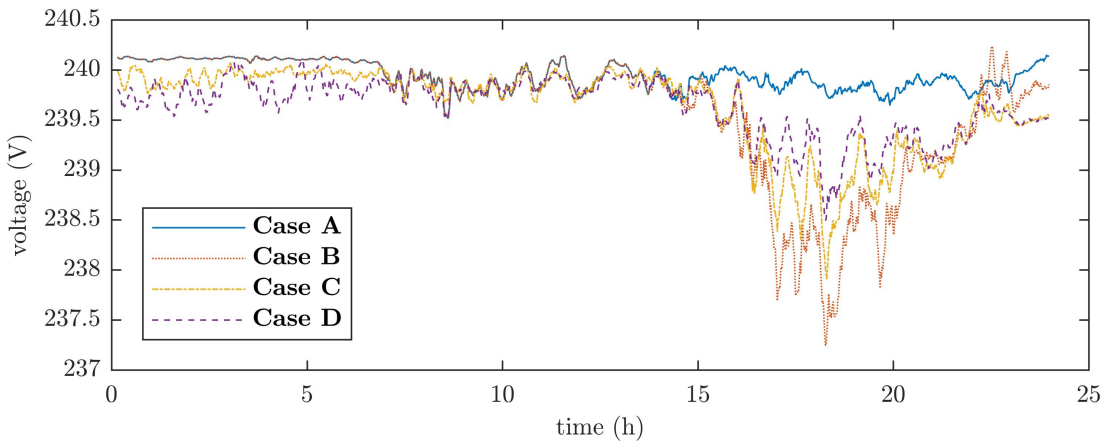


Figure 6.6: Mean voltage profiles for all four test cases over a single day.

For the assessment of improving voltage levels, results are compared for the algorithms' performances at reducing bus voltage deviation; particularly by increasing the lowest recorded bus voltage. Each load's bus voltage was recorded, from which a sample voltage profile, Figure 6.6, was extracted, where the bus voltage fluctuation over time becomes apparent. It can be seen that the introduction of EVs has significantly lowered the line-to-neutral voltage. Adding energy BESS devices did raise the voltage levels during times of peak demand, as can be seen between 17:00 and 21:00, where the AIMD+ algorithm has elevated voltages further than the AIMD scenario.

To obtain a better understanding of the level of improvement, the voltage frequency distribution of all buses along the feeder was generated and plotted in a histogram in Figure 6.7.

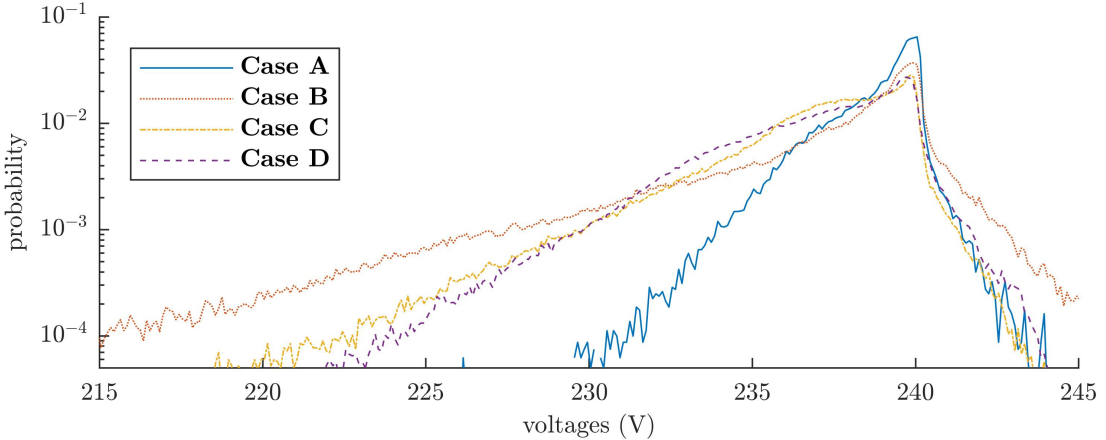


Figure 6.7: Voltage level probability distribution for the entire feeder where  $\zeta_C^* = -0.153$  and  $\zeta_D^* = -0.135$ .

In this histogram, the voltage PD for all four cases were normalised and plotted against each other. Here, the previously seen drop in voltages by introducing EVs is recorded as a shift in the voltage distribution towards the left. The widened left hand tail of **Case B** can be clearly observed in Figure 6.7. This voltage drop is then mitigated by the introduction of the storage solutions, since the voltage PD is shifted towards higher voltage bands, i.e. towards the right. Since the difference between the BESS controlled by AIMD and AIMD+ is difficult to see, a comparison of their underlying performance metrics is necessary. In Figure 6.7, for the IEEE EU LV Test feeder, the AIMD+-controlled batteries outperform the AIMD devices since the resulting  $\zeta_C^*$  is greater than  $\zeta_D^*$ .

However, to gain a full understanding of the performance of the AIMD and AIMD+ algorithms, a full sweep of EV and BESS uptake combinations was simulated on all available power distribution networks. The resulting parameters were averaged and plotted in Figure 6.8.

These figures show that the AIMD+ control algorithm reduces voltage deviation

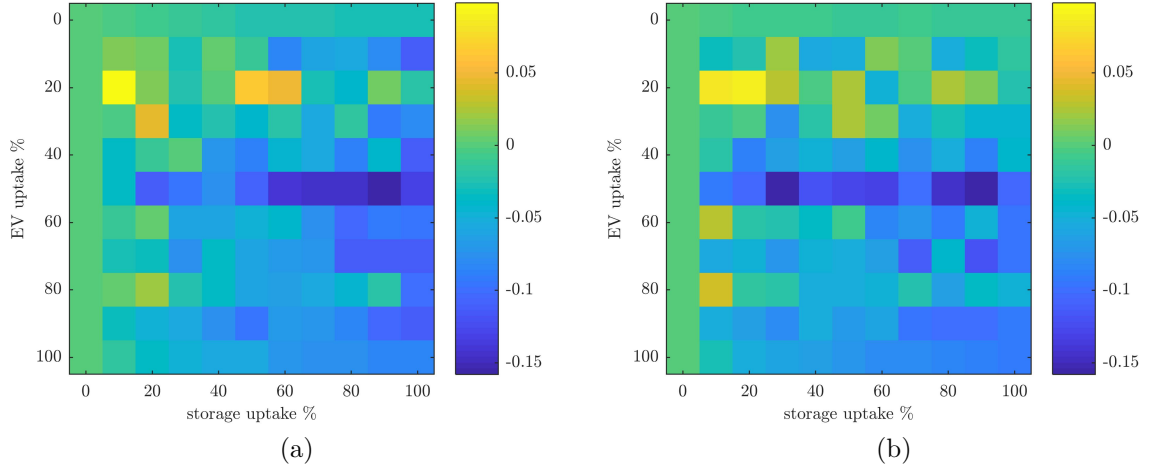


Figure 6.8: Comparison of voltage improvement indices for (a)  $\zeta_C^*$  indices (AIMD); (b)  $\zeta_D^*$  indices (AIMD+).

more effectively as the uptake in storage and EVs increases. For low storage uptake, the AIMD algorithm does not perform as strongly since more  $\zeta_C^*$  values are positive and larger than their corresponding  $\zeta_D^*$  value. This becomes more apparent when averaging all  $\zeta_C^*$  and  $\zeta_D^*$  values for their common storage uptake and across all EV uptakes. The resulting averaged metrics are plotted in Figure 6.9.

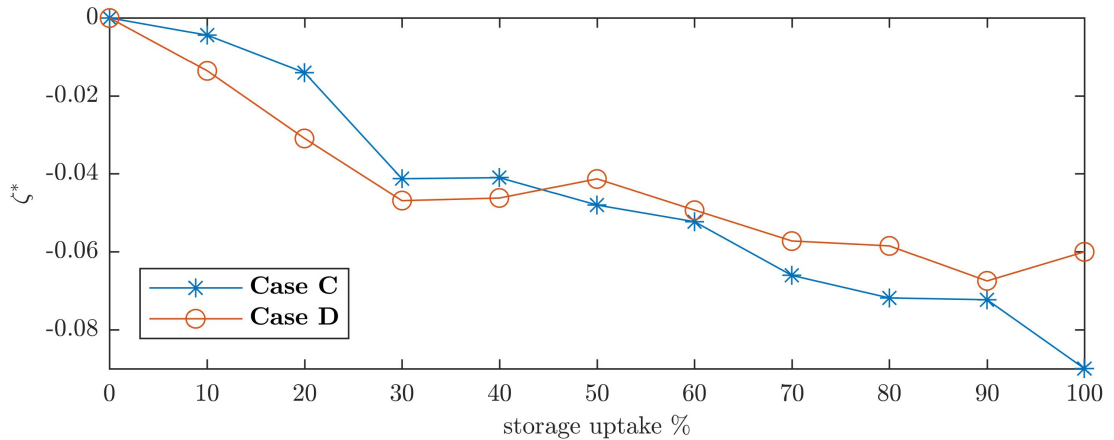


Figure 6.9: Average  $\zeta_C^*$  and  $\zeta_D^*$  values recorded against the corresponding storage uptake.

In this last figure, Figure 6.9, it can be seen how the sole impact of BESS uptake reflects in a continuing improvement of voltage levels. In fact, both compared

algorithms improved the bus voltage, which coincides with the findings in the case studies. On average, this is the case for all BESS uptakes, as  $\zeta_C^* \approx \zeta_D^*$ . Nonetheless, it should be noted that the AIMD+ algorithm had reduced the frequency of severe voltage deviations in comparison to the AIMD algorithm and is more effective during scenarios with lower BESS uptake.

### 6.6.2 Line Overload Analysis

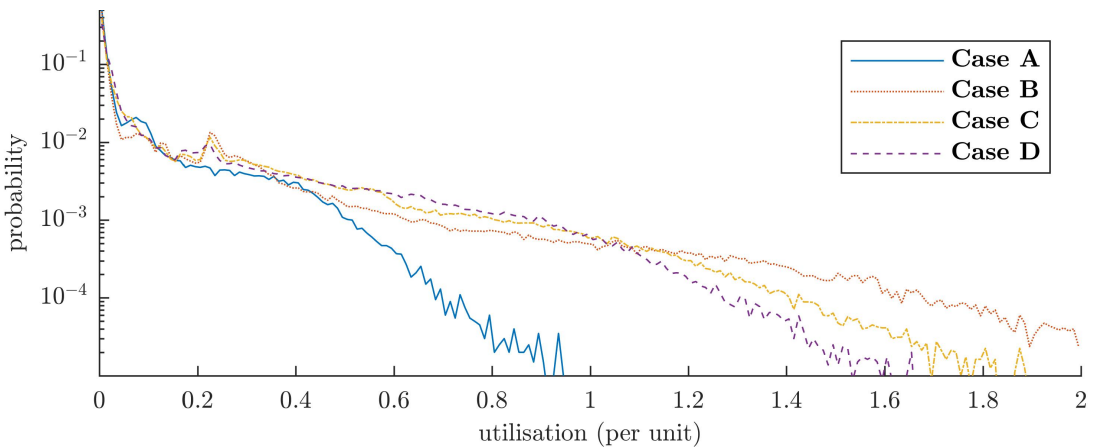


Figure 6.10: Line utilisation probability distribution of all lines in the simulated feeder where  $\zeta_C^{**} = -0.360$  and  $\zeta_D^{**} = -0.518$ .

Similar to the voltage PD analysis, a PD of the line utilisation was generated and plotted in Figure 6.10. This figure shows a normalised PD plot of the per unit current in all lines, for each of the four scenarios (here, 1 p.u. represents a 100% line usage, i.e., a line current of the same value as the line's nominal current rating). Whilst the case without any charging EVs, i.e. **Case A**, shows no overloading, **Case B** has significantly widened the probability spectrum. AIMD and AIMD+ controlled BESS can mitigate the effect of this EV introduction, and the difference in performance becomes more apparent than it did for the voltage PD analysis. In Figure 6.10 the PDs for **Case C** and **Case D** intersect at 1 p.u. load, yet for the AIMD+ scenario, overloads are less likely than for the AIMD controlled scenario. However, in this figure it can also be observed that the used test network is of insufficient capacity to

cater for the chosen EV uptake, since the probability of line over-utilisation is still above zero.

Nonetheless, the AIMD+ controlled storage devices yielded a noticeable reduction in line overloads, despite being a voltage driven control method. This improvement is apparent through the compressed width of the probability distribution and the negative  $\zeta_{\mathbf{D}}^{**}$  value. In contrast, the AIMD controlled storage devices do not fully utilise the line capacity as effectively, which leads to a positive value of  $\zeta_{\mathbf{C}}^{**}$ . To evaluate the line utilisation improvement across all simulations, the full range of EV and storage uptake was evaluated. The resulting plots are shown in Figure 6.11.

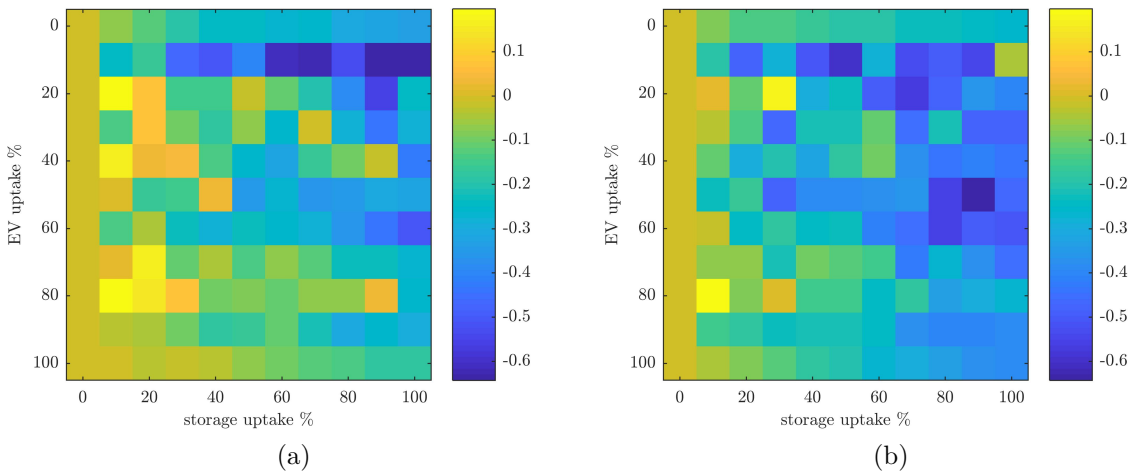


Figure 6.11: Comparison of line utilisation improvement indices for (a)  $\zeta_{\mathbf{C}}^*$  indices (AIMD); (b)  $\zeta_{\mathbf{D}}^*$  indices (AIMD+).

In these figures, it can be seen how the performance metrics change as EV uptake and storage uptake increase. For the AIMD-controlled BESS, the resulting  $\zeta_{\mathbf{C}}^{**}$  values are distributed around zero, whereas the AIMD+ algorithm achieved negative values of  $\zeta_{\mathbf{D}}^{**}$  for nearly 90% of the performed simulations. These negative values confirm the better usage of available line capacity. This becomes particularly apparent for scenarios where very low EV uptake is combined with larger BESS uptake. Here, AIMD-controlled storage devices commence their initial charge simultaneously. As

they are located closer to the substation, they do not measure a sufficient bus voltage offset to regulate down their charging power. This behaviour causes a number of line overloads at the very beginning of the simulated days. The AIMD+ algorithm on the other hand, with its adjusted thresholds, is more responsive to non-optimal network operation and, therefore, increases the charging rate gradually.

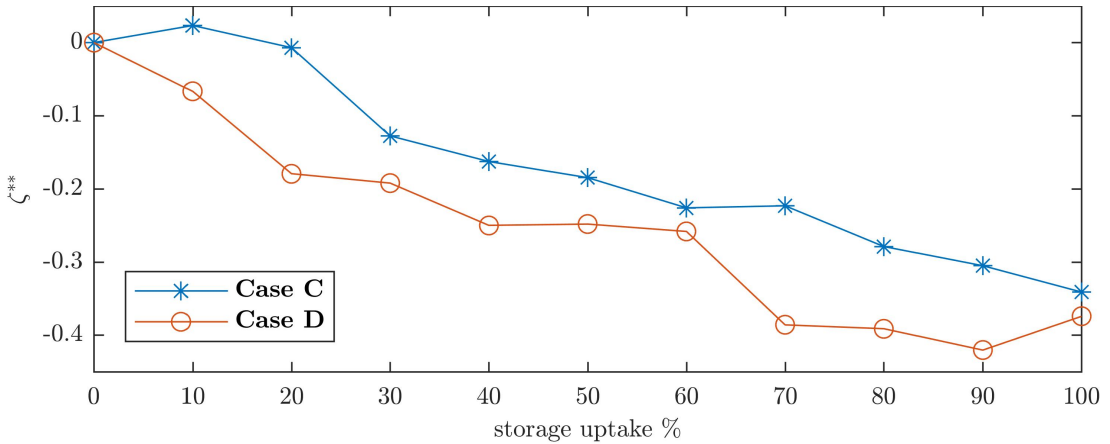


Figure 6.12: Average  $\zeta_{\mathbf{C}}^{**}$  and  $\zeta_{\mathbf{D}}^{**}$  values recorded against the corresponding storage uptake.

This gradual adjustment is based on the fact that the bus voltages in the AIMD+ algorithm are closer to their nominal voltages (i.e., bus voltages found by simulating the feeder with its equally-distributed nominal load) than they are in the conventional AIMD case. A greater voltage disparity, which is the case in AIMD, causes a prolonged additive adjustment to the battery's power. This prolonged adjustment is particularly apparent for batteries situated at the bottom of the feeder, as their voltage measurements deviate the furthest from the substation voltage level. AIMD+ on the other hand prevents this behaviour by setting the voltage threshold based on the network's nominal voltage drop, which is dependent on the distance between the BESS and its feeding substation. As a result, the set-point voltage thresholds at the bottom of the feeder are lower than those closer to the substation. Hence, the additive power adjustment becomes equal for all BESS along the feeder. Therefore, by applying these individualised control thresholds, the sensitivity of the algorithm

is corrected, whilst successfully mitigating the severity of line overloads.

Averaging the  $\zeta_{\mathbf{C}}^{**}$  and  $\zeta_{\mathbf{D}}^{**}$  values over all EV uptakes gives a clearer indication of performance, as this is now the only variable in the performance analysis. The result is plotted in Figure 6.12. Here, the hypothesis that AIMD-controlled energy storage devices do not improve line utilisation is confirmed. In contrast, the AIMD+-controlled devices succeed at effectively reducing line overloads. This is also demonstrated by the values of  $\zeta_{\mathbf{C}}^{**}$ , which remain positive yet close to zero, whereas  $\zeta_{\mathbf{D}}^{**}$  decreases with increasing uptake of battery storage devices, as shown in Figure 6.12.

Whilst the deployment of energy storage has often been seen as a possible solution to defer network reinforcements, the presented results show that this is not always the case. In fact, due to technical limitations, choosing an appropriate control algorithm enables the BESS to perform optimally. This becomes particularly apparent when, e.g. energy storage devices need to recharge their injected energy for times of peak demand. For the AIMD case, this recharging was not controlled in accordance to the underlying network properties, which led to higher line currents. The proposed AIMD+ algorithm was not as susceptible to this kind of behaviour, as it has been designed to take battery location into account. This immunity and well-controlled power flow caused little to no additional strain on the network's equipment, allowing the deployed storage devices to also provide voltage support.

### 6.6.3 Battery Utilisation Analysis

In this part of the analysis, the batteries' equality of use was evaluated by comparing the battery cycling for each AIMD implementation. As already mentioned, a single battery cycle is defined as a full discharge and recharge. In Figure 6.13, the battery power profiles are plotted along the horizontal axis and they are ordered by increasing distance to the substation:

Figure 6.13 shows that only half of the deployed storage devices were active in

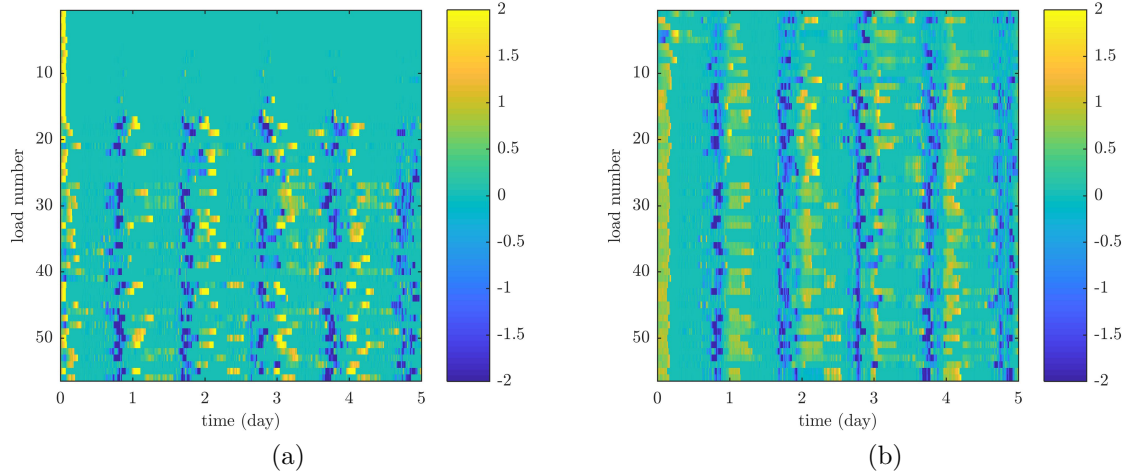


Figure 6.13: Battery power profiles of each load's battery storage device over four days for (a) **Case C** and (b) **Case D**.

**Case C** (AIMD control), whereas all devices are utilised in **Case D** (AIMD+ control).

From the recorded battery SOC profiles, the net cycling of each battery was computed and divided by the duration of the simulation to give an average daily cycling value. This value is plotted for each load in Figure 6.14a - the corresponding statistical analysis is included in Figure 6.14b:

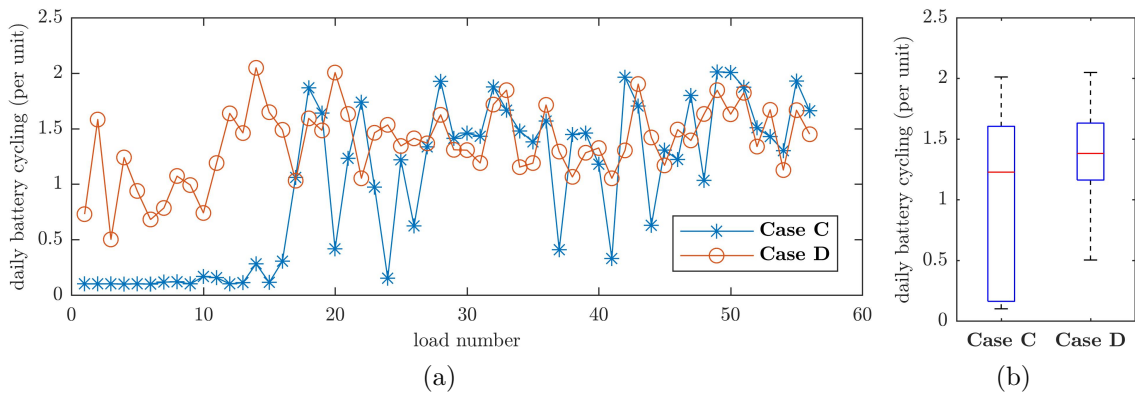


Figure 6.14: Each load's battery cycling compared for (a) each BESS and (b) the two cases, where  $\zeta_{\text{C}}^{***} = 3.89$  and  $\zeta_{\text{D}}^{***} = 2.54$ .

These two plots in Figure 6.14 show the under-use of AIMD controlled batteries, as well as the variance in battery usage under AIMD control (**Case C**) and AIMD+

control (**Case D**). In fact, when using the AIMD control, 20 out of 55 batteries experienced a battery cycling of less than 10% per day, whereas the remaining devices were utilised fully. This discrepancy causes the cycling performance metric of **Case C** (i.e.  $\zeta^{***}$ ) to be higher than the performance metric of **Case D** (i.e.  $\zeta_D^{***}$ ). Such a difference supports the assumption that AIMD+ yields a more equal battery cycling than traditional AIMD. For a more detailed comparison however, the PARs of the batteries' daily cycling over the full range of EV and storage uptake scenarios are plotted in Figure 6.15 (Section 6.5.2 gave details on all performance metrics, including  $\zeta^{***}$ , i.e. PAR, which is defined in Equation 6.19 and Equation 6.20):

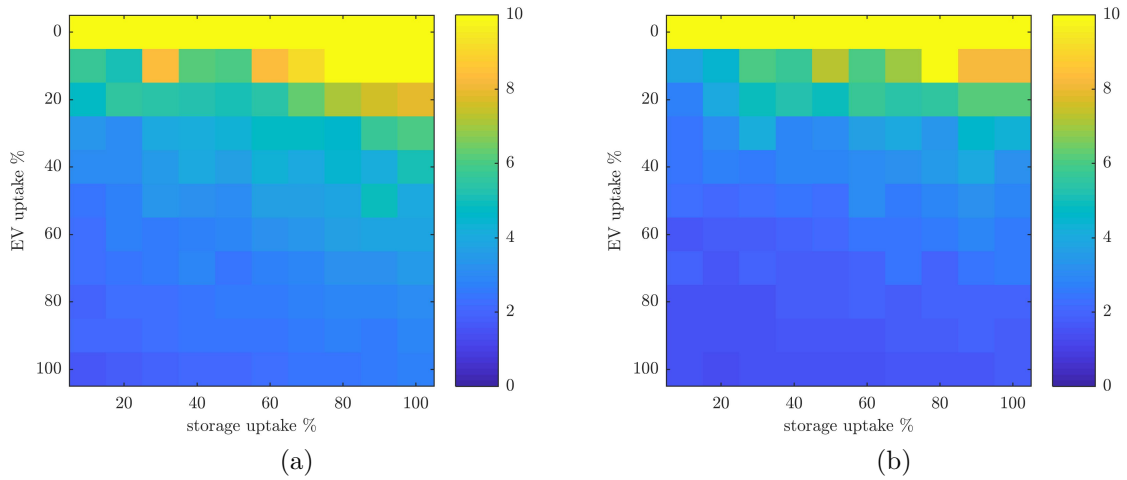


Figure 6.15: Peak-to-Average Ratios (PAR) of the battery cycling profiles of each load's battery storage device over four days for (a) **Case C** and (a) **Case D**.

In Figure 6.15, it can be seen that for any EV uptake scenario, AIMD-controlled energy storage units were cycled less equally than the AIMD+ controlled devices. The results also show that with an increasing storage uptake, BESS were cycled less equally for both control methods. However, AIMD+ (i.e. **Case D**) always outperformed the traditional AIMD algorithm (i.e. **Case C**). When averaging the values for  $\zeta^{***}$  of all batteries' SOC profiles and over all EV uptake percentages, then a clear performance difference between AIMD and AIMD+ can be observed. These resulting averaged

PARs are plotted in the subsequent figure, Figure 6.16.

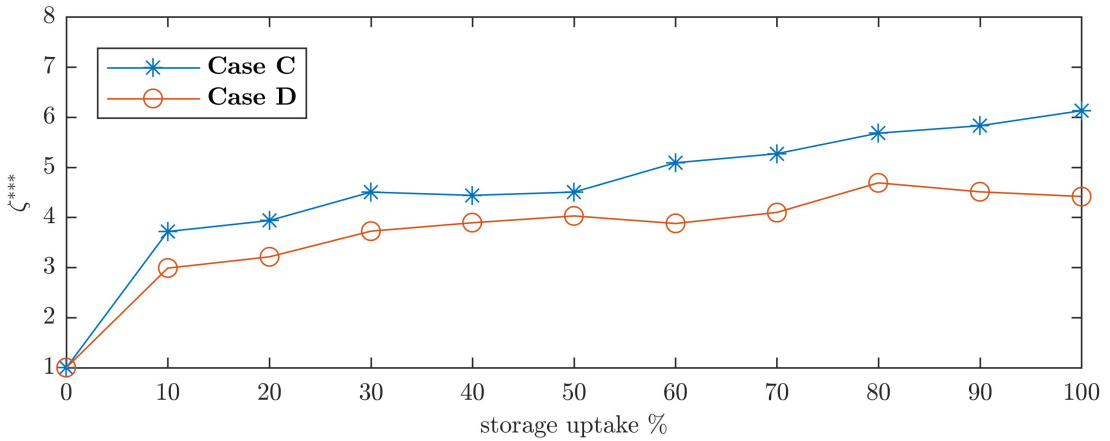


Figure 6.16: The performance index  $\zeta^{***}$  for AIMD storage and  $\zeta^{***}$  for AIMD+ storage control against storage uptake.

Although the AIMD controlled batteries were, on average, cycled less than the batteries controlled by the proposed AIMD+ algorithm, inspecting the average by itself produces a distorted understanding of the algorithm's performance. After all, since more than half of the assigned AIMD BESS devices never partook in the network control, a lower average cycling would be expected to begin with. The difference in cycling across all batteries, or the cycling PAR, reveals the difference between usage equality as well as effective usage. And since a lower PAR indicates a more equal usage of the deployed batteries, AIMD+ clearly outperforms AIMD when subjected to the provided data.

## 6.7 Summary

In this chapter, Chapter 6, an algorithm is proposed for distributed battery energy storage, in order to mitigate the negative impact of highly variable and uncontrolled loads; such as the charging of EVs. Unlike previous algorithms the improved algorithm, i.e. AIMD+, only uses local bus voltage measurements to issue control instructions. It implements a reference voltage profile which is derived from power

flow analysis of the distribution network for its set-point control. Taking the distance to the feeding substation into account allows optimising the algorithm's parameters for each BESS. Simulations were performed on the IEEE EU LV Test feeder and a set of real UK LV network models. Comparisons were made of the standard AIMD algorithm with a fixed voltage threshold against the proposed AIMD+ algorithm. A set of European demand profiles and a realistic EV travel model were used to feed load data into the simulations. For all conducted simulations, the performance of the distributed BESS was improved by using the proposed AIMD+ algorithm instead of traditional AIMD control. The improved algorithm resulted in a reduction of voltage variation and an increased utilisation of available line capacity, which also reduced the frequency of line overloads. Additionally, the same algorithm equalised the cycling and utilisation of battery energy storage, making better use of the deployed battery assets. Despite being data driven, all findings indicate a similar improvement in performance when extending the traditional AIMD based control to AIMD+. As a result, **Objective 4** (outlined in Section 1.2 of this thesis) has been met since all the aforementioned benefits were achieved without the use of any ICT infrastructure whilst satisfying all assumptions that were outlined in Section 6.3.1.



# Chapter 7

## Conclusion

Throughout this thesis, aspects concerning the scheduling and control of energy storage devices on the LV network for system support have been studied. More specifically, each chapter has presented its own findings and conclusions, and thus this thesis presents several contributions to knowledge. Therefore, this chapter, Chapter 7, is going to retrospectively summarise those contributions to knowledge and link them back to the overarching problem statement presented in Section 1.2. At first, Chapter 7 summarises the main findings in Section 7.1. Then, the contributions to knowledge are presented in Section 7.2, before the limitations of the conducted research and the potential future work are, respectively, being discussed in Section 7.3 and Section 7.4.

### 7.1 Overview of Main Findings

This thesis' problem statement, which has been presented in Chapter 1, can be summarised as follows:

- The aim of this thesis is to investigate how BESS in the LV network should be controlled in order to achieve best possible network support, including the

reduction of peak load, voltage deviations and phase balance.

- To assess the impact of BESS on the LV network's topology, simulations are being run to compare on-line and off-line control performance.
- Given that BESS can operate flexibly but have a limited energy resource and often have a predetermined half-hourly schedule, the research studies whether sub-half-hourly corrections can improve the performance of LV networks by incorporating load forecasts.

The reviewed literature in Chapter 2 as well as the findings from Chapter 3 emphasise the need for improved methods of control for energy storage in the LV network. In Chapter 3, a set of key network parameters were introduced to highlight the breadth of possible network improvement functions. Using the LV connected BESS, its impact on each of these key network parameters was assessed by optimising each parameter through its corresponding cost function. The same BESS would traditionally have been operated with a half-hourly schedule that dictates the device's active powers. Using this operation as a benchmark, sub-half-hourly phasor adjustments were proposed to tune the BESS operation to achieve optimal impact for any given key network parameter, yet without violating the higher resolution power constraints. As shown in several resulting time-series plots in Section 3.5, and as summarised in Table 3.1, optimising BESS operation for certain key network parameters has two resulting impacts. Firstly, the targeted key network parameter and the associated network operation are improved, and secondly, other key network parameters are also impacted. The second impact however need not be a positive impact since, e.g. reducing voltage deviation can lead to a significantly worse power factor due to the injection of reactive power. Nonetheless, showing that sub-half-hourly phasor adjustments can result in improved network operation formed the basis for the subsequent chapter, Chapter 4, where the half-hourly active power constraint is eliminated.

Chapter 4 presented a novel approach in combining both on-line and off-line energy storage control to dynamically reduce both daily and minutely load peaks. This load reduction was achieved without reaching a surplus of shortage of stored energy since a half-hourly BESS schedule (similar to Chapter 3) was used, too. Unlike the preceding chapter however, the BESS control in Chapter 4 had operational flexibility within a certain tolerance band around the predetermined schedule. Combined with a MPC to estimate the sub-half-hourly power volatility, results were achieved that noticeably reduced peak loads in comparison to the traditional forecast driven control. In fact, as shown in Figure 4.9, the mean peak load reduction increased from 1.7kW to around 5kW for different types of MPC. These findings from Chapter 3 and Chapter 4 thus form the contribution to knowledge i.e. **Objective 1** and **Objective 2**, respectively.

However, the findings in Chapter 3 and Chapter 4 assumed the inter-device communication to e.g. allow network information to be used in the derivation of BESS control instructions. Chapter 5 therefore develops a new smart-charging algorithm and uses a novel MAS implementation that operates in an intentionally desynchronised manner, in order to assess the algorithm performance if the previously assumed communications become less reliable. Since uncoordinated EV charging is expected to put the most significant stress on the LV network, any algorithm failure, i.e. to coordinate this charging, would become noticeable. And indeed, the findings indicate that the algorithm's converging behaviour is less sensitive to its control parameters in a desynchronised environment, when compared to the traditional synchronised execution. However, when comparing the overall performance at avoiding charing peaks between the synchronised case (i.e. Figure 5.8) and the fully desynchronised peak case (i.e. Figure 5.12), this parameter sensitivity is no longer observed. Chapter 5 therefore achieved **Objective 3** by developing and assessing the smart-charging algorithm in regards to communication desynchronisation.

From the lessons learnt in Chapter 5, and to circumvent the need to commu-

nifications altogether, Chapter 6 proposes a communication-less control method for distributed BESS to reduce peak load, voltage deviation and unequal asset utilisation. This communication-less control is achieved by using individualised control parameters in an improved AIMD algorithm. Co-locating dynamic loads, i.e. un-coordinated EVs, to maximise the stress on the LV network that the BESS control algorithm had to mitigate. The results show that for different EV uptake levels, BESS could always yield improvements for both AIMD and the proposed AIMD+ control methods. However, as seen in Figure 6.13, only the latter method did compensate uniformly across the LV network, since it took into account the network specific voltage characteristics. Therefore, the finding form the contribution to knowledge stated in Section 1.2 **Objective 4**.

The research over these four chapters has shown that energy storage algorithm can be improved by merging on-line and off-line control at high and low temporal resolution. Additionally, the research has shown that desynchronised control instructions can yield significantly different operation of otherwise synchronised control algorithms, yet this issue can be avoided by mitigating the need for ICT. In each chapter the thesis comprehensively tested the presented control algorithms on real demand data, which allowed it to encapsulate varying demand behaviour and characteristics at both high and low temporal resolutions. The overarching finding from Chapter 3 to Chapter 6 is, that there is not currently a single control algorithm that will consistently outperform all proposed covered aspects of the research. However, the results show that focused control can be tuned to achieve a significantly higher impact on a narrow set of key parameters, which is why the chapters that implement such methods do also present the means of implementing their control and thus achieve the subsequent improvements. One can thus conclude that the research that has been presented in this thesis is therefore beneficial to both industry and the academic research community. All objectives that were set out in the problem statement have

been met and the aforementioned key contributions have been made.

## 7.2 Knowledge Contribution

In Chapter 2, the literature is reviewed that surrounds the current and present control methods of DNO owned storage devices on the LV network. This literature review supports the thesis problem statement in Section 1.2 since it concluded with the identified gaps in literature in which further investigation and research was deemed necessary and beneficial for both the industry and academic research community. All chapters that are presented in this thesis make contributions within these identified gaps, and these contributions are summarised here:

- In accordance with **Objective 1**, a closed-loop phasor adjustment method is presented to control DNO owned BESS to maximise its beneficial impact on key network parameters of the LV network. Findings in Chapter 3 show how issues including e.g. voltage deviation, neutral currents, phase unbalance and losses can be individually reduced when adjusting BESS operation at a sub-half-hourly resolution, even when the device is constrained by an active power schedule at half-hourly time scale. However, this constraint still imposes limitations to the otherwise flexible BESS operation, but it also shows the benefits that can be achieved despite this constraint.
- In accordance with **Objective 2**, a dynamic schedule correcting BESS control method is presented to control DNO owned BESS to maximise its capabilities at reducing both daily demand peaks, i.e. at half-hourly resolution, whilst also mitigating volatile load peaks, i.e. at sub-half-hourly resolution. Findings in Chapter 4 show how the control method outperforms traditional BESS control and how the probability of reducing peak load can be noticeably increased. However, to achieve this improvement, the implicit assumption of an ICT infras-

ture could limited algorithm deployability when distributed across multiple devices.

- In accordance with **Objective 3**, a smart-charging algorithm for distributed control of an EV fleet was developed and deployed on a standardised MAS, which was desynchronised to assess the algorithm's performance. Findings in Chapter 5 show that the execution of the algorithm becomes less dependent on the underlying control parameters executed in a desynchronised environment, yet the overall performance of the algorithm remains intact. However, mitigating the need for ICT altogether would not only circumvent the issue of potential desynchronisation, but it would also lower deployment requirements and system cost.
- In accordance with **Objective 4**, a communication-less control method for distributed BESS was developed to assess its ability at reducing the negative impact from the charging of co-located EVs. Findings in Chapter 6 show that the developed AIMD+ algorithm does not only reduce peak loads or voltage deviation, but it also equalises the asset utilisation across the entire feeder. However, without any communication infrastructure, the performance of the proposed algorithm may be unable to address issues like e.g. phase unbalance, that have already been assessed in Chapter 3.

### 7.3 Research Limits

Several assumptions have been made throughout this thesis, and these assumptions imposed limitations on the presented research. These limitations are discussed here, in the subsequent subsections.

### **7.3.1 Energy storage model**

The developed model to capture the dynamics of the energy storage system was based on the system that was deployed during the NTVV project with SSEN. The simplicity of the energy storage model will limit the scope of the presented work when simulating the different storage control algorithms, especially when preparing for the deployment of an actual BESS. For instance, this model does not take into account any non-linear charging or discharging behaviours, nor does it consider operating temperature and heat radiation that would impact its dynamic efficiency. When anticipating to deploy the proposed BESS control algorithms that are presented in this thesis to an actual BESS, these limitations will need to be tested.

### **7.3.2 Electric vehicle charging**

In the previous chapter of this thesis, Chapter 6, a stochastic EV model was developed to simulate the predicted increase in electricity demand due to the uptake of EVs. This model assumed that vehicles are charged at home and begin their charging process immediately after being connected. This so called “dumb-charging” is mitigated by the control strategies that are proposed in the same chapter. However, recent smart-charging strategies promises to reduce the negative impacts from traditional EV charging. Therefore, the inclusion of smart charging is seen as a future work, since the implementation, validation and extension of available smart-charging schemes currently lies beyond the scope of this thesis.

### **7.3.3 Data**

All findings throughout the presented work were generated from historic demand data. This data has both limitations in temporal resolution and data length, which therefore limit the data’s ability to capture all possible load scenarios at the necessary accuracy

to guarantee correct algorithm operation. Since the entire work that is presented in this thesis relies on carrying out data driven simulations, using datasets with varying characteristics of demand profiles is necessary to assure the results cover a wide range of possibilities.

Also, since historic demand data does not capture the expected change in energy consumption, accompanying demand models had to be developed that also rely on several fundamental assumptions. For instance, the stochastic EV charging model in Chapter 6 assumed that driving behaviour will not change, apart from the location where vehicles are being refuelled or recharged. Being unable to make exact predictions about future loads lead to the development of such models since preventive BESS control algorithms could not be showcased.

#### 7.3.4 Network models

The dominant network model that was used throughout the research was a European LV model published by the IEEE. This so called “LV Test Case” complemented some of the in-house network models that were provided by SSEN, particularly since reproducibility of the findings could be assured. Different LV networks do however have noticeably different characteristics that can only be discovered and included in the research if the number of network models increases. Beside the shortage of EU network models, their accuracy cannot be guaranteed since old assets’ electrical characteristics might have degraded. A higher number of detailed and accurate network models would thus allow the proposed algorithms to be tested on a larger variety of networks, which would in turn improve certainty that the proposed algorithms will function correctly if deployed.

## **7.4 Future Work**

Based on the lessons learnt, the experience gained and the assumptions made whilst conducting the presented research, potential steps for future work are presented here, in the subsequent subsections:

### **7.4.1 Energy storage model**

Although the energy storage model that was used throughout this research is based on similar assumptions as those models that are used in other state of the art literature, there are still certain assumptions regarding this model that need not be disregarded in future research. The nonlinearity regarding the battery's charging behaviour for instance can be included since more battery characteristics have been discovered over the recent past. Characteristics regarding constant-current constant-voltage charging paradigms, temperature and battery condition have become better understood. Especially with the dissemination of EV information and their charging curves, previously proprietary data has started to become ubiquitous and available to the public domain. In future work, such data could not only aid the simulation battery control algorithms, but could also take into account the battery conditions itself to maximise its life.

### **7.4.2 Network model and power flow simulation**

Future work will also incorporate the algorithms into a more accurate and standardised network model. Power flow simulations on OpenDSS, PowerSim, GridLab-D or similar tools are frequently used throughout literature to create accurate network assessments. Having learnt the standardised network model structure that is specified by the IEEE in the recently published European test feeder will allow any future work to utilise the updated collection of network models in a compliant manner. Such

compliance would also allow the assessment of network failures, harmonic studies and islanded operation, which would previously have been impossible. Furthermore, with improved and updated network information, simulation tools would also give more accurate results regarding, e.g. the location and scaling of LV assets. Finally, by cooperating with research institutes, i.e. EPRI and NERL in the United States, it has now become possible to accelerate the simulation of network models by parallelising the power flow simulations. Therefore extending the number of trials would also improve the finding's certainty and lead to more conclusive results.

#### **7.4.3 Different MPC**

So far, the selection of MPC was based on both literature recommendations and the scope of the presented research. However, computer science driven areas of research including, e.g. artificial intelligence (AI), are becoming increasingly popular and have also begun penetrating the control of power network assets. With the ever increasing abilities of computers, such complex control approaches are likely to outperform traditional deterministic and probabilistic methods. Future work is therefore likely to also include AI aspects to assess their performance and to also understand how AI can safely be implemented.

#### **7.4.4 Governance**

At the present time there is also a considerable discussion regarding the changes in governance required for DNOs to own and operate energy storage devices, as well as whether DNOs will have access to customer's smart-meter data. These changes are likely to be important, in order for the findings and methods that are presented in this thesis to fit into the DNO's business strategy and capability.

### **7.4.5 Data acquisition and estimation**

The data that was used for simulations to trigger certain control instructions may not be available in reality. Although substation monitoring and voltage measurements at the energy storage were a certain prerequisite for most of the presented research, other network parameters, e.g. customer voltages, can only be obtained at significant financial cost or at low resolution. Being able to include a data acquisition mechanisms that are comparable to reality (e.g. data acquisition through the deployment of smart-meters) would strengthen the validity of the resulting findings. In cases where data acquisition is not possible either due to the lack of measuring equipment or the legal barriers that uphold customer privacy, endpoint data needs to be estimated instead. Developing a reliable method of estimating the endpoint data, e.g. customer voltages, from a limited number of measuring points is still an open research objective. Future work will therefore develop a method that uses BESS and substation data to maximise the certainty of endpoint data, which in turn can be used to improve future BESS control methods.



# References

- [1] National Grid, “Future Energy Scenarios How to use this document To help you find the information you need quickly and easily we have published the FES,” Tech. Rep. July, 2017.
- [2] Deloitte, “Energy storage: Tracking the technologies that will transform the power sector,” tech. rep., 2016.
- [3] M. Coulthard, M. Fila, G. Evans, R. Potter, and Scottish and Southern Energy Power Distribution, “New Thames Valley Vision, SDRC 9.8a (4) Report, LV Network Energy Storage ESMU Trials,” tech. rep., 2015.
- [4] HM Government, *The UK Low Carbon Transition Plan: National strategy for climate and energy*. 2009.
- [5] Royal Academy of Engineering, *Generating the Future: UK energy systems fit for 2050*. 2010.
- [6] A. Poghosyan, D. V. Greetham, S. Haben, and T. Lee, “Long term individual load forecast under different electrical vehicles uptake scenarios,” *Appl. Energy*, vol. 157, pp. 699–709, 2014.
- [7] National Grid, “Winter Review and Consultation - 2017,” Tech. Rep. June, 2017.

- [8] S. Cuddihy and S. Mockford, “Engineering Design Standar - EDS 08-0115 - Loading of Secondary Distribution Transformers,” Tech. Rep. 1, UK Power Networks, 2015.
- [9] Health and Safety Executive, “Electricity Safety, Quality and Continuity Regulations (ESQCR),” 2002.
- [10] Energy Networks Association, “Engineering Recommendation G59 Issue 3: Recommendations for the Connection of Generating Plant to the Distribution Systems of Licensed Distribution Network Operators,” tech. rep., 2013.
- [11] Electricity North West Ltd, “Low Voltage Network Solutions, A First Tier Low Carbon Networks Fund Project, Closedown Report,” Tech. Rep. June, 2014.
- [12] A. Woyte, V. V. Thong, R. Belmans, and J. Nijs, “Voltage fluctuations on distribution level introduced by photovoltaic systems,” *IEEE Trans. Energy Convers.*, vol. 21, no. 1, pp. 202–209, 2006.
- [13] I. Richardson, M. Thomson, D. Infield, and C. Clifford, “Domestic electricity use: A high-resolution energy demand model,” *Energy Build.*, vol. 42, no. 10, pp. 1878–1887, 2010.
- [14] T. Yunusov, D. Frame, W. Holderbaum, and B. Potter, “The impact of location and type on the performance of low-voltage network connected battery energy storage systems,” *Appl. Energy*, vol. 165, pp. 202–213, 2016.
- [15] X. Fang, S. Misra, G. Xue, and D. Yang, “Smart Grid — The New and Improved Power Grid: A Survey,” *IEEE Commun. Surv. Tutorials*, vol. 14, no. 4, pp. 944–980, 2012.
- [16] G. Ault, D. Frame, N. Hughes, and N. Strachan, “Electricity Network Scenarios for Great Britain in 2050,” tech. rep., 2008.

- [17] H. Chen, T. N. Cong, W. Yang, C. Tan, Y. Li, and Y. Ding, “Progress in electrical energy storage system: A critical review,” *Prog. Nat. Sci.*, vol. 19, no. 3, pp. 291–312, 2009.
- [18] G. P. Harrison, A. Piccolo, P. Siano, and a. R. Wallace, “Exploring the tradeoffs between incentives for distributed generation developers and DNOs,” *IEEE Trans. Power Syst.*, vol. 22, no. 2, pp. 821–828, 2007.
- [19] M. J. Zangs, P. B. E. Adams, T. Yunusov, W. Holderbaum, and B. A. Potter, “Distributed energy storage control for dynamic load impact mitigation,” *Energies*, vol. 9, no. 8, 2016.
- [20] T. van der Klauw, J. Hurink, and G. Smit, “Scheduling of Electricity Storage for Peak Shaving with Minimal Device Wear,” *Energies*, vol. 9, p. 465, 2016.
- [21] D. M. Greenwood, N. S. Wade, P. C. Taylor, P. Papadopoulos, and N. Heyward, “Storage and Real-Time Thermal Ratings to Defer Network Reinforcement,” *IEEE Trans. Sustain. Energy*, vol. 8, no. 1, pp. 374–384, 2017.
- [22] N. S. Wade, P. C. Taylor, P. D. Lang, and P. R. Jones, “Evaluating the benefits of an electrical energy storage system in a future smart grid,” *Energy Policy*, vol. 38, no. 11, pp. 7180–7188, 2010.
- [23] O. Palizban and K. Kauhaniemi, “Energy storage systems in modern grids — Matrix of technologies and applications,” *J. Energy Storage*, vol. 6, pp. 248–259, 2016.
- [24] Y. Yang, H. Li, A. Aichhorn, J. Zheng, and M. Greenleaf, “Sizing strategy of distributed battery storage system with high penetration of photovoltaic for voltage regulation and peak load shaving,” *IEEE Trans. Smart Grid*, vol. 5, no. 2, pp. 982–991, 2014.

- [25] C. J. Bennett, R. A. Stewart, and J. W. Lu, “Development of a three-phase battery energy storage scheduling and operation system for low voltage distribution networks,” *Appl. Energy*, vol. 146, pp. 122–134, 2015.
- [26] L. Wang, D. Liang, A. F. Crossland, P. C. Taylor, D. Jones, and N. S. Wade, “Coordination of Multiple Energy Storage Units in a Low Voltage Distribution Network,” *IEEE Trans. Power Syst.*, vol. 6, no. 6, pp. 2906–2918, 2015.
- [27] C. Cecati, C. Citro, and P. Siano, “Combined operations of renewable energy systems and responsive demand in a smart grid,” *IEEE Trans. Sustain. Energy*, vol. 2, no. 4, pp. 468–476, 2011.
- [28] A. Chaouachi, R. M. Kamel, R. Andoulsi, and K. Nagasaka, “Multiobjective Intelligent Energy Management for a Microgrid — Aymen Chaouachi - Academia,” *IEEE Trans. Ind. Electron.*, vol. 60, no. 4, pp. 1688–1699, 2013.
- [29] R. Palma-Behnke, C. Benavides, F. Lanas, B. Severino, L. Reyes, J. Llanos, and D. Saez, “A microgrid energy management system based on the rolling horizon strategy,” *IEEE Trans. Smart Grid*, vol. 4, no. 2, pp. 996–1006, 2013.
- [30] A. Khodaei, “Microgrid Optimal Scheduling With Multi-Period Islanding Constraints,” *IEEE Trans. Power Syst.*, vol. 29, no. 3, pp. 1383–1392, 2014.
- [31] S. Salinas, M. Li, P. Li, and Y. Fu, “Dynamic Energy Management for the Smart Grid With Distributed Energy Resources,” *Smart Grid, IEEE Trans.*, vol. 4, no. 4, pp. 2139–2151, 2013.
- [32] Y. Huang, S. Mao, and R. M. Nelms, “Adaptive electricity scheduling in microgrids,” in *INFOCOM, 2013 Proc. IEEE*, pp. 1142–1150, 2013.
- [33] Y. Huang, S. Mao, and R. M. Nelms, “Adaptive electricity scheduling in microgrids,” *IEEE Trans. Smart Grid*, vol. 5, no. 1, pp. 270–281, 2014.

- [34] S. Sun, M. Dong, and B. Liang, “Joint Supply, Demand, and Energy Storage Management Towards Microgrid Cost Minimization,” *IEEE Int. Conf. Smart Grid Commun. Jt.*, pp. 109–114, 2014.
- [35] G. Mokhtari, G. Nourbakhsh, and A. Ghosh, “Smart coordination of energy storage units (ESUs) for voltage and loading management in distribution networks,” *IEEE Trans. Power Syst.*, vol. 28, no. 4, pp. 4812–4820, 2013.
- [36] M. R. Sarker, M. A. Ortega-Vazquez, and D. S. Kirschen, “Optimal Coordination and Scheduling of Demand Response via Monetary Incentives,” *IEEE Trans. Smart Grid*, vol. 6, no. 3, pp. 1341–1352, 2015.
- [37] K. Baker, J. Guo, G. Hug, and X. Li, “Distributed MPC for Efficient Coordination of Storage and Renewable Energy Sources Across Control Areas,” *IEEE Trans. Smart Grid*, vol. 7, no. 2, pp. 992–1001, 2016.
- [38] T. Baumann and F. Baumgartner, “Home Batteriespeicher Studie für solarpar,” tech. rep., Zurich University of Applied Science - School of Engineering, 2017.
- [39] E. Sortomme, M. M. Hindi, S. D. J. MacPherson, and S. S. Venkata, “Coordinated Charging of Plug-In Hybrid Electric Vehicles to Minimize Distribution System Losses,” *IEEE Trans. Smart Grid*, vol. 2, no. 1, pp. 198–205, 2011.
- [40] M. G. Vaya and G. Andersson, “Centralized and decentralized approaches to smart charging of plug-in Vehicles,” in *IEEE Power Energy Soc. Gen. Meet.*, (San Diego, CA), pp. 1–8, IEEE, 2012.
- [41] J. García-Villalobos, I. Zamora, J. San Martín, F. Asensio, and V. Aperribay, “Plug-in electric vehicles in electric distribution networks: A review of smart charging approaches,” *Renew. Sustain. Energy Rev.*, vol. 38, pp. 717–731, oct 2014.

- [42] E. L. Karfopoulos and N. D. Hatziargyriou, “A Multi-Agent System for Controlled Charging of a Large Population of Electric Vehicles,” *IEEE Trans. Power Syst.*, vol. 28, pp. 1196–1204, may 2013.
- [43] P. Samadi, H. Mohsenian-Rad, R. Schober, and V. W. S. Wong, “Advanced Demand Side Management for the Future Smart Grid Using Mechanism Design,” *IEEE Trans. Smart Grid*, vol. 3, no. 3, pp. 1170–1180, 2012.
- [44] Y. Liu, C. Yuen, S. Huang, N. Ul Hassan, X. Wang, and S. Xie, “Peak-to-average ratio constrained demand-side management with consumer’s preference in residential smart grid,” *IEEE J. Sel. Top. Signal Process.*, vol. 8, no. 6, pp. 1084–1097, 2014.
- [45] H. Liang, A. K. Tamang, W. Zhuang, and X. S. Shen, “Stochastic Information Management in Smart Grid,” *IEEE Commun. Surv. Tutorials*, vol. PP, no. 99, pp. 1–25, 2014.
- [46] T. L. Baldwin and S. A. Lweis, “Distribution Load Flow Methods for Shipboard Power Systems,” *IEEE Trans. Ind. Appl.*, vol. 40, no. 5, pp. 1183–1190, 2004.
- [47] N. L. Díaz, J. C. Vasquez, and J. M. Guerrero, “A Communication-less Distributed Control Architecture for Islanded Microgrids with Renewable Generation and Storage,” *IEEE Trans. Power Electron.*, vol. 8993, no. c, pp. 1–1, 2017.
- [48] M. Wilks, “Demand side response : Conflict between supply and network driven optimisation. A report to DECC,” Tech. Rep. November, 2010.
- [49] US Department of Energy, “DOE Global Energy Storage Database,” 2017.
- [50] G. Garton and D. E. A. Grimwood, “Energy Storage in the UK An Overview,” Tech. Rep. 07621, 2016.

- [51] F. R. Kalhammer, “Energy-Storage Systems,” *Sci. Am.*, vol. 241, no. 6, pp. 42–51, 1979.
- [52] J. Eyer and G. Corey, “Energy Storage for the Electricity Grid : Benefits and Market Potential Assessment Guide,” tech. rep., Sandia National Laboratories, 2010.
- [53] M. Katsanevakis, R. A. Stewart, and J. Lu, “Aggregated applications and benefits of energy storage systems with application-specific control methods: A review,” *Renew. Sustain. Energy Rev.*, vol. 75, no. August 2016, pp. 719–741, 2017.
- [54] M. S. Guney and Y. Tepe, “Classification and assessment of energy storage systems,” *Renew. Sustain. Energy Rev.*, vol. 75, no. February 2016, pp. 1187–1197, 2017.
- [55] R.-C. Leou, “An economic analysis model for the energy storage systems in a deregulated market,” *Electr. Power Energy Syst.*, vol. 34, no. 1, p. 132, 2012.
- [56] S. Koohi-Kamali, V. V. Tyagi, N. A. Rahim, N. L. Panwar, and H. Mokhlis, “Emergence of energy storage technologies as the solution for reliable operation of smart power systems: A review,” *Renew. Sustain. Energy Rev.*, vol. 25, pp. 135–165, 2013.
- [57] W. C. Dobie, “Electrical Energy Storage,” *Power Eng. J.*, vol. 12, no. 4, pp. 177–181, 1998.
- [58] S. Rehman, L. M. Al-Hadhrami, and M. M. Alam, “Pumped hydro energy storage system: A technological review,” *Renew. Sustain. Energy Rev.*, vol. 44, pp. 586–598, 2015.
- [59] E. Barbour, “Energy Storage Sense,” 2015.

- [60] E. Barbour, I. A. G. Wilson, J. Radcliffe, Y. Ding, and Y. Li, “A review of pumped hydro energy storage development in significant international electricity markets,” *Renew. Sustain. Energy Rev.*, vol. 61, pp. 421–432, 2016.
- [61] H. Bevrani and T. Hiyama, *Intelligent Automatic Generation Control*. CRC Press, 2011.
- [62] J. F. Cole, “Battery energy-storage systems — an emerging market for lead/acid batteries,” *J. Power Sources*, vol. 53, no. 2, pp. 239–243, 1995.
- [63] M. A. Kashem and G. Ledwich, “Energy requirement for distributed energy resources with battery energy storage for voltage support in three-phase distribution lines,” *Electr. Power Syst. Res.*, vol. 77, no. 1, pp. 10–23, 2007.
- [64] P. Kulkarni, J. H. Sayer, J. D. Boyes, G. P. Corey, and G. H. Peek, “The United States of Storage,” *IEEE Power Energy Mag.*, vol. 3, no. 2, pp. 31–39, 2005.
- [65] P. Kundur, *Power System Stability And Control*. McGraw-Hill Inc., 1993.
- [66] A. Chakraborty, S. K. Musunuri, A. K. Srivastava, and A. K. Kondabathini, “Integrating STATCOM and battery energy storage system for power system transient stability: A review and application,” *Adv. Power Electron.*, p. 12, 2012.
- [67] S. Kolluri, S. Member, and N. Orleans, “Application of Distributed Superconducting Magnetic Energy Storage System ( D-SMES ) in the Entergy System to Improve Voltage Stability,” in *IEEE Power Eng. Soc. Winter Meet.*, (New York, NY, USA), pp. 838–841, 2002.
- [68] L. Wang, L. Muh, and L. Huang, “Damping subsynchronous resonance usinf superconducting magnetic energy storage unit,” *IEEE Trans. Energy Convers.*, vol. 9, no. 4, pp. 770–777, 1994.

- [69] J. H. Sayer, “Guide to Estimating Benefits and Market Potential for Electricity Storage in New York,” tech. rep., 2007.
- [70] G. Huff, A. B. Currier, B. C. Kaun, D. M. Rastler, S. B. Chen, D. T. Bradshaw, and W. D. Gauntlett, “DOE/EPRI 2013 electricity storage handbook in collaboration with NRECA,” Tech. Rep. July, 2013.
- [71] A. Saez-de Ibarra, A. Milo, H. Gaztanaga, I. Etxeberria-Otadui, P. Rodríguez, S. Bacha, and V. Debusschere, “Analysis and comparison of battery energy storage technologies for grid applications,” *PowerTech (POWERTECH), 2013 IEEE Grenoble*, pp. 1–6, 2013.
- [72] E. Reihani, M. Motalleb, R. Ghorbani, and L. Saad Saoud, “Load peak shaving and power smoothing of a distribution grid with high renewable energy penetration,” *Renew. Energy*, vol. 86, pp. 1372–1379, 2016.
- [73] M. E. T. Gerards and J. L. Hurink, “Robust peak-shaving for a neighborhood with electric vehicles,” *Energies*, vol. 9, no. 8, 2016.
- [74] S. M. Schoenung and W. Hassenzahl, “Characteristics and Technologies for Long-vs. Short-Term Energy Storage A: Study by the DOE Energy Storage Systems Program,” Tech. Rep. March, 2001.
- [75] G. Putrus, J. Wijayakulasooriya, and P. Minns, “Power quality: Overview and monitoring,” in *ICIIS 2007 - 2nd Int. Conf. Ind. Inf. Syst. 2007, Conf. Proc.*, pp. 551–558, 2007.
- [76] J. Miret, M. Castilla, J. Matas, J. Guerrero, and J. Vasquez, “Selective Harmonic-Compensation Control for Single-Phase Active Power Filter With High Harmonic Rejection,” *IEEE Trans. Ind. Electron.*, vol. 56, no. 8, pp. 3117–3127, 2009.

- [77] H. Khani, M. R. D. Zadeh, and R. Seethapathy, “Large-Scale Energy Storage Deployment in Ontario Utilizing Time-of-Use and Wholesale Electricity Prices: An Economic Analysis,” in *2014 CIGRÉ Canada Conf. Int. Cent.*, 2014.
- [78] N. K. C. Nair and N. Garimella, “Battery energy storage systems: Assessment for small-scale renewable energy integration,” *Energy Build.*, vol. 42, no. 11, pp. 2124–2130, 2010.
- [79] R. Luthander, J. Widén, J. Munkhammar, and D. Lingfors, “Self-consumption enhancement and peak shaving of residential photovoltaics using storage and curtailment,” *Energy*, vol. 112, pp. 221–231, 2016.
- [80] A. Oudalov, R. Cherkaoui, S. Member, and A. Beguin, “Sizing and Optimal Operation of Battery Energy Storage System for Peak Shaving Application,” in *2007 IEEE Lausanne Power Tech*, pp. 621–625, 2007.
- [81] K. Mackey, R. McCann, K. Rahman, and R. Winkelman, “Evaluation of a battery energy storage system for coordination of demand response and renewable energy resources,” *2013 4th IEEE Int. Symp. Power Electron. Distrib. Gener. Syst.*, pp. 1–8, 2013.
- [82] J. Aghaei and M. I. Alizadeh, “Demand response in smart electricity grids equipped with renewable energy sources: A review,” *Renew. Sustain. Energy Rev.*, vol. 18, pp. 64–72, 2013.
- [83] B. Zakeri and S. Syri, “Electrical energy storage systems: A comparative life cycle cost analysis,” *Renew. Sustain. Energy Rev.*, vol. 42, pp. 569–596, 2015.
- [84] W. Jewell and R. Ramakumar, “The effects of moving clouds on electric utilities with dispersed photovoltaic generation,” *IEEE Trans. Energy Convers.*, vol. EC-2, no. 4, pp. 570–576, 1987.

- [85] P. Taylor, C. Patsios, S. Munoz Vaca, D. Greenwood, and N. Wade, *Energy Storage Integration*. Elsevier Inc., 2016.
- [86] R. J. Bravo, R. Salas, T. Bialek, and C. Sun, “Distributed energy resources challenges for utilities,” *2015 IEEE 42nd Photovolt. Spec. Conf. PVSC 2015*, 2015.
- [87] A. Mohd, E. Ortjohann, A. Schmelter, N. Hamsic, D. Morton, S. Westphalia, A. Sciences, D. Soest, and L. Ring, “Challenges in integrating distributed Energy storage systems into future smart grid,” in *2008 IEEE Int. Symp. Ind. Electron.*, pp. 1627–1632, 2008.
- [88] G. N. Koureoumpezis, A. S. Safianni, G. S. Demetzos, and J. G. Kendristakis, “Investigation of the distributed generation penetration in a medium voltage power distribution network,” *Int. J. Energy Res.*, vol. 34, no. 7, pp. 585–593, 2010.
- [89] I. T. H. E. Resilience, “The Grid: Stronger, Bigger, Smarter?,” *IEEE Power Energy Mag.*, vol. 13, no. April, pp. 58–66, 2015.
- [90] S. Grillo, M. Marinelli, S. Massucco, and F. Silvestro, “Optimal management strategy of a battery-based storage system to improve renewable energy integration in distribution networks,” *IEEE Trans. Smart Grid*, vol. 3, no. 2, pp. 950–958, 2012.
- [91] M. Rowe, T. Yunusov, S. Haben, C. Singleton, W. Holderbaum, and B. Potter, “A Peak Reduction Scheduling Algorithm for Storage Devices on the Low Voltage Network,” *IEEE Trans. Smart Grid*, vol. 5, no. 4, pp. 2115–2124, 2014.
- [92] M. Hosseina, S. Mohammad, and T. Bathae, “Optimal scheduling for distribution network with redox flow battery storage,” *Energy Convers. Manag.*, vol. 121, pp. 145–151, 2016.

- [93] N. Li, C. Uckun, E. M. Constantinescu, J. R. Birge, K. W. Hedman, and A. Botterud, “Flexible Operation of Batteries in Power System Scheduling with Renewable Energy,” *IEEE Trans. Sustain. Energy*, vol. 7, no. 2, pp. 685–696, 2016.
- [94] Scottish and Southern Energy Power Distribution, DNV-GL, GE, Honeywell, L. Fund, University of Reading, and Bracknell Forest Council, “Thames Valley Vision - Project library - Published documents,” 2016.
- [95] P. F. Lyons, N. S. Wade, T. Jiang, P. C. Taylor, F. Hashiesh, M. Michel, and D. Miller, “Design and analysis of electrical energy storage demonstration projects on UK distribution networks,” *Appl. Energy*, vol. 137, pp. 677–691, 2015.
- [96] E.ON Energy, “E.ON breaks ground on Blackburn Meadows battery project,” 2017.
- [97] L. Dann, “Scottish Power pilots smart batteries in customer homes,” 2016.
- [98] P. D. F. Ferreira, P. M. S. Carvalho, L. A. F. M. Ferreira, and M. D. Ilic, “Distributed energy resources integration challenges in low-voltage networks: Voltage control limitations and risk of cascading,” *IEEE Trans. Sustain. Energy*, vol. 4, no. 1, pp. 82–88, 2013.
- [99] W. Shi, N. Li, C. C. Chu, and R. Gadh, “Real-time energy management in microgrids,” *IEEE Trans. Smart Grid*, vol. PP, no. 99, pp. 228–238, 2015.
- [100] H. Sun, Q. Guo, B. Zhang, W. Wu, and J. Tong, “Development and applications of system-wide automatic voltage control system in China,” *2009 IEEE Power Energy Soc. Gen. Meet. PES '09*, pp. 1–5, 2009.

- [101] M. Zangs, T. Yunusov, W. Holderbaum, and B. Potter, “On-line adjustment of battery schedules for supporting LV distribution network operation,” in *2016 Int. Energy Sustain. Conf. IESC 2016*, 2016.
- [102] M. Liserre, T. Sauter, and J. Y. Hung, “Future energy systems: Integrating renewable energy into the smart power grid through industrial electronics,” *IEEE Ind. Electron. Mag.*, vol. 4, no. March, pp. 18–37, 2010.
- [103] N. Wade, P. Taylor, P. Lang, and J. SVENSSON, “Energy storage for power flow management and voltage control on an 11kV UK distribution network,” *20th Int. Conf. Electr. Distrib.*, no. June, p. 0824, 2009.
- [104] F. Overbeeke and S. Cobben, “Operational aspects of a microgrid with battery storage,” in *Innov. Smart Grid Technol. Eur. (ISGT Eur. IEEE*, pp. 1–5, 2010.
- [105] GROWDERS, “Grid Reliability and Operability with Distributed Generation using Transportable Final activity report,” tech. rep., 2011.
- [106] H. Sugihara, K. Yokoyama, O. Saeki, K. Tsuji, and T. Funaki, “Economic and efficient voltage management using customer-owned energy storage systems in a distribution network with high penetration of photovoltaic systems,” *IEEE Trans. Power Syst.*, vol. 28, no. 1, pp. 102–111, 2013.
- [107] UK Power Networks, “Use of smart meter information for network planning and operation,” tech. rep., 2014.
- [108] Ofgem, “RIO - Electricity Distribution - Annual Report 2015-16,” Tech. Rep. February, 2017.
- [109] Ofgem, “December 2013 UK Storms Review – impact on electricity distribution customers,” Tech. Rep. March, 2014.

- [110] G. Putrus, P. Suwanapingkarl, D. Johnston, E. Bentley, and M. Narayana, “Impact of electric vehicles on power distribution networks,” in *2009 IEEE Veh. Power Propuls. Conf.*, pp. 827–831, 2009.
- [111] J. R. Pillai and B. Bak-Jensen, “Vehicle-to-grid systems for frequency regulation in an islanded Danish distribution network,” *2010 IEEE Veh. Power Propuls. Conf. VPPC 2010*, 2010.
- [112] H. J. Kunisch, K. G. Kramer, and H. Dominik, “Battery Energy Storage - Another Option for Load-Frequency-Control and Instantaneous Reserve,” *IEEE Power Eng. Rev.*, vol. PER-6, no. 9, pp. 24–25, 1986.
- [113] H. J. Kunisch, K. G. Kramer, and H. Dominik, “Battery Energy Storage Another Option for Load-Frequency-Control and Instantaneous Reserve,” *IEEE Trans. Energy Convers.*, vol. EC-1, no. 3, pp. 41–46, 1986.
- [114] A. Engler and N. Soultanis, “Droop control in LV-grids,” in *2005 Int. Conf. Futur. Power Syst.*, (Amsterdam), IEEE, 2005.
- [115] U. B. Tayab, M. A. B. Roslan, L. J. Hwai, and M. Kashif, “A review of droop control techniques for microgrid,” *Renew. Sustain. Energy Rev.*, vol. 76, no. March, pp. 717–727, 2017.
- [116] Y. Riffonneau, S. Bacha, F. Barruel, and S. Ploix, “Optimal Power Flow Management for Grid Connected PV Systems With Batteries,” *IEEE Trans. Sustain. Energy*, vol. 2, no. 3, pp. 309–320, 2011.
- [117] A. Sani Hassan, L. Cipcigan, and N. Jenkins, “Optimal battery storage operation for PV systems with tariff incentives,” *Appl. Energy*, vol. 203, pp. 422–441, 2017.

- [118] A. De Paola, D. Angeli, and G. Strbac, “Distributed Control of Micro-Storage Devices With Mean Field Games,” *IEEE Trans. Smart Grid*, vol. 7, no. 2, pp. 1119–1127, 2016.
- [119] Scottish and Southern Electricity Networks, “Battery Storage Workshop - Walton Park,” Tech. Rep. April, 2016.
- [120] M. Rowe, T. Yunusov, S. Haben, W. Holderbaum, and B. Potter, “The real-time optimisation of DNO owned storage devices on the LV network for peak reduction,” *Energies*, vol. 7, no. 6, pp. 3537–3560, 2014.
- [121] K. H. Chua, Y. S. Lim, P. Taylor, S. Morris, and J. Wong, “Energy storage system for mitigating voltage unbalance on low-voltage networks with photovoltaic systems,” *IEEE Trans. Power Deliv.*, vol. 27, no. 4, pp. 1783–1790, 2012.
- [122] K. Baker, G. Hug, and X. Li, “Energy Storage Sizing Taking Into Account Forecast Uncertainties and Receding Horizon Operation,” *IEEE Trans. Sustain. Energy*, vol. 8, pp. 331–340, jan 2017.
- [123] Y. Wang, X. Lin, and M. Pedram, “Adaptive control for energy storage systems in households with photovoltaic modules,” *IEEE Trans. Smart Grid*, vol. 5, no. 2, pp. 992–1001, 2014.
- [124] S. Haben, J. Ward, D. Vukadinovic Greetham, C. Singleton, and P. Grindrod, “A new error measure for forecasts of household-level, high resolution electrical energy consumption,” *Int. J. Forecast.*, vol. 30, no. 2, pp. 246–256, 2014.
- [125] F. Blaabjerg, R. Teodorescu, M. Liserre, and A. V. Timbus, “Overview of Control and Grid Synchronization for Distributed Power Generation Systems,” *IEEE Trans. Ind. Electron.*, vol. 53, no. 5, pp. 1398–1409, 2006.

- [126] L. Malesani and P. Tenti, “A Novel Hysteresis Control Method for Current-Controlled Voltage-Source PWM Inverters with Constant Modulation Frequency,” *IEEE Trans. Ind. Appl.*, vol. 26, no. 1, pp. 88–92, 1990.
- [127] Z. Xu, J. Ostergaard, and M. Togeby, “Demand as frequency controlled reserve,” *IEEE Trans. Power Syst.*, vol. 26, no. 3, pp. 1062–1071, 2011.
- [128] M. C. Such and C. Hill, “Battery energy storage and wind energy integrated into the Smart Grid,” in *2012 IEEE PES Innov. Smart Grid Technol.*, pp. 1–4, 2012.
- [129] T. Gybel, L. F. S. Larsen, K. Edlund, and J. Bagterp, “Model predictive control technologies for efficient and flexible power consumption in refrigeration systems,” *Energy*, vol. 44, no. 1, pp. 105–116, 2012.
- [130] N. D. Hatziargyriou, D. Škrlec, T. Capuder, P. S. Georgilakis, and M. Zidar, “Review of energy storage allocation in power distribution networks: applications, methods and future research,” *IET Gener. Transm. Distrib.*, pp. 1–8, 2015.
- [131] W. Li and Z. G. Zhang, “Based on time sequence of ARIMA model in the application of short-term electricity load forecasting,” *ICRCCS 2009 - 2009 Int. Conf. Res. Challenges Comput. Sci.*, pp. 11–14, 2009.
- [132] H. Nie, G. Liu, X. Liu, and Y. Wang, “Hybrid of ARIMA and SVMs for short-term load forecasting,” *Energy Procedia*, vol. 16, no. PART C, pp. 1455–1460, 2011.
- [133] T. Sannomiya, H. Hayashi, T. Ishii, and R. Ikeda, “Test results of compensation for load fluctuation under a fuzzy control by a 1 kWh/1 MW SMES,” *IEEE Trans. Appl. Supercond.*, vol. 11, no. 1, pp. 1908–1911, 2001.

- [134] S. X. Chen, H. B. Gooi, and M. Q. Wang, “Solar radiation forecast based on fuzzy logic and neural networks,” *Renew. Energy*, vol. 60, pp. 195–201, 2013.
- [135] H. Xia, H. Chen, Z. Yang, F. Lin, and B. Wang, “Optimal energy management, location and size for stationary energy storage system in a metro line based on genetic algorithm,” *Energies*, vol. 8, no. 10, pp. 11618–11640, 2015.
- [136] H. Liu, H. Tian, X. Liang, and Y. Li, “New wind speed forecasting approaches using fast ensemble empirical model decomposition, genetic algorithm, Mind Evolutionary Algorithm and Artificial Neural Networks,” *Renew. Energy*, vol. 83, pp. 1066–1075, 2015.
- [137] S. A. Kalogirou, E. Mathioulakis, and V. Belessiotis, “Artificial neural networks for the performance prediction of large solar systems,” *Renew. Energy*, vol. 63, pp. 90–97, 2014.
- [138] H. Quan, D. Srinivasan, and A. Khosravi, “Short-term load and wind power forecasting using neural network-based prediction intervals,” *IEEE Trans. Neural Networks Learn. Syst.*, vol. 25, no. 2, pp. 303–315, 2014.
- [139] D. Lee and R. Baldick, “Short-term wind power ensemble prediction based on gaussian processes and Neural networks,” *IEEE Trans. Smart Grid*, vol. 5, no. 1, pp. 501–510, 2014.
- [140] H. Pezeshki, P. Wolfs, S. Member, and G. L. S. Member, “A Model Predictive Approach for Community Battery Energy Storage System Optimization,” in *PES Gen. Meet. / Conf. Expo. 2014 IEEE*, pp. 27–31, 2014.
- [141] A. G. R. Vaz, B. Elsinga, W. G. J. H. M. van Sark, and M. C. Brito, “An artificial neural network to assess the impact of neighbouring photovoltaic systems in power forecasting in Utrecht, the Netherlands,” *Renew. Energy*, vol. 85, pp. 631–641, 2016.

- [142] L. Xiao, W. Shao, M. Yu, J. Ma, and C. Jin, “Research and application of a hybrid wavelet neural network model with the improved cuckoo search algorithm for electrical power system forecasting,” *Appl. Energy*, vol. 198, pp. 203–222, 2017.
- [143] M. Mansouri-Samani and M. Sloman, “Monitoring Distributed Systems,” *IEEE Netw.*, vol. 5, no. 6, pp. 20–30, 1993.
- [144] M. D. Nelson, “Load Management from a Power System Operator’s Perspective,” *IEEE Power Eng. Rev.*, vol. PER-5, no. 2, pp. 38–39, 1985.
- [145] K. Matsuzawa, M. Suzuki, Y. Okuhara, Y. Kishida, Y. Kudo, and T. Yamashita, “New energy management system for central dispatching center of Tokyo Electric Power Co., Inc,” *IEEE Trans. Power Syst.*, vol. 5, no. 4, pp. 1112–1117, 1990.
- [146] National Grid, “Managing the UK’s electricity system,” 2017.
- [147] P. N. Vovos, A. E. Kiprakis, A. R. Wallace, and G. P. Harrison, “Centralized and distributed voltage control: Impact on distributed generation penetration,” *IEEE Trans. Power Syst.*, vol. 22, no. 1, pp. 476–483, 2007.
- [148] J. M. Guerrero, L. Hang, and J. Uceda, “Control of Distributed Uninterruptible Power Supply Systems,” *IEEE Trans. Ind. Electron.*, vol. 55, no. 8, pp. 2845–2859, 2008.
- [149] A. Bidram, F. Lewis, and A. Davoudi, “Distributed Control Systems for Small-Scale Power Networks,” *IEEE Control Syst.*, vol. 34, no. December, pp. 56–77, 2014.
- [150] O. M. Toledo, D. Oliveira, A. Diniz, J. H. Martins, and M. H. M. Vale, “Methodology for Evaluation of Grid-Tie Connection of Distributed Energy Resources-

Case Study With Photovoltaic and Energy Storage,” *IEEE Trans. Power Syst.*, vol. 28, no. 2, pp. 1132–1139, 2013.

- [151] F. Marra, G. Y. Yang, Y. T. Fawzy, C. Træholt, E. Larsen, R. Garcia-Valle, and M. M. Jensen, “Improvement of local voltage in feeders with photovoltaic using electric vehicles,” *IEEE Trans. Power Syst.*, vol. 28, no. 3, pp. 3515–3516, 2013.
- [152] S. Gill, I. Kockar, and G. W. Ault, “Dynamic optimal power flow for active distribution networks,” *IEEE Trans. Power Syst.*, vol. 29, no. 1, pp. 121–131, 2014.
- [153] M. J. Dolan, G. W. Ault, D. F. Frame, S. Gill, I. Kockar, O. Anaya-Lara, S. Galloway, B. O’Neill, C. Foote, and A. Svalovs, “Northern Isles New Energy Solutions: Active network management stability limits,” *Innov. Smart Grid Technol. (ISGT Eur. 2012 3rd IEEE PES Int. Conf. Exhib.)*, pp. 1–9, 2012.
- [154] R. Atia and N. Yamada, “Sizing and Analysis of Renewable Energy and Battery Systems in Residential Microgrids,” *IEEE Trans. Smart Grid*, vol. 7, no. 3, pp. 1204–1213, 2016.
- [155] A. Bidram and A. Davoudi, “Hierarchical Structure of Microgrids Control System,” *IEEE Trans. Smart Grid*, vol. 3, no. 4, pp. 1963–1976, 2012.
- [156] Z. Wang, B. Chen, J. Wang, and J. Kim, “Decentralized Energy Management System for Networked Microgrids in Grid-Connected and Islanded Modes,” *IEEE Trans. Smart Grid*, vol. 7, no. 2, pp. 1097–1105, 2016.
- [157] J. M. Guerrero, M. Chandorkar, T.-L. Lee, and P. C. Loh, “Advanced Control Architectures for Intelligent Microgrids - Part I: Decentralized and Hierarchical Control,” *IEEE Trans. Ind. Electron.*, vol. 60, pp. 1254–1262, apr 2013.

- [158] J. M. Guerrero, P. C. Loh, T.-L. Lee, and M. Chandorkar, “Advanced Control Architectures for Intelligent Microgrids - Part II: Power Quality, Energy Storage, and AC/DC Microgrids,” *IEEE Trans. Ind. Electron.*, vol. 60, no. 4, pp. 1263–1270, 2013.
- [159] S. Russell and P. Norvig, *Artificial Intelligence - A modern Approach (Third Edition)*. Prentice Hall, 2010.
- [160] M. Wooldridge and N. R. Jennings, “The Knowledge Engineering Review,” in *Knowl. Eng. Rev.*, vol. 10, ch. Intelligen, pp. 115–152, Cambridge University Press, jul 1995.
- [161] A. Al-Hinai and A. Feliachi, “Application of intelligent control agents in power systems with distributed generators,” in *Power Syst. Conf. Expo. 2004. IEEE PES*, pp. 1514–1519 vol.3, IEEE, 2004.
- [162] A. L. Dimeas and N. D. Hatziaargyriou, “Operation of a multiagent system for microgrid control,” *IEEE Trans. Power Syst.*, vol. 20, no. 3, pp. 1447–1455, 2005.
- [163] C. Dou, Z. Zhang, D. Yue, and Y. Zheng, “MAS-Based Hierarchical Distributed Coordinate Control Strategy of Virtual Power Source Voltage in Low-Voltage Microgrid,” *IEEE Access*, vol. 5, pp. 11381–11390, 2017.
- [164] M. Vasirani, R. Kota, R. L. Cavalcante, S. Ossowski, and N. R. Jennings, “An Agent-Based Approach to Virtual Power Plants of Wind Power Generators and Electric Vehicles,” *IEEE Trans. Smart Grid*, vol. 4, pp. 1314–1322, sep 2013.
- [165] J. J. Gómez-Sanz, S. Garcia-Rodriguez, N. Cuartero-Soler, and L. Hernandez-Callejo, “Reviewing Microgrids from a Multi-Agent Systems Perspective,” *Energies*, vol. 7, pp. 3355–3382, may 2014.

- [166] J. K. Kok, C. J. Warmer, and I. G. Kamphuis, “PowerMatcher: Multiagent control in the electricity infrastructure,” *Proc. fourth Int. Jt. Conf. Auton. agents multiagent Syst. - AAMAS '05*, vol. 48, no. 3, p. 75, 2005.
- [167] H. Li, H. Sun, J. Wen, S. Cheng, and H. He, “A fully decentralized multi-agent system for intelligent restoration of power distribution network incorporating distributed generations,” *IEEE Comput. Intell. Mag.*, vol. 7, no. 4, pp. 66–76, 2012.
- [168] F. Ding and K. A. Loparo, “Feeder Reconfiguration for Unbalanced Distribution Systems With Distributed Generation: A Hierarchical Decentralized Approach,” *IEEE Trans. Power Syst.*, vol. 31, no. 2, pp. 1633–1642, 2016.
- [169] M. a. López, S. Martín, J. a. Aguado, and S. De La Torre, “Optimal microgrid operation with electric vehicles,” in *IEEE PES Innov. Smart Grid Technol. Conf. Eur.*, (Manchester), pp. 1–8, IEEE, 2011.
- [170] B. Ramachandran, S. K. Srivastava, and D. A. Cartes, “Intelligent power management in micro grids with EV penetration,” *Expert Syst. Appl.*, vol. 40, pp. 6631–6640, nov 2013.
- [171] I. Grau Unda, P. Papadopoulos, S. Skarvelis-Kazakos, L. M. Cipcigan, N. Jenkins, and E. Zabala, “Management of electric vehicle battery charging in distribution networks with multi-agent systems,” *Electr. Power Syst. Res.*, vol. 110, pp. 172–179, may 2014.
- [172] M. E. Baran and I. M. El-Markabi, “A Multiagent-Based Dispatching Scheme for Distributed Generators for Voltage Support on Distribution Feeders,” *IEEE Trans. Power Syst.*, vol. 22, no. 1, pp. 52–59, 2007.
- [173] V. M. Catterson, E. Davidson, and S. D. J. Mcarthur, “Issues in Integrating Existing Multi-Agent Systems for Power Engineering Applications,” in *Proc.*

*13th Int. Conf. on, Intell. Syst. Appl. to Power Syst.*, (Arlington, VA), pp. 396–401, Ieee, 2005.

- [174] S. D. J. McArthur, S. M. Strachan, and G. Jahn, “The design of a multi-agent transformer condition monitoring system,” *IEEE Trans. Power Syst.*, vol. 19, no. 4, pp. 1845–1852, 2004.
- [175] J. A. Hossack, J. Menal, S. D. J. McArthur, and J. R. McDonald, “A multiagent architecture for protection engineering diagnostic assistance,” *IEEE Trans. Power Syst.*, vol. 18, no. 2, pp. 639–647, 2003.
- [176] W. He, G. Chen, Q.-l. Han, W. Du, J. Cao, and F. Qian, “Multiagent Systems on Multilayer Networks : Synchronization Analysis and Network Design,” *IEEE Trans. Syst. Man, Cybern. Syst.*, vol. 47, no. 7, pp. 1655–1667, 2017.
- [177] A. R. Hota, M. Juvvanapudi, and P. Bajpai, “Issues and solution approaches in PHEV integration to smart grid,” *Renew. Sustain. Energy Rev.*, vol. 30, pp. 217–229, feb 2014.
- [178] L. Liu, F. Kong, X. Liu, Y. Peng, and Q. Wang, “A review on electric vehicles interacting with renewable energy in smart grid,” *Renew. Sustain. Energy Rev.*, vol. 51, pp. 648–661, 2015.
- [179] V. Shah and J. Boorem-Phelps, “F.I.T.T. for Investors: Crossing the Chasm,” tech. rep., 2015.
- [180] A. H. Mohsenian-Rad, V. W. S. Wong, J. Jatskevich, R. Schober, and A. Leon-Garcia, “Autonomous demand-side management based on game-theoretic energy consumption scheduling for the future smart grid,” *IEEE Trans. Smart Grid*, vol. 1, no. 3, pp. 320–331, 2010.

- [181] S. Deilami and A. S. Masoum, “Real-time coordination of plug-in electric vehicle charging in smart grids to minimize power losses and improve voltage profile,” *IEEE Trans. Smart Grid*, vol. 2, no. 3, pp. 456–467, 2011.
- [182] W. Surles and G. P. Henze, “Evaluation of automatic priced based thermostat control for peak energy reduction under residential time-of-use utility tariffs,” *Energy Build.*, vol. 49, pp. 99–108, 2012.
- [183] A. S. Masoum, S. Deilami, and M. A. S. Masoum, “Fuzzy Approach for Online Coordination of Plug-In Electric Vehicle Charging in Smart Grid,” *IEEE Trans. Sustain. Energy*, vol. 6, no. 3, pp. 1112–1121, 2015.
- [184] J. Leadbetter and L. Swan, “Battery storage system for residential electricity peak demand shaving,” *Energy Build.*, vol. 55, pp. 685–692, 2012.
- [185] H. Thieblemont, F. Haghigat, R. Ooka, and A. Moreau, “Predictive Control Strategies based on Weather Forecast in Buildings with Energy Storage System: A Review of the State-of-the Art,” *Energy Build.*, vol. Available, 2017.
- [186] Z. Jiang, L. Gao, and R. A. Dougal, “Adaptive Control Strategy for Active Power Sharing in Hybrid Fuel Cell/Battery Power Sources,” *IEEE Trans. Energy Convers.*, vol. 22, no. 2, pp. 507–515, 2007.
- [187] D.-M. Chiu and R. Rain, “Analysis of the increase and decrease algorithms for congestion avoidance in computer networks,” in *Comput. Networks ISDN Syst.*, pp. 1–14, Elsevier, 1989.
- [188] F. Wirth, S. Stuedli, J. Y. Yu, M. Corless, and R. Shorten, “IBM Research Report: Nonhomogeneous Place-Dependent Markov Chains, Unsynchronised AIMD, and Network Utility Maximization,” tech. rep., IBM, 2014.

- [189] S. Stüdli, E. Crisostomi, R. Middleton, and R. Shorten, “A flexible distributed framework for realising electric and plug-in hybrid vehicle charging policies,” *Int. J. Control.*, vol. 85, no. 8, pp. 1130–1145, 2012.
- [190] S. Studli, W. Griggs, E. Crisostomi, and R. Shorten, “On Optimality Criteria for Reverse Charging of Electric Vehicles,” *IEEE Trans. Intell. Transp. Syst.*, vol. 15, no. 1, pp. 451–456, 2014.
- [191] S. Stüdli, E. Crisostomi, R. Middleton, and R. Shorten, “Optimal real-time distributed V2G and G2V management of electric vehicles,” *Int. J. Control.*, vol. 87, no. 6, pp. 1153–1162, 2014.
- [192] S. Stüdli, E. Crisostomi, R. Middleton, J. Braslavsky, and R. Shorten, “Distributed Load Management Using Additive Increase Multiplicative Decrease Based Techniques,” in *Plug Electr. Veh. Smart Grids*, pp. 173–202, Springer Singapore, 2015.
- [193] T. Yunusov, W. Holderbaum, and B. Potter, “Cost function for sub-agent elements in multi-agent energy management system,” in *2011 2nd IEEE PES Int. Conf. Exhib. Innov. Smart Grid Technol.*, pp. 1–8, 2011.
- [194] American National Standards Institute Inc., “ANSI/NEMA MG 1-2011,” tech. rep., American National Standards Institute Inc., 2011.
- [195] Power and Energy Society, “Distribution Test Feeders,” 2017.
- [196] H. A. Mostafa, R. E. Shatshat, and M. M. A. Salama, “A Correlated Equilibrium Game-Theoretic Approach for Multiple Participants Electric Distribution Systems Operation,” *IEEE Trans. Smart Grid*, vol. 7, no. 1, pp. 32–42, 2016.
- [197] “Foundation for Intelligent Physical Agents (FIPA) Standard Status Specification.”

- [198] Commission for Energy Regulation (CER), “Irish Social Science Data Archive. CER Smart Metering Project,” 2002.
- [199] M. Luck, R. Ashri, and M. D’Inverno, *Agent-Based Software Development*. Norwood, MA, USA: Artech House, Inc., 2004.
- [200] Telecom Italia, “Java Agent Development Framework,” 2015.
- [201] Foundation For Intelligent Physical Agents, “FIPA Agent Management Specification,” tech. rep., Foundation For Intelligent Physical Agents, 2002.
- [202] F. Y. S. Eddy and H. B. Gooi, “Multi-agent system for optimization of microgrids,” in *8th Int. Conf. Power Electron. - ECCE Asia*, (Jeju), pp. 2374–2381, Ieee, may 2011.
- [203] M.-T. Kuo and S.-D. Lu, “Design and Implementation of Real-Time Intelligent Control and Structure Based on Multi-Agent Systems in Microgrids,” *Energies*, vol. 6, pp. 6045–6059, nov 2013.
- [204] S. Mocci, N. Natale, S. Ruggeri, and F. Pilo, “Multi-agent control system for increasing hosting capacity in active distribution networks with EV,” in *2014 IEEE Int. Energy Conf.*, (Cavtat), pp. 1409–1416, Ieee, may 2014.
- [205] W. Li, T. Logenthiran, V. T. Phan, and W. L. Woo, “Intelligent Multi-Agent System for Power Grid Communication,” *IEEE Reg. 10 Annu. Int. Conf. Proceedings/TENCON*, pp. 3386–3389, 2017.
- [206] P. H. Nguyen, W. L. Kling, I. G. Kamphuis, and P. Ribeiro, “Integration of agent-based functions to facilitate operation of Smart Distribution Networks,” in *2011 2nd IEEE PES Int. Conf. Exhib. Innov. Smart Grid Technol.*, (Manchester), pp. 1–5, Ieee, dec 2011.

- [207] T. Nagata and S. Fukunaga, “An autonomous distributed agent approach to power system restoration,” *16th Int. Conf. Intell. Syst. Appl. to Power Syst.*, pp. 1–5, sep 2011.
- [208] T. Nagata, Y. Ueda, and M. Utatani, “A multi-agent approach to smart grid energy management,” in *2012 10th Int. Power Energy Conf.*, (Ho Chi Minh City), pp. 327–331, Ieee, nov 2012.
- [209] I. Mareels, T. Alpcan, M. Brazil, J. de Hoog, and D. a. Thomas, “A distributed electric vehicle charging management algorithm using only local measurements,” in *Innov. Smart Grid Technol. Conf. (ISGT), 2014 IEEE PES*, (Washington, DC), pp. 1–5, 2014.
- [210] L. Xia, J. D. Hoog, T. Alpcan, and M. Brazil, “Electric Vehicle Charging : A Noncooperative Game Using Local Measurements,” in *Int. Fed. Autom. Control*, (Cape Town), pp. 5426–5431, 2014.
- [211] J. Munkhammar, J. D. Bishop, J. J. Sarralde, W. Tian, and R. Choudhary, “Household electricity use, electric vehicle home-charging and distributed photovoltaic power production in the city of Westminster,” *Energy Build.*, vol. 86, pp. 439–448, 2015.
- [212] D. Dallinger and M. Wietschel, “Grid integration of intermittent renewable energy sources using price-responsive plug-in electric vehicles,” *Renew. Sustain. Energy Rev.*, vol. 16, pp. 3370–3382, jun 2012.
- [213] Infas and Deutsches Zentrum für Luft- und Raumfahrt e.V, “Mobilität in Deutschland 2008,” tech. rep., Bonn und Berlin, Deutschland, 2008.
- [214] National Grid, “Future Energy Scenarios 2015,” Tech. Rep. July, 2015.

- [215] I. Laresgoiti, S. Käbitz, M. Ecker, and D. U. Sauer, “Modeling mechanical degradation in lithium ion batteries during cycling: Solid electrolyte interphase fracture,” *J. Power Sources*, vol. 300, pp. 112–122, 2015.
- [216] UK Government Digital Service, “Vehicle free-flow speeds (SPE01),” 2013.
- [217] UK Office for Low Emission Vehicles, “Electric Vehicle Homecharging Scheme - Guidance for manufacturers and installers,” tech. rep., 2016.
- [218] I. P. Society and Energy, “European Low Voltage Test Feeder,” 2015.
- [219] I. T. Papaioannou, A. Purvins, and C. S. Demoulias, “Reactive power consumption in photovoltaic inverters: a novel configuration for voltage regulation in low-voltage radial feeders with no need for central control,” *Prog. Photovoltaics Res. Appl.*, vol. 23, no. 5, pp. 611–619, 2015.
- [220] Tesla Motors Inc., “Tesla Powerwall,” 2015.



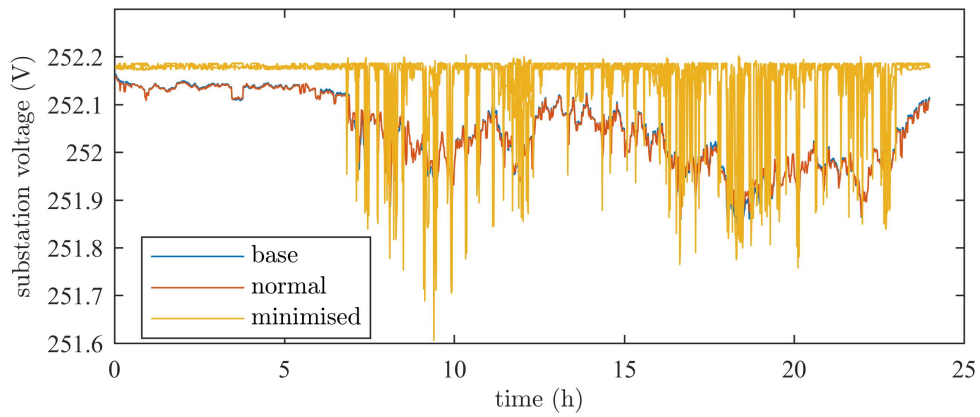
# **Appendix A**

## **Additional Results**

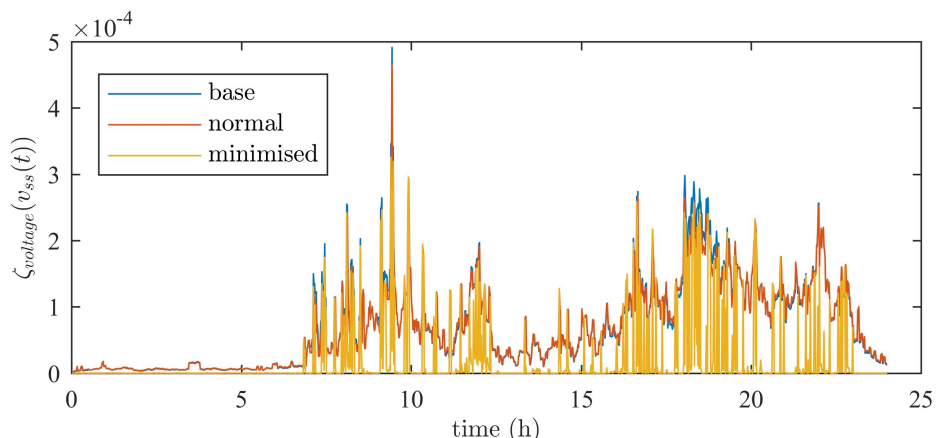
### **A.1 Improving operation performance of battery schedules at sub-half-hourly resolution**

#### **A.1.1 Additional Time Series Analysis**

Since the plots in Section 3.5.1 are averages over a 10 minute moving average window (in order to aid visual representation of the volatile data), the raw and unfiltered data is included for reference in this appended section.

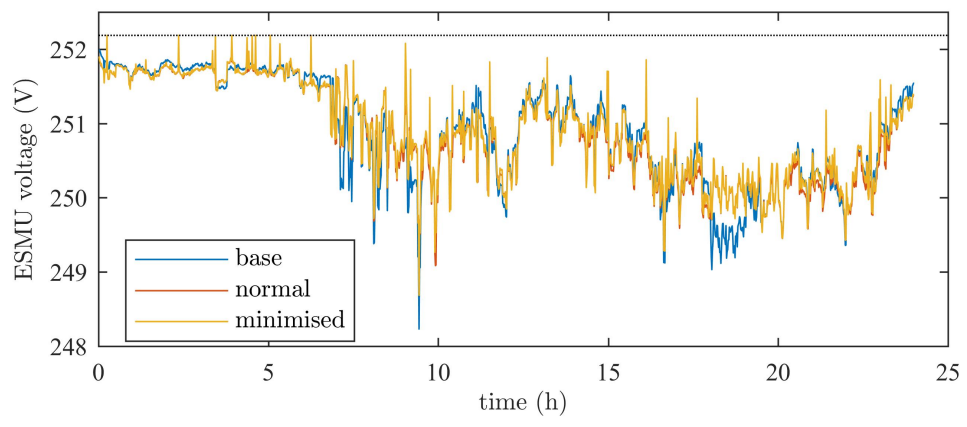


(a) Voltage levels as measured at the substation

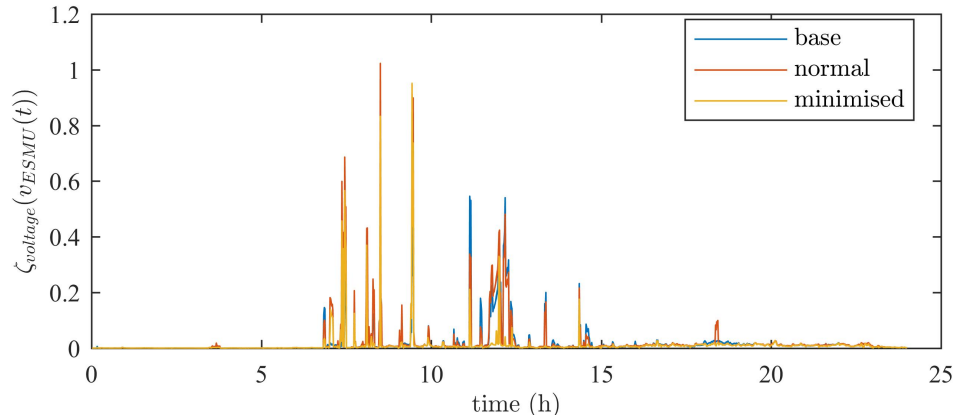


(b) Cost associated with the voltage levels as measured at the substation

Figure A.1: Additional substation voltage level comparison between base, normal and the case where the ESMU's schedule was adjusted.

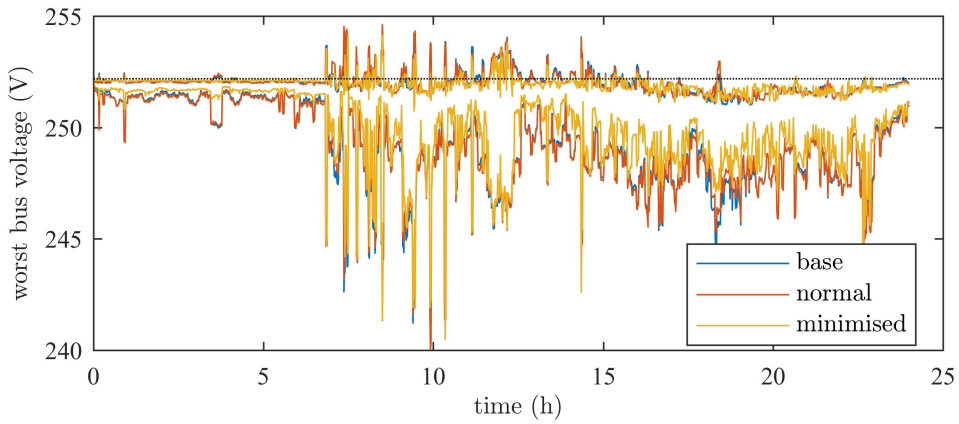


(a) ESMU voltage levels

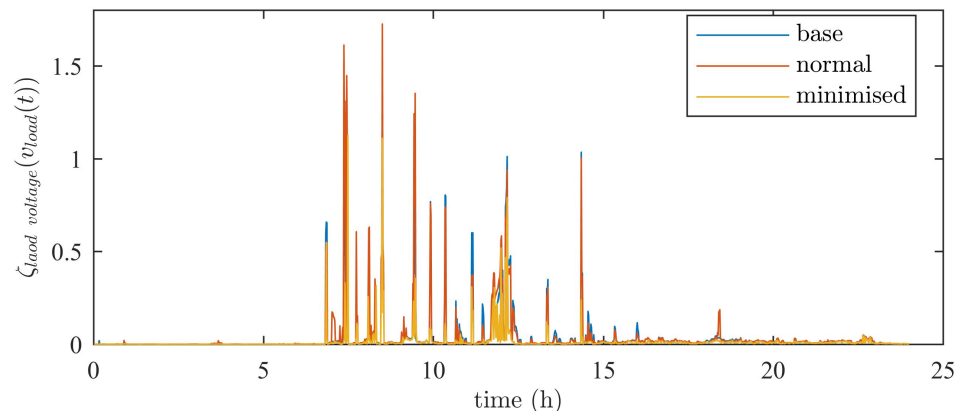


(b) Cost associated with the ESMU voltage levels

Figure A.2: Additional ESMU voltage level comparison between base, normal and the case where the ESMU's schedule was adjusted.

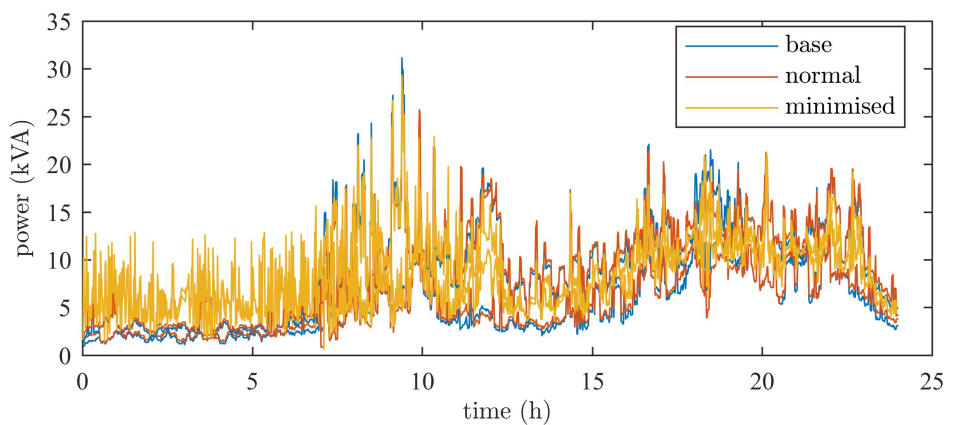


(a) Highest and lowest voltage levels in entire network

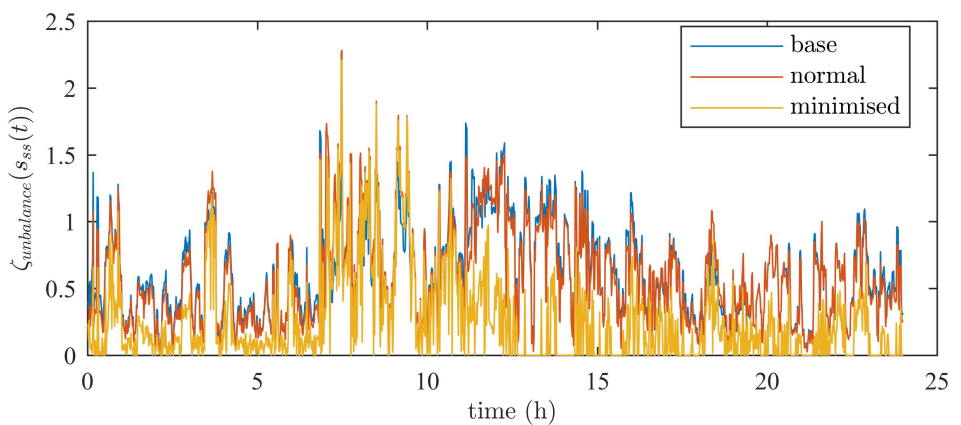


(b) Cost associated with highest and lowest voltage levels in entire network

Figure A.3: Additional voltage level comparison between base, normal and the case where the ESMU's schedule was adjusted.

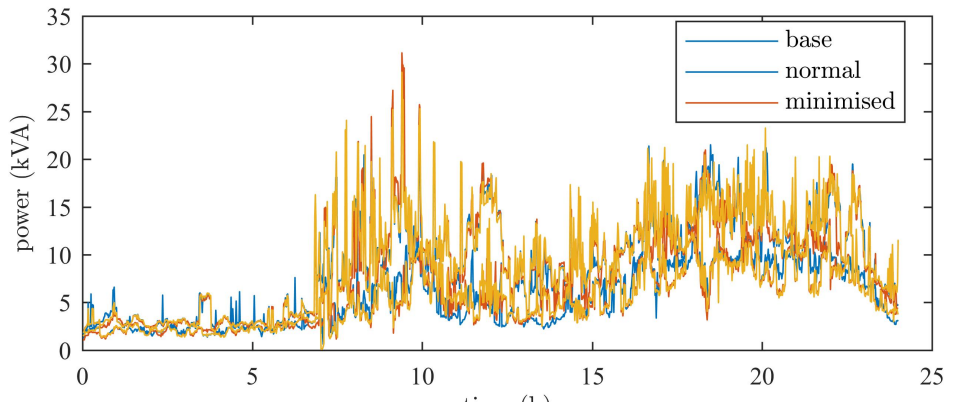


(a) Highest and lowest phase power

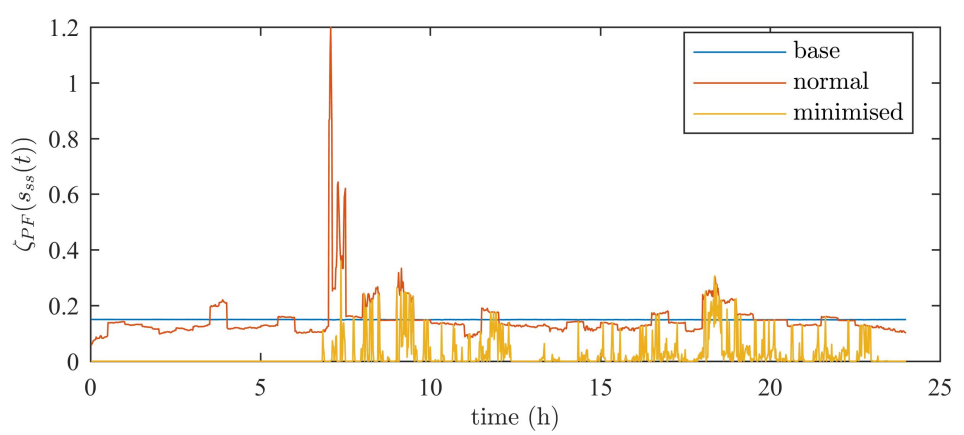


(b) Phase unbalance cost

Figure A.4: Additional phase unbalance cost comparison between base, normal and the case where the ESMU's schedule was adjusted.

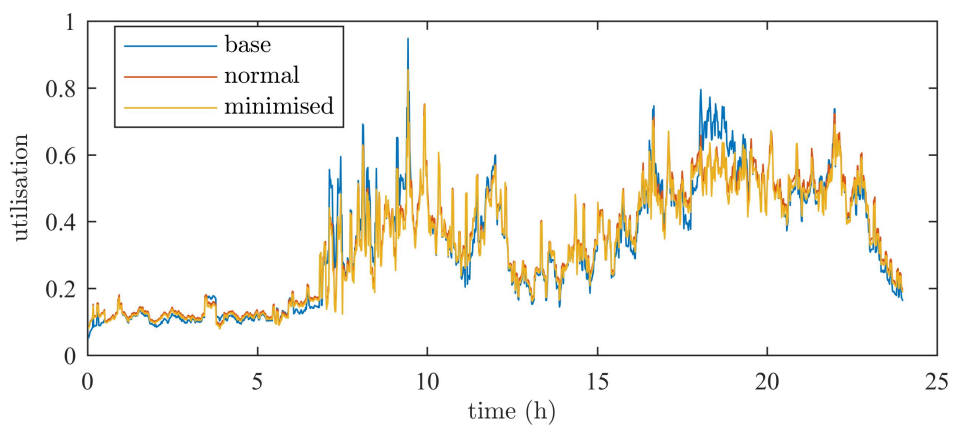


(a) Network load

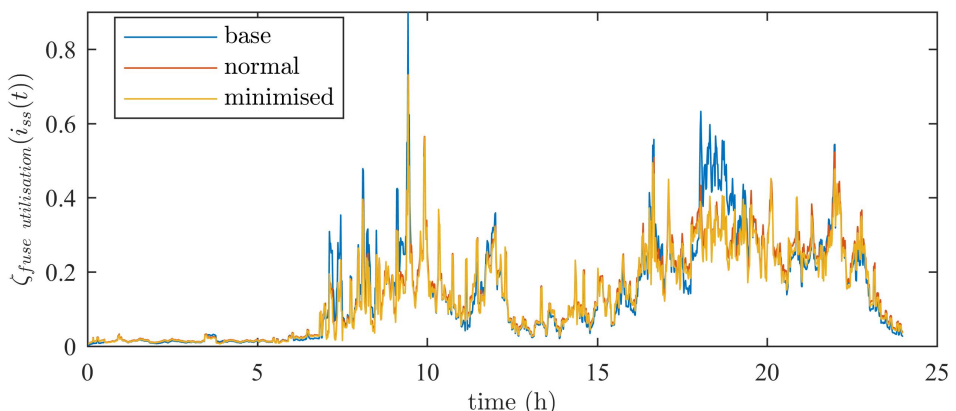


(b) Power factor

Figure A.5: Additional power factor cost comparison between base, normal and the case where the ESMU's schedule was adjusted.

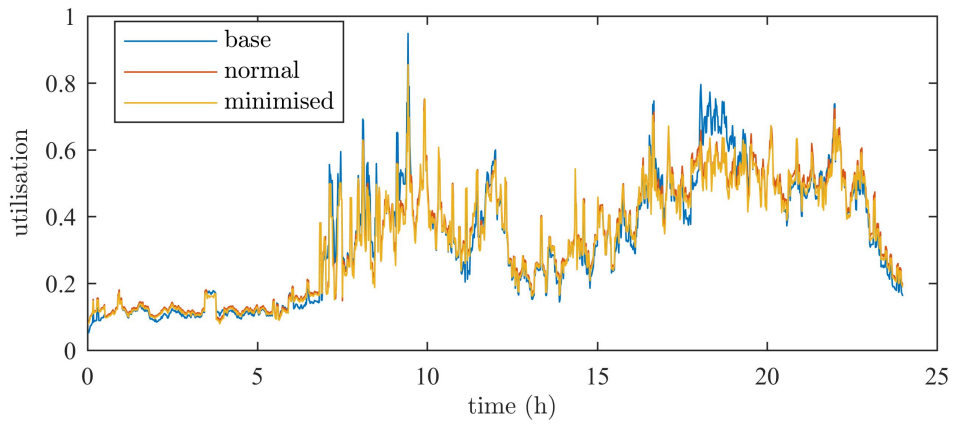


(a) Utilisation of the substation fuse

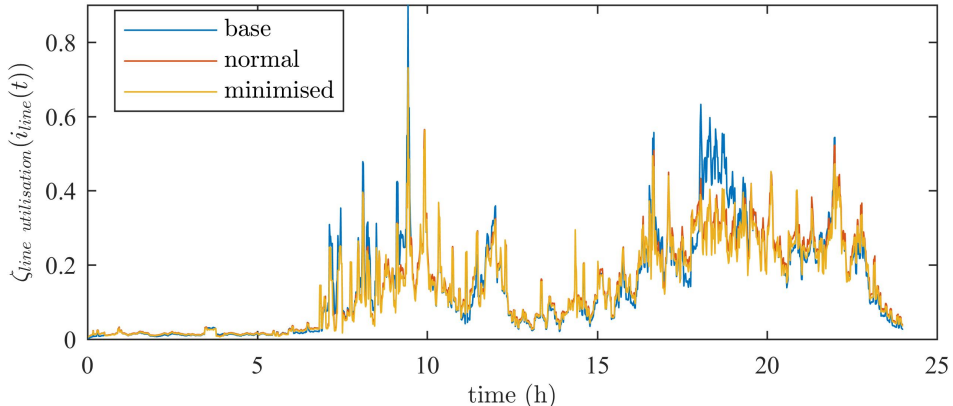


(b) Cost associated with the utilisation of the substation fuse

Figure A.6: Additional comparison of the substation fuse utilisation between base, normal and the case where the ESMU's schedule was adjusted.

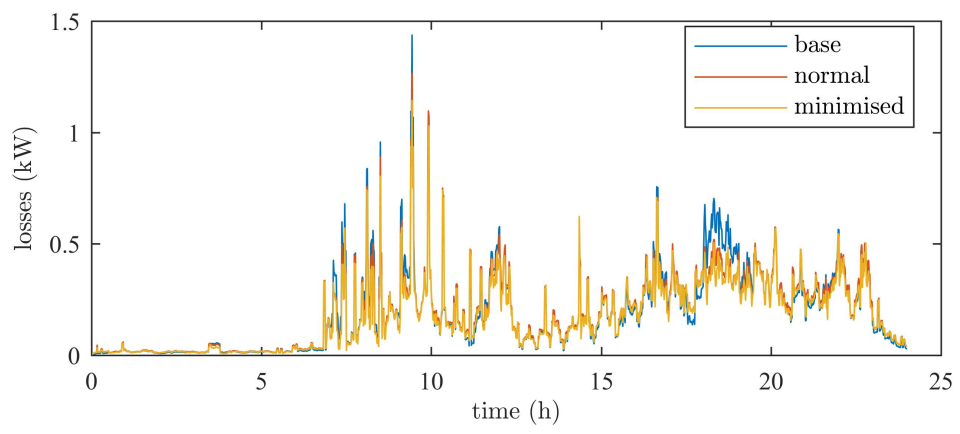


(a) The highest line utilisation of any line in the entire network

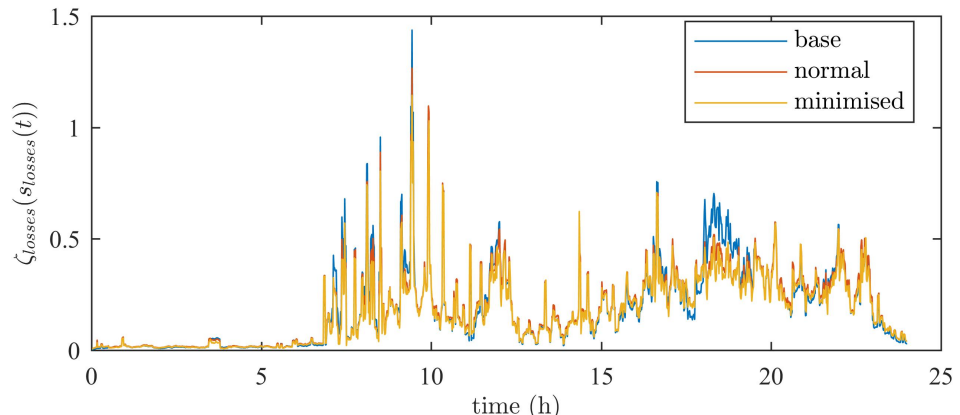


(b) The highest cost associated to the highest line utilisation of any line in the entire network

Figure A.7: Additional line utilisation comparison between base, normal and the case where the ESMU's schedule was adjusted.



(a) Distribution losses



(b) Cost associated to distribution losses

Figure A.8: Additional comparison of distribution loss cost between base, normal and the case where the ESMU's schedule was adjusted.

### A.1.2 Additional Difference Analysis

Only the cost differences for the case of actual cost minimisation were compared in Section 3.5.2. Therefore, all remaining cost differences have been included in this appended section.

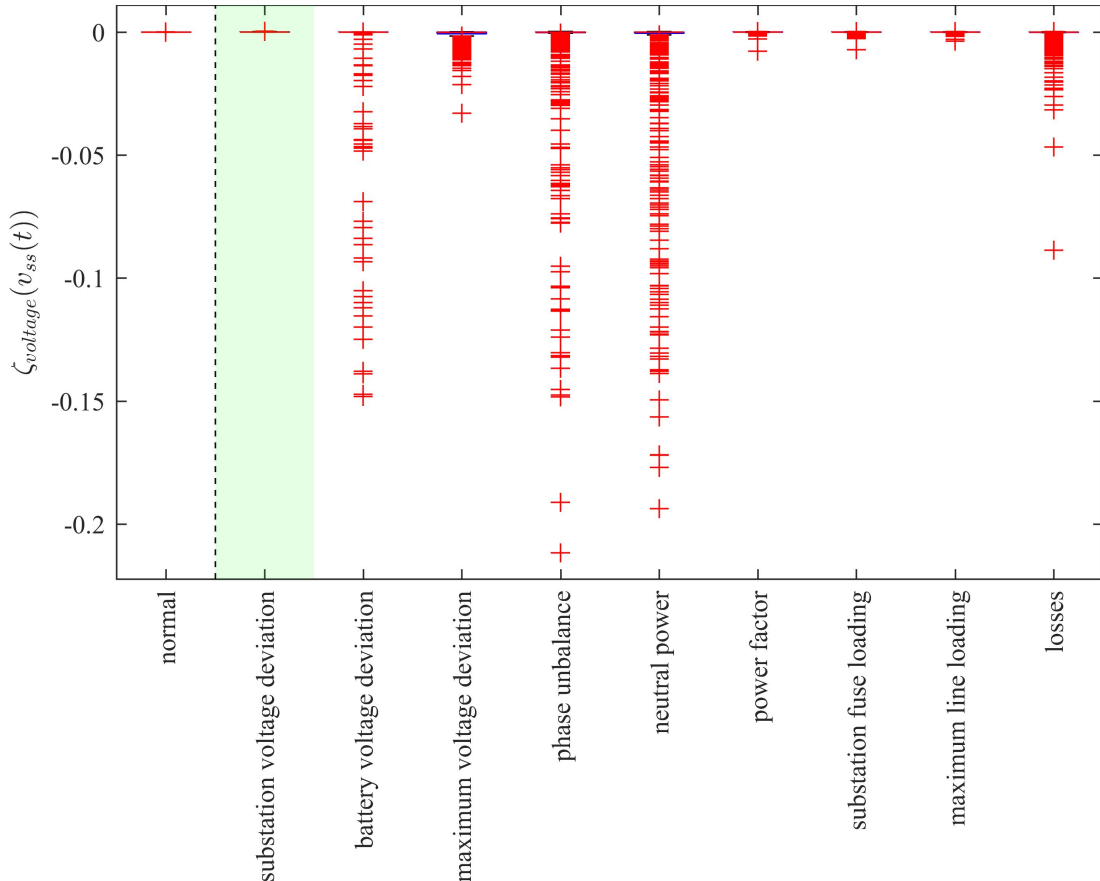


Figure A.9: Cost difference spread, based on the ESMU schedule adjustment to minimise substation voltage deviation

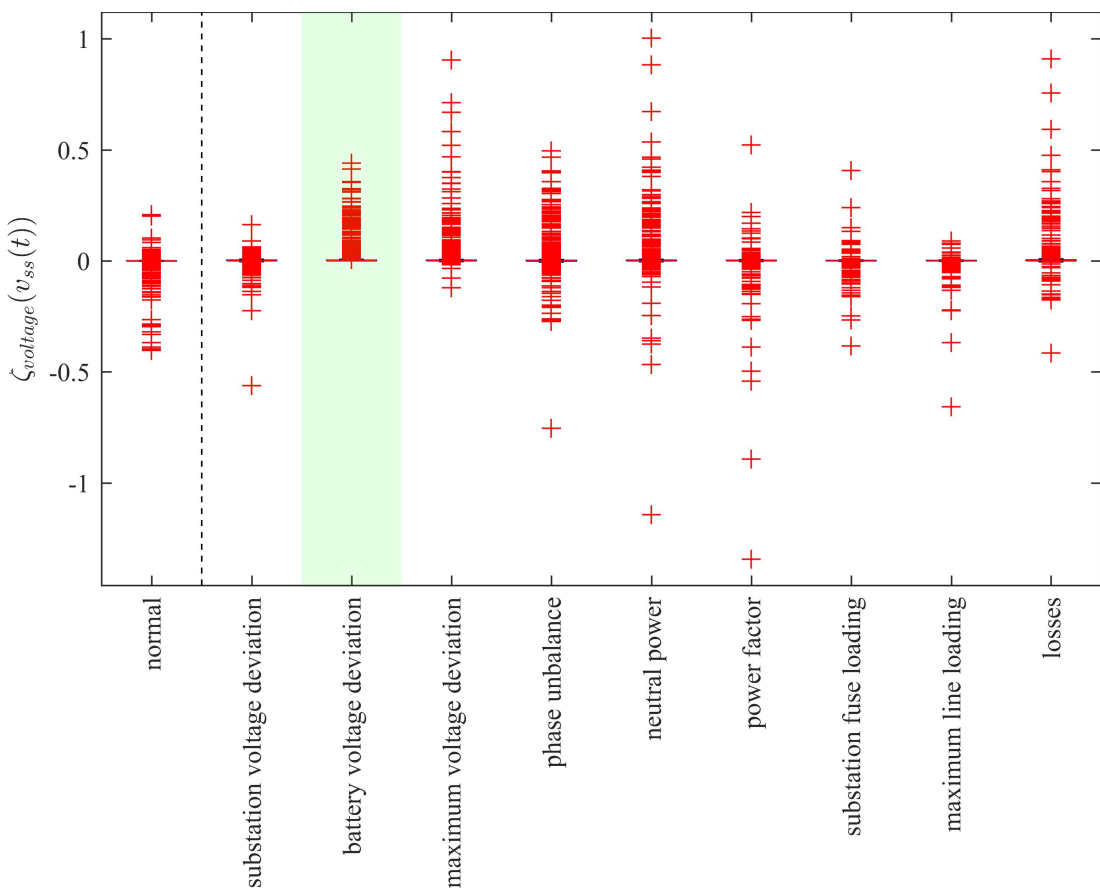


Figure A.10: Cost difference spread, based on the ESMU schedule adjustment to minimise ESMU's PCC voltage deviation

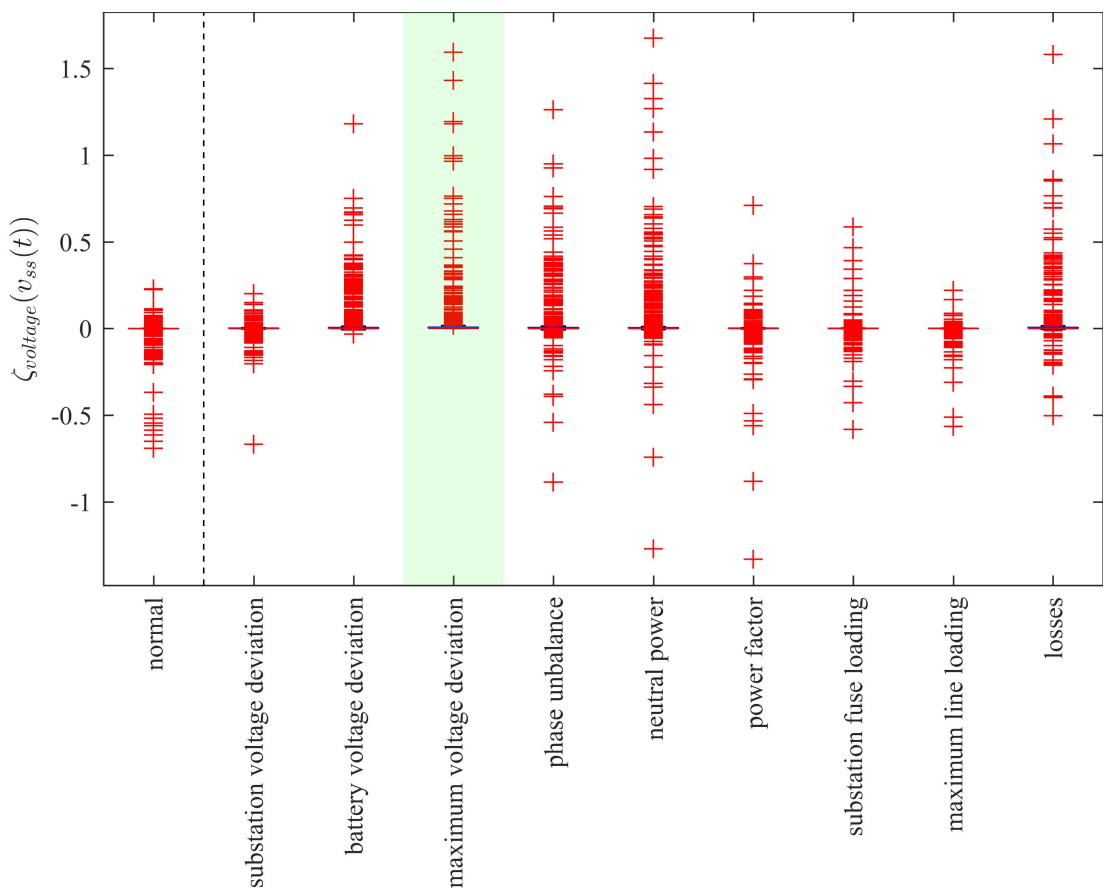


Figure A.11: Cost difference spread, based on the ESMU schedule adjustment to minimise the maximum voltage deviation on any bus of the network

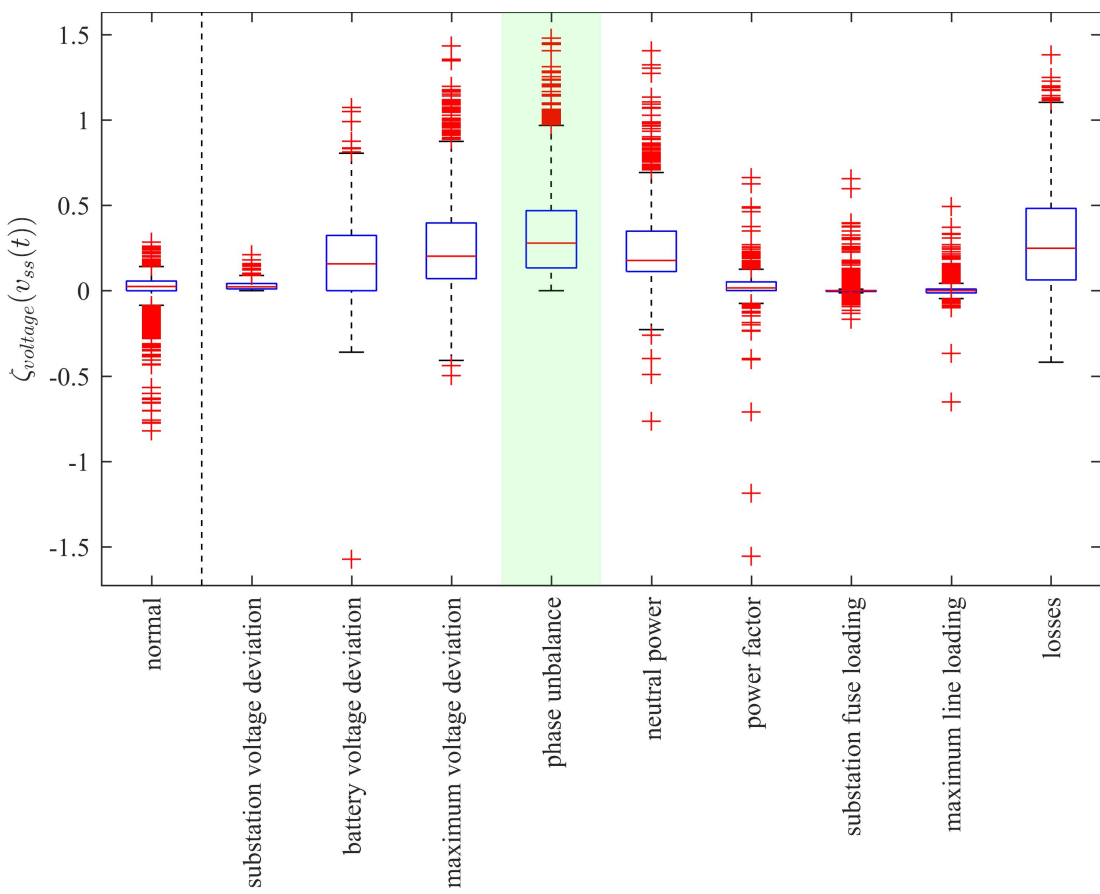


Figure A.12: Cost difference spread, based on the ESMU schedule adjustment to minimise the network's phase unbalance

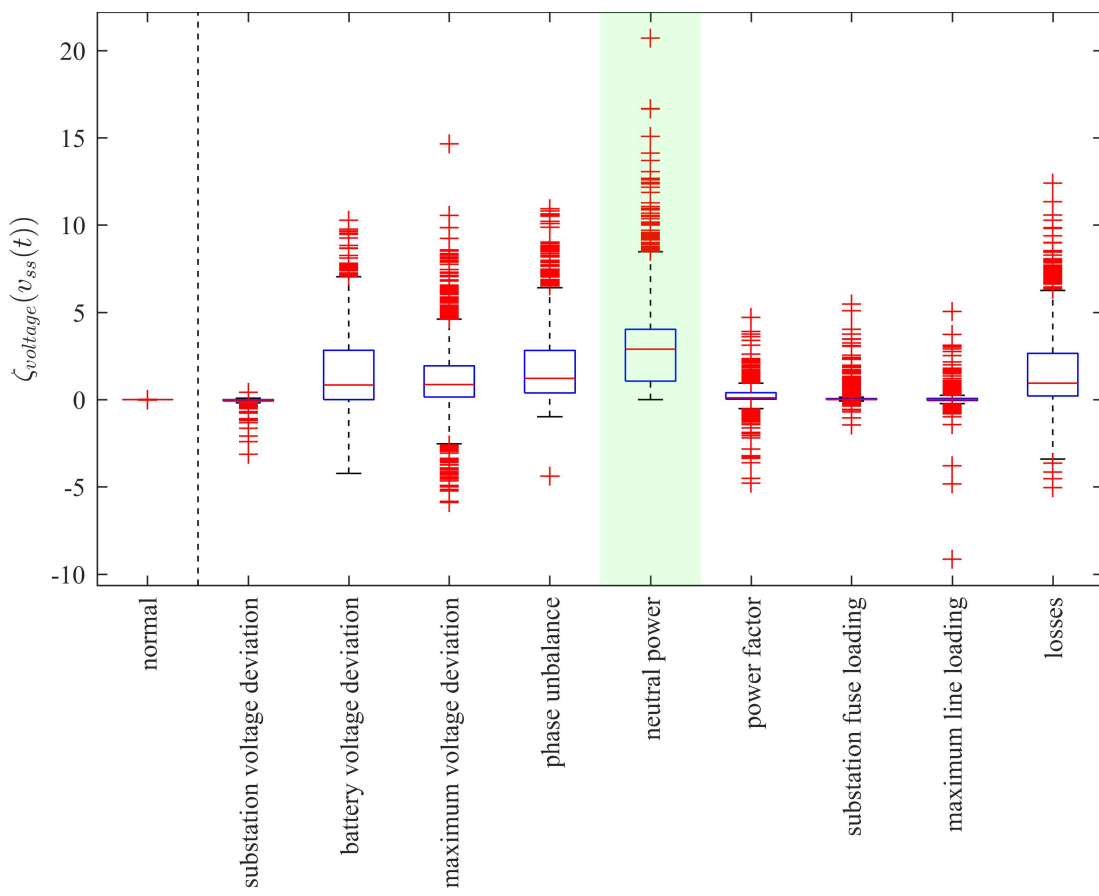


Figure A.13: Cost difference spread, based on the ESMU schedule adjustment to minimise the network's power flow in the neutral conductor

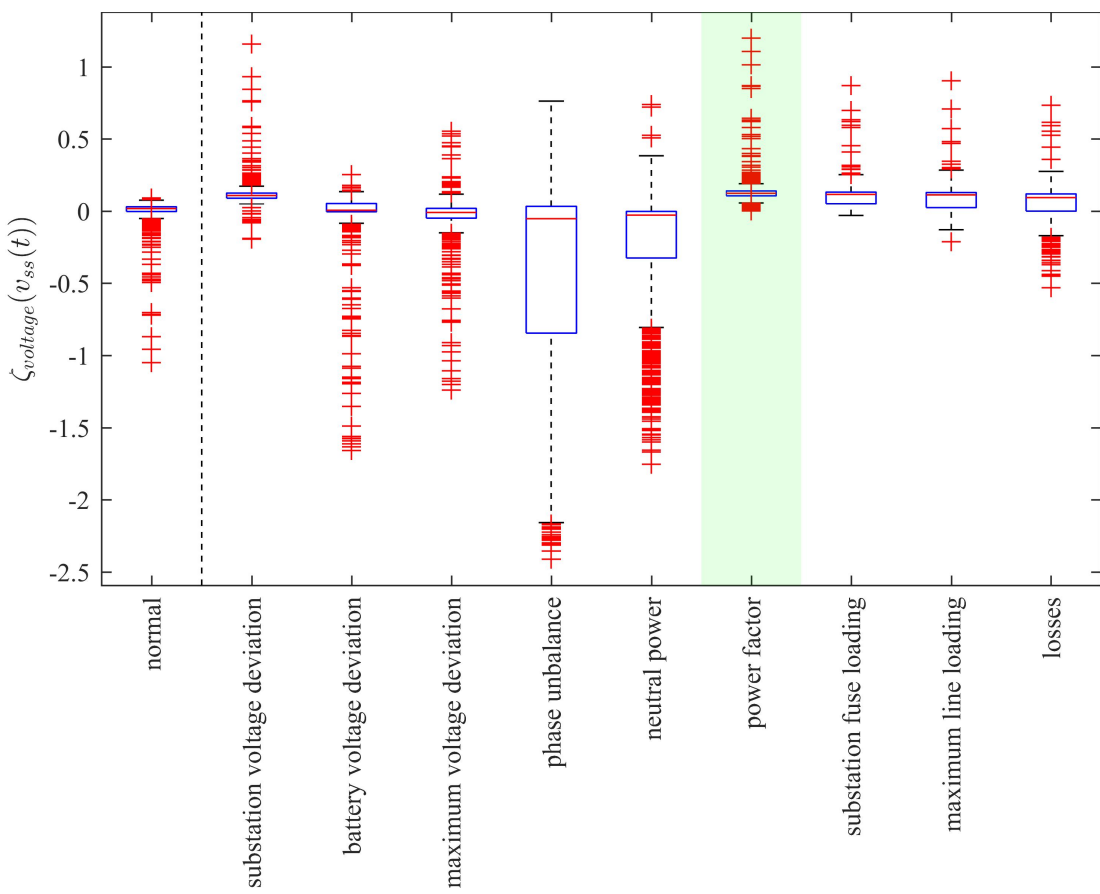


Figure A.14: Cost difference spread, based on the ESMU schedule adjustment to minimise the network's offset to unity power factor

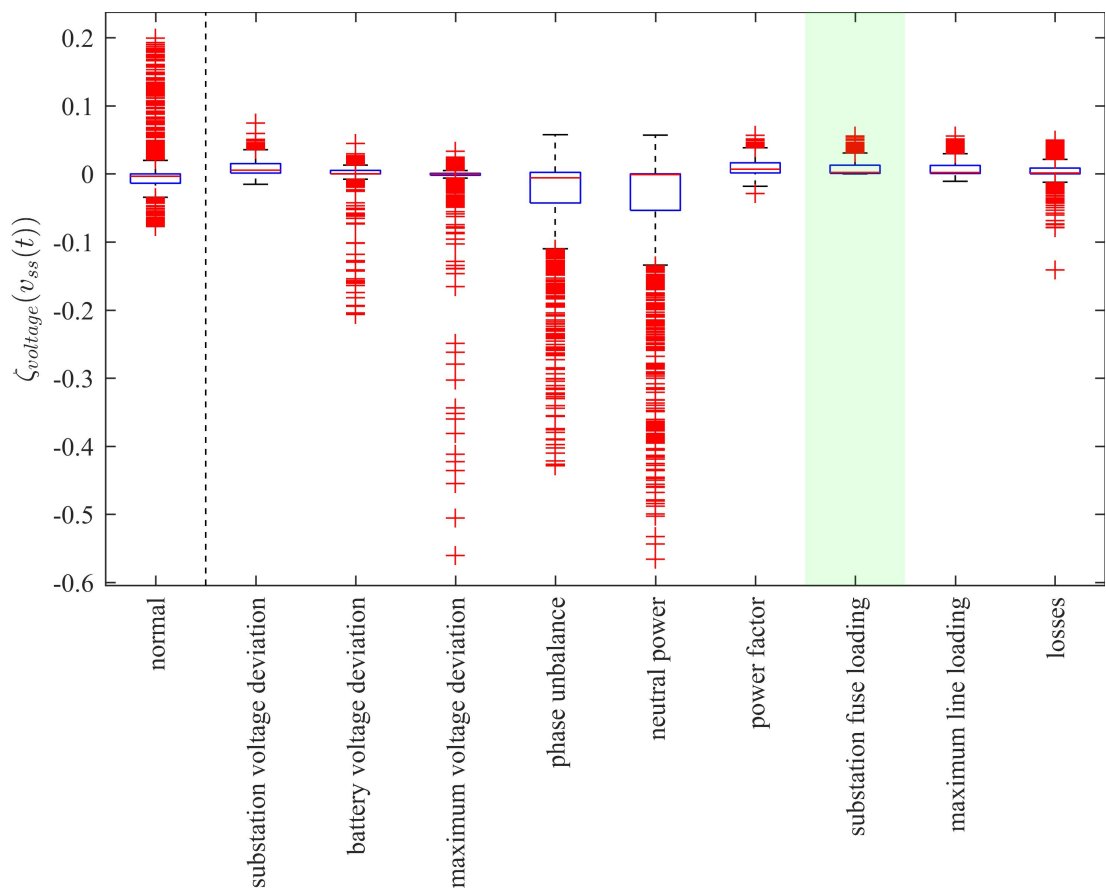


Figure A.15: Cost difference spread, based on the ESMU schedule adjustment to minimise the substation's fuse utilisation

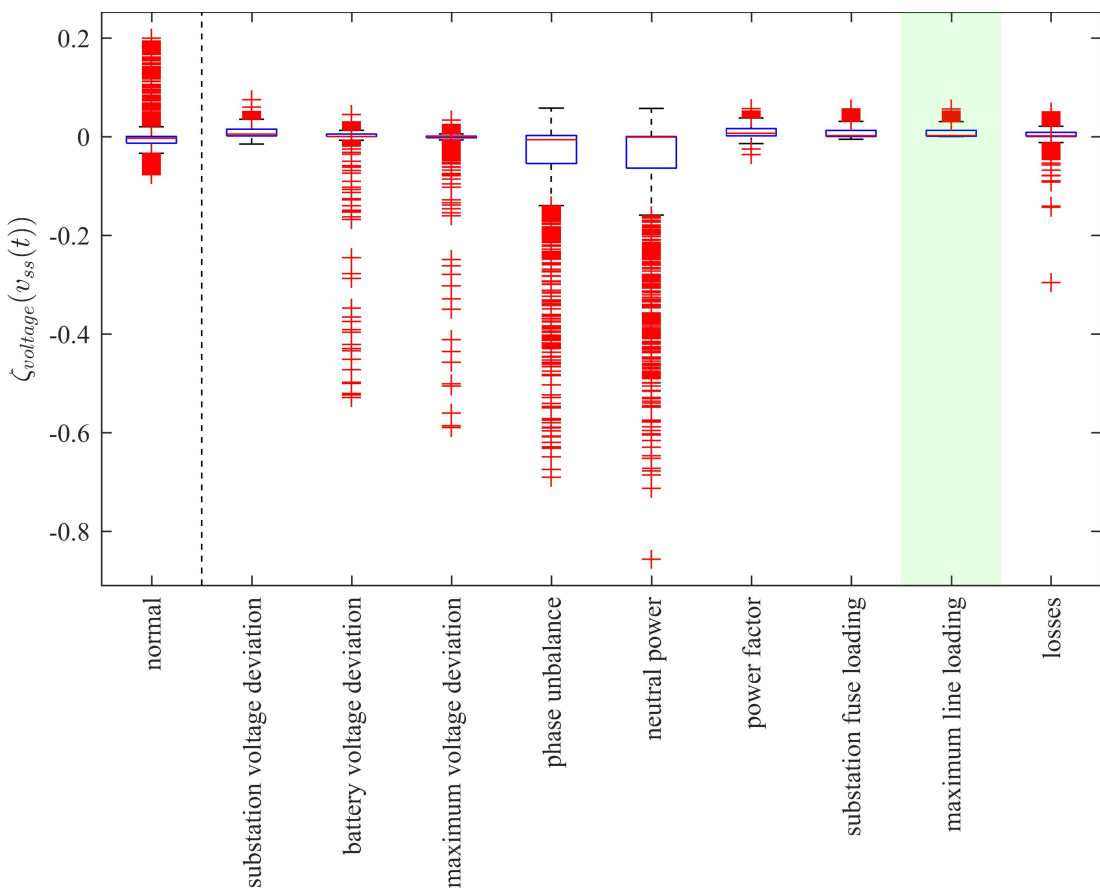


Figure A.16: Cost difference spread, based on the ESMU schedule adjustment to minimise the maximum line utilisation of any line in the network

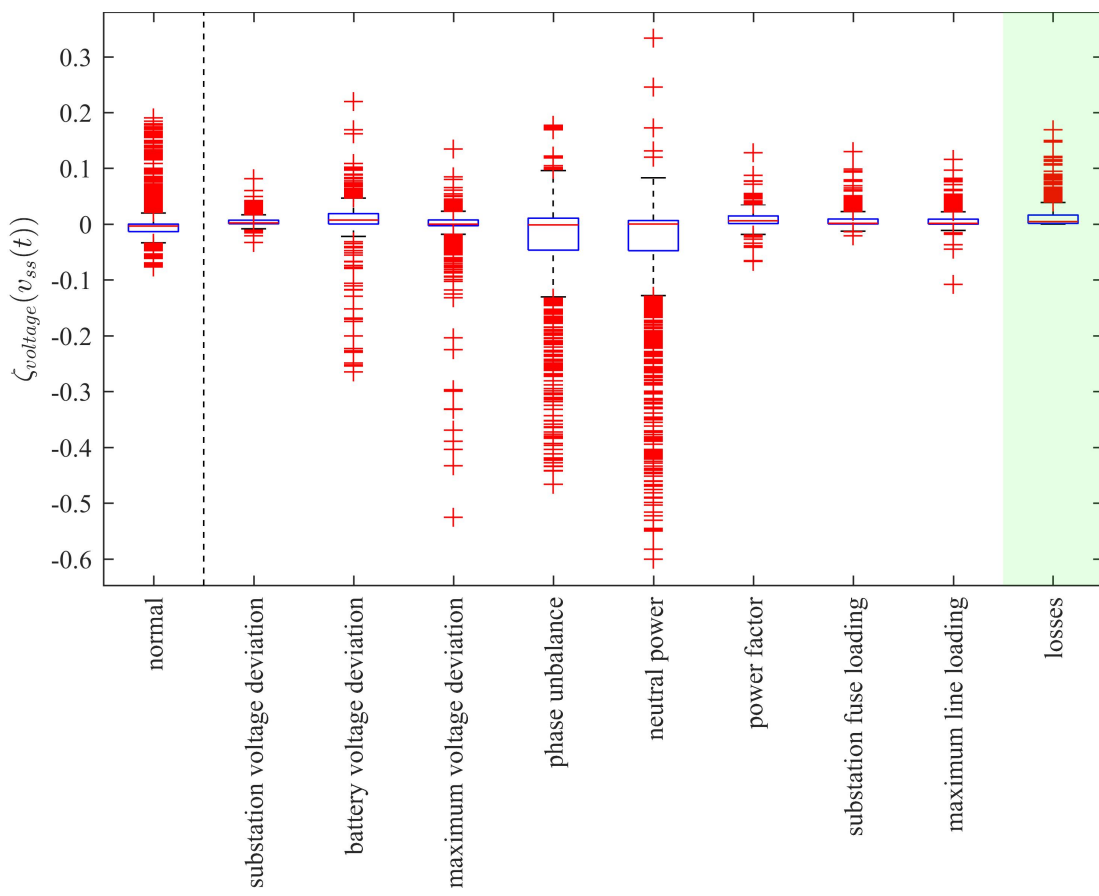


Figure A.17: Cost difference spread, based on the ESMU schedule adjustment to minimise distribution losses

### A.1.3 Probability Density Analysis

The details described in this section address the prerequisites for the performed null hypothesis test in Section 3.5.3. These steps lie beyond the content of the corresponding chapter, yet have been included for completeness. Here, each step to condition the raw data for the  $t$ -test is explained in detail.

The original data is a highly volatile and non-stationary time-series that has a non-gaussian probability distribution. However, in order to apply the  $t$ -test, these criteria have to be met. Data conditioning steps were followed for each dataset that would modify the properties of the time-series without modifying their context. These steps are listed below and go as follows: First

1. the time-series is rescaled using the  $\log()$  function, then
2. the rescaled values is averaged over  $N$  samples, then
3. the averages are split into two distinct sections (one prior to 11am and one after 11am), then
4. the sections are compared against each other (i.e. by computing the difference), then
5. the comparison's auto-correlation is computed to check for the presence of self-dependence.
  - (a) If the self-dependence is low enough (i.e. within confidence interval) the  $t$ -test is executed
  - (b) otherwise the data is feathered and the auto-correlation is tested again, and
  - (c) if the results still indicate a self-dependence, then a different  $N$  is chosen and the steps are repeated.

To visualise this procedure, the dataset corresponding to the minimisation of distribution losses, i.e.  $\zeta_{\text{losses}}()$ , is presented and the data modifications are explained. Since the steps apply to all data sets, only one is being presented in this appendix.

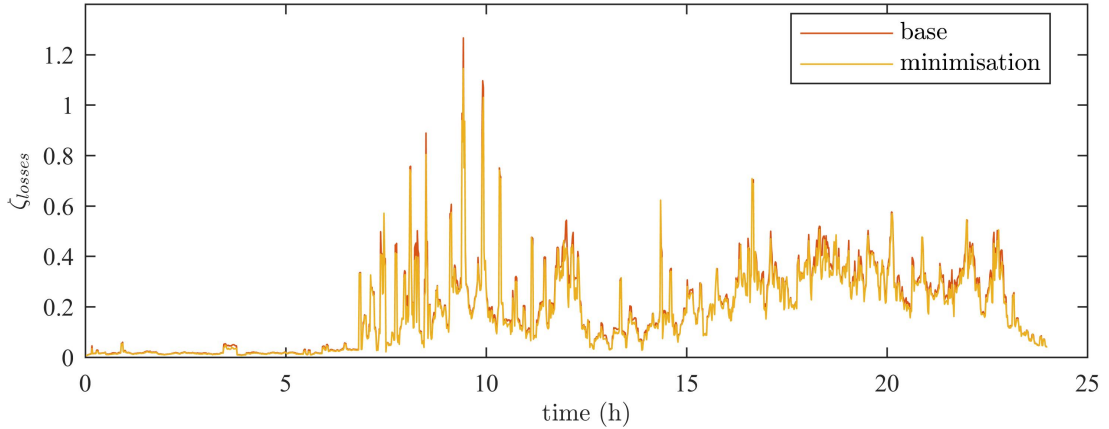


Figure A.18: Raw time-series that are supposed to be compared.

Figure A.18 shows the raw data of the two time-series that are going to be compared in the  $t$ -test. Since this data is very spiky and has many values located closely to zero, they are scaled using the  $\log()$  function.

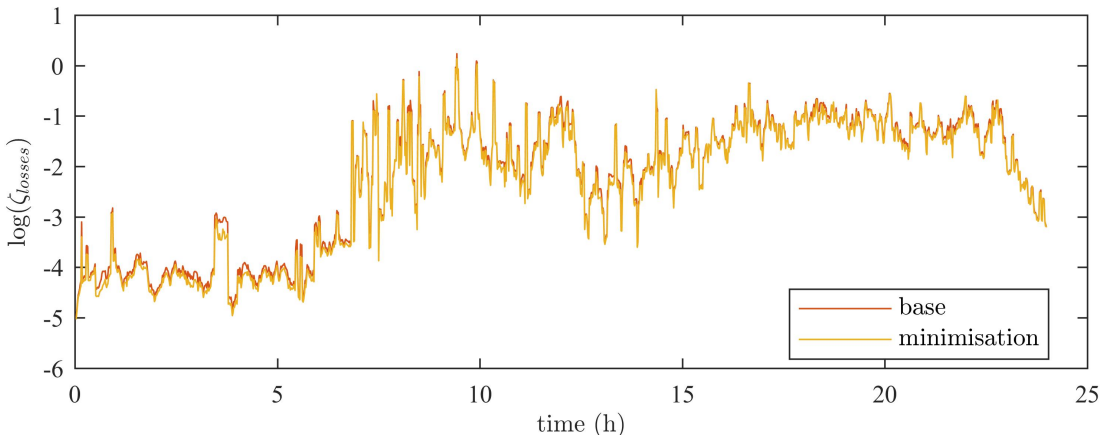


Figure A.19: Rescaled time-series that are supposed to be compared.

Figure A.19 shows this rescaled cost. It can be observed how differences, e.g. the increase in load during the morning hours, has become more apparent. Nonetheless, this data is still volatile and is averaged over  $N$  values.

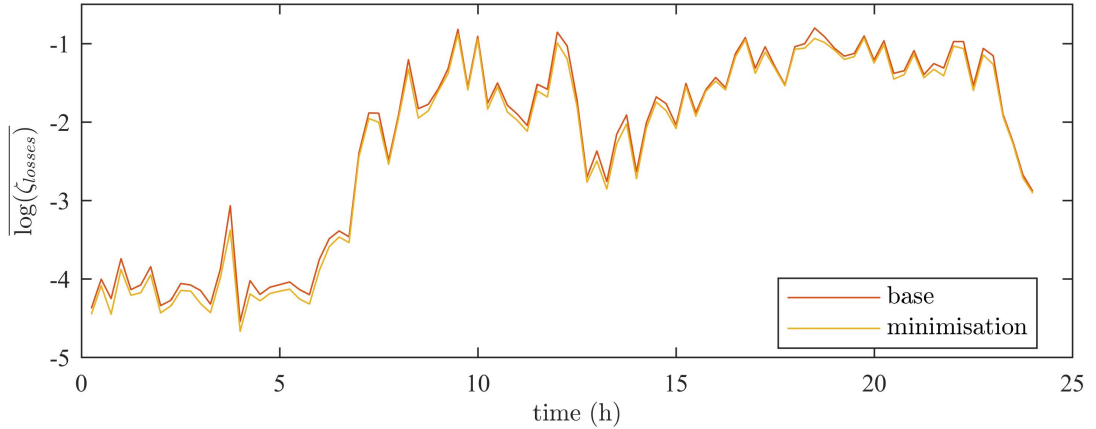


Figure A.20: Averaged log-scaled time-series.

The two different levels in the data can clearly be observed in Figure A.20. This distinction in levels allows an easy separation of the data into two sections: *morning* and *afternoon*.

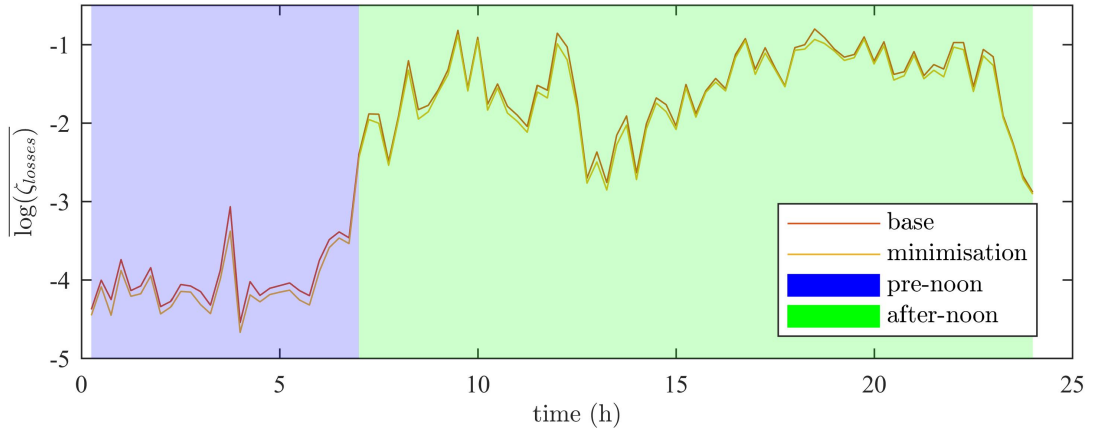


Figure A.21: Splitting of the conditioned data into two stationary sections

The preconditioned data in the two sections, that are highlighted in Figure A.21, are now compared by computing their difference. Figure A.22 shows this difference.

This difference is now auto-correlated and to indicate if any “self-dependence” (i.e. indicating auto-regression) is still present in the data. Results from both sections are shown in Figure A.23

Using the statistics package *MINITAB*, the significance bounds are determined. If any auto-correlation value lies outside this bound, then the data still contains

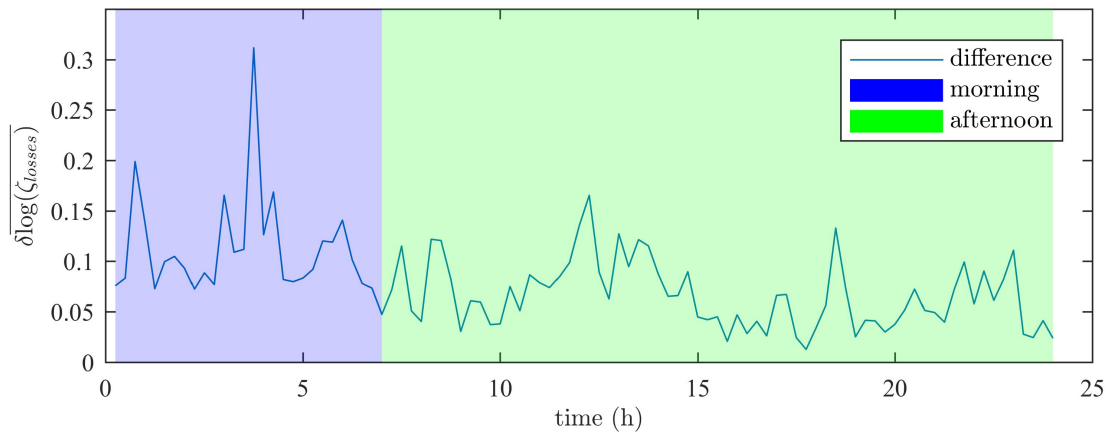


Figure A.22: Difference of the two pre-conditioned time-series.

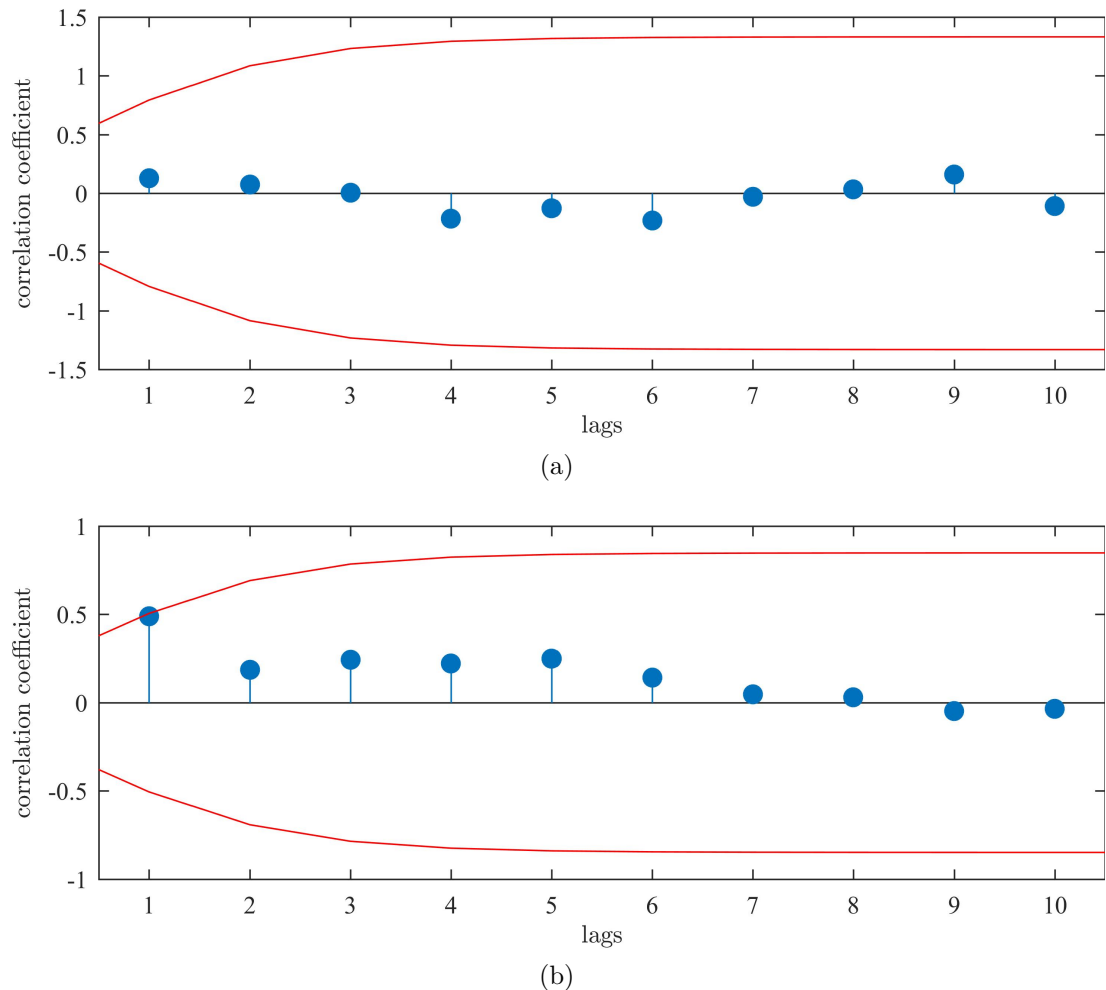


Figure A.23: Auto-correlation of signal for (A.23a) morning and (A.23b) afternoon sections

significant self-dependence and must be re-conditioned. In the case presented in Figure A.23 however, the auto-correlation indices lie within the bounds for all lags. Therefore, the criteria for the *t*-test are met and the data can be assessed. In this case, the *t*-test resulted in  $p < 0.001$ , which is the same value that is used in the “Probability Density Analysis” Section 3.5.



# Appendix B

## Multi-Agent Systems

This appendix, Appendix B, presents additional details on the MAS implementation. More specifically, the method used to implement FIPA are presented, and the main communication protocols that war used within this method are detailed.

### B.1 FIPA Implementation

The Foundation for Intelligent Physical Agents (FIPA) has established a standard set of protocols that allow agents to interact with each other. These protocols form the so called Agent Communication Language (ACL) Telecom Italia has successively begun to develop a JAVA Agent Development Framework (JADE) that puts the entire ACL at the programmer's disposal. Published under LGPL (i.e. the Lesser General Public License Version 2), JADE is a free software package that can easily be used to construct large MASs.

In order to perform optimisation functions however, a way to interact with OpenDSS was required. On Microsoft Windows, the ActiveX COM server provided a simple access point to MATLAB and OpenDSS specific functions, and the JAVA COM Bridge (JACOB) made this server accessible to the JAVA run-time environment.

JADE and JACOB were, respectively, obtained from the following two sources:

- JADE: <http://jade.tilab.com>
- JACOB: <https://sourceforge.net/projects/jacob-project/>

By including the *jade.jar* and *jacob.jar*, and the corresponding Dynamic Linked Libraries (DLLs) *jacob-1.8-M2-x86.dll* and *jacob-1.8-M2-x64.dll*, FIPA was fully implemented and linked to MATLAB and OpenDSS.

## B.2 Communication Protocols

The main three protocols that were used within Chapter 5 are:

1. FIPA Query Protocol (FIPA-standard-SC00027H)
2. FIPA Brokering Protocol (FIPA-standard-SC00033H)
3. FIPA ContractNet Protocol (FIPA-standard-SC00029H)

The flowcharts for these three protocols were taken from the corresponding standards and, for completeness, are explained in the following three subsections.

### B.2.1 FIPA Query Protocol

Figure B.1 shows the complete flow chart of the FIPA Query protocol. This protocol is initiated by an “*initiator*” that send a “*query*” message (either “if” or “reference” message) to a “*Participant*”. In Chapter 5, the initiators were the brokering agents of the loads and the participant were the brokering agents of the energy supplier. The *participant* replies either with an “*agree*” to inform the *initiator* that the query is received, or a “*refuse*” message is sent to terminate the communication. After an *agree* message, the *participant* sends the required information in an “*inform*” message (as a reply to the “if” or “reference” query), or a “*failure*” is sent when no data is available. In Chapter 5, the data that is sent in the *inform* messages includes the daily load profile onto which the EV agents should superimpose their charging demand.

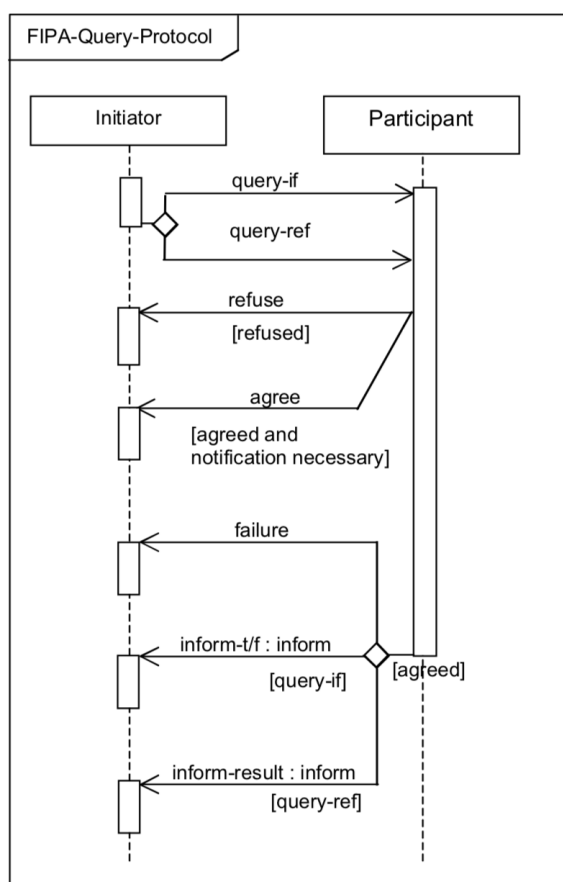


Figure B.1: FIPA Query Protocol flow chart

### B.2.2 FIPA Brokering protocol

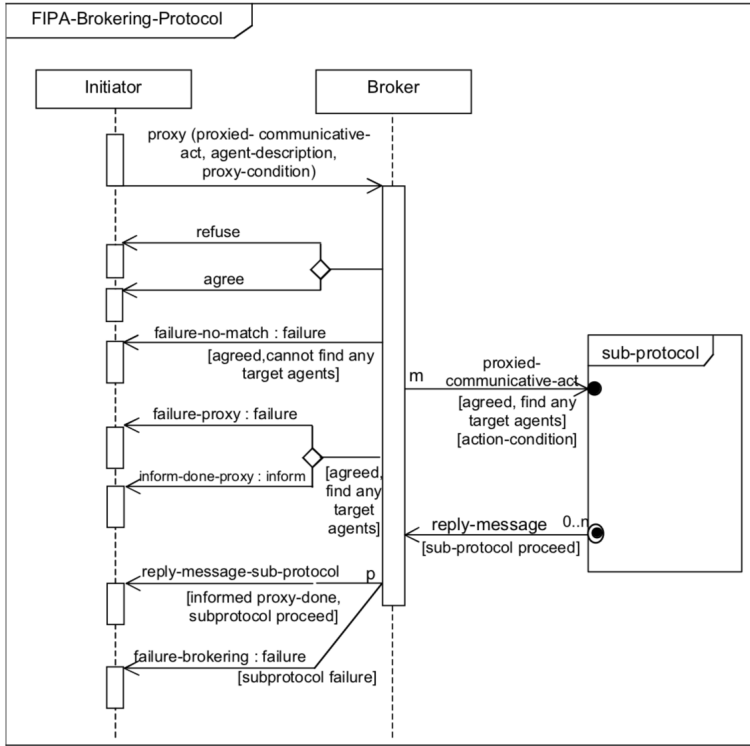


Figure B.2: FIPA Brokering Protocol flow chart

The brokering protocol, as shown in Figure B.2, is used to delegate an agent's task to a different agent in order to free up its own computational resources. In Chapter 5 for instance, the load agents never communicate with the energy supplier directly, since the applying and undoing of power profiles is delegated to their brokering agents. The protocol is initiated by assigning a broker to a load agent by sending a “*proxy*” message. This message contains the required information for the broker, e.g. the power profile a buying broker should apply. If the broker can fulfil this request, then an “*agree*” message is sent, otherwise a “*refuse*” message is sent. The broker uses the FIPA Query protocol, as explained in Section B.2.1, to obtain a list of broker agents that are linked to energy suppliers, which can be used to apply the load's demand profile. However, if no such broker is found, then a “*failure*” (i.e. “no match”) message is sent. Alternatively, the broker begins its delegating task and it

forwards the requested demand profile to the corresponding energy supplier (i.e. it uses the FIPA ContractNet protocol as outlined in the next section, Section B.2.3). If an error occurs during this delegating process, then a “*failure*” message is sent (i.e. “proxy failure” or “inform failure”). Upon successful delegation, the broker replies to the “*Initiator*” with a “*reply*” message that contains information about the applied demand profile. Theoretically, this information can also contain pricing information, yet this feature was disregarded since it lies outside the scope of this thesis.

### B.2.3 FIPA ContractNet Protocol

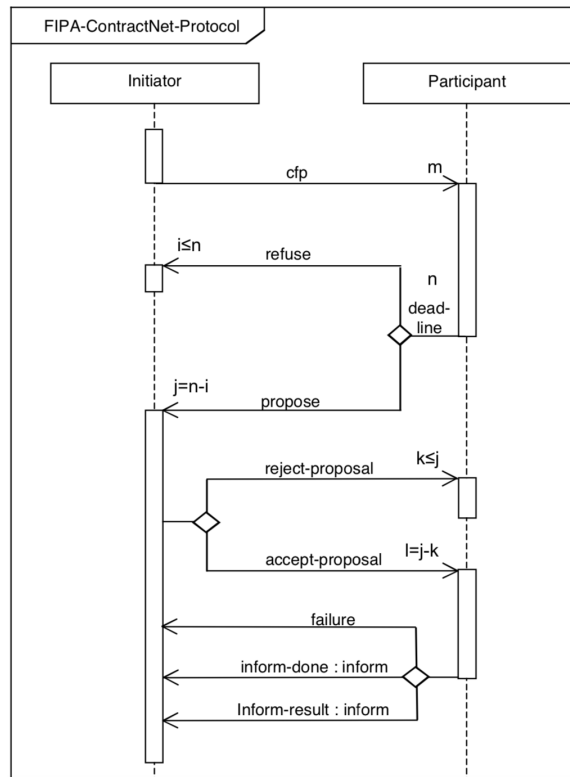


Figure B.3: FIPA ContractNet Protocol flow chart

Figure B.3 shows the FIPA ContractNet Protocol that allows an agent to negotiate a binding contract. After executing this dual handshake protocol, all contract participants are informed about the final contract decision and no information is lost during the message exchange. The protocol is initiated by an “*Initiator*”, who sends

a “*Call For Proposal*” (*cfp*) to  $m$  “*Participants*”. This *cfp* contains a deadline within which all agents that do want to participate should reply. They can reject their participation by sending a “*refuse*” message, or acknowledge their participation by sending a “*propose*” message that also contains proposition information (e.g. pricing information). Once all participants have replied or the deadline has expired, the *initiator* continues executing. It collects and assesses all proposals, chooses the accepted and rejected ones and, respectively, issues “*accept*” and “*reject*” notifications. The participating agents reply with an “*inform*” message if they acknowledge the “*accept*” or “*reject*” message, and in case of an error, they reply with a “*failure*” message.